Review

Progress in ceramic materials and structure design toward advanced thermal barrier coatings

Zhi-Yuan WEI[a,†], Guo-Hui MENG[a,†], Lin CHEN[a,†], Guang-Rong LI[a,†], Mei-Jun LIU[a,†],
Wei-Xu ZHANG[b,†], Li-Na ZHAO[c,†], Qiang ZHANG[d,†], Xiao-Dong ZHANG[e,†],
Chun-Lei WAN[f,†], Zhi-Xue QU[g,†], Lin CHEN[h,†], Jing FENG[h,†], Ling LIU[i,†],
Hui DONG[j,†], Ze-Bin BAO[k,†], Xiao-Feng ZHAO[l,†], Xiao-Feng ZHANG[m,†],
Lei GUO[n,†], Liang WANG[o,†], Bo CHENG[p,†], Wei-Wei ZHANG[q,†], Peng-Yun XU[r,†],
Guan-Jun YANG[a,*], Hong-Neng CAI[a,*], Hong CUI[c,*], You WANG[e,*], Fu-Xing YE[n,*],
Zhuang MA[i,*], Wei PAN[f,*], Min LIU[m,*], Ke-Song ZHOU[m,*], Chang-Jiu LI[a,*]

[a]*State Key Laboratory for Mechanical Behavior of Materials, School of Materials Science and Engineering, Xi'an Jiaotong University, Xi'an 710049, China*
[b]*State Key Laboratory for Strength and Vibration of Mechanical Structures, Department of Engineering Mechanics, School of Aerospace Engineering, Xi'an Jiaotong University, Xi'an 710049, China*
[c]*Xi'an Aerospace Composite Research Institute, Xi'an 710025, China*
[d]*AECC Beijing Institute of Aeronautical Materials, Beijing 100095, China*
[e]*School of Materials Science and Engineering, Harbin Institute of Technology, Harbin 150001, China*
[f]*State Key Laboratory of New Ceramics & Fine Processing, School of Materials Science and Engineering, Tsinghua University, Beijing 100084, China*
[g]*Faculty of Materials and Manufacturing, Key Laboratory of Advanced Functional Materials, Education Ministry of China, Faculty of Materials and Manufacturing, Beijing University of Technology, Beijing 100124, China*
[h]*Faculty of Materials Science and Engineering, Kunming University of Science and Technology, Kunming 650093, China*
[i]*School of Materials Science and Engineering, Beijing Institute of Technology, Beijing 100081, China*
[j]*Xi'an Key Laboratory of High Performance Oil and Gas Field Materials, School of Materials Science and Engineering, Xi'an Shiyou University, Xi'an 710065, China*
[k]*Shi-Changxu Innovation Center for Advanced Materials, Institute of Metal Research, Chinese Academy of Sciences, Shenyang 110016, China*
[l]*Shanghai Key Laboratory of Advanced High-temperature Materials and Precision Forming, Shanghai Jiao Tong University, Shanghai 200240, China*
[m]*National Engineering Laboratory for Modern Materials Surface Engineering Technology, the Key Lab of Guangdong for Modern Surface Engineering Technology, Institute of New Materials, Guangdong Academy of Sciences, Guangzhou 510650, China*
[n]*School of Materials Science and Engineering, Tianjin University, Tianjin 300072, China*
[o]*Integrated Computational Materials Research Centre, Shanghai Institute of Ceramics,*

† These authors contributed equally to this work.

* Corresponding authors.

E-mail: G.-J. Yang, ygj@mail.xjtu.edu.cn; H.-N. Cai, hntsai@mail.xjtu.edu.cn; H. Cui, cuih1969@126.com; Y. Wang, y-wang@hit.edu.cn;
F.-X. Ye, yefx@tju.edu.cn; Z. Ma, hstrong929@bit.edu.cn; W. Pan, panw@mail.tsinghua.edu.cn; M. Liu, liumin@gdas.gd.cn;
K.-S. Zhou, kszhou2004@163.com; C.-J. Li, licj@mail.xjtu.edu.cn

Chinese Academy of Sciences, Shanghai 201899, China
[p]State Key Laboratory of Advanced Processing and Recycling of Non-ferrous Metal,
Lanzhou University of Technology, Lanzhou 730050, China
[q]School of Materials Science and Engineering, Chang'an University, Xi'an 710064, China
[r]Department of Mechanical and Electrical Engineering, Ocean University of China, Qingdao 266100, China

Abstract: Thermal barrier coatings (TBCs) can effectively protect the alloy substrate of hot components in aeroengines or land-based gas turbines by the thermal insulation and corrosion/erosion resistance of the ceramic top coat. However, the continuous pursuit of a higher operating temperature leads to degradation, delamination, and premature failure of the top coat. Both new ceramic materials and new coating structures must be developed to meet the demand for future advanced TBC systems. In this paper, the latest progress of some new ceramic materials is first reviewed. Then, a comprehensive spalling mechanism of the ceramic top coat is summarized to understand the dependence of lifetime on various factors such as oxidation scale growth, ceramic sintering, erosion, and calcium–magnesium–aluminium–silicate (CMAS) molten salt corrosion. Finally, new structural design methods for high-performance TBCs are discussed from the perspectives of lamellar, columnar, and nanostructure inclusions. The latest developments of ceramic top coat will be presented in terms of material selection, structural design, and failure mechanism, and the comprehensive guidance will be provided for the development of next-generation advanced TBCs with higher temperature resistance, better thermal insulation, and longer lifetime.

Keywords: thermal barrier coatings (TBCs); ceramic material; degradation and failure; structure design; long lifetime

1 Introduction

Aeroengine and land-based gas turbine technology is the source power of the aircraft industry and clean electric plants. The turbine gas temperature is the main symbol of the technical level of aeroengines and land-based gas turbines. The harsh service environment under extremely high temperatures poses a severe challenge to the strength, design, and manufacture of high-temperature hot-section parts such as combustors, blades, and nozzles. The current operating temperature can no longer meet the needs of aeroengines with higher thrust-weight ratios [1,2]. The main ways to further raise the gas temperature are as follows: The first is to develop higher-grade high-temperature materials, the second is to develop an efficient blade cooling structure design, the third is to prepare directional crystal or single-crystal superalloy blades, and the fourth is to develop advanced thermal barrier technology.

Thermal barrier coatings (TBCs) are widely used on hot-section components of aeroengines and land-based gas turbines to protect superalloy substrates (SUB). The TBC system can effectively isolate the high-temperature gas from hot parts, protecting the superalloy by reducing the alloy surface temperature. Thus the propulsion of aeroengines can be further improved [3]. The conventional TBC system consists of four layers, namely, substrate (SUB), bond coat (BC), thermally grown oxide (TGO), and top coat (TC), each of which is composed of materials with different properties and functions, as shown in Fig. 1. The substrate is generally a high-temperature nickel-based or cobalt-base alloy to bear the mechanical load. The bond coat is an antioxidation alloy transition layer prepared on the substrate to protect the substrate from oxidation and reduce the mismatch of the coefficient of thermal expansion (CTE) between TC and SUB. The TGO layer forms between TC and BC due to the oxidation of bond coat and its formation is inevitable. The ceramic top coat is the key part of TBCs to achieve
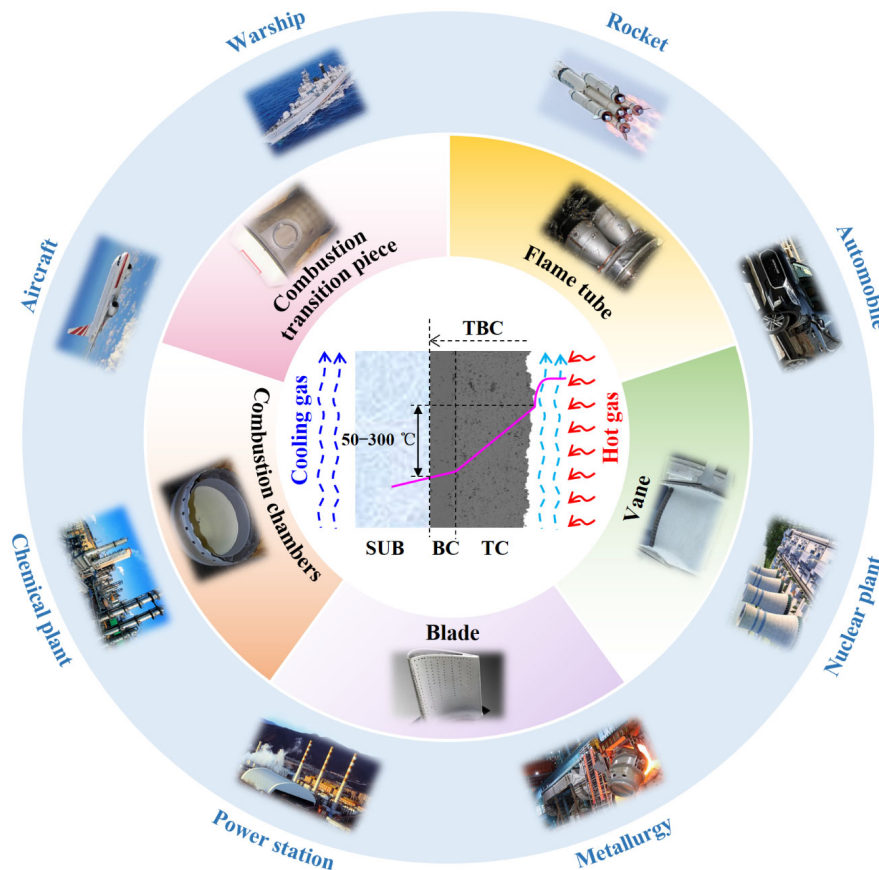
Fig. 1 Typical double-layer TBC system composed of the ceramic top coat and bond coat, and its application to alloy structural components in industrial fields.

thermal insulation.

Atmospheric plasma spraying (APS), electron beam physical vapor deposition (EB-PVD), and plasma spray physical vapor deposition (PS-PVD) are three major approaches to prepare the ceramic top coats. Commonly, the ceramic layer prepared by APS has typical layered structure characteristics. The bonding interface areas between splats (flattened and solidified ceramic particles) in the conventional APS top coat only account for less than one-third of the total interface areas. The non-bonded interface provides a low thermal conductivity but reduces fracture toughness [4]. Different from APS TBCs, the ceramic layer prepared by EB-PVD has a typical columnar structure feature. The columns are perpendicular to the substrate, regularly distributed, and weakly bonded, which remarkably improves the strain tolerance of the coating [5,6]. Therefore, the EB-PVD coating has a better anti-spalling ability, especially under thermal cycling. PS-PVD is a new film and coating preparation technology developed by combining the characteristics of plasma spraying and physical vapor deposition

technology. The coating prepared by PS-PVD has a feather columnar structure, which has the advantages of APS coating and EB-PVD coating. A comparison of the thermal insulation performance and cyclic lifetime of the coatings prepared by these three methods is presented in Fig. 2.

The ceramic top coat should have the characteristics of a high melting point, low thermal conductivity, good phase stability, high CTE matching with superalloys, good sintering resistance, etc. The top coat is a prerequisite for realizing the heat insulation function and is the key part of the TBC structure [12]. There are few materials suitable for high-temperature TBCs. Yttria partially stabilized zirconia (YSZ) is a typical TBC material with the advantages of high toughness, large CTE, and good stability. However, the phase transformation of YSZ ceramic is inevitable during the long-term service of TBCs at high temperatures, especially for long-term thermal exposure of > 10,000 h [13]. Moreover, ceramic sintering at high temperatures can cause grain growth and porosity reduction, resulting in a decline in the thermal insulation performance of

the coating. With the increase in sintering time and service temperature, the tetragonal toughening phase in the YSZ ceramic decreases, and the cracking resistance of the coating is lost. To obtain TBCs with higher thermal insulation and longer lifetime, many new ceramic materials have been developed [14–19], such as rare-earth zirconate, niobate, and tantalate, as shown in Fig. 3. These materials have excellent properties of low
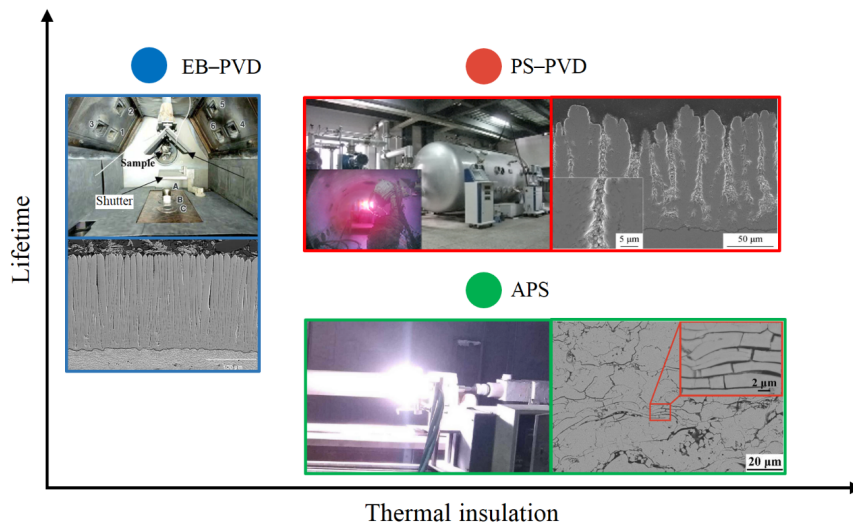

Fig. 2 Comparison of the microstructure, thermal insulation performance, and thermal cycle life of TBCs obtained by several popular preparation methods such as APS, EB-PVD, and PS-PVD. Reproduced with permission from Ref. [7], © ASM International 2015; Ref. [8], © The Nonferrous Metals Society of China and Springer-Verlag GmbH Germany, part of Springer Nature 2020; Ref. [9], © ASM International 2009; Ref. [10], © The Nonferrous Metals Society of China and Springer-Verlag GmbH Germany, part of Springer Nature 2018; Ref. [11], © Springer Science + Business Media, Inc. 2005.
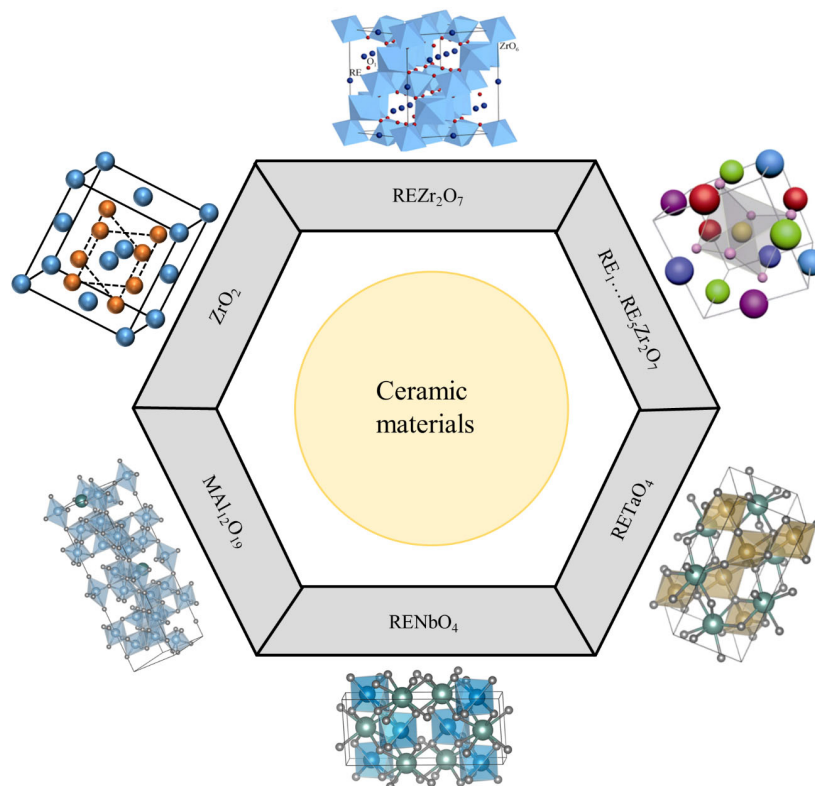

Fig. 3 Crystal structures of conventional zirconia, rare-earth zirconate, and some promising ceramic materials used for the top coat of TBCs. Reproduced with permission from Ref. [2], © The Nonferrous Metals Society of China and Springer-Verlag GmbH Germany, part of Springer Nature 2019; Ref. [15], © The Author(s) 2019.

thermal conductivity, high phase stability, and high sintering resistance. However, some intrinsic characteristics such as lower CTE and fracture toughness limit their development and application. Since the highest operation temperature of most advanced superalloys is less than 1100 ℃, these new ceramic materials are often used in conjunction with conventional YSZ to form a double ceramic structure, which can significantly improve the thermal insulation performance and service lifetime of TBCs.

Due to the extremely high-temperature service environment, delamination and failure of coatings occur after several thermal cycles. The premature failure induced by the spalling of the ceramic top coat is the critical factor hindering application of TBCs for a long service lifetime. The degradation of the ceramic top coat is caused by the propagation and linking of multiple microcracks, not by the sudden propagation of a single crack [20–22]. For APS TBCs, a large number of non-bonded lamellar interfaces in the ceramic layer act as preset cracks [4]. When the strain energy at the crack tip exceeds the fracture toughness of the material under thermal- mechanical loading, the crack will propagate. The growth and coalescence of microcracks between lamellae can result in the formation of large cracks. The connection between large horizontal and vertical cracks induces the local ceramic spalling, which ultimately leads to the failure of the coating structure [23,24]. To improve the performance of coatings and propose optimization strategies, it is urgent to have a comprehensive understanding of the failure mechanism of coatings.

There are many factors resulting in the spalling of the ceramic top coat. The TBC is a multilayer structural system. There is certain residual stress after coating preparation [25], which is an important cause of early crack propagation. When the coating undergoes multiple thermal cycles, thermal mismatch stress (σ_t) will be induced due to the different thermo-mechanical properties between the layers [26]. Many research results have indicated that TGO growth at high temperatures is one of the critical causes affecting the coating failure [27,28]. Ceramic sintering at high temperatures is another key factor for coating degradation and delamination [29,30]. Sintering can induce grain growth, microcrack healing, and porosity reduction. The changes of microstructure will increase the elastic modulus and hardness of the coating, decrease the strain tolerance, and then induce coating degradation. In addition to the intrinsic factors, calcium–magnesium–aluminium–silicate (CMAS) corrosion [31–35]

and foreign object impact [36] are also vital elements leading to the coating failure. CMAS from the external environment will lead to a decrease in yttrium oxide content and promote phase transformation. Moreover, CMAS penetration seriously reduces the strain tolerance of columnar TBCs. The damage forms of TBCs during service are shown in Fig. 4. An in-depth understanding of the failure mechanism of TBCs under actual service conditions can contribute to the development of advanced coatings at higher operating temperatures. Based on the understanding of crack growth control factors, many efforts have been made to obtain high resistance and long lifetime TBCs, such as new material development, TGO growth control, and spraying process optimization. Additionally, the thermal cycling lifetime can also be extended by decreasing the coating thickness while a top coat with a high strain tolerance is used [37,38]. The quasi-columnar structure can be obtained by preparing segment cracks through the coating [26,39], which can significantly improve the strain tolerance and spalling resistance of the coating.

The purpose of this paper is to review the progress of ceramic coat materials, TBC degradation mechanisms, and structure design with a long lifetime. In this work, the research progress on the promising new materials such as rare-earth zirconate, tantalate, and niobate for ceramic top coats is first summarized from the aspects of crystal structure and thermal-mechanical properties. During the service, TBC failure may be caused by stress, oxidation, corrosion, erosion, etc. An overview of the cracking and spalling mechanisms of ceramic top coats under different conditions is presented. In addition, some structural design methods of long-life coatings are also introduced from the perspective of layered, columnar, and nano structures. This will contribute to the development of advanced TBCs at higher temperatures.

2　Ceramic materials for top coat

There are strict requirements for the selection of TBC materials. The materials for ceramic top coat in TBCs should possess the properties such as low thermal conductivity, high melting point, high sintering resistance, good phase stability, and the matching CTE with the substrate. In addition, these materials should also have excellent corrosion resistance and erosion resistance. Therefore, there are few ceramic materials
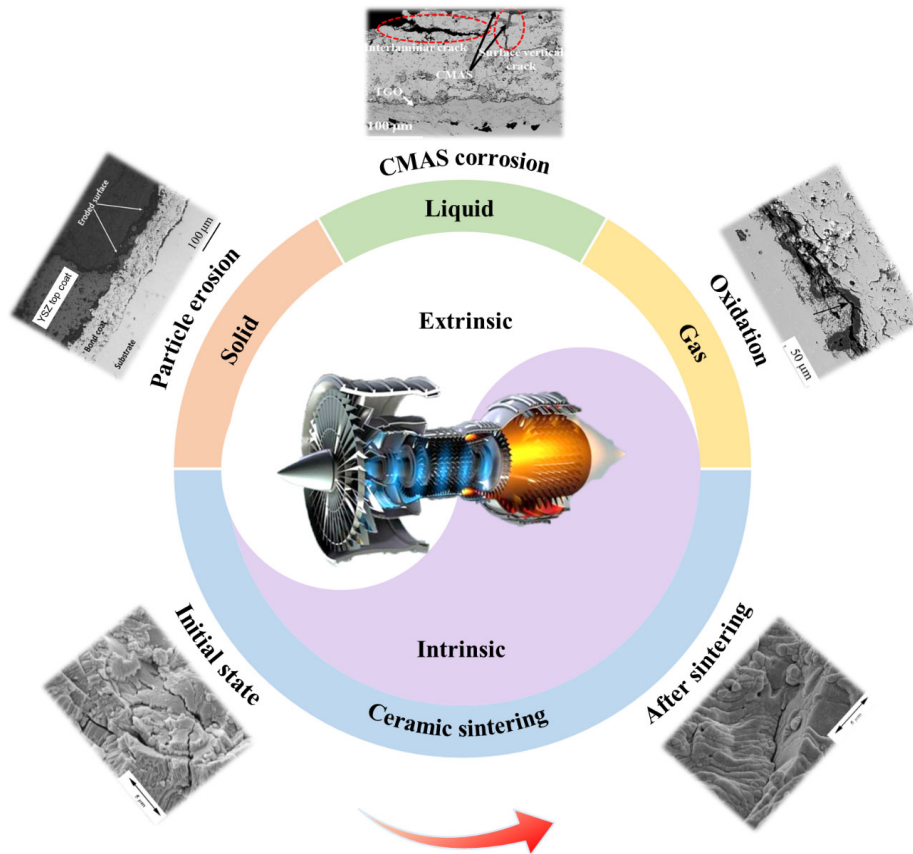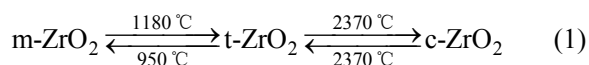
Fig. 4 TBC failure caused by extrinsic (particle erosion, CMAS corrosion, oxidation, etc.) and internal factors (ceramic sintering) under the actual service environment. Reproduced with permission from Ref. [29], © ASM International 2004; Ref. [40], © Society for Experimental Mechanics 2020; Ref. [41], © ASM International 2017; Ref. [42], © ASM International 2021.

suitable for TBCs. In addition to traditional zirconia, researchers have also developed some new ceramic materials such as rare-earth tantalate and niobate using the advantages of material chemistry and rare-earth chemistry. The development of these new materials will serve as an important foundation for research of high-performance coatings.

2. 1   Zirconia-based ceramics

In the oxide ceramics, the properties of ZrO_2 approach to the above requirements: the melting point is 2700 ℃, the thermal conductivity is 2.0–2.4 $W \cdot m^{-1} \cdot K^{-1}$, and the average CTE is approximately 10.8×10^{-6} K^{-1}. For these reasons, ZrO_2 becomes the best choice for the ceramic layer [43,44]. ZrO_2 has three crystal structures: monoclinic phase (m-ZrO_2), tetragonal phase (t-ZrO_2), and cubic phase (c-ZrO_2). The reversible phase transformation temperatures between these three phases are given as Eq. (1):

$$\text{m-}ZrO_2 \underset{950\,℃}{\overset{1180\,℃}{\rightleftharpoons}} \text{t-}ZrO_2 \underset{2370\,℃}{\overset{2370\,℃}{\rightleftharpoons}} \text{c-}ZrO_2 \qquad (1)$$

When the temperature reaches 1180 ℃, the phase of ZrO_2 changes from m-ZrO_2 to t-ZrO_2 with volume shrinkage. However, as the temperature decreases to 950 ℃, the phase of ZrO_2 changes from t-ZrO_2 to m-ZrO_2 with volume expansion. The internal stress is caused by the volume change, which leads to cracking in the ceramic. To avoid the degradation caused by phase transformation, it is necessary to stabilize ZrO_2. To improve the stability of ZrO_2, cations with different radii or valence states are doped in ZrO_2 to change the lattice constant of ZrO_2 or introduce oxygen vacancies into the lattice. The usual stabilizers used for ZrO_2 include Y_2O_3, CaO, MgO, and CeO_2. The 7–8 wt% YSZ has excellent thermal shock resistance and is most widely used in TBCs [45].

YSZ has low intrinsic thermal conductivity, high fracture toughness, and high melting point, which makes it a suitable material for ceramic top coats [46–48]. The benefits of using TBCs are that they can increase the lifetime of hot-section components by lowering the working temperature of the superalloy and improve the

efficiency and performance of the engine by improving the operating temperature. Because of the nonequilibrium tetragonal phase structure (t'-ZrO$_2$), YSZ can be used under 1100–1400 ℃ in the long-term operation before YSZ phase transformation from t'-ZrO$_2$ to m-ZrO$_2$ and c-ZrO$_2$. The volume expansion accompanying the phase transformation can lead to coating cracking failure. If the contents of impurities in YSZ are too high, rapid ceramic sintering will cause the modulus to increase, the toughness to decrease, and the lifetime to decrease.

There are three types of YSZ powders commonly used for plasma spraying. Fused and crushed (FC) powder shows an angular appearance and a dense inner structure. Agglomerated and sintered (AS) powder shows a spherical appearance, coarse surface, and possible porous inner structure. Plasma processed hollow sphere (HS) powder shows a spherical appearance, smooth surface, and shell structure with a large pore in the center. Compared with FC and AS powders, HS powder has many merits. It can be melted better in a plasma flame due to the large ratio of surface area to mass. Moreover, the YSZ ceramic top coat prepared using HS powder has a distinct microstructure such as a larger fraction of splat interface and smaller splat thickness, which make TBCs have lower thermal conductivity and higher sinter resistance. This is because there are peculiar fluid dynamics producing a counterjet during the impact and spreading of hollow droplets melted from HS powder [49].

The manufacturing process of FC powder contains the following steps: The first step is to take the fusion YSZ powder into bulk; the second step is to crush the bulk to certain small-size particles; and the third step is to screen out the powder particles with a defined particle size range. The advantages of this process are that the method is oversimplified and the particles are compact. The disadvantages of this process are that the prepared powders have irregular particle morphology, undesirable mobility, and high impurity content. The manufacturing process of AS powder can be divided into the following steps: first, reconstituting micro YSZ particles by spray granulation; second, sintering the micro YSZ particles to improve the cohesion of particles and removing impurities in particles.

The atmospheric plasma processing of porous YSZ agglomerated powders is an effective method to produce HS powder because the plasma flame has a higher temperature than 5000 ℃. When a porous particle is fed into the plasma flame, the particle surface is first molten, and a liquid film is formed on the surface quickly [50,51]. Gas in particles is entrapped due to the surface tension of the liquid film. As a result, a liquid droplet with gas inside is formed. When the liquid droplet leaves out the high-temperature region in the plasma flame, it solidifies and forms HS with a single pore in the center. For HS powder, at a given particle mass, the thinner the shell thickness and the higher the surface/mass ratio is, the easier it is to melt by the plasma flame, which is essentially important for coating preparation under low plasma arc power during APS. The relative shell thickness (ratio of shell thickness and particle diameter) of the HS powder produced by the plasma process is determined by the amount of gas entrapped and the temperature of the entrapped gas [52]. HS YSZ with a thinner shell thickness can be obtained using AS powder with a larger initial porosity under a higher temperature of entrapped gas. Gulyaev [53] modified the shell thickness of HS powder by remelting under controlled ambient pressure.

When the particle is fully melted, the formed droplet has a force balance among inner pressure, surface tension, and ambient pressure [11]. The higher the inner temperature is, the higher the inner pressure is. The droplet expands with larger volume and thinner shell thickness. However, when the outer temperature of the droplet is lower than the melting point of YSZ, it begins to solidify gradually from the surface to the center. At this time, the droplet cannot expand further. However, if the ambient temperature is preserved above the melting point, the outer surface of the droplet will not solidify, and the droplet can still expand with the increase in inner temperature. Thus, a particle with a larger volume and a thinner thickness will be obtained after the droplet solidifies. With the heat preservation zone, the droplet can expand better. HS powder with a larger volume and a thinner shell thickness can be obtained accordingly [50,51].

The microstructures of nano YSZ, AS YSZ, and HS YSZ are demonstrated in Fig. 5. The range of particle size is from 5 to 20 nm for nano YSZ. AS YSZ is subspherical, rough, and porous. HS YSZ has a spherical smooth surface and a hollow interior. Compared with FC YSZ, AS YSZ has more homogeneous particle size distribution and high purity.

Aside from the stacking lamellar splats, the TBC structure also contains features of pores and cracks. The powder particle structure influences the defects of TBCs [54–56]. Kulkarni *et al.* [54] prepared TBCs by
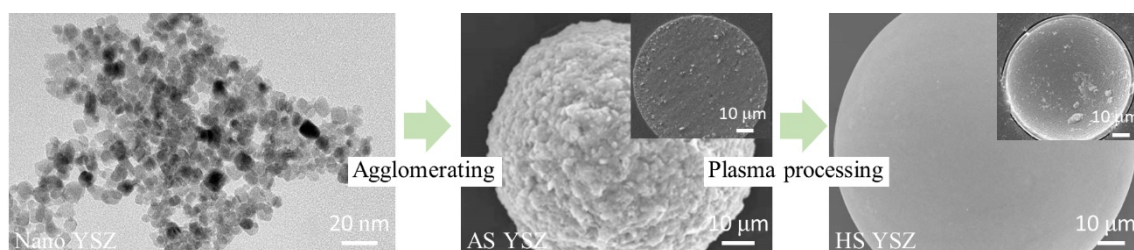
Fig. 5 Scanning electron microscopy (SEM) images of YSZ powders with different structures.

plasma spraying with the same spraying parameters but different structures of powders. The coatings prepared with FC YSZ contain the minimum porosity, consisting of interlamellar pores, cracks, and globular pores. However, TBCs prepared with AS YSZ have the maximum porosity. TBCs prepared with HS YSZ possess fewer globular pores, more interlamellar pores, and more cracks.

The chemical composition issues of YSZ include the content of Y_2O_3, the existing form and the distribution uniformity of Y_2O_3, and the content of impurities. The Y_2O_3 content affects the phase structure, mechanical strength, and thermal conductivity of YSZ. The nonuniform distribution of Y_2O_3, uncompleted solid solution, and appearance of the m-phase, t-phase, and c-phase in TBCs can lead to phase transformation and coating failure. Thus, improving the distribution uniformity of Y_2O_3, enhancing its solid solubility in ZrO_2, and increasing the cooling rate during the spraying process are beneficial to raise the thermal stability of TBCs.

The purity of YSZ mainly affects the sintering-resistance of TBCs. When the TBCs contain the oxide impurities such as SiO_2 and Al_2O_3, these impurities would be enriched at the grain boundary, which could accelerate the ceramic sintering to make the tiny pores disappear. Such results may increase the modulus and thermal conductivity of TBCs. The research by Vaßen *et al*. [57] revealed that the shrinkage rate of TBCs increased with increasing impurity content. The test of (0.1%–0.2% SiO_2 + Al_2O_3)–YSZ TBCs and (0.01%–0.05% SiO_2 + Al_2O_3)–YSZ TBCs after sintering for 20 h at 1400 ℃ by Paul *et al*. [58], indicated that the shrinkage decreased by 1/5–1/3 with the impurity in TBCs decreasing from 0.1%–0.2% to 0.01%–0.05%. After TBC sintering for 100 h at 1400 ℃, the research by Xie *et al*. [59] showed that with the decrease in impurity content in TBCs, the m-phase content decreased from 16% to 1%. Therefore, improving the purity of YSZ is a key factor to improve the sintering

resistance of TBCs.

The 6–8 wt% Y_2O_3 stabilized ZrO_2 (6YSZ–8YSZ) exhibits good performance. However, the degradation of the YSZ coating will occur by phase transformation in which metastable t′ decomposes to the m-phase and c-phase [60]. Additionally, the accelerated sintering of YSZ coatings also occurs at high temperatures, which will decrease the strain tolerance and thermal barrier performance of TBCs [61]. Therefore, new TBC materials are under investigation to reduce thermal conductivity and improve sintering resistance.

Extensive efforts were made to improve the phase stability and reduce the thermal conductivity of the TBC materials. To stabilize the high temperature t′-phase or c-phase to room temperature, different rare-earth oxide additives are added to YSZ. Considerable efforts are being invested in the search for alternative additives, such as Gd_2O_3, Nb_2O_5, Sm_2O_3, Yb_2O_3, and Sc_2O_3 [23]. Partial substitution of Gd and Yb in YSZ can enhance the phase stability. The addition of rare-earth oxides is accompanied by the generation of oxygen vacancies and the square of the atomic weight difference between the solute and host cations, all of which can increase phonon scattering and further reduce the thermal conductivity. Additives such as Yb_2O_3, Nd_2O_3, Gd_2O_3, and La_2O_3 have been found to be particularly effective in reducing the thermal conductivity of YSZ TBCs. Ji *et al*. [62] calculated the lattice distortion and bond population of ZrO_2 as a consequence of rare-earth element doping by first principles based on plane-wave pseudopotential theory. The results show that Gd–O has the smallest bond population among the rare-earth oxides, and implies the smallest thermal diffusion coefficient. The effects of adding two additives, Nd_2O_3–Yb_2O_3, Gd_2O_3–Yb_2O_3, or Sm_2O_3–Yb_2O_3 on the thermal conductivity of YSZ were investigated by Bansal and Zhu [63]. It is found that codoping two or more rare-earth oxides into YSZ can significantly reduce the thermal conductivity, and the lowest thermal conductivity was observed when the

total dopant concentration was 10 wt%. Bansal and Zhu [63] enhanced phase stability by substituting Gd and Yb in YSZ. This means that larger atomic weight difference between the solute (Gd,Yb) and host (Zr), compared with that between Y and Zr, contributes to the lower thermal conductivity of 5 wt% Gd_2O_3 and 5 wt% Yb_2O_3 co-doped 8YSZ (GYb–YSZ). On the other hand, the substitution of Gd^{3+} and Yb^{3+} for Zr^{4+} causes substitutional defects and extra oxygen vacancies for charge compensation [64]. GYb–YSZ are synthesized by the process of hydrothermal crystallization. The thermal conductivity of TBCs with GYb–YSZ at 1000 ℃ is investigated and compared with that of TBCs with 8YSZ, as shown in Fig. 6.

The thermal conductivity of TBCs with GYb–YSZ was approximately 0.85 $W \cdot m^{-1} \cdot K^{-1}$, which was 60%–70% of that of 8YSZ. This was because the larger atomic radius difference between Gd, Yb, and Zr, compared with that between Y and Zr, contributed to a lower thermal conductivity of GYb–YSZ. Moreover, the
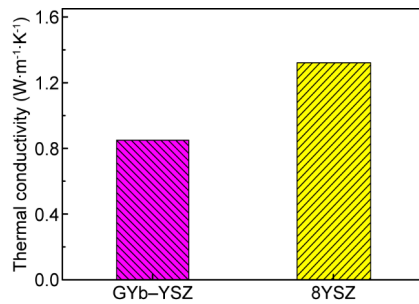
substitution of Gd^{3+} and Yb^{3+} for Zr^{4+} caused substitutional defects and extra oxygen vacancies for charge compensation, which could increase phonon scattering and further reduce the thermal conductivity.

In brief, zirconia-based ceramics are a typical top coat material with excellent toughness and comprehensive performance. Except for widely applied YSZ, more rare-earth elements and their combination can be further added into zirconia to probe the further possibility of reducing the thermal conductivity and improving the high temperature stability. In addition, from the view of sintering resistance, the purification of these ceramics is also a promising approach considering the balance between performance and economy.

2.2 Rare-earth niobates

In addition to zirconate-based ceramics, there is still a high demand for the exploration of new ceramic materials for TBCs. In this case, rare-earth niobates that are widely used as dielectric materials, magnetic materials, protonic ceramic fuel cells (PCFC), and luminescent materials have been considered as new ceramic TBC materials [65–70]. As shown in Fig. 7, there are four binary La–Nb–O compounds, with chemical formulae of RE_3NbO_7, $RENbO_4$, $RENb_3O_9$, and $RE_2Nb_{15}O_{33}$ where RE means rare-earth elements [71]. $RENb_3O_9$ and $RE_2Nb_{15}O_{33}$ will not be used for ceramic top coat due to their low melting points. Hence, among the rare-earth niobates, the RE_3NbO_7 and $RENbO_4$ with relatively high melting points may be suitable for ceramic TBC materials.

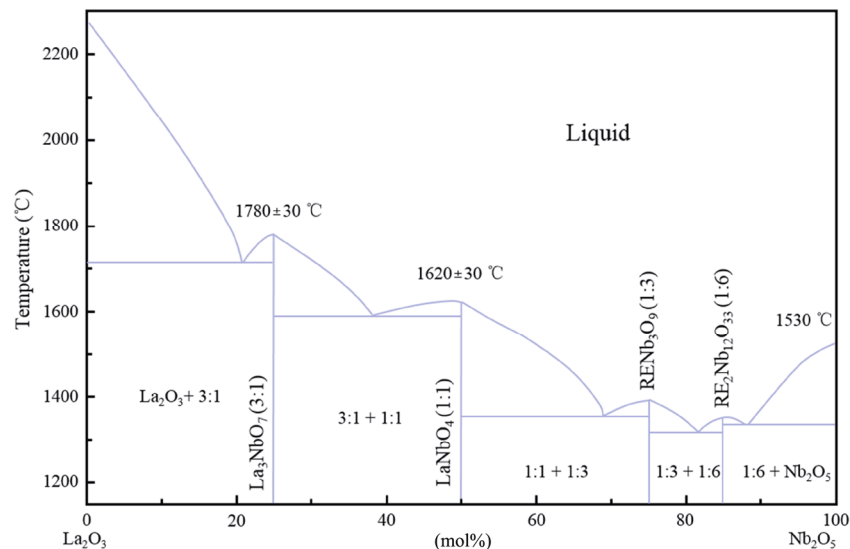**Fig. 6** Thermal conductivities of TBCs with GYb–YSZ or 8YSZ at 1000 ℃.

Fig. 7 Binary phase diagram of the La–Nb–O system. Reproduced with permission from Ref. [71], © Optical Society of America 2014.

RE₃NbO₇ was recently proposed as a new type of promising ceramic TBC material [72–76]. The crystal structure of RE₃NbO₇ is related to the ionic radii of rare-earth elements. RE₃NbO₇ has two kinds of crystal structures: an ordered orthorhombic weberite phase and a disordered cubic fluorite phase. RE₃NbO₇ (RE = Dy–Lu and Y) shows a cubic fluorite phase similar to that of rare-earth zirconates when RE³⁺ has small ionic radii and a corresponding space group $Fm\bar{3}m$. For RE³⁺ having large ionic radii, the crystal structure of RE₃NbO₇ is an orthorhombic weberite phase, with two different space groups *Cmcm* (RE = La, Pr, and Nd) and *C*222₁ (RE = Sm–Gd) according to the space symmetry. In weberite RE₃NbO₇, both cations and anions are (including 1/8 oxygen vacancies) orderly arranged in the crystal lattice. For RE₃NbO₇ with the *Cmcm* space group, RE³⁺ occupies the Wyckoff positions of 4a and 8g, and Nb⁵⁺ occupies the 4b position. While for *C*222₁ space group, RE³⁺ has two Wyckoff positions 4b and 8c with different chemical environments, and Nb⁵⁺ also occupies 4b position. In fact, O²⁻ also occupies 5 Wyckoff positions with different chemical environments in space group *C*222₁.

This kind of crystal structure with a high concentration of intrinsic oxygen vacancies has strong scattering effects on phonons that can decrease the thermal conductivity of RE₃NbO₇. To obtain low thermal conductivity, a typical way is to increase the disorder of the structure, e.g., by introducing defects, especially point defects. By introducing at least 3–5 types of substitutional atoms, ceramic materials can approach their theoretical lowest thermal conductivities. However, such systems dramatically increase the complexity of components, which makes it difficult to prepare new TBCs with designed stoichiometric ratios during thermal spray processes. It is proven that RE₃NbO₇ (RE = Dy, Y, Er, and Yb), a simple series of binary compounds, has much lower thermal conductivities than that of YSZ and most new ceramic TBC materials (Fig. 8(a)). The thermal conductivities of RE₃NbO₇ (RE = Dy, Y, Er, Yb) are in the range of 1.25–1.55 W·m⁻¹·K⁻¹ at 1273 K with an amorphous-like temperature dependence (Figs. 8(b)–8(e)). The theoretical minimum thermal conductivities of RE₃NbO₇ (RE = Dy, Y, Er, Yb) are estimated by the Cahill–Waston–Pohl (CWP) model. The measured thermal conductivities of RE₃NbO₇ (RE = Dy, Y, Er, Yb) show the same increasing tendency with the calculated thermal conductivities, which almost approach their amorphous limits. The large chemical inhomogeneity caused by the charge disorder and
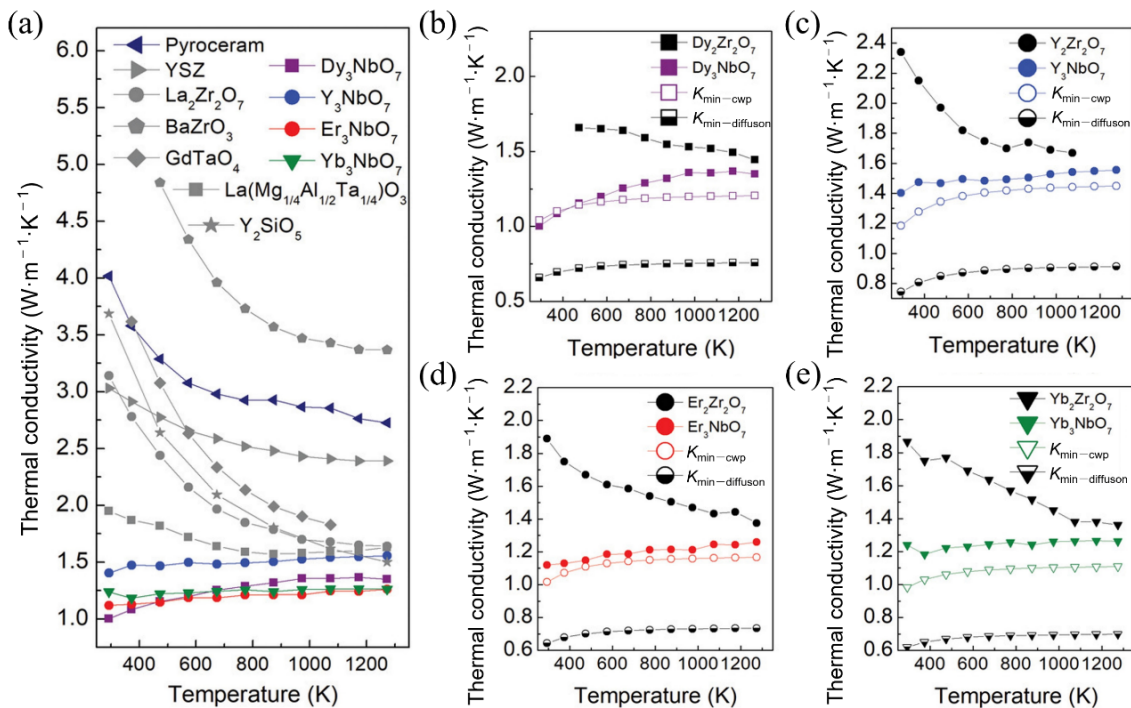

Fig. 8 Thermal properties of RE₃NbO₇ (RE = Dy, Y, Er, Yb). (a) Thermal conductivities of RE₃NbO₇ compared to other new ceramic TBC materials and conventional 7YSZ; (b–e) thermal conductivities of RE₃NbO₇ and RE₂Zr₂O₇ and the minimum thermal conductivity calculated by the CWP model and diffusion model. Reproduced with permission from Ref. [72], © WILEY-VCH Verlag GmbH & Co. KGaA, Weinheim 2019.

bonding fluctuation plays a key role in the low thermal conductivity in compounds with simple compositions. The ratio of Young's modulus and thermal conductivity (E/λ) is investigated, which is an index for the phonon scattering rate of the vibration state. RE_3NbO_7 (RE = Dy, Y, Er, and Yb) shows extremely large E/λ values. The E/λ value of Dy_3NbO_7 far exceeds those of other low thermal conductivity materials. High E/λ values suggest an unprecedented scattering rate for rare-earth niobates.

The CTEs of weberite RE_3NbO_7 (RE = Dy, Y, Er, Yb) are investigated as shown in Fig. 9(a). The CTEs of RE_3NbO_7 are higher than those of $La_2Zr_2O_7$ and comparable to those of YSZ. Dy_3NbO_7 has the largest CTEs that is approximately 11.0×10^{-6} K^{-1} at 1473 K. The oxygen barrier property, chemical stability under CMAS corrosion, and chemical compatibility with TGO of RE_3NbO_7 (RE = Dy, Y, Er, and Yb) (Figs. 9(b)–9(d)) are better than those of YSZ. The oxygen conductivities of RE_3NbO_7 are approximately three orders of magnitude lower than that of YSZ, indicating its excellent oxygen barrier property. A better CMAS resistance is desirable for new ceramic TBC materials that can retard the failure of TBCs. The corrosion depth from CMAS of RE_3NbO_7 is approximately 20–60 μm, which is much smaller than that of YSZ (~200 μm) under the same corrosion conditions,

suggesting that RE_3NbO_7 has better CMAS resistance. The reaction between TGO and ceramic TBC materials should be avoided as it can accelerate the failure of TBCs. There is no reaction between RE_3NbO_7 and Al_2O_3 (the main component of TGO), revealing the better chemical stability of RE_3NbO_7.

The mechanical properties of RE_3NbO_7 (RE = Dy, Y, Er, and Yb), in terms of fracture toughness, Vickers hardness, and E, are explored. The fracture toughness of RE_3NbO_7 is approximately 1.0 MPa·$m^{1/2}$, which is smaller than that of YSZ but comparable to rare-earth zirconates. The elastic modulus E and Vickers hardness of RE_3NbO_7 are slightly lower than those of YSZ, with values in the range of 200–235 and 8.5–10.0 GPa, respectively.

Rare-earth niobates with the chemical formula $RENbO_4$ (RE = La–Lu) are materials with ferroelasticity below the critical temperatures (T_c) [77–79]. $RENbO_4$ has two different structures: fergusonite-type and scheelite-type structure. A reversible ferroelastic phase transformation from the monoclinic fergusonite structure to a tetragonal scheelite structure occurs approximately T_c. A typical criterion for new ceramic TBC materials is whether phase transformation occurs during application. The ferroelastic phase transformation of $RENbO_4$ is acceptable as it is a second-order phase transformation
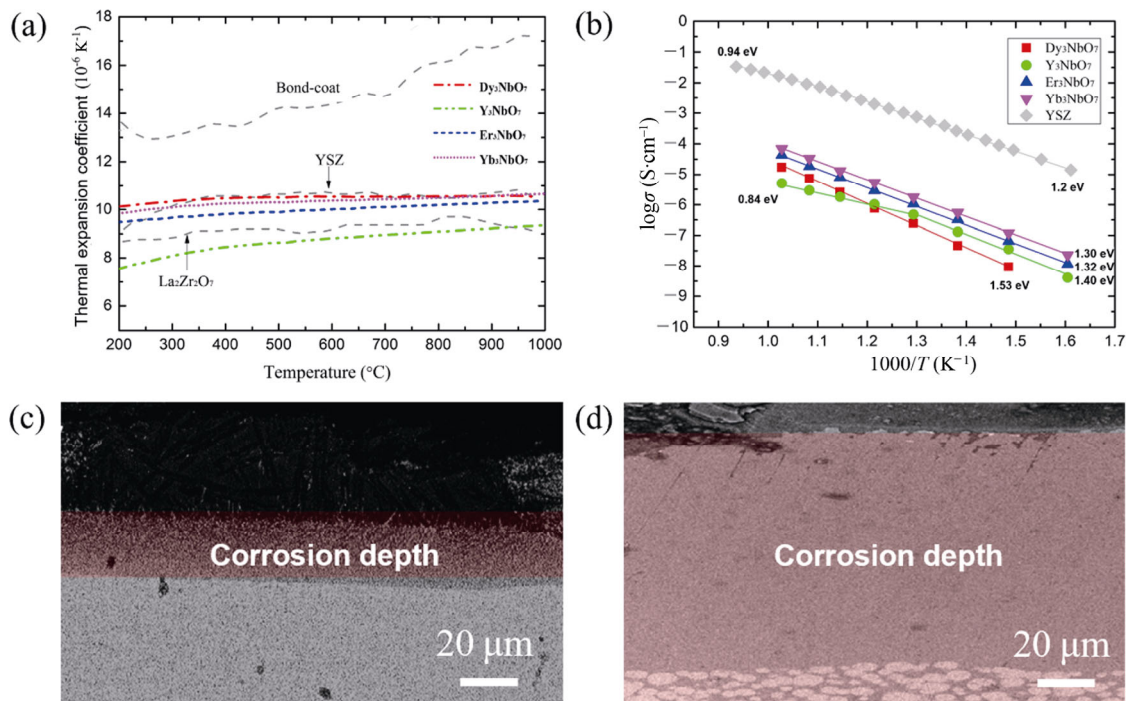

Fig. 9 Thermal, oxygen resistance, and CMAS resistance of RE_3NbO_7 (RE = Dy, Y, Er, and Yb) compounds. (a) CTE, (b) Arrhenius plots for RE_3NbO_7 ceramic electronic conductivity, and (c, d) CMAS corrosion depths of Dy_3NbO_7 and YSZ. Reproduced with permission from Ref. [75], © The American Ceramic Society 2019.

without any variation in volume or latent heat [80]. In other words, no extra stress is introduced during the phase transformation of RENbO$_4$. The crystal structure of RENbO$_4$ is shown in Fig. 10, revealing the lattice distortion as a function of the ionic radii of RE^{3+}. The two structures of RENbO$_4$ are composed of REO$_8$ dodecahedra and NbO$_4$ tetrahedra. The lattice distortion is represented by the ratio of the distance of RE–O and Nb–O in related polyhedra, which decreases as inionic radii of RE^{3+} decrease.

The RENbO$_4$ (RE = Nd, Sm, Gd, Dy, Er, and Yb) compounds exhibit lower thermal conductivities than that of YSZ, in the range of 1.80–2.26 W·m^{-1}·K^{-1} at 1273 K, as shown in Fig. 11(a). The low thermal conductivities of RENbO$_4$ are attributed to the large chemical inhomogeneity in terms of the charge difference of cations and fluctuation of bonding length. The CTEs of RENbO$_4$ (RE = Nd, Sm, Gd, Dy, Er, and Yb) compounds are not like those of conventional ceramic TBC materials, with a linearly increasing tendency at elevated temperatures (Fig. 11(b)). The CTEs of m-RENbO$_4$ show an increasing tendency and reach the largest values at the ferroelastic phase transformation temperature. After phase transformation, the CTE of t-RENbO$_4$ decreases inversely with temperature. NdNbO$_4$

has the largest CTE (12.8×10^{-6} K^{-1}) at the phase transformation temperature, which is much higher than that of YSZ due to the severe systematic distortion.

One of the important reasons why YSZ has high fracture toughness is its ferroelasticity. As RENbO$_4$ (RE = Nd, Sm, Gd, Dy, Er, and Yb) compounds also have ferroelasticity, their fracture toughness was investigated. The fracture toughness of RENbO$_4$ (RE = Nd, Sm, Gd, Dy, Er, and Yb) is in the range of 1.93–2.77 MPa·m$^{1/2}$, which is lower than that of YSZ but higher than those of most new ceramic TBC materials. The crack propagation behavior of GdNbO$_4$ indicates that the ferroelastic domain state is varied by the interaction between the crack and ferroelastic domain, inducing crack bridging and crack deflection to absorb crack energy and increase the fracture toughness (Figs. 11(c) and 11(d)).

In conclusion, rare-earth niobates with low thermal conductivity and high temperature stability show higher toughness than most new ceramic TBC ceramics owing to ferroelasticity. To further increase the fracture toughness of niobates, its ferroelastic domain needs to be more deeply understood. Furthermore, crack bridging and crack deflection behavior should also be extensively investigated in the future.
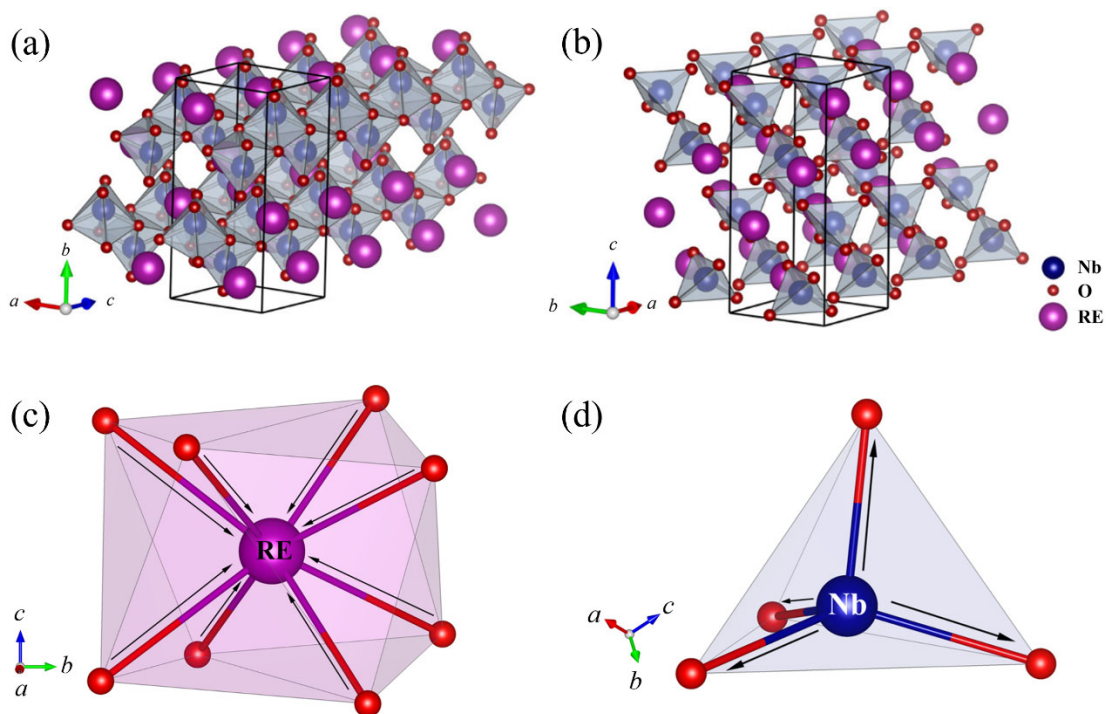

Fig. 10 Crystal structures of RENbO$_4$: (a) fergusonite-type crystal structure of m-phase, (b) scheelite-type crystal structure of t-phase, (c) REO$_8$ dodecahedron, and (d) NbO$_4$ tetrahedron. Reproduced with permission from Ref. [77], © Acta Materialia Inc. 2020.
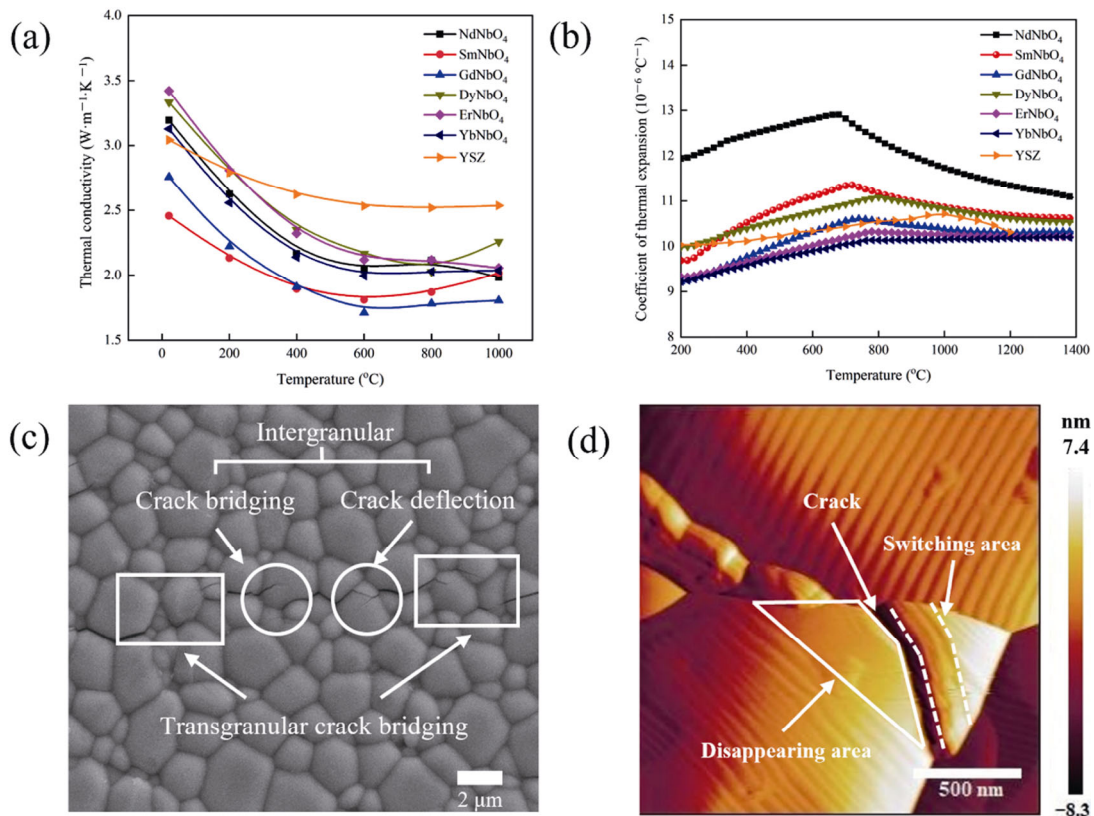
Fig. 11 Thermal properties, crack propagation, and domain state of RENbO$_4$ (RE = Nd, Sm, Gd, Dy, Er, Yb) ceramics: (a) thermal conductivity, (b) CTE, (c) crack propagation path, crack bridging, and deflection, and (d) ferroelastic domain state. Reproduced with permission from Ref. [77], © Acta Materialia Inc. 2020.

2.3 Rare-earth tantalates

Tantalate-based ceramics are another new type of alternative for TBCs. YTaO$_4$, one type of TBC, is expected to be used in an environment where the temperature exceeds 1600 ℃ [81]. Moreover, RETaO$_4$ (RE = Nd, Eu, Gd, Dy, Er, Yb, and Lu) ceramics will be used to replace YTaO$_4$ to obtain TBCs with lower thermal conductivity and better fracture toughness at high temperatures. XRD patterns and Raman spectra of these ceramic materials are shown in Fig. 12. Previous studies [82,83] reported that the rare-earth tantalate RETaO$_4$ with a relatively high RE^{3+} concentration will be a promising new candidate material for microchip lasers and has attracted much attention as a potential rare-earth-doped laser host. Wang *et al.* [84] reported that doped and un-doped RETaO$_4$ have chemical stability and show many other promising characteristics such as photoelectronic activity, ion conductivity, and luminescence. Lanthanum rare-earth tantalates (RETaO$_4$) are also proposed as replacement materials for next-generation TBCs because of their excellent thermal properties and low hardness at high temperatures.

RETaO$_4$ materials were investigated in terms of the synthesis, Vickers hardness, heat capacity, and thermal conductivity. The RETaO$_4$ ceramics were fabricated using a solid-state reaction. The YbTaO$_4$ and LuTaO$_4$ compounds were m′-phases with the space group $P2/a$ (13), and the others were m-phases with the space group $I2$ (5). According to group theory, the difference in crystalline symmetry and vibration mode between m- and m'-phases may cause Raman shifts [85]. Compared with the m-phase, YbTaO$_4$ and LuTaO$_4$ in the m'-phase have a larger mean atomic mass and shorter ion radius, which decrease the crystalline volume and increase the bulk density. Thus, the anharmonic vibration among the atoms is strong. The typical microstructures of RETaO$_4$ samples are shown in Fig. 13. Granular RETaO$_4$ was observed in the microstructure with a grain size of approximately 2–14 μm.

Based on the Neumann–Kopp rule [86], the specific heat capacities of the RETaO$_4$ specimens were calculated as a sum of the atomic heat capacities of the constituent oxides. The specific heat capacities of the compounds are shown in Fig. 14(a). The specific heat capacities rapidly increase with increasing temperature because
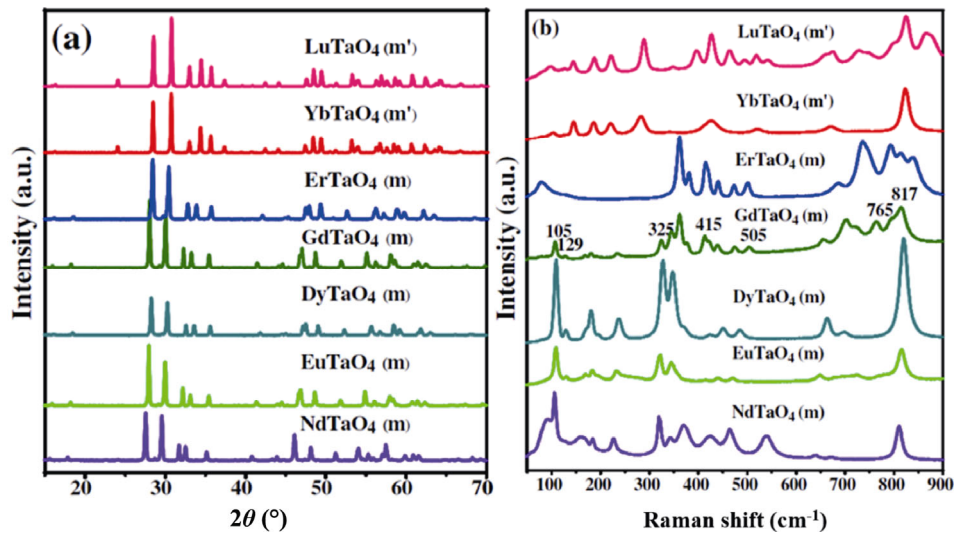
Fig. 12 (a) XRD patterns and ICDD PDF data of RETaO$_4$ (RE = Nd, Eu, Gd, Dy, Er, Yb, and Lu) ceramics and (b) room-temperature Raman spectra. Reproduced with permission from Ref. [84], © Acta Materialia Inc. 2016.
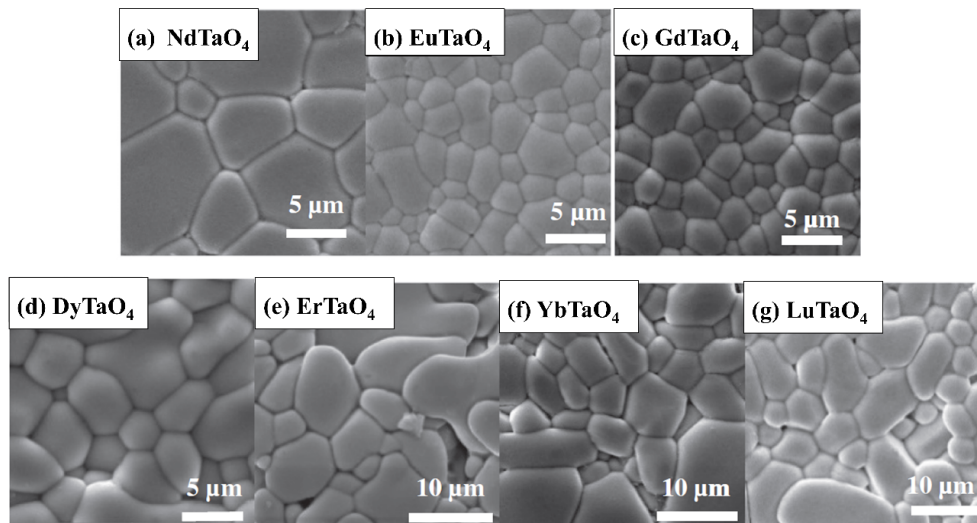

Fig. 13 SEM photographs of RETaO$_4$ (RE = Nd, Eu, Gd, Dy, Er, Yb, and Lu) ceramics. (a) NdTaO$_4$, (b) EuTaO$_4$, (c) GdTaO$_4$, (d) DyTaO$_4$, (e) ErTaO$_4$, (f) YbTaO$_4$, and (g) LuTaO$_4$. Reproduced with permission from Ref. [84], © Acta Materialia 2016.
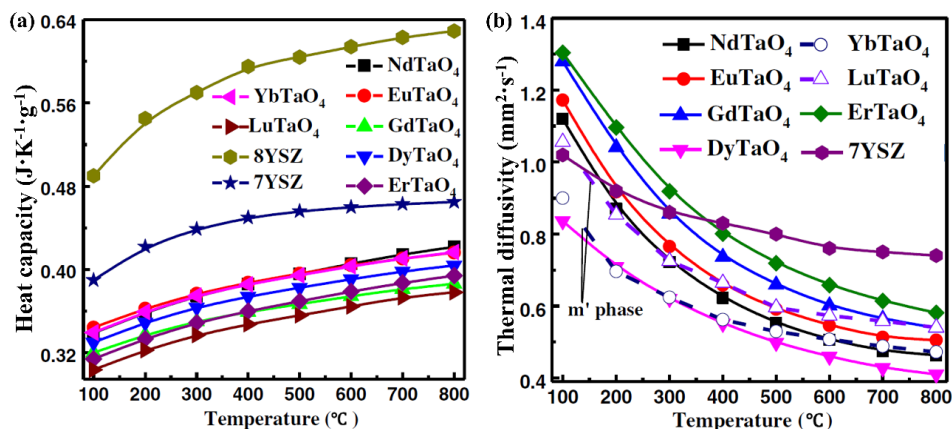

Fig. 14 Specific heat capacities and thermal diffusivities of RETaO$_4$. (a) Dependence of the specific heat capacities of RETaO$_4$ (RE = Nd, Eu, Gd, Dy, Er, Yb, and Lu) ceramics on the temperature and (b) thermal diffusivities of RETaO$_4$ compounds and 7YSZ. Reproduced with permission from Ref. [84], © Acta Materialia 2016; Ref [87], © Chinese Journal of Aeronautics 2012.

of the volumetric expansion and phonon excitation. The RETaO$_4$ specimens have much lower heat capacities than those of 7–8YSZ [87,88], which decreases the thermal conductivity of RETaO$_4$ ceramics. The thermal diffusivities of the RETaO$_4$ samples are shown in Fig. 14(b). The RETaO$_4$ specimens with higher thermal diffusivities at low temperatures slowly decrease with increasing temperature, possibly because of the effect of the porosity and phonon conduction behavior.

At low temperatures, the mean free path of phonons is determined by the factors such as the in-harmonic lattice vibration, grain size, or grain boundary. The phonon mean free path $l(\omega,T)$ can be divided into several independent parts as Eq. (2) [89]:

$$\frac{1}{l(\omega,T)} = \frac{1}{l_i(\omega,T)} + \frac{1}{l_p(\omega,T)} + \frac{1}{l_b} \qquad (2)$$

where $l_i(\omega, T)$, $l_p(\omega)$, and l_b are the phonon mean free paths because of the intrinsic phonon–phonon scattering, point defect scattering, and grain-boundary scattering, respectively. As reported, when RETaO$_4$ ceramics are single-phase (m-phase), and there are no substitution ions, $l_p(\omega)$ can be neglected. Moreover, the mean free path of the phonon is lower than the grain size, with RETaO$_4$ ceramics, the grain boundary scattering l_b can also be omitted. Therefore, the phonon mean free path is mainly controlled by the phonon Umklapp scattering processes. When the temperature is higher than the Debye temperature, the interactions among acoustic phonons are affected by anharmonic Umklapp processes. The thermal conductivity (λ) is calculated as Eq. (3) [90]:

$$\lambda = \frac{1}{3} \int_0^{\omega_m} C(\omega) l(\omega,T) V d\omega \qquad (3)$$

where $C(\omega)$, V, and ω_m are the specific heat capacity of the material, average phonon velocity, and maximum vibrational frequency, respectively. $C(\omega)$ is a constant when the temperature is higher than the Debye temperature. V is determined by the interatomic interaction. Therefore, the thermal conductivities are mainly determined by the phonon mean free paths. According to Wu *et al.* [91], the phonon mean free path is inversely proportional to the temperature ($l \propto 1/T$). Consequently, with an increase in the temperature, the vibrational energy, frequency, and impact probability of phonons increase, whereas the phonon mean free paths decrease, which results in the decreased thermal conductivity. Thus, the thermal conductivity of the RETaO$_4$ ceramics decreases with increasing temperature.

In general, an increase in the complexity of the crystal structure tends to decrease the thermal conductivity because the number of optical phonons that is not significantly responsible for thermal transport increase. Table 1 shows that Yb^{3+} and Lu^{3+} have smaller ionic radius and larger atomic mass than the Nd^{3+}, Eu^{3+}, Dy^{3+}, Gd^{3+}, and Er^{3+} ions, which leads to different phase-transition temperatures and crystal structures of rare-earth tantalite. It is well known that different phases have different phonon mean free paths and heat transfer behaviors, which lead to different thermal conductivities of the samples. NdTaO$_4$, EuTaO$_4$, DyTaO$_4$, GdTaO$_4$, and ErTaO$_4$ are m-phase, and YbTaO$_4$ and LuTaO$_4$ are m′-phase. All of them belong to the m-phase, and their crystal structures are not complicated. In addition, because the m- and m′-phases have similar chemical bonds, the m- and m′-phases have little difference in thermal conductivity.

When the temperature increases to 800 ℃, the thermal conductivities of the RETaO$_4$ ceramics approach their minimum values. The lowest thermal conductivity was 1.38 W·m^{-1}·K^{-1} at 800 ℃ for DyTaO$_4$. The thermal conductivity of NdTaO$_4$ with 1.41 W·m^{-1}·K^{-1} at 800 ℃ was close to that of DyTaO$_4$. The low thermal conductivities of RETaO$_4$ ceramics are likely because of the ion radius, number and size of pores, and low specific heat and thermal diffusivities from RETaO$_4$ ceramics. Additionally, 7–8YSZ has many oxygen vacancies at low temperatures, which decreases the thermal conductivities of 7–8YSZ. Thus, 7–8YSZ has lower thermal conductivities than NdTaO$_4$, DyTaO$_4$, ErTaO$_4$, YbTaO$_4$, and LuTaO$_4$ at low temperatures. However, oxygen vacancies weakly affect the thermal conductivities and the anharmonic effect is obvious when the temperature increases. Hence, NdTaO$_4$, DyTaO$_4$, ErTaO$_4$, YbTaO$_4$, and LuTaO$_4$ have lower thermal conductivities than that of 7YSZ at high temperatures.

Table 1   Space groups, lattice parameters, cell volumes, and densities of RETaO$_4$ ceramics

RE	Space group	a (Å)	b (Å)	c (Å)	RE^{3+} (Å)	V (Å^3)	ρ (g·cm^{-3})
Nd	$I2$ (5)	5.5205	11.2581	5.1203	0.983	316.65	8.164
Eu	$I2$ (5)	5.4127	11.0740	5.0848	0.938	303.33	8.807
Gd	$I2$ (5)	5.4339	11.1122	5.0682	0.947	305.61	8.626
Dy	$I2$ (5)	5.3556	10.9805	5.0617	0.912	269.26	9.080
Er	$I2$ (5)	5.3169	10.9103	5.0503	0.890	291.61	9.389
Yb	$P2/a$ (13)	5.2528	5.4298	5.0702	0.868	143.77	9.655
Lu	$P2/a$ (13)	5.2382	5.4298	5.0604	0.861	143.13	9.620

In summary, tantalate-based ceramics are good candidates for TBCs, particularly in high-temperature applications. The high density and the high cost will be compensated by its excellent properties. Due to a lack of comprehensive understanding of tantalate compound coatings, experiments on both the coating deposition and thermal exposure behavior should be further systematically investigated in the future.

2. 4 Rare-earth zirconates

Rare earth zirconate materials exhibit the potential to become a new generation of TBC materials. The properties of rare-earth zirconates are inseparable from their unique structure. According to $r(\text{RE}^{3+})/r(\text{Zr}^{4+})$ and temperature, rare-earth zirconates ($\text{RE}_2\text{Zr}_2\text{O}_7$) usually have a pyrochlore structure (P) or a defective fluorite structure (F), as shown in Fig. 15, which both belong to a face-centered cubic space lattice. The pyrochlore structure belongs to the $Fd3m$ (227) space group, which can be regarded as an ordered defective fluorite structure. There are four crystallographically unequal atomic positions, which can be written as $\text{RE}_2\text{Zr}_2\text{O}_6\text{O}'$. The 16d position is usually occupied by cations with a larger radius (such as rare-earth elements) in the crystal structure of pyrochlore, which can coordinate with 8O^{2-} to form a cube. Zr^{4+} with a smaller radius is located at the 16c position and only 6O^{2-} surround to form an octahedron. There are three different O^{2-} lattice positions in the pyrochlore-type rare-earth zirconate structure: 8b, 48f, and 8a, where O' is at the 8b spatial position; O is at the 48f spatial position; and the oxygen vacancy is located at 8a and in a tetrahedron formed by 4Zr^{4+}. The fluorite structure can be represented by AO_2. The cation of the fluorite structure has only one crystallographic position, and O^{2-} also has only one crystallographic position, which is in the center of the surrounding cations. For the defective fluorite structure of rare-earth zirconate, 1/8 of the 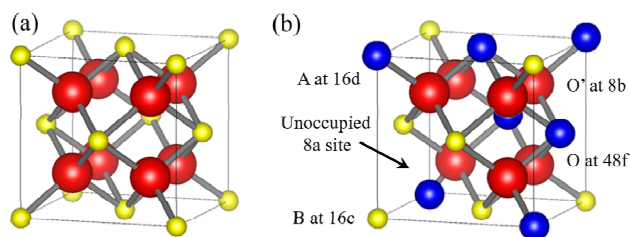oxygen ion vacancies are randomly distributed. The orderly distribution of oxygen vacancies is the main difference between the pyrochlore structure and defective fluorite structure. Some rare-earth zirconates such as $\text{Gd}_2\text{Zr}_2\text{O}_7$, $\text{Sm}_2\text{Zr}_2\text{O}_7$, and $\text{Nd}_2\text{Zr}_2\text{O}_7$ will change their crystal structure as the temperature increases, while some rare-earth zirconates such as $\text{La}_2\text{Zr}_2\text{O}_7$ can maintain a stable pyrochlore phase from room temperature to the melting point.

Whether in the pyrochlore structure or the defective fluorite structure, there is an oxygen vacancy in the molecular unit of rare-earth zirconate $\text{A}_2\text{B}_2\text{O}_7$, which can enhance the phonon scattering to reduce the thermal conductivity. Therefore, rare-earth zirconate materials have low thermal conductivity. According to the results reported by Wu *et al*. [92] and Maloney [93], the thermal conductivities of $\text{La}_2\text{Zr}_2\text{O}_7$, $\text{Sm}_2\text{Zr}_2\text{O}_7$, $\text{Nd}_2\text{Zr}_2\text{O}_7$, and $\text{Gd}_2\text{Zr}_2\text{O}_7$ are between 1.5 and 2 $\text{W·m}^{-1}\text{·K}^{-1}$ at 800 ℃, which is significantly lower than that of YSZ. Feng *et al*. [94] calculated the thermal conductivity of rare-earth zirconate pyrochlore materials using first principles and showed that the thermal conductivity of $\text{Gd}_2\text{Zr}_2\text{O}_7$ and $\text{Nd}_2\text{Zr}_2\text{O}_7$ was anisotropic. Table 2 lists the thermal conductivity of some rare-earth zirconates at 1473 K [95]. Xu *et al*. [96] synthesized $\text{Dy}_2\text{Zr}_2\text{O}_7$ with a defective fluorite structure, whose thermal conductivity is 1.31 $\text{W·m}^{-1}\text{·K}^{-1}$ at 800 ℃. Aruna *et al*. [97] prepared $\text{La}_2\text{Zr}_2\text{O}_7$ coatings by APS, and the thermal conductivity of the coatings was only 1.08 $\text{W·m}^{-1}\text{·K}^{-1}$. Yu *et al*. [98] found that the thermal conductivity of $\text{Sm}_2\text{Zr}_2\text{O}_7$ coatings prepared by APS was in the range of 0.36–0.46 $\text{W·m}^{-1}\text{·K}^{-1}$. Wan *et al*. [99] found that the doping of Yb^{3+} could cause the $\text{Sm}_2\text{Zr}_2\text{O}_7$ to undergo an order–disorder transition, and due to the increase in phonon scattering, the lowest thermal conductivity occurred at $(\text{Sm}_{2/3}\text{Yb}_{1/3})_2\text{Zr}_2\text{O}_7$. High-entropy rare-earth zirconate materials, which further improve the performance of rare-earth zirconates, have extremely low thermal conductivity due to their complex composition and a large amount of lattice distortion. Li *et al*. [15] prepared high-entropy $(\text{La}_{0.2}\text{Nd}_{0.2}\text{Sm}_{0.2}\text{Eu}_{0.2}\text{Gd}_{0.2})_2\text{Zr}_2\text{O}_7$ and found

Fig. 15 Crystal structure of the rare-earth zirconate: (a) fluorite structure and (b) pyrochlore structure.

Table 2 Thermal conductivities of some rare-earth zirconate materials at 1473 K [95]

Material	Thermal conductivity ($\text{W·m}^{-1}\text{·K}^{-1}$)
$\text{La}_2\text{Zr}_2\text{O}_7$	1.98
$\text{Gd}_2\text{Zr}_2\text{O}_7$	1.91
$\text{Sm}_2\text{Zr}_2\text{O}_7$	2.09
$\text{Nd}_2\text{Zr}_2\text{O}_7$	1.83

that its thermal conductivity was lower than 1 W·m^{-1}·K^{-1}, which is much lower than those of conventional rare-earth zirconates. The crystal structure and thermal conductivity of the high-entropy rare-earth zirconate are shown in Fig. 16. Li *et al.* [100] prepared the $Sm_2Zr_2O_7$–$NiCr_2O_4$ composites, which showed great radiant heat barrier capability. Ma *et al.* [101] added SiC particles to $Sm_2Zr_2O_7$ to reduce its photon thermal conductivity, as shown in Fig. 17.

In addition, the increase in the oxygen vacancy concentration increases the asymmetry of the potential well, which is conducive to the increase in the CTEs. Fan *et al.* [102] calculated the CTEs of rare-earth zirconate materials with the molecular dynamics method, and the results are shown in Table 3. The CTEs of rare-earth zirconate materials are mainly affected by Zr–O bonds due to the anharmonicity of atomic vibrations. For the same composition, the fluorite structures always have a high CTE relative to the corresponding pyrochlore structures due to weak bonding strength. Shimamura *et al.* [103] tested the CTEs of a series of rare-earth zirconates and found that the CTE of $RE_2Zr_2O_7$ decreases with increasing radius of the rare-earth ions. Zhou and Yi [104] prepared a series of $La_2Zr_2O_7$ doped with Dy and Ce. The doped material exhibits lower thermal conductivity and higher CTE than undoped $La_2Zr_2O_7$. In addition, they found that doping rare-earth cations at the RE^{3+} site in $RE_2Zr_2O_7$ pyrochlore significantly reduced the thermal conductivity, and doping Ce^{4+} cations at the Zr^{4+} cation site in $RE_2Zr_2O_7$ resulted in higher CTE. Liu *et al.* [105,106] prepared $(Mg_xLa_{0.5-x}Sm_{0.5})_2(Zr_{0.7}Ce_{0.3})_2O_{7-x}$ and $(La_{0.4}Sm_{0.5}Yb_{0.1})_2(Zr_{0.7}Ce_{0.4})_2O_{7.4}$, whose composition and structure were relatively complicated. This complexity of composition and structure can significantly reduce the thermal conductivity and increase the CTE.

Different from the thermo-physical properties, the bonding strength of the rare-earth zirconate coatings is lower than that of the YSZ coatings. For the Y_2O_3 and Ta_2O_5 co-doped $Gd_2Zr_2O_7$, Xue *et al.* [107] reported that after doping, not only the thermal conductivity of doped materials decreases but also both *E* and the high-temperature phase stability increases. References [108,109] have shown that the bonding strength of rare-earth zirconate coatings can be greatly improved by selecting an appropriate powder particle size and
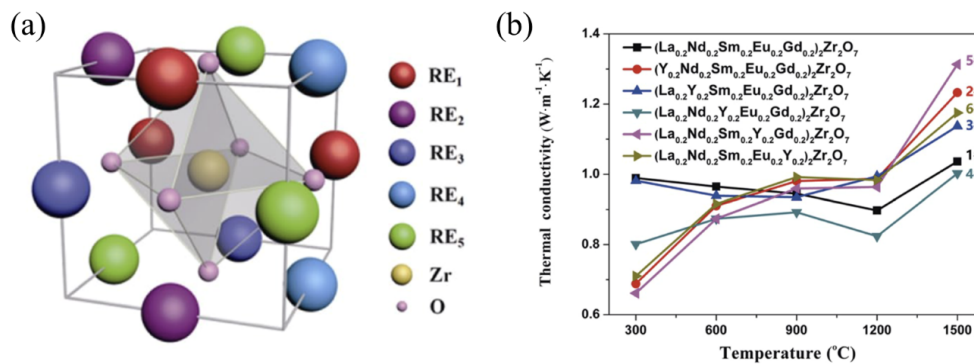

Fig. 16   Structure and thermal property of high-entropy rare-earth zirconates: (a) crystal structure and (b) thermal conductivities. Reproduced with permission from Ref. [15], © The Author(s) 2019.
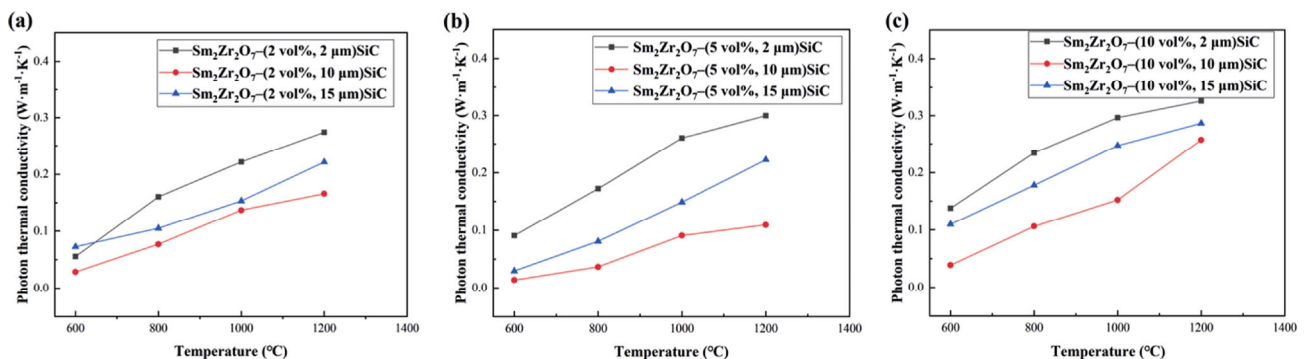

Fig. 17   Photon thermal conductivities of $Sm_2Zr_2O_7$–SiC composites: (a) 2 vol% SiC, (b) 5 vol% SiC, and (c) 10 vol% SiC. Reproduced with permission from Ref. [101], © The Author(s) 2020.

Table 3 CTEs of rare-earth zirconate materials calculated by the molecular dynamics method [102]

Material	CTE of pyrochlore (10^{-6} K^{-1})	CTE of fluorite (10^{-6} K^{-1})
$Nd_2Zr_2O_7$	7.80	9.71
$Sm_2Zr_2O_7$	7.77	9.55
$Eu_2Zr_2O_7$	7.81	8.88
$Gd_2Zr_2O_7$	7.91	9.18
$Er_2Zr_2O_7$	8.00	9.02
$Yb_2Zr_2O_7$	7.99	9.37
$Lu_2Zr_2O_7$	8.57	9.39

spraying parameters. The $RE_2Zr_2O_7$/YSZ double-layered coatings were prepared to effectively improve the bonding strength of the coatings effectively. In addition, the research by Doleker *et al*. [110] indicated that the TGO growth rate of $La_2Zr_2O_7$/YSZ double-layer coatings is lower than that of YSZ because of the low oxygen diffusion rate. Jasik *et al*. [111] prepared the $La_2Zr_2O_7$/ $La_2Zr_2O_7$ + 8YSZ/8YSZ coating, which has a smaller interlayer mismatch and higher service life.

Although the thermal conductivity of rare-earth zirconate has been reduced compared with YSZ, there are still several problems that urgently need to be solved to utilize the advantages of rare-earth zirconates. (1) Efforts are required to explore approaches to develop rare-earth zirconates with lower thermal conductivity and higher CTE. The CTE of $RE_2Zr_2O_7$ is still low which has a certain mismatch with the NiCoCrAlY bond coat. (2) Improving the mechanical properties of rare-earth zirconate materials is needed. The fracture toughness and lifetime of the $RE_2Zr_2O_7$ coatings are lower than those of the YSZ coatings. (3) The higher temperature properties of $RE_2Zr_2O_7$ are still not well understood. Thus, research is still needed to clarify how the properties of $RE_2Zr_2O_7$ materials change at higher temperatures. (4) Research into the infrared radiation properties of rare-earth zirconate at high temperatures is necessary. The contribution of thermal radiation to heat transfer has increased at high temperatures and cannot be ignored, and high emissivity results in TBCs with a certain thermal radiation blocking ability.

In short, although YSZ has many excellent characteristics, such as high toughness and large CTE, and increasing the purity of YSZ can improve its sintering resistance, it is prone to phase transformation at temperatures higher than approximately 1200 ℃. New materials to replace YSZ are being developed to meet the operating environment of TBCs. Co-doping

multiple rare-earth oxides into YSZ can significantly reduce the thermal conductivity. Other new ceramic materials, such as RE_3NbO_7, $RETaO_4$, and $RE_2Zr_2O_7$, show lower thermal conductivity than YSZ. In addition, they also have high chemical stability and CTE comparable to YSZ. However, the fracture toughness of these new materials is usually lower than that of YSZ. Although TBCs directly deposited with new materials exhibit high thermal insulation performance, the lifetime of these coatings is usually relatively low. Therefore, the multiple-layered ceramic coating systems composed of YSZ and new materials have become a promising strategy to obtain high-performance TBCs.

3 Degradation and delamination of ceramic top coat

The spalling of the ceramic layer, which limits the lifetime of TBCs, is caused by many factors. All these factors lead to the mechanical strain and stress which are the direct driving forces for coating spalling. After the coating is prepared, a certain level of residual stress appears within the TBCs. Under the actual service conditions of the TBCs, the harsh operating environment also results in mechanical strain and stress. These include stresses induced by thermal mismatch, ceramic sintering, and phase transformation. All stresses are important causes of coating cracking. Moreover, the crack evolution in ceramic layers is also affected by oxide growth. In addition, external corrosion and erosion are also critical factors inducing ceramic cracking. A comprehensive understanding of the failure mechanism of coatings has become a prerequisite for the development of new TBCs.

3. 1 Ceramic delamination by top coat stresses

3.1.1 *Quenching stress*

Quenching stress is the first important stress within a thermal sprayed top coat. Compared with the conventional bulk structure, a thermal sprayed ceramic coating has low modulus and bonding strength [112], while quenching stress is related to the evolution of residual stress in a thermal sprayed top coat. The cracks and pores between lamellae are two essential characteristics of thermal sprayed ceramic coatings. These two essential characteristics reveal that large cracking stress is produced during coating deposition.

Obviously, understanding the origin of deposition stress would be of great importance for further coating structure design.

Intra-splat cracks are directly related to the deposition stress. However, the final intra-splat crack patterns are always considered disordered and irregular [113] since the detailed formation process of intra-splat cracks has been scarcely concerned. To identify the regularities of intra-splat crack patterns, both geometry and topology were stated and distinguished, as shown in Fig. 18. According to topology theory, edges and vertices are applied to the description of the space-dividing network. A vertex in topology is the point where a younger crack meets an older one, and an edge is the part of the crack between two of these adjacent vertices. According

to geometry theory, "sides" and "wedges" (or "corners") must be taken into consideration to describe the shape of a cell. A side of a pattern is the part of the contour that is delimited by two wedge-shaped singularities (corners) [114–116]. Moreover, a side can be curved, but its curvature should be continuous in geometry. Consequently, the points where two edges intersect in the specified pattern belong to the vertices in topology but do not necessarily form the wedges in geometry. In this way, both the number of sides and neighbors for crack patterns were statistically analyzed, as shown in Fig. 19. The statistical analyses yield that the average number of sides and neighbors is approximately 4 and 6, respectively [117].

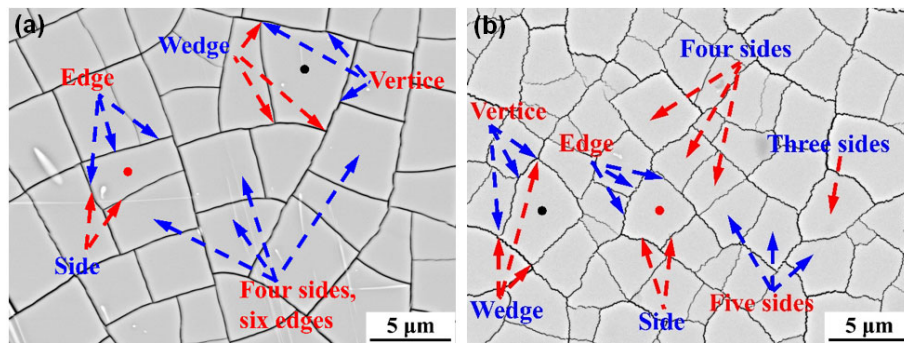The crack patterns can be reconstructed with successive

Fig. 18 Geometry and topology: (a) distinction between topology and geometry of $La_{0.5}Sr_{0.5}CoO_3$ patterns with straight crack paths and (b) $La_2Zr_2O_7$ patterns with zigzag crack paths. Reproduced with permission from Ref. [116], © ASM International 2016.

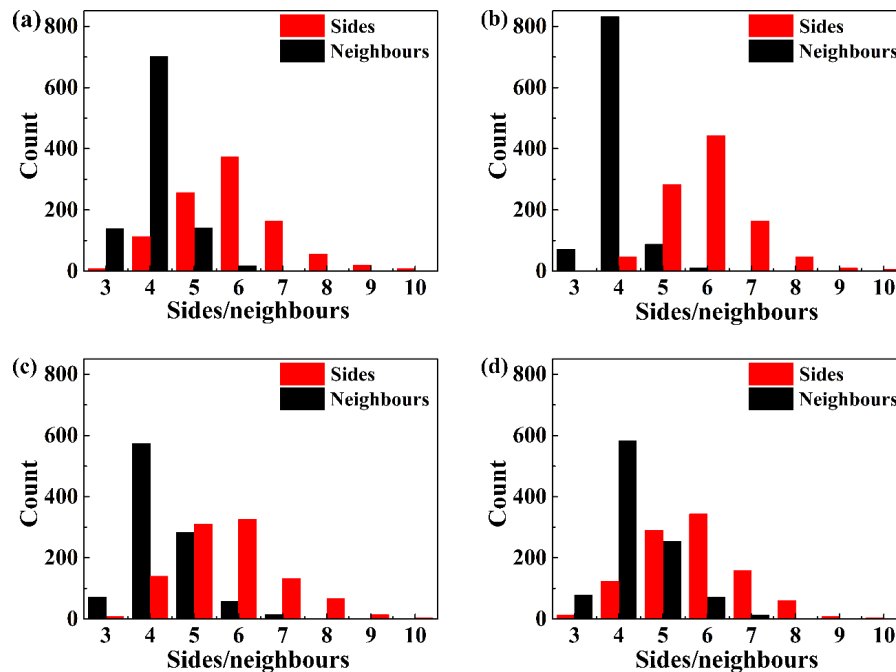**Fig. 19** Statistical histograms of the number of sides (black bars) and neighbors (red bars) for patterns in (a) TiO_2, (b) $La_{0.5}Sr_{0.5}CoO_3$, (c) $La_2Zr_2O_7$, and (d) YSZ splats. Reproduced with permission from Ref. [116] for (a–c), © ASM International 2016; Ref. [117] for (d), © ASM International 2016.

domain divisions based on the cracking criterion of the greatest motivation [117], as shown in Fig. 20. The domain in Fig. 20(a) is selected to present the evolution of crack patterns from Figs. 20(b) to 20(f). When the crack driving force further develops, a crack arises near the center and joins the edge at 90°, as shown in Fig. 20(c). As the driving force develops, cracking occurs successively and divides the domain into increasingly smaller patterns in Figs. 20(d)–20(f). With decreasing domain size, the crack extension trajectory becomes increasingly deterministic. Domain divisions proceed iteratively in this way and never stop until the greatest motivation of patterns is insufficient to drive cracking. Finally, a peculiar hierarchy emerges.

It is widely believed that the interlamellar pores are retained during the formation process of splats for some reasons, such as low impact pressure [118], condensates and adsorbates on the substrate surface [119,120], rather than deposition stress. However, various epitaxial growth [121–125] of various splat/substrate combinations was found under extremely low deposition temperatures and large lattice mismatches. This clearly suggests that deposition stress dominates the formation of lamellar pores. To understand the origin of deposition stress, the epitaxial interfaces were examined by a high-resolution transmission electron microscope (HR-TEM) in detail. As a result, anomalous incommensurate homoepitaxial growth [126] with mismatch-induced dislocations in thermally-sprayed YSZ splats to create a homo-interface was observed, as shown in Fig. 21.

Apparently, the anomalous epitaxial growths are related to deposition processing. During thermal spray deposition, the epitaxial film formation goes through five stages, as shown in Fig. 22. First, the molten droplet heated and accelerated by the plasma torch impacts the substrate with a high velocity, as shown in Fig. 22(a). Then, the droplet rapidly spreads on the substrate forming a liquid film, as shown in Fig. 22(b). During the third stage, solidification/epitaxial growth starts, and the liquid film transforms into a solid epitaxial film on the single-crystal substrate, as shown in Fig. 22(c). After epitaxial growth, the film together with the substrate rapidly cooled to room temperature, as shown in Fig. 22(d). Finally, an epitaxial film bonded on the single-crystal substrate was observed, as shown in Fig. 22(e).

Obviously, dislocations and cracking formed during either the solidification or cooling process. During film
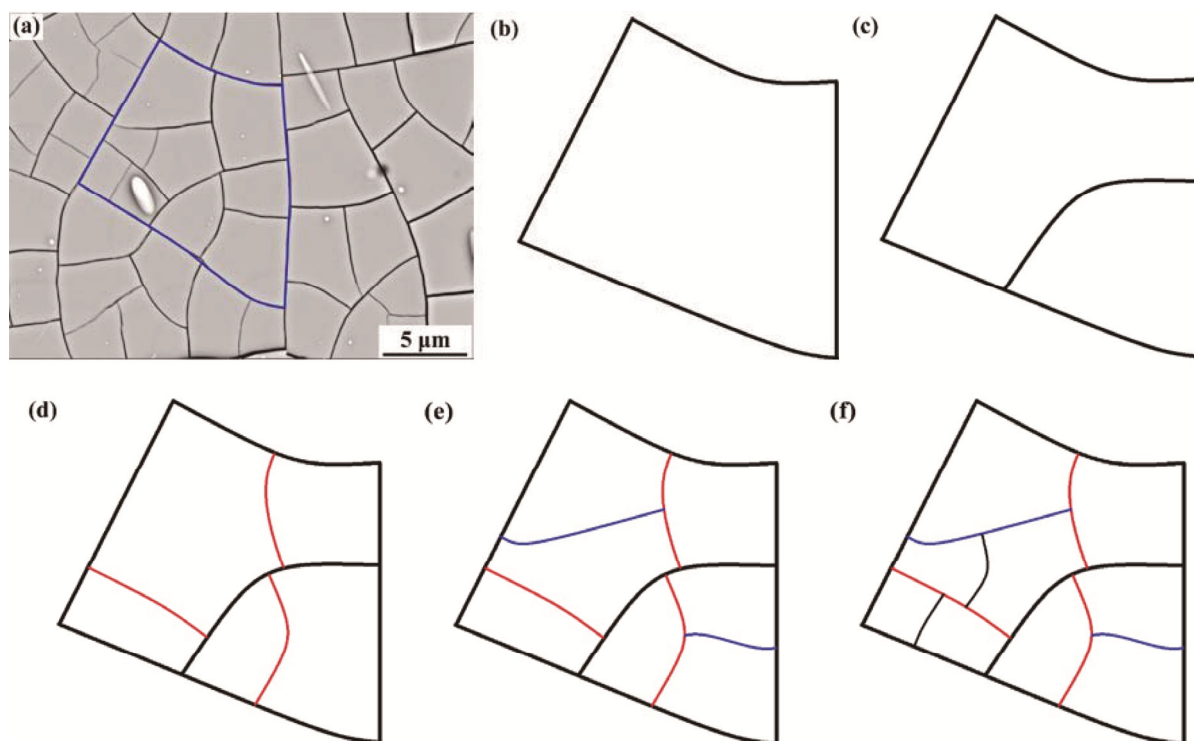

Fig. 20 Propagation from large to small scale. As the crack driving force develops, the crack patterns in (a) the selected domain evolve from (b) to (f). The crack orders from (c) to (f) are the first (bold black line), second (red lines), third (blue lines), and fourth orders (fine black lines), respectively. Reproduced with permission from Ref. [116], © ASM International 2016.
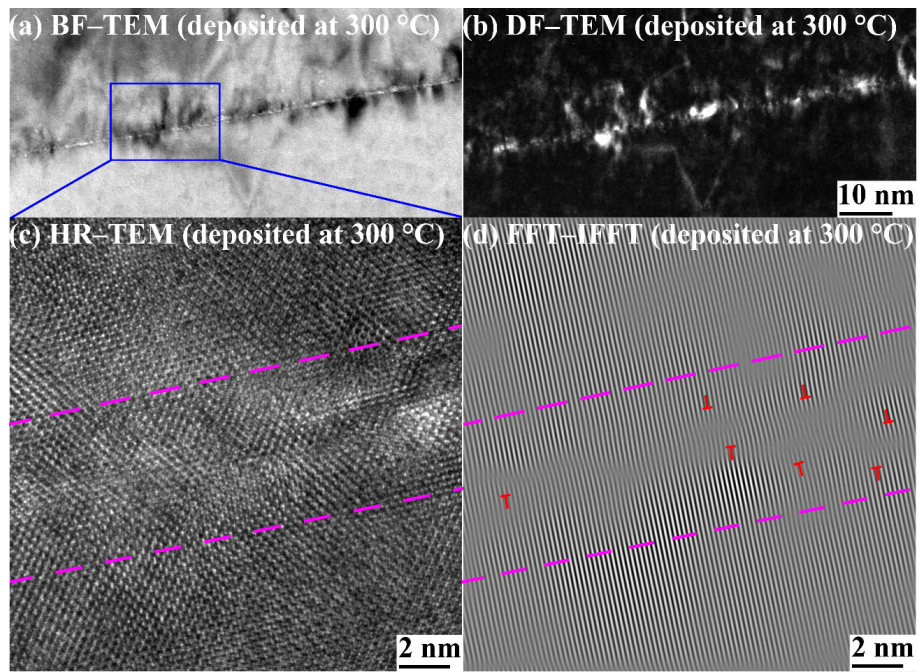
Fig. 21 Microstructure and quantitative characterization of the homoepitaxial YSZ–YSZ interface. (a) Bright-field (BF)-TEM, (b) dark field (DF)-TEM, (c) HR-TEM, and (d) fast Fourier transform (FFT)–inverse fast Fourier transform (IFFT) images of the film deposited at 300 ℃. The interface region is marked by two pink dashed lines. The dislocations in (d) are marked by red signs. Reproduced with permission from Ref. [126], © ASM International 2017.
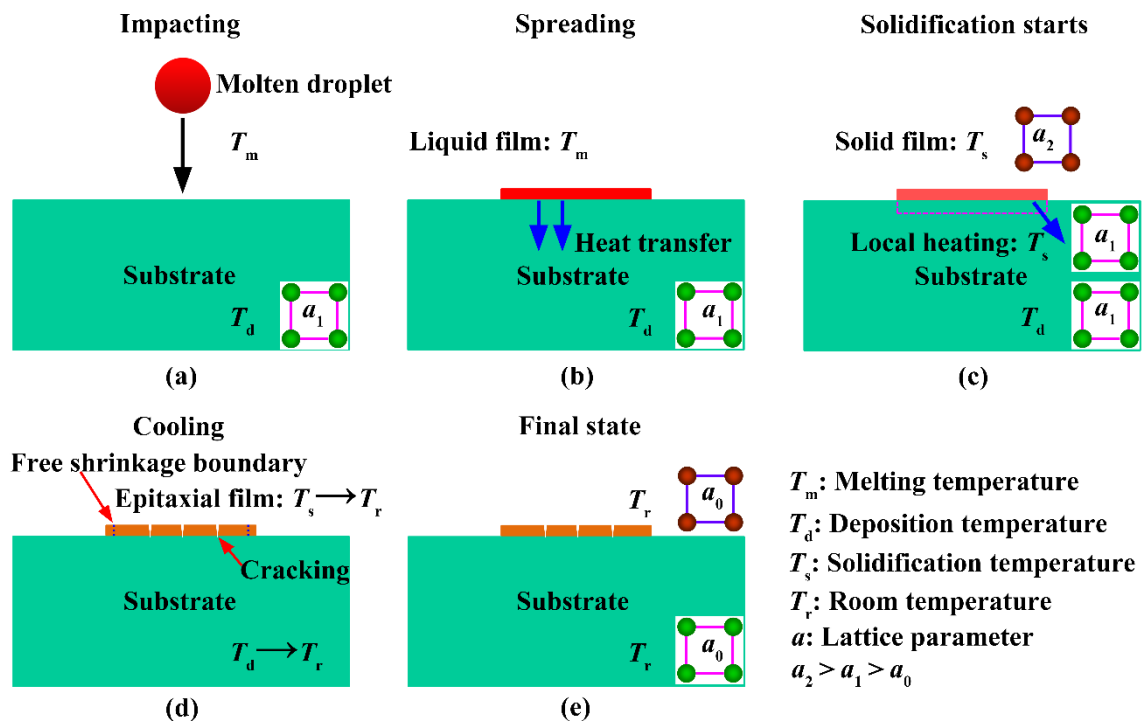
Fig. 22 Detailed film formation process during the present liquid homoepitaxy by thermal spray technology. (a) Molten droplet with high-speed impacts on single-crystal substrate surface, (b) droplet quickly spreads on the substrate forming a liquid film, (c) liquid film starts solidification on substrate forming a solid epitaxial film, (d) during the subsequent cooling, the epitaxial film would shrink with the temperature from T_s to T_r, and (e) epitaxial film/substrate system was formed at room temperature. The blue dashed lines in the epitaxial film in (d) denote the position in the case of free shrinkage. Reproduced with permission from Ref. [126], © ASM International 2017.

spreading and solidification, the lattice parameter of the film decreased with decreasing temperature. However, since the substrate was much larger than the film in all three dimensions, the substrate worked as a rigid body. As a result, the temperature in the whole substrate (except the region covered by the molten film) remained nearly unchanged. As expected, the localized substrate covered by the molten film was significantly heated during the film spreading and solidification process, but the expansion of this region was strongly constrained by its cold surroundings, as shown in Fig. 22(c). Consequently, the lattice parameter of the film was larger than that of this locally-heated substrate during epitaxial growth, and net dislocations were produced in the interfacial layer to negate the lattice mismatch at the film–substrate interface. After epitaxial growth, the film together with the substrate would rapidly cool to room temperature, as shown in Fig. 22(d). However, the degree of thermal shrinkage between the film and substrate was significantly different. The temperature change in the epitaxial film during cooling was from T_s to T_r, while it was actually only from T_d to T_r for the corresponding substrate, as shown in Fig. 22(d). Compared with free shrinkage (marked by the blue dashed lines in Fig. 22(d)), large tensile stress in the epitaxial film was thus produced due to the constraints of the substrate.

Therefore, large quantities of dislocations were produced during the solidification process, while cracking occurred during the cooling process. Both were due to the constraint effect of cold surroundings on the locally-heated substrate. In other words, quenching stress is produced in a temperature range from the melting point of splat to the deposition temperature (*in-situ* substrate temperature), while the thermal mismatch stress σ_t (introduced in Section 3.1.2) is produced in a temperature range from the deposition temperature to room temperature.

In brief, quenching stress is produced during coating preparation by rapid cooling after the solidification of hot splat on the cold substrate surface. Although intra-splat cracks and inter-splat pores release some of this quenching stress, the chemical bonding region between the splats will maintain some quenching stress in the as-sprayed ceramic top coat.

3.1.2 Thermal mismatch stress

In addition to quenching stress, thermal mismatch-induced stress is another important stress for TBCs. For the as-prepared TBCs, both quenching stress and σ_t contribute to residual stress, which can be examined by both experiment and simulation [25,127,128]. Furthermore, during thermal cycling, a much larger mismatch stress will be produced due to the different CTEs of the superalloy substrate and the ceramic top coat.

After the coating is prepared, it will go through the process of heating and cooling in the process of thermal cycling. The CTE of the superalloy substrate is usually slightly higher than that of the bond coat, and the CTE of the bond coat is higher than that of the ceramic layer. Although the thickness of TGO is very thin, it has the highest modulus and the lowest CTE compared with the other layers. At the same time, TGO will continuously grow at high temperatures, leading to an increase in its thickness. During the thermal cycle, the different CTEs of each layer will induce a large σ_t [129–131]. In addition, the growth of TGO at high temperatures leads to the local irreversible plastic deformation of the bond coat. Therefore, the internal stress of the ceramic layer near the interface induced by thermal mismatch will continue to increase in the heating or cooling stage of the subsequent thermal cycle.

If only one two-dimensional (2D) stress–strain model containing substrate and coating is considered, σ_t can be expressed as Eq. (4):

$$\sigma_t = E_c \Delta\alpha\Delta T \frac{1+\upsilon}{1-\upsilon^2} \tag{4}$$

where $\Delta\alpha$ is the difference in the CTE between the coating and the substrate, ΔT is the temperature difference during cooling, υ is the Poisson's ratio of the coating, and E_c is the elastic modulus of the coating. In fact, the coating thickness is not considered in this analytical formula. Therefore, it is not applicable when the coating thickness is considered in the model. It is noted that the interface morphology and roughness of the ceramic layer and bond coat have a great influence on the local stress state and amplitude in the coating, which is not considered in the above theoretical formula.

Many studies on σ_t have been reported [25,26,132]. It is shown that the thermal mismatch degree between the ceramic and substrate layers directly affects the service life of TBCs. Wei *et al.* [133] studied the internal stress state of a ceramic layer induced by a thermal mismatch during a thermal cycle without TGO growth by the finite element method, as shown in Fig. 23. It can be seen that tensile stress appears at the

ceramic layer near the top of the bond coat at the heating end. Since TGO growth at the high temperature stage is not considered, the stress in the coating does not change in the dwelling stage. When the coating is cooled from high temperature to room temperature, the tensile stress above the peak and the compressive stress in the valley increase. The shear stress is located near the peak during the thermal cycle.

Moreover, Wei *et al.* [133] also studied the accumulation and change in the crack tip energy of a ceramic layer induced by thermal mismatch during thermal cycling, as shown in Fig. 24. When TGO growth is not considered, the energy at the crack tip is still close to zero during the cooling phase. When TGO growth is included, the energy at the crack tip reaches approximately 62 J·m^{-2}. Moreover, when the coating undergoes the cooling process, the energy at the crack tip further increases to 72 J·m^{-2}. The comparison between Figs. 24(c) and 24(d) shows that TGO growth is very important to the evolution of the crack driving
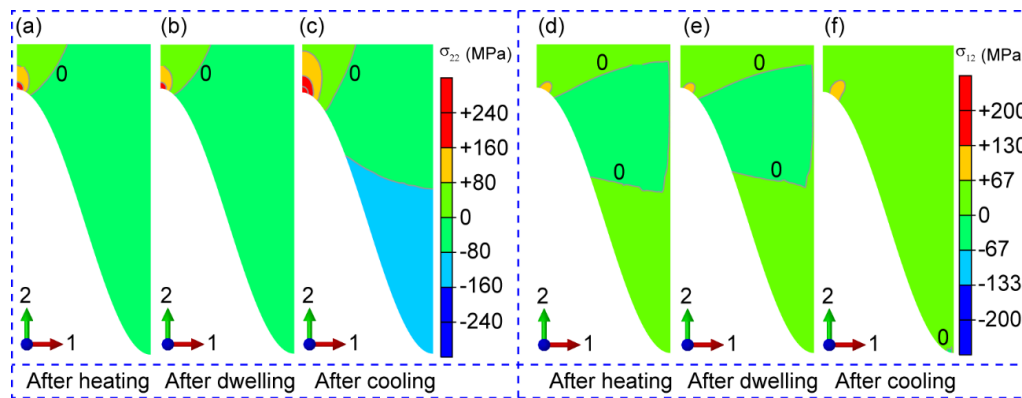
Fig. 23 Stress distributions in the ceramic layer during one thermal cycle: (a–c) normal stress and (d–f) shear stress. Reproduced with permission from Ref. [133], © ASM International 2019.

Fig. 24 Evolution of strain energy at the crack tip under different stages during one thermal cycle: (a) heating stage, (b) dwelling stage, and (c, d) cooling stage. The models only in (a)–(c) contain the TGO growth. Reproduced with permission from Ref. [133], © ASM International 2019.

force in the coating, which cannot be ignored. The comparison between Figs. 24(b) and 24(c) shows that the growth of TGO affects the stress induced by thermal mismatch in the subsequent cooling process, which is caused by the permanent deformation of the bond coat.

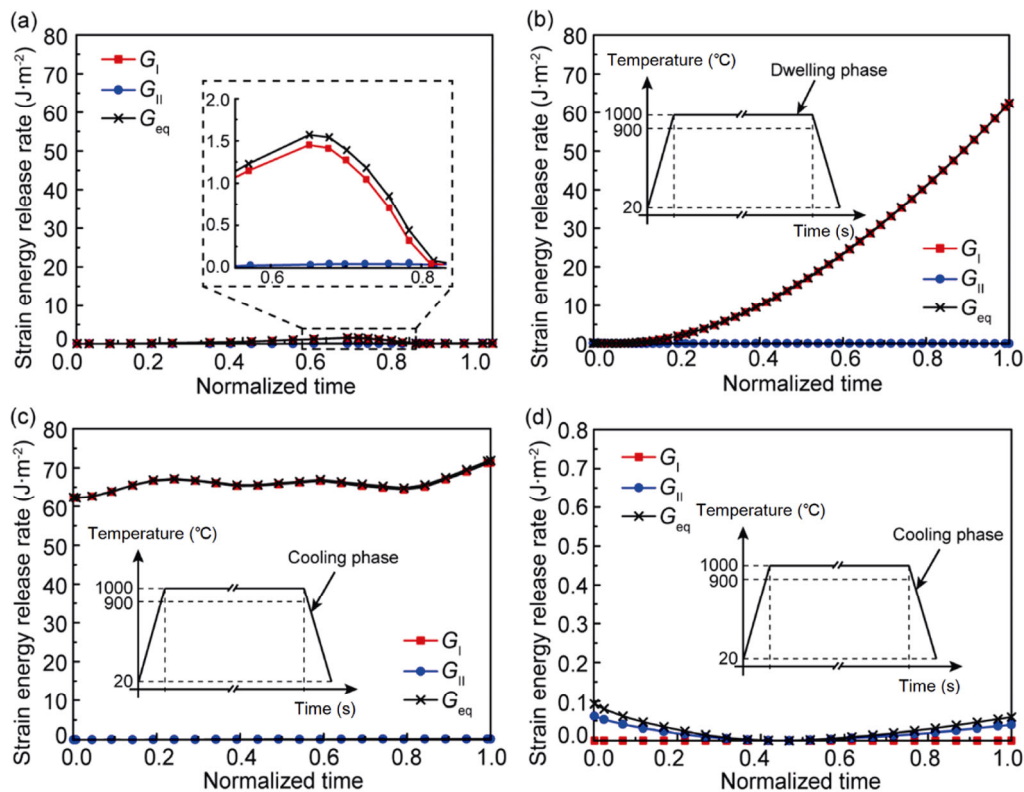Because the TBC sample is a three-dimensional (3D) structure, the σ_t in the coating analyzed by the 2D model may be different from that in the real coating. Bäker and Seiler [134] used two kinds of 3D models to study σ_t in the ceramic layer during a cooling process, as shown in Fig. 25. It can be seen that the tensile stress is still located near the ceramic layer, which is consistent with the 2D model analysis. However, the difference is that the tensile stress range under the 3D

model is larger. Of course, the amplitude and TGO thickness of the model adopted by the two authors are different, so the stress amplitude is not comparable. In general, the predicted stress distribution in the ceramic layer induced by thermal mismatch is the same whether using the 2D or 3D model.

Krishnasamy *et al.* [135] analyzed the stress state and crack propagation behavior induced by σ_t during cooling by using the macro–micro integration model, as shown in Fig. 26. The thermal mismatch dominated by the substrate leads to the initiation and propagation of coating edge cracks during cooling. Moreover, it can be observed from the splat model that the combination of microcracks leads to the formation of large cracks. Ranjbar-Far *et al.* [136] built a ceramic layer model

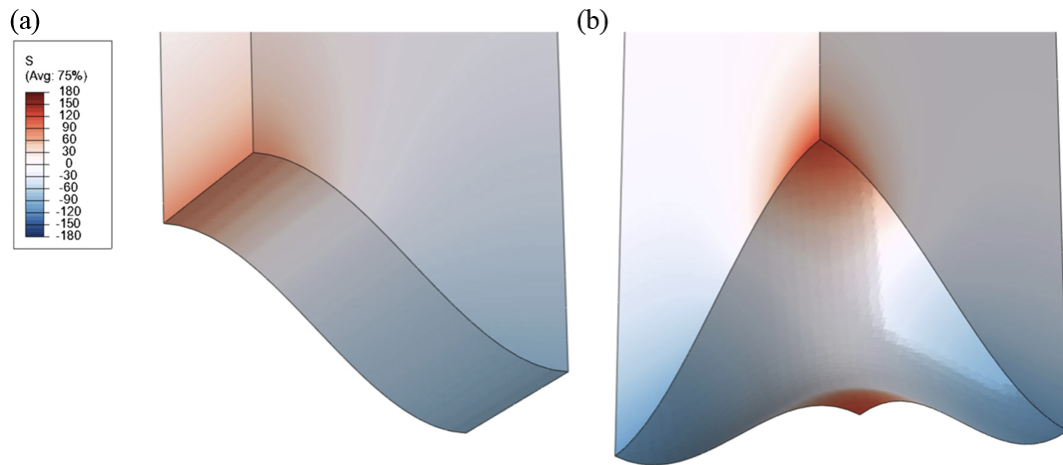**Fig. 25** σ_{22} stress distribution in the TC layer under different 3D models cooled to room temperature: (a) grooved model and (b) sinusoidal model. Reproduced with permission from Ref. [134], © ASM International 2017.
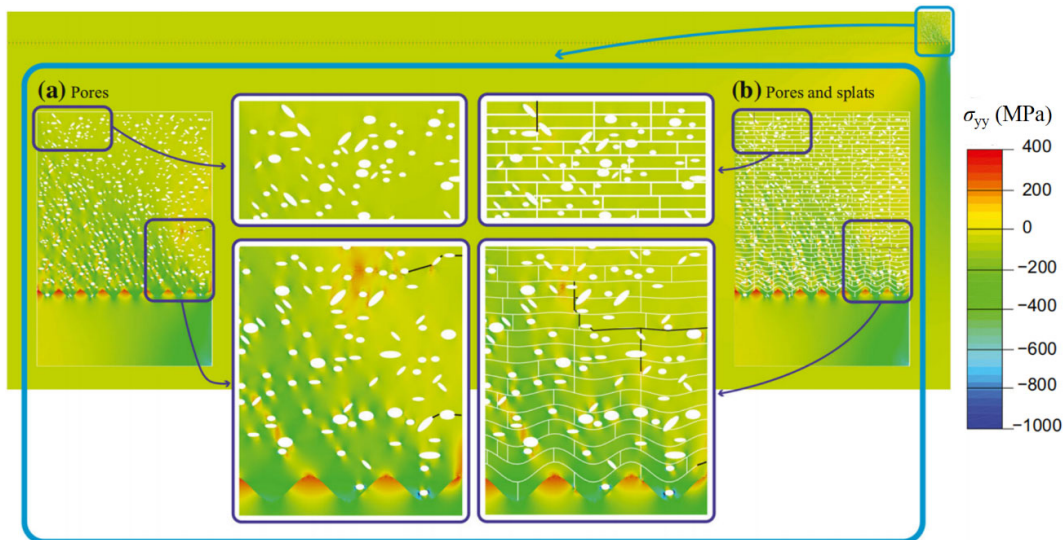

Fig. 26 Stress state and crack behavior at room temperature in different models: (a) pore model and (b) splat model. Reproduced with permission from Ref. [135], © The Author(s) 2019.

formed by stacking flattened particles through a self-developed program to study the interface crack and ceramic crack propagation behavior induced by thermal mismatch between layers, as shown in Fig. 27. Due to the difference in CTE between the ceramic layer and substrate, a large σ_t appears at the tip of cracks in the ceramic layer and at the interface. When the cumulative strain energy at the crack tip is greater than the fracture toughness of the coating, crack propagation occurs. Moreover, with the cooling process, σ_t increases, and then the crack length is extended. Therefore, the thermal mismatch between layers is very important for the delamination and failure of the ceramic layer.

Based on the research results on σ_t, there are two methods to improve the spalling resistance of the coating. One is to find new ceramic materials with CTE close to the substrate, and the other is to release σ_t by preparing a vertical crack through the coating. To reduce σ_t and improve the TBC lifetime, both aspects need more investigation in the future.

3.1.3 Sintering stress

During thermal exposure, sintering of the ceramic top coat will occur because the ceramic coatings often appear to be porous. Usually, sintering leads to obvious
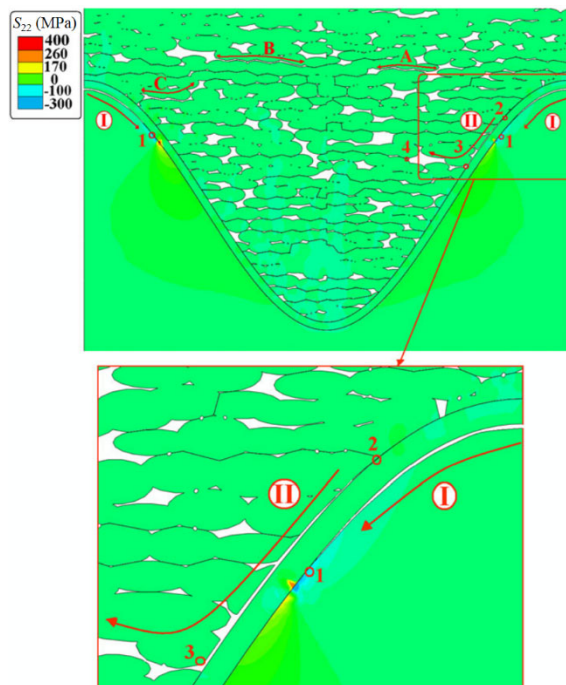

Fig. 27 Crack states in the TC layer at room temperature without considering TGO growth. Reproduced with permission from Ref. [136], © ASM International 2012.

structural changes resulting in performance degradation [137,138]. First, the thermal insulation effect is reduced due to increased thermal conductivity [139,140]. Therefore, sintering distinctly threatens the thermal barrier function. Second, sintering makes the coatings stiffen [141]. The poor strain tolerance facilitates the generation of sintering stress [142–145]. This is one of the main causes for the spallation or delamination of TBCs since it promotes the formation of large-scale cracks. Therefore, the sintering is one driving force responsible for failure and threatens the durability of TBCs [143,146,147]. Overall, sintering stress is inevitable during thermal exposure and has negative effects on TBC performance. This section reviews the sintering of TBCs from the following aspects: (i) intrinsic characteristics of TBCs; (ii) essential structural changes during sintering; (iii) sintering mechanism of TBCs; and (iv) sintering stress and its effect on cracking. A better understanding of sintering stress would contribute to the development of advanced TBCs with long life spans.

The intrinsic characteristic of TBCs is the basis for understanding the sintering process. It is well known that plasma-sprayed TBCs are porous structures that benefit the thermal insulation and strain tolerance. Therefore, examination of the evolution of porosity is a common way to characterize the sintering process. However, porosity cannot effectively present the structural changes in TBCs. There are at least two reasons. On the one hand, TBCs often present unique porous structures, as shown in Fig. 28 [7,148]. Plasma spraying is a widely-used method to prepare the top coat of TBCs. The coating is formed in a layer-by-layer manner. Each layer consists of many splats generated from molten particles in a plasma flame. During the spraying process, a stream of molten particles is impacted on the substrate. Subsequently, the molten particles undergo lateral flattening, rapid solidification, cooling, and finally form disk-shaped splats [149,150]. Therefore, a thermally-sprayed coating often exhibits a lamellar microstructure, which makes the pores appear to have multiple morphologies. The imperfect bonding between lamellar splats results in the formation of inter-splat pores that often have an in-plane orientation (parallel to substrate). The net-form cracks inside splats, called intra-splat cracks, further divide the splats into several segments. The inter-splat pores and intra-splat cracks appear to be approximately several micrometers to several tens of micrometers, whereas they only have
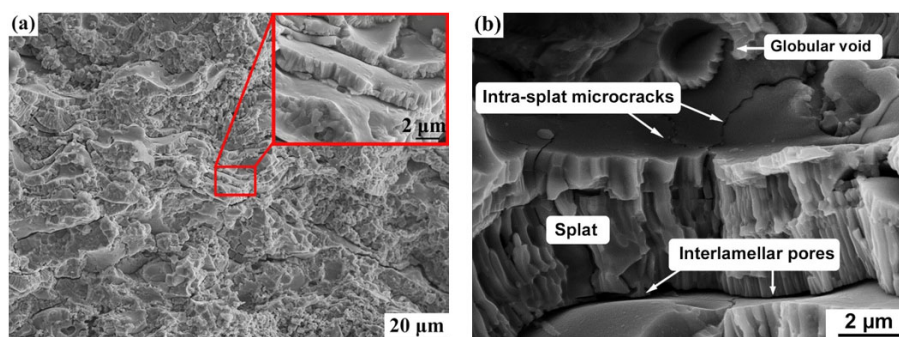
Fig. 28 Structural characteristics of plasma-sprayed TBCs: (a) lamellar structure formed by layer-stacking. Reproduced with permission from Ref. [7], © ASM International 2015. (b) Three kinds of pores. Reproduced with permission from Ref. [148], © ASM International 2013.

scales of approximately several nanometers to several tens of nanometers in the third direction. Therefore, they can be regarded as 2D defects [7,151]. Moreover, the 2D-shaped intra-splat cracks and inter-splat pores are actually linked with each other, forming a 2D pore network, as shown in Fig. 29 [7]. In addition, some globular voids can still be seen in plasma-sprayed TBCs. These 3D voids are caused by the incomplete filling of molten droplets onto the rough surface (substrate or prior deposit). The co-existence of 2D pores and 3D pores makes the plasma-sprayed TBCs a unique porous structure. In contrast, for porous ceramic structures that were prepared by conventional processing methods, the voids often appear to be in 3D spherical shapes only. Due to the unique microstructure, the porosity of plasma-sprayed TBCs is approximately 10%–15% [139,140]. In contrast, the thermal conductivities [139,148,152–154] and elastic moduli [155–158] of coatings are often lower than 50% with respect to the corresponding bulk materials. In brief, plasma-sprayed TBCs exhibit unique lamellar structures. The intrinsic characteristic is the 2D splats around with 2D pores or cracks, similar to the composited structure.
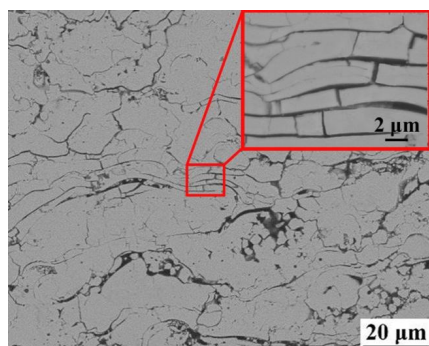

Fig. 29 2D pore network formed by the connection of inter-splat pores and intra-splat cracks. Reproduced with permission from Ref. [7], © ASM International 2015.

Sintering leads to structural changes in TBCs in a special way. Densification is a common result of sintering in porous ceramic structures. Thus, the porosity should decrease. However, as mentioned above, the porosity change cannot essentially characterize the structure of plasma-sprayed TBCs. It has been reported that the degree of change in porosity during thermal exposure is less than 30% [139]. In contrast, the changing degrees of mechanical and thermal properties can be as large as 50% or more [141]. The structural changes should be consistent with the properties. Given the unique porous structure of plasma-sprayed TBCs, the 2D pores play a significant role in the sintering process. Figure 30 shows the evolution of the polished cross-section of plasma-sprayed TBCs during thermal exposure [13]. It is easy to recognize several significant changes. From an apparent view, the initial state was a porous structure, whereas it became much denser. When taking a closer view, it is found that the 2D pores (including inter-splat pores and intra-splat cracks) disappeared significantly. As a result, some continuous lines were divided into several segments, which means that the 2D pores become much shorter. The width or opening of 2D pores significantly affects the disappearance of 2D pores. Pores with large widths can still be seen even after long-term thermal exposure. The width-related healing behavior of 2D pores is revealed during thermal exposure [159]. In addition to direct observation, the changes in 2D pores can be investigated statistically, which presents the changes in the length density of 2D pores at different states [160]. During thermal exposure, the degree of change in the 2D pore length density is over 50%, which is closer to the properties and much greater than that of the porosity. This suggests that the change in 2D pores is consistent with the property changes. The relationships between

hardness and microstructure that are characterized by 2D pores and porosity were reported [161]. If the porosity and 2D pore density change to 0, the normalized hardness should be 1. The predicted limit value based on 2D pore density is 1.02, which is much closer to the theoretical value (i.e., 1). As a comparison, the predicted limit value based on porosity is 1.4. Another phenomenon to prove the 2D pore change is the disappearance of large voids of approximately several tens of microns. These large voids arise from the preparation of polished samples [162]. In the as-sprayed state, weak bonding between splats leads to spalling of some splats, which appear to have a void-like morphology. After sintering, the bonding is enhanced due to the sintering of inter-splat pores. Therefore, nearly no large voids can be seen after thermal exposure. In brief, the essential structural change during sintering is the healing of 2D pores, which can be well correlated to the change in properties.

Sintering of 2D pores proceeds in a special way that is different from conventional sintering of porous structures. As a result, the sintering kinetics are different at different sintering stages [160]. The rates of change at the initial dwell time are much faster. Then they slow down significantly. As a result, the initial dwell time finishes most of the changing degrees. For example [161], the changing degrees of porosity, 2D pore density, and hardness were 83%, 66%, and 83%, respectively. These results suggested that the total sintering process is obviously nonlinear. It can be transformed into nearly linear trends by taking the logarithm treatment. The total evolution can be approximately divided into two stages according to the change rates. The dividing boundary is located at 10–20 h and is dependent on temperature [163]. The increasing slope and increment at the first stage were much larger than those in the following stage. The stage-sensitive sintering process is highly related to the unique microstructure of plasma-sprayed TBCs.

Commonly, the objective of sintering is to decrease the free energy by matter transfer. Therefore, the sintering of porous ceramic structures is inevitable due to the high surface energy caused by pores. For conventional powder metallurgy, sintering proceeds by forming necks between ceramic powders, followed by their growth in diameter. However, for plasma-sprayed TBCs, the sintering process is structure specific due to the 2D pores, especially the inter-splat pores between layers. Cipitria *et al*. [151] made a large step to investigate the sintering process based on the layer-stacking model. However, their predicted results cannot account for the stage-sensitive sintering kinetics since the healing of inter-splat pores proceeds by a gradual increase in the bonding area. In fact, the healing of inter-splat pores is completed in a multi-contact way. As shown in Fig. 31 [164], the pores change from continuous lines to separated segments. In other words, some areas of the pores were bridge-connected. The multiple contacts are caused by roughening of the pore surface. The roughening effect has been reported in previous reports with different materials, such as YSZ [165]. As shown in Fig. 32 [164], the initial pore surface is smooth. After thermal exposure, the surface evolves to be roughened by grain boundary grooving and surface faceting effects. At the narrow part of the pores, the roughening causes multiple contacts of the counter-surfaces of pores. During sintering, the sintering rate is determined by the rate of matter transfer. The multiple contacts between pores provide more ways to transfer matter at the same time. As a result, the sintering kinetics are much higher at the first stage driven by the multiple contacts. In summary, the sintering of plasma-sprayed TBCs proceeds in a multi-contact way due to the unique microstructure. This special sintering process results in an ultrafast increase in the mechanical and thermal properties, which affects the performance of TBCs.
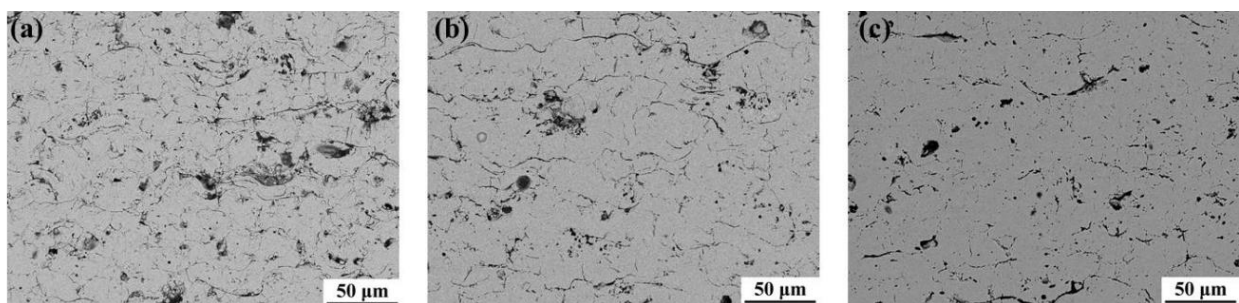

Fig. 30 Evolution of the polished cross-section of plasma-sprayed TBCs during thermal exposure at 1400 ℃: (a) 0 h, (b) 20 h, and (c) 100 h. Reproduced with permission from Ref. [13], © ASM International 2018.
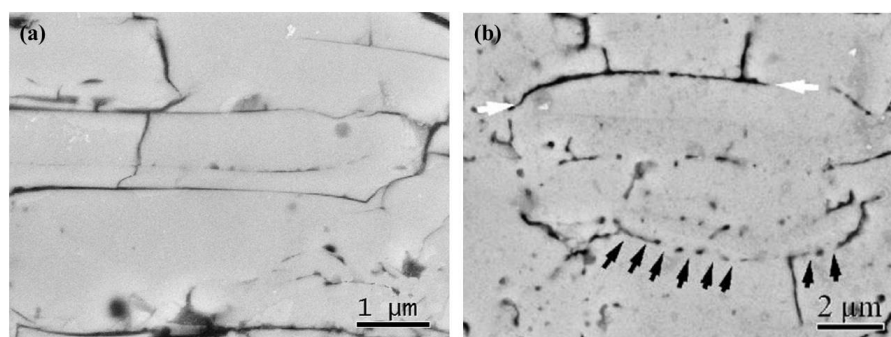
Fig. 31 Changes in 2D pores during thermal exposure at 1300 ℃: (a) 0 h and (b) 1 h. Reproduced with permission from Ref. [164], © ASM International 2015.
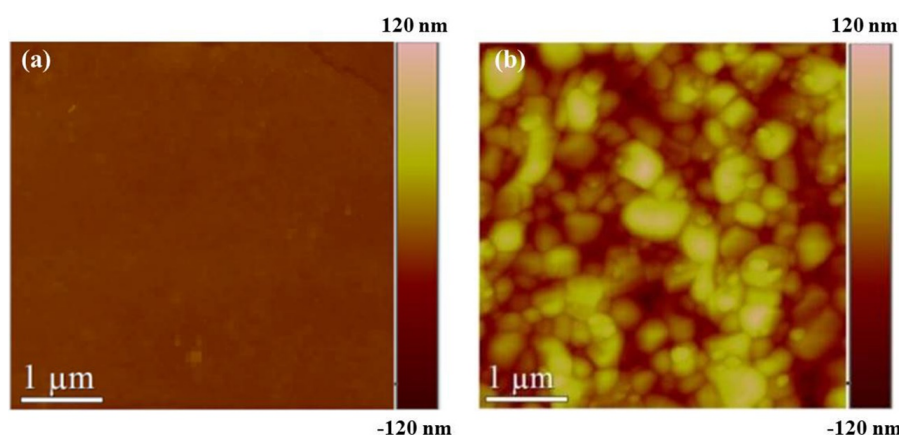

Fig. 32 Roughening behavior of the pore surface during thermal exposure at 1300 ℃: (a) 0 h and (b) 100 h. Reproduced with permission from Ref. [164], © ASM International 2015.

Sintering stress is mainly caused by stiffening of TBCs. The sintering stress is highly related to the sintering process and has a significant effect on the life span of TBCs. As mentioned above, the sintering process mainly refers to the healing of 2D pores, which is dominantly responsible for the stiffening of TBCs (or increase in elastic modulus). Some papers correlated the change in elastic modulus with 2D pores by structural models. Li *et al*. [166] developed a structural model formed by the stacking of disk-shaped splats with limited bonding area. The model predicted an out-of-plane elastic modulus that is well consistent with the experimental data. In further work, they modified the structural model by inserting intra-splat cracks to form a 2D pore network [7]. The anisotropy of the elastic modulus can be well predicted. Moreover, this model can simulate the change in bonding ratio at different stages that refer to the healing of inter-splat pores. Therefore, a more reasonable relationship between the elastic modulus and structural change during thermal exposure can be obtained [160]. From an overall view, the model prediction exhibits two-stage trends that are

consistent with experimental data, despite temperatures or directions. Moreover, the ultrafast healing of 2D pores by multi-contact can be realized by the ultrafast increase in the bonding ratio. Therefore, the change in elastic modulus at the first stage can be well captured. In brief, sintering of plasma-sprayed TBCs proceeds mainly by healing 2D pores, which causes the stiffening of TBCs.

Based on the sintering-induced stiffening behavior, the effects of sintering on the stress and driving force of interfacial cracking (strain energy release rate (SERR)) upon stiffening were investigated [167], as shown in Fig. 33. With the increase in the elastic modulus, the stress at the crack tip was significantly increased. After thermal exposure, the driving force for interfacial cracking can be two times larger than that of the as-deposited state. The effect of the elastic modulus on the SERR can be quantitatively obtained from Eq. (5) [141]:

$$G_i = \int_0^h \frac{E_{(y)}\varepsilon^2}{2(1-\upsilon)}\mathrm{d}h \tag{5}$$

where G_i is the SERR, h is the distance from the crack

to the coating surface, $E_{(y)}$ is the elastic modulus at a depth of y from the free surface, and ε is the applied strain.

Furthermore, the stress state upon temperature cycling was also investigated [168]. During thermal cycling, the coatings become stiffened, controlled by a subroutine. Similarly, the stress concentrated at the crack tip increases during sintering, meaning that the crack more easily propagates, as shown in Fig. 34. The stiffening caused by sintering also results in a distinct increase in SERR. The change in SERR appears to be a non-linear feature, which is consistent with the increase in the elastic modulus. The change in SERR is faster at the initial stage.

The layer-stacking structure with a large quantity of 2D pores effectively prevents heat flux [148]. This is the advantage of plasma-sprayed TBCs on thermal barrier performance. However, a sintering-induced increase in stress and driving force for cracking results in a short life span for plasma-sprayed TBCs. This is the main limit for conventional plasma-sprayed TBCs if compared to the sintering-resistant TBCs with hybrid structures [169] or columnar structures, such as TBCs that are prepared by EB-PVD [170] or the dense-vertically cracked technique (DVC) [171]. In fact, the as-deposited TBCs exhibit high strain tolerance due to the micropore network [143,157,160]. However, sintering leads to the healing of 2D pores. The coating becomes stiffened, and
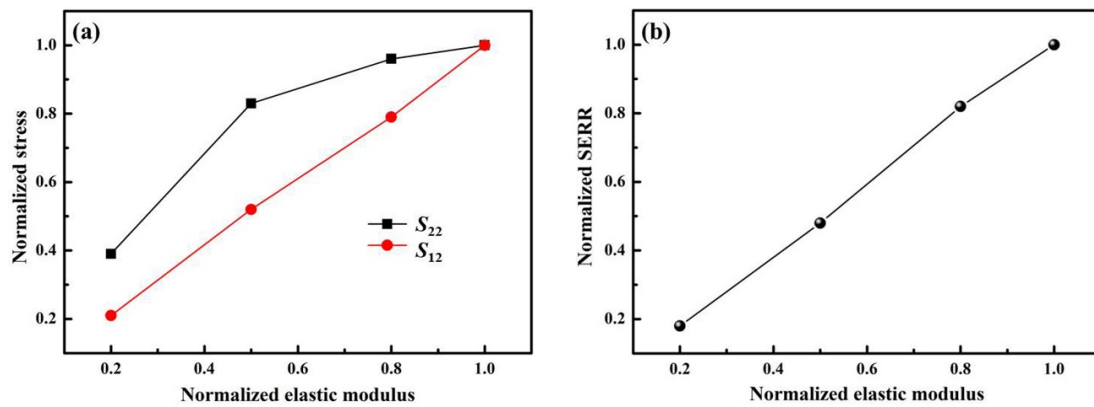
Fig. 33 Effects of sintering on stress and SERR at the crack tip: (a) stress and (b) SERR. Reproduced with permission from Ref. [167], © Elsevier Ltd and Techna Group S.r.l. 2019.
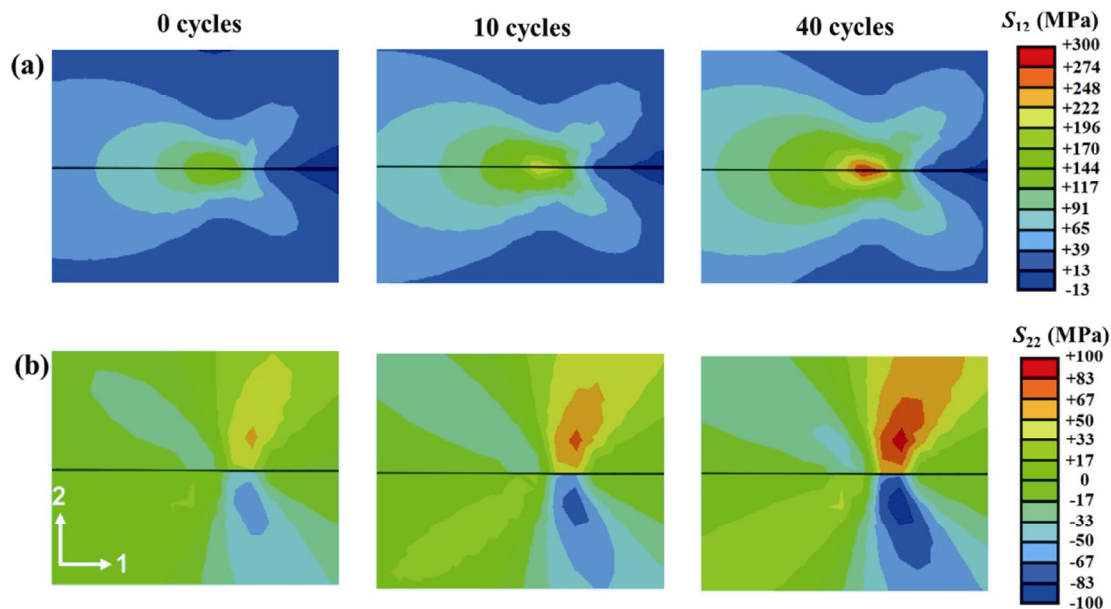

Fig. 34 Evolution of stress at the crack tip with temperature: (a) shear stress and (b) normal stress. Reproduced with permission from Ref. [168], © Published by Elsevier Ltd on behalf of The editorial office of Journal of Materials Science & Technology 2021.

the stress is increased significantly. This is one of the main causes responsible for the failure of plasma-sprayed TBCs.

To prolong the TBC lifetime, the sintering resistance of the ceramic top coat needs to be further improved. In addition to use new materials with better sintering resistance, pore structure tuning is also a promising strategy toward enhancing high temperature sintering resistance for longer lifetimes of next-generation TBCs.

3.1.4 Phase transformation stress

Phase transformation of the ceramic top coating produces extremely large stress due to the different specific densities of different phases. Two kinds of phase transformations are investigated for typical TBCs. One is the physical phase transformation which means only the crystal structure changes and no chemical component changes, and the other is the chemical phase transformation such as oxidation of the bond coat.

The physical phase transformation of zirconia leads to the exceptional deformation ability, high toughness, and reliability of TBCs, which mainly involves the t-to-m transformation. From high temperature to low temperature, pure zirconia has three phases, i.e., c-phase, t-phase, and m-phase. The c-phase is stable above 2643 K. When the temperature decreases to 2643 K, a c-to-t phase transformation occurs. The t-phase is metastable. When the temperature further decreases to 1223–1373 K, the t-phase will change to an m-phase with a 3%–4% volume expansion. Since phase transformations occur alongside huge volume strain and shear strain, large stress will generate inside the zirconia ceramics, which will often induce cracks. As shown in Fig. 35, at a fixed temperature and pressure,
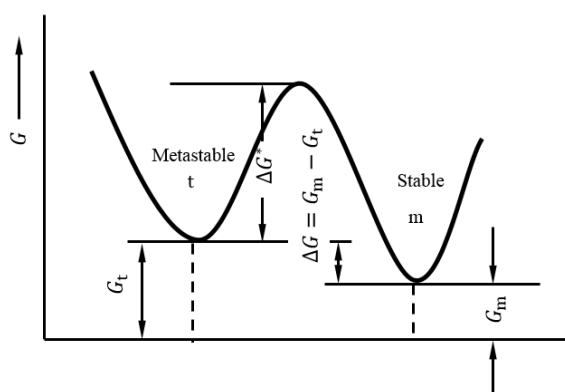

Fig. 35 Illustration of the free energy relation between metastable t-phase and stable m-phase.

the Gibbs free energy (ΔG) relation of the t-phase and m-phase is illustrated. There is an energy barrier (ΔG^*) between these two phases. Controlling ΔG^* can control phase transformation kinetics. Through alloying another oxide with pure zirconia will increase ΔG^* or decrease the driving force of phase transformation and thus can stabilize or partially stabilize the t-phase [172].

The t-to-m phase transformation is a non-diffusion controlled process and is martensitic. Thermal energy and/or stress can drive atoms to overcome the barrier, and crystals shift between the two phases. On the one hand, the phase transformation leads to the thermoelastic and ferroelastic properties of zirconia [173,174], which is the origin of toughness. On the other hand, the huge volume expansion and shape change alongside the m-to-t phase transformation over 1443 K induce huge stress and lead to failure [175], which is the main bottleneck of the higher temperature application as YSZ TBCs. During service, YSZ is constrained by the substrate, and the total free energy change (ΔG_{m-t}) consists of three parts:

$$\Delta G_{m-t} = \Delta G + \Delta U_e + \Delta U_i \tag{6}$$

where ΔG is the difference in chemical-free energy between the t-phase and m-phase, ΔU_e is the elastic energy change during phase transformation, and ΔU_i is the interface energy generated between two phases. The phase transformation stress depends mainly on ΔU_e. The third term ΔU_i indicates that the particle size and morphology also influence the phase transformation, which has been observed [176]. The stress generated during phase transformation in zirconia is very complicated due to the complex phase distribution and orientation. When developing new TBCs, new ceramic materials have to be introduced to form double layer TBCs or gradient TBCs to ensure that the YSZ works below 1443 K [177,178], e.g., to introduce $La_2Zr_2O_7$ in TBCs.

To date, there have been many types of research on the phase transformation of zirconia ceramics, mainly related to TBCs. The phase transformation in EB-PVD YSZ during annealing was carefully investigated by XRD [179]. The phase content, evolution, and yttria distribution were analyzed during annealing. The residual strains and stress originating from the distortion related to the phase distribution were also discussed. The present phase transformation mechanism is complicatedly dependent on temperature, stress, and environment. However, utilizing the key mechanisms governing the martensitic transition, the 2D phase-field model can

still present a rather reasonable simulation [180]. During cooling from high temperature, microcracks will form in zirconia due to t-to-m phase transformation. Some experimental studies showed that cracking is produced by the thermal expansion mismatch between groups of the crystallographic variant [175]. Under uniaxial compression, the deformation of zirconia nanopillars is determined both by dislocation and phase transformation. The simulation results showed that the plastic deformation of zirconia nanopillars strongly depends on the crystallographic orientation [181]. Because the phase transformation at a microscopic level is very complicated, there are only very few well-developed continuum models to describe the deformation and stress of the t-to-m phase transformation.

Chemical phase transformation in the TBC field mainly means the oxidation of the bond coat. During TGO growth, large compressive stress is generated at the oxide-metal interface, which leads to the spallation of TBCs [182–185]. Numerous studies have been conducted on this subject. During long-term service, the TGO develops in two stages, first Al_2O_3 forms, and then porous mixed oxides form. The mixed oxides grow much faster than Al_2O_3. This will lead to catastrophic stress in TBCs and eventually induces delamination of TBCs [186]. In addition, ceramic sintering will accelerate this procedure [187]. The finite element method has been extensively applied to study the TGO effect on the failure of TBCs. Recently, a finite element model considering phase transformation with mechanics was developed for the lifetime estimation of TBCs, in which TGO was simulated by an Allen–Cahn type phase-field approach, and the predication of the plastic strain and stress due to TGO growth is possible [188]. The residual stress in TGO can be measured by photoluminescence piezospectroscopy. It was found that the average residual stress with rough morphology decreases with thermal cycling and eventually leads to failure along the TGO/YSZ interface [189–191].

In some circumstances, the physical and chemical phase transformations are coupled, e.g., the oxidation of zircaloy. During the oxidation process, t-zirconia first appears at the interface between the oxide and zircaloy. Upon oxide thickening, the t-phase transforms to the m-phase, and the transformation and cracking in zirconia lead to the breakaway oxidation of zircaloy [192]. Some scholars have also pointed out that the chemical-dependent phase transformation of bond coats is a prominent driving force for the spallation of TBCs. To prevent the early failure of TBCs, minimizing the formation rate of γ' and the martensitic phases is necessary [193].

The phase transformation of zirconia ceramics is a double-edged sword for TBCs. On the one hand, it makes YSZ an exceptionally tough ceramic. On the other hand, it induces huge stress in TBCs above 1443 K. For the further development of TBCs serving for higher temperatures, new materials and new structures must be applied in the future.

3. 2 Ceramic delamination by oxidation scale growth

3.2.1 TGO growth during thermal exposure

The growth of TGO generated by the oxidation of the bond coat is an important factor leading to the spalling failure of the TBCs. This is because the strain energy in TGO has a positive linear relationship with the thickness of the TGO layer. When TGO grows to a critical thickness, usually 5–10 μm, the large strain energy accumulated in TGO will eventually lead to cracking in the TGO or near TGO layer, resulting in subsequent TBCs failure.

An accurate understanding of the TGO growth kinetics is of great practical significance because it can be used to correctly predict the lifetime of TBCs. Usually, the growth behavior of the TGO layer can be described by a conventional parabolic kinetics model. According to this model, the influence of grain boundary diffusion on the growth of TGO is ignored, and it is assumed that the growth behavior of the TGO layer is completely dominated by bulk diffusion. In this case, the growth rate of TGO is shown in Eq. (7), which is a parabolic rule.

$$t = k\delta^2 \tag{7}$$

where δ is the TGO thickness, k is the rate constant, and t is the oxidation time. However, it has been reported that the growth of α-Al_2O_3 is dominated by the diffusion of oxygen ions through grain boundaries [194]. Therefore, the growth behavior of TGO cannot be accurately described by using the conventional parabolic kinetics model.

An alternative TGO growth model is reported based on the growth behaviors of TGO thickness and grain size changing with time [194]. It can be seen from Eq. (8) that this model is a modified model based on a conventional parabolic kinetics model, which is derived

by treating the TGO growth rate constant as a variable varying with the TGO grain size.

$$t = 366.9(e^{0.5\delta} - 0.5\delta - 1.02) \qquad (8)$$

As shown in Fig. 36, in a relatively short oxidation time, the results obtained by this model are in good agreement with the results predicted by the conventional parabolic kinetics model and are consistent with the actual experimental results. For a longer oxidation time, the modified model is more consistent with the actual experimental results and gradually deviates from the parabola rule.

Since grain boundary diffusion plays a key role in the growth of TGO, the growth rate of the TGO layer can be reduced by increasing the grain size of TGO. Meng *et al.* [195–198] prepared a TGO layer with a large grain size on the surface of the bond coat by developing a series of controlled atmosphere pretreatments. A TGO layer with an average grain size up to 1 μm can be prepared by controlling the initial oxide film morphology on the surface thermal sprayed MCrAlY bond coat by adjusting the oxygen partial pressure of the heat treatment [195,196]. It can be seen from Fig. 37 that when the TGO grows to the same thickness, the time required by the heat-treated bond coat is 14 times slower than that of the as-sprayed bond coat [195]. The larger grain size of the TGO layer significantly inhibited the TGO growth rate.

3.2.2 Cracking by TGO growth

To understand the mechanism of TBC cracking caused by TGO growth, the formation of TGO must be first understood. In the early stage of TGO formation, TGO is mostly alumina. However, the mechanism of
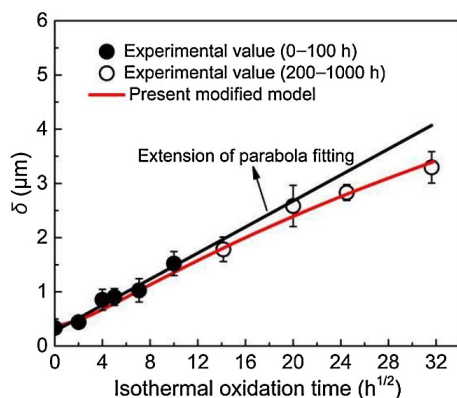

Fig. 36 Comparison between conventional parabolic kinetics and Zhang's non-parabolic kinetics. Reproduced with permission from Ref. [194], © Elsevier B.V. 2017.
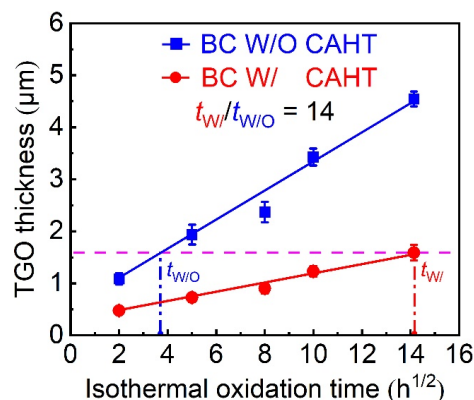

Fig. 37 Comparison between the growth rate of the heat-treated bond coat and the as-sprayed bond coat. Reproduced with permission from Ref. [195], © Elsevier Ltd. 2020.

controlling TGO growth has been controversial. Sun *et al.* [199] argued that the diffusion of aluminum is inhibited by the reactive elements in BC and TC, and TGO growth is mainly affected by the oxygen inward diffusion rate. Meanwhile, the columnar grain structure of TGO is formed, which is more conducive to oxygen diffusion. Most of the new oxides are located at the interface between the TGO and bond coat. Additionally, a small part of the oxide forms in the grain boundary of TGO [200]. Nevertheless, some studies indicate that TGO growth is dominated by Al diffusion since it has a larger diffusion rate than oxygen [201]. In this stage, its thickness increases with exposure time at a quite low growth rate. As shown in Fig. 38 [202], for a short exposure period, the TGO is mainly alumina as well as a few mixed oxides consisting of alumina, spinel, nickel oxide (ASN) and chromia, spinel, and nickel oxide (CSN) [203,204]. The thickness of the TGO gradually increases. The TGO layer is still protective since the dense alumina can suppress oxygen diffusion. However, the process of TGO growth consuming Al will lead to the formation of an Al-depleted zone underneath the former oxide layer. Once the Al-depleted zone appears, the oxidation rate of the BC will sharply accelerate. This can be attributed to the outward diffusion of the more reactive Cr, Co, and Ni elements in the bond coat and its oxidation forming the mixed oxide. Meanwhile, the Al depletion and the increase in the content of Cr with oxidation time occurring in TGO suggest that the alumina layer gradually dissolves into the mixed oxides [36,205], and the BC surface roughness has an obvious influence on Al depletion; the alumina scales with occasionally mixed oxides form on the peak of

the bond coat, while the scale contains mixed oxides in the valley [206]. Therefore, the TGO becomes porous, and its morphology varies with the roughness. In Ref. [203], when the oxidation time is less than 1000 h, the dark layer dominantly comprising α-Al_2O_3 and the grey layer consisting of (Ni, Co)(Cr,Al)$_2O_4$ spinel and α-Cr_2O_3 can be clearly distinguished. After 1000 h, the dark layer is almost completely replaced by the porous grey layer. However, in Ref. [202], the dark layer and grey layer still have evident interfaces, although they have experienced twenty-five 100 h cycles (Fig. 38). Moreover, the amount of detrimental mixed oxides can be decreased by vacuum heat treatment and low-pressure heat treatment, developing a TGO comprised of a predominantly alumina layer.

Since the TGO layer is located in a multilayer system, TGO growth is constrained by the adjacent layer. Its growth will bring about a high-stress state in TBCs. The TGO growth mainly affects the stress state from two aspects: On the one hand, the volume expansion during TGO formation leads to a large compressive stress. On the other hand, the CTE of TGO is smaller than those of TC and bond coat. Upon cooling, the thermal mismatch changes the thermal stress state. The tensile stress always results in Mode I fracture, whereas the shear stress often causes Mode II fracture. Therefore, the two kinds of stress have been discussed in many works. Bäker and Seiler [134] studied the influence of TGO thickness on the stress evolution in TBCs. The results indicated that normal stress in the second

direction is governed by the thermal mismatch between the TC and bond coat without TGO or with a thin TGO. The TC peak undergoes tensile stress, and its valley is under a compressive stress state. However, a significant stress shift occurs with the thickening of TGO, that is, the transformation from initial tensile stress to compressive stress in the peak and the compressive stress to tensile stress in the valley region. There are two factors leading to the stress shift. First, the TGO growth strains accumulate with the increased TGO thickness in the condition where the TC/TGO interface is rough. These strains obviously cause the stress shift. Second, the thermal mismatch exacerbates the stress shift. Since the TGO has a smaller CTE, it contracts less than the ceramic layer, which enlarges the compressive stress in the peak and the tensile stress in the valley during the cooling phase. In the study by Wei *et al*. [133], the role of TGO growth strain in the TBC failure was discussed in detail. TGO growth includes two parts, namely, thickening and lengthening growth. The distribution of the stress in the TC layer is explored without TGO growth. Figure 39 demonstrates the distributions of the residual stress under different conditions. The results show that the peak is under tension and that the valley region endures compression after cooling. The shear stress appears near the peak region, and its distribution has no obvious change during the whole cycle. Neither the normal stress nor shear stress increases continuously with the thermal cycles. If only TGO thickening strain is considered, the
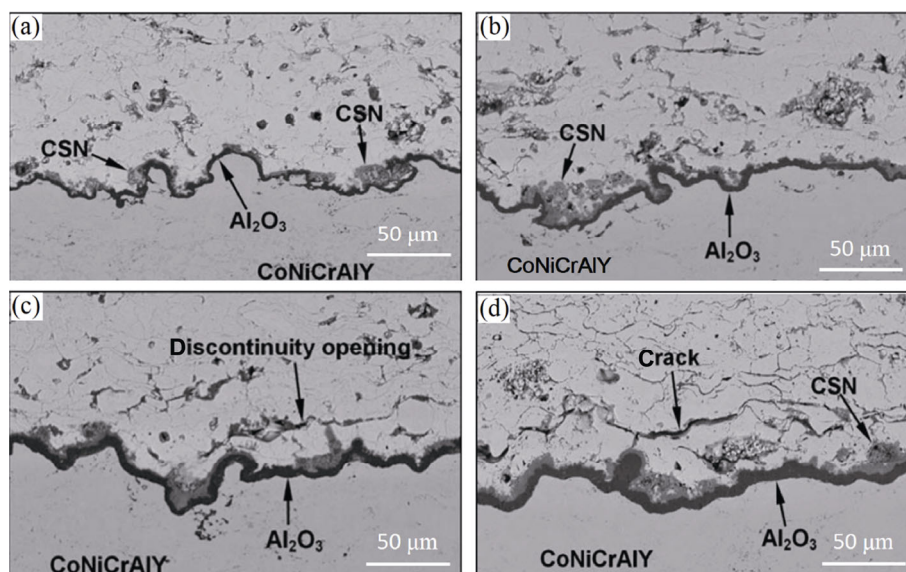

Fig. 38 TGO layer under different cycles: (a) one 100 h cycle, (b) five 100 h cycles, (c) ten 100 h cycles, and (d) twenty-five 100 h cycles. Reproduced with permission from Ref. [202], © ASM International 2008.
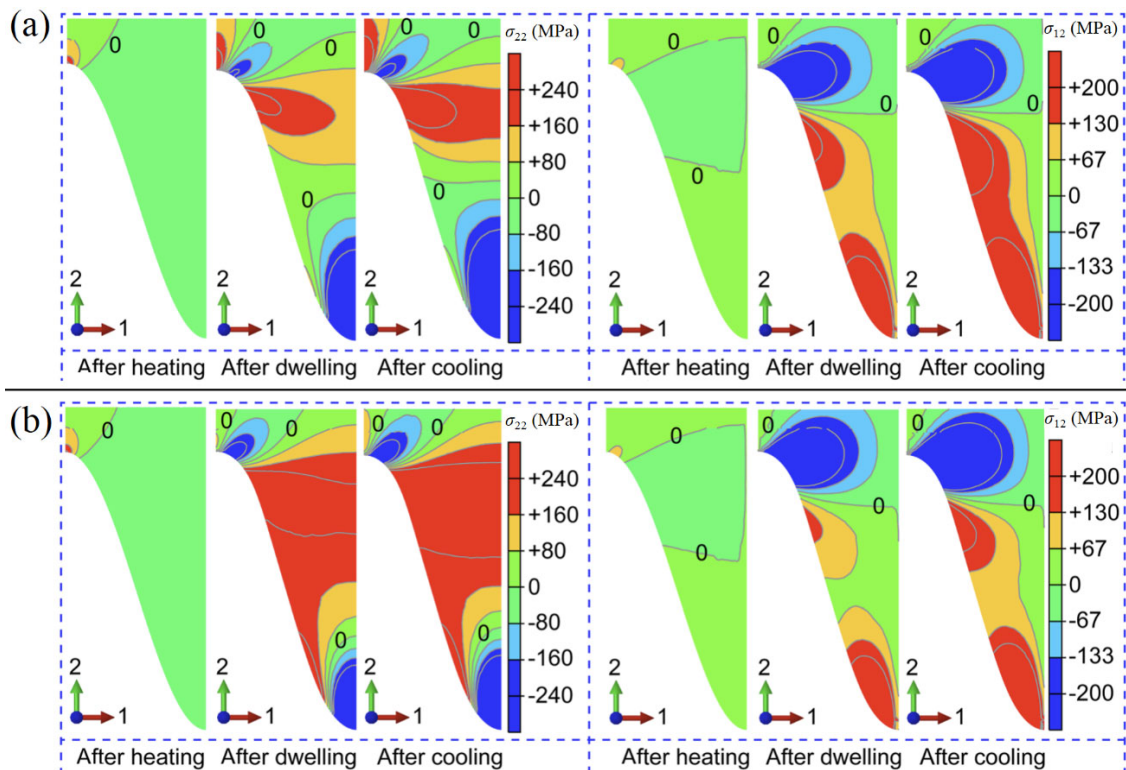
Fig. 39 Distributions of the residual normal (left) and shear (right) stresses in the TC under different TGO growth conditions: (a) only with TGO thickening growth and (b) with TGO thickening and lateral growth. Reproduced with permission from Ref. [133], © ASM International 2019.

distribution of normal and shear stress at the end of the heating stage is similar to that without TGO growth. After the dwelling stage, the tensile stress increases in the middle region between the peak and the valley. Upon cooling, the stress states do not change. When both TGO thickening and lateral growth are included in the model, the tensile stress still maintains the previous trend, but the distribution range of the high tensile stress is expanded. Such distribution of tensile stress may easily induce the incipient formation of TC cracks. Gupta *et al*. [207] also researched the residual stress near the TC/BC interface based on a real interface topography. The stress shift theory has been verified again in both 2D and 3D simulations. The TGO morphology follows the original rough TC/BC interface due to TGO forming between TC and BC. In Ref. [199], the effect of TGO roughness on the TBC stress state was studied. It has been found that the normalized stresses at the interfaces decrease with the ratio of the local radius (R) to TGO thickness (δ), which is consistent with the situation of a planar TGO layer. The TGO hoop stress has the opposite trend. It gradually increases with increasing R/δ. Eriksson *et al*. [205] emphatically studied the influence of chromia-spinel–

NiO (CSN) clusters on the TBC failure by finite element modeling. The formation of CSN clusters has three stages, and the last stage is divided into two conditions. It has been found that when the metallic core transforms into NiO without volumetric expansion, the tensile stress cluster occurring in the NiO results in the cracking of CSN. This phenomenon occurs in the last stage of CSN cluster formation and is attributed to the large thermal mismatch between NiO and other oxides. Furthermore, the volume expansion with NiO formation has no significant effect on the cracking of CSN clusters as cracking occurs in such a condition where volumetric expansion is prone to appear at elevated temperatures instead of in the cooling phase.

When TGO growth stress plays the main role in the coating failure, the following possible microcrack patterns can be observed, as shown in Fig. 40: interface delamination and cracking in TC and TGO [36]. As for the TGO/BC and TGO/TC interfacial delamination, they occur at the BC peak and TGO valley, respectively, where they endure tensile stress. Since the APS TBC has a lamellar structure, the discontinuities between poorly-bonded lamellae can be considered inherent cracks. The tension region above the interface valley is

expanded due to TGO thickening. The pre-existing cracks start to extend during thermal exposure [208]. Naumenko et al. [206] found that the crack initiated in the peak region of the TGO/BC interface, and then propagated along with the interface profile. That is because the peak of the TGO/BC interface is under tension. The interfacial tensile stress is released. At the same time, the interfacial in-plane shear stress enlarges as the crack propagates toward the valley of the interface. When the shear stress reaches its critical value, TGO fracture appears, and the crack penetrates into the TGO layer. The crack propagation path in the TGO layer is roughly in the parallel direction since TGO has a columnar grain structure [199]. Therefore, cracking in the TC layer appears in the parallel direction. Ranjbar-far et al. [136] also investigated how the propagation of pre-existing cracks was situated at the interface and within the TC layer under different TGO asperities and thicknesses. Three failure mechanisms are examined by developing a thermo-mechanical model in which the TC layer has a lamellar structure. It has been found that the cracking scenarios are affected by the interface morphology and TGO thickness. When the TGO thickness is 3 μm, the cracks first form along the lamellas and stop at the TC/TGO interface. Then, cracks subsequently occur at the peak of the TGO/BC interface (Mechanism I). Meanwhile, the former cracks proceed to extend along the TC/TGO interface due to the larger tensile stress (Mechanism II), and the cracking is almost changed when TGO is 5 μm. However, when the TGO thickness reaches approximately 7 μm, horizontal cracks develop at quite a large distance from the peaks and propagate up to TC delamination. The influence of interface morphology on crack propagation indicates that the nonuniform morphology promotes the extension of cracks compared with the uniform morphology. In Ref. [133], a crack lying above the valley of the TC/TGO interface is set to investigate the fracture mechanism of TBCs. The variation in an equivalent Mode I energy release rate (G_{eq}) with the normalized crack length (a) indicates that the crack driving force continuously increases with increasing crack length. At the beginning of crack propagation, it is located in the tension-dominant region so that its growth is controlled by Mode I. Then Mode II becomes more obvious due to the enlarging shear stress. In brief, the ceramic cracking induced by TGO growth greatly contributes to the failure of TBCs.

3.2.3 Delamination by TGO growth

The delamination of TBCs caused by TGO depends on the growth mode of TGO. TGO is divided into α-Al$_2$O$_3$-based TGO and other oxides (such as spinel, chromia, and nickel, collectively named mixed oxides), depending on the growth characteristics [209,210]. The characteristics of the delamination and durability of TBCs related to TGO growth were profiled separately in terms of the α-Al$_2$O$_3$-based TGO and the mixed oxides.

In the term of α-Al$_2$O$_3$-based TGO, the delamination location of APS TBCs transfers from the inside of the YSZ coating to the interface of the YSZ coating/bond coat, depending on the α-Al$_2$O$_3$ thickness and independent of the cycling-test method, as shown in Fig. 41. The TGO generated at the interface of the YSZ/bond coat has characteristics of wedge-type growth, low CTE, and high in-plane interior stress, which deteriorates the adhesive strength of the interface in TBCs [211–213]. However, the adhesive strength at the interface is higher than the cohesive strength in the YSZ when TGO is in the initial growth phase [214,215]. Thus, delamination cracks propagate in the YSZ
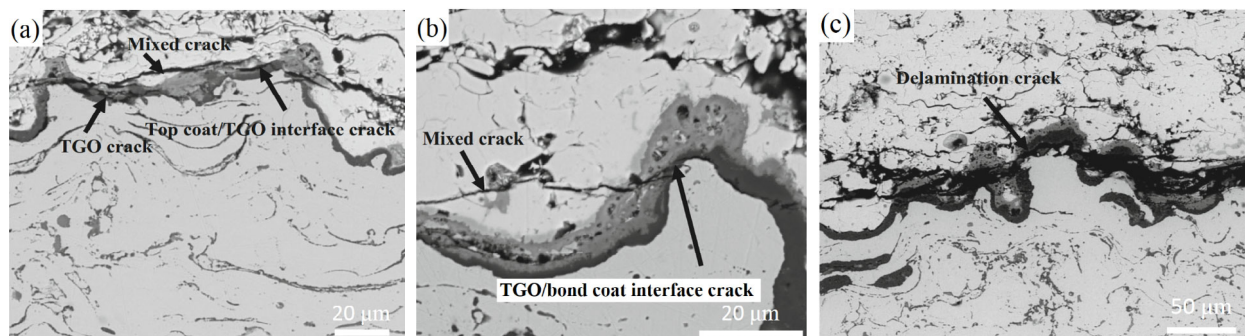

Fig. 40 SEM examination of cracks in the APS TBC specimen aged at 1050 ℃ for (a) 200 h, (b) 900 h, and (c) 1970 h. Reproduced with permission from Ref. [36], © ASM International 2020.
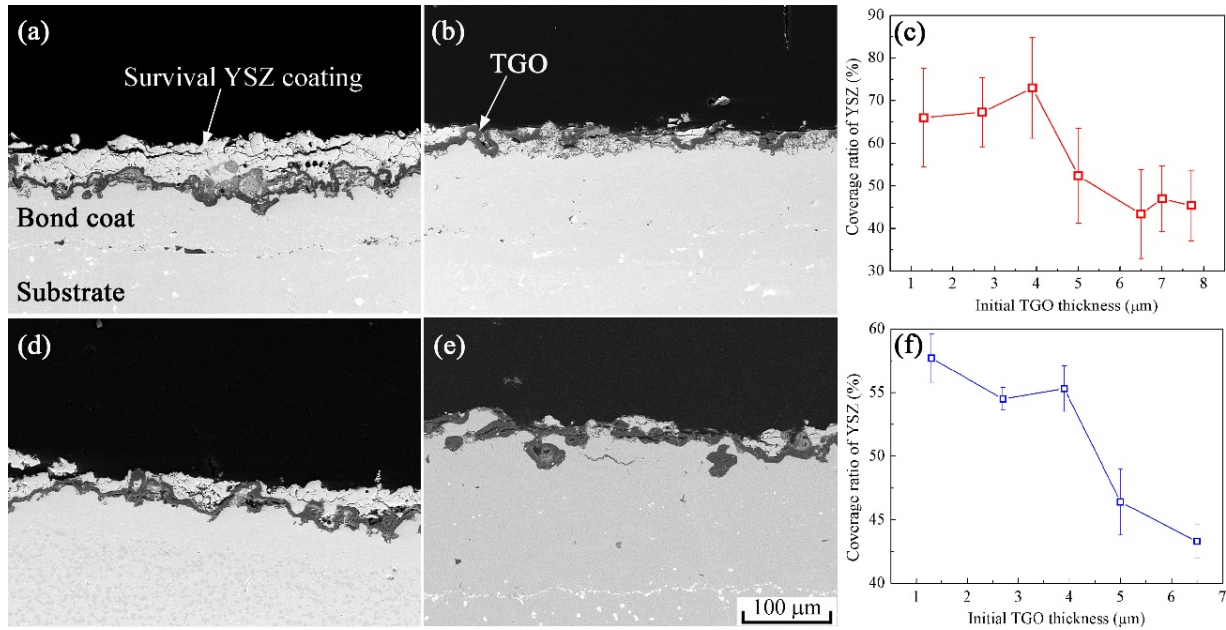
Fig. 41 Cross-sectional microstructures of APS TBCs with different initial α-Al₂O₃-based TGO thicknesses after failure: (a) 1.3 μm and (b) 6.5 μm TGO under burner cycling, (d) 1.3 μm and (e) 6.5 μm TGO under furnace cycling, and (c, f) coverage ratios of the YSZ coating on the fracture surface.

neighboring the interface. The TGO growth is accompanied by the deterioration of the adhesive strength of the interface. Subsequently, some separations initiate at the interface once the TGO thickness reaches a threshold value [41]. These separations propagate and coalesce, forming an interface delamination crack during service. Ultimately, the whole YSZ coating spalls [41,216]. Moreover, the out-plane stress at the interface gradually turns from compression to tension as TGO grows [217,218], which is also a primary factor that dominates the delamination path transition. This stress nature turning is dominated by the relationship between the TGO thickness and the surface roughness of the bond coat, which turns while the TGO thickness grows up to half of the surface roughness of the bond coat.

The coverage ratio of the YSZ on the fracture surface reflects the delamination-crack propagation path. The coverage ratio sketched in Figs. 41(c)–41(f) indicates that the coverage ratio of YSZ on the fracture surface has an identical changing rule in both cycling test methods: It maintains a high level at the initial growth phase and sharply decreases when the TGO thickness exceeds 5 μm.

A completely identical crack-propagation behavior derived from the indentation test was also achieved [214]. Compared with the APS TBCs, the EB-PVD TBCs have a completely different microstructure and interface profile. However, there is a similar crack-propagation behavior in EB-PVD and APS TBCs [219]. Thus, the crack-propagation path transition of TBCs depending on the TGO thickness is an inherent characteristic of TBCs, regardless of the test method and the deposition method.

With the increase in TGO thickness, the lifetime tendency of TBCs is comparable, whether the burner thermal cycling test or furnace cycling test is employed, as shown in Fig. 42. The regression result of the experimental data is used due to the various durability data caused by the test method. The durability depending
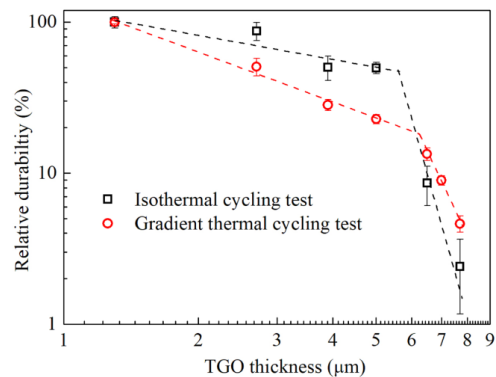

Fig. 42 Relative durabilities of APS TBCs plotted as a function of the TGO thicknesses under the burner cycling test and the furnace cycling test. Reproduced with permission from Ref. [41], © ASM International 2017; Ref. [215], © The American Ceramic Society 2014.

on the TGO thickness is defined by power functions with different exponent values, and deflection points appear in the curves, corresponding to a sharp decrease of durability. The deflection points in the curves correspond to the critical TGO thickness at which the delamination-path transition, i.e., the delamination path dominates the tendency of APS TBC durability. It is an inherent characteristic of APS TBCs, which is independent of the durability-test method.

In summary, both types of TBCs, including EB-PVD and APS TBCs, are comparable, as far as the critical α-Al_2O_3-based TGO thickness corresponds to the spallation-path transition. The columnar microstructure of the YSZ coating has a positive role in the durability of TBCs [220], while it is independent of the critical TGO thickness. The critical thickness is essentially in the range of 5–6 μm, which is independent of the deposition method.

In addition, the mixed oxides are generated when Al in the bond coat is depleted. These types of oxides have a characteristic of high-rate local growth [221–223]. The local protruding TGO, in some cases, is considered the "jack" inserted in TBCs. The numerous "jacks" with high-rate growth delaminate the YSZ coating quickly, and TBC failure occurs, as shown in Fig. 43 [224]. The decrease in TBC durability depends on the magnitude of mixed oxides generated at the interface of the YSZ coating/bond coat. The magnitude of mixed oxides is generally described by the coverage ratio. The decrease level of durability of TBCs could be evaluated semi-quantitatively via the growth-strain velocity and the coverage ratio of the mixed oxides [209,222,223]. The durability of TBCs decreases linearly with the product of the growth-strain velocity and the coverage ratio [223]. The delamination path depends on the volume of the mixed oxides and
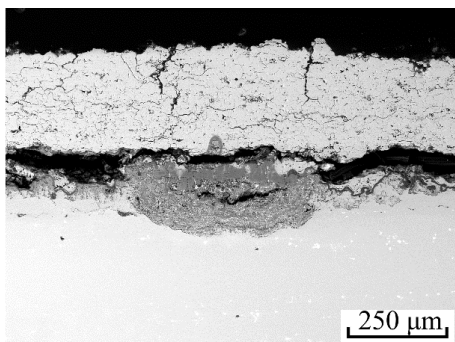
the α-Al_2O_3-based TGO thickness in the fracture time [223,224]. In general, the densification of the bond coat is an available method to postpone the generation of mixed oxides.

Based on the discussion of TGO-induced cracking and delamination, it can be concluded that localized and overall TGO thickening is the dominant mechanism, leading to spalling failure of the ceramic top coat. To increase the lifetime of TBCs from the point view of TGO induced stress, reducing the TGO growth rate needs to be further investigated in the future.

3.2.4 Diffusion barrier (DB) for bond coat

To prevent cracking between the bond coat and substrate due to interface degradation and direct substrate degradation by interface reaction resultant, DB is necessary for both long lifetime TBCs and metallic protective coatings, including aluminide (simple [225] or modified [226,227]) and MCrAlY overlay coatings [228,229]. They can serve as standalone or bond coats in TBCs. Due to the chemical gradient, the occurrence of element inter-diffusion between the coating and superalloy substrate during service is inevitable. This inter-diffusion would affect the coating and substrate alloy in three aspects: (1) Inward diffusion promotes meaningless Al loss from the coating; (2) outward diffusion facilitates refractory elements (W, Mo, Ta, etc.) to participate in oxidation at the coating surface, destroying the integrity of the alumina scale; (3) inter-diffusion deteriorates the mechanical properties (such as fatigue creep resistance and rupture life) of a single crystal (SX) superalloy by forming acicular precipitates of topologically-close-packed (TCP) phase, which usually accompanies the appearance of the secondary reaction zone (SRZ).

The destructive effect of the exotic coating on the mechanical properties of the single crystal superalloy showed a clear dependence on the SX superalloy itself: Higher generation of SX results in a greater reduction in rupture life. The fourth-generation single crystal superalloy TMS-138 decreased the creep-rupture life by 86%, in contrast to 63% and 77% for second-generation CMSX and third-generation TMS-75, respectively [230]. Figure 44 displays the rupture life impact of inter-diffusion by the PtAl coating on the various generations of superalloys. Therefore, it is of great importance to inhibit or suppress the undesirable inter-diffusion between the bond coat and SX substrate.
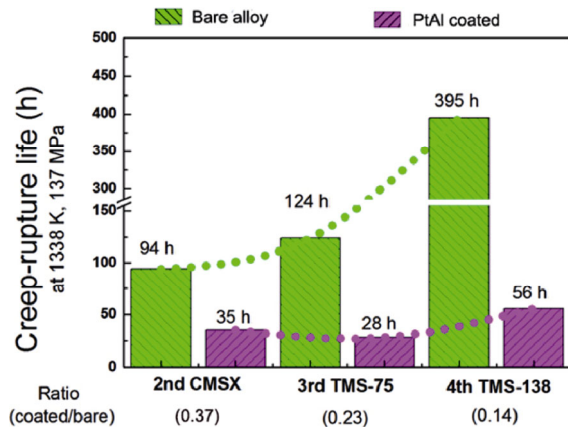

250 μm

Fig. 43 Delamination cracks in TBCs depended on the mixed oxides. Reproduced with permission from Ref. [224], © Elsevier Ltd and Techna Group S.r.l. 2017.

Fig. 44 Creep-rupture life reduction for different SXs covered with PtAl coating.

To achieve the objective of controlling/restraining this inter-diffusion, two aspects can be coordinated, according to Fick's law given in Eq. (9):

$$J_{Al} = -D_{Al} \cdot \frac{\delta \mu_{Al}}{\delta_X} \tag{9}$$

where J_{Al} denotes the diffusion flux of Al, D_{Al} represents the Al diffusivity within the system, and $\frac{\delta \mu_{Al}}{\delta_X}$ is the concentration gradient between the coating and substrate. That is, both reducing D_{Al} and decreasing the concentration gradient $\frac{\delta \mu_{Al}}{\delta_X}$ help to acquire a low J_{Al}. Practically, we can use customized coatings that hold low chemical potential concentrations, including equilibrium (EQ) [231,232] and nanocrystalline coatings [233,234]. Relying on the principle of phase EQ, the inter-diffusion between γ' coating and γ'/γ dominant single crystal superalloy could be as low as minimal. Similarly, the specific nanocrystalline coating basically resembles the composition of SX alloy, where the inter-diffusion lacks the driving force to trigger.

The other rational solution is to reduce D_{Al}. The diffusion rate of this element is always high due to its relatively low melting point. Generally, D_{Al} values in nickel-based β and γ'/γ phases are extraordinarily high, which exhibits a serious diffusion extent at high temperature. Accordingly, incorporating a DB between the bond coat and substrate, which has a satisfactorily

low D_{Al} for Al passing through, is reasonable. The DB could be metallic [235,236], ceramic [237,238], or reactive layers [239,240].

A good DB should have the following four characteristics: (1) low diffusion rate, which requires the diffusion coefficients of elements passing through the DB to be necessarily low; (2) good structural stability, which means that the microstructure and phase constitution of the DB are sufficiently stable for long-term high-temperature exposure; (3) good bonding strength, requiring that the DB combines well with both the coating and the substrate; and (4) reasonable costs, in which the cost of DB must be accessible and reasonably controlled so that it can be more widely investigated and utilized in practice. Among these traits, a low diffusion rate, good bonding strength, and structural stability are vital for designing an ideal DB. In the following section, various reported DBs will be introduced as case studies, where particular perspectives will be focused on the three characteristics.

The first option to inhibit elemental inter-diffusion is to prepare a direct ceramic layer such as Al_2O_3 [237] because ceramic DB has the intrinsic nature of high stability and low diffusivity for Al. In fact, the inhibiting effect of such ceramic DB is so powerful that almost no diffusion of elements could be allowed for passing through. In addition to stable oxides, nitrides are promising candidates to serve as the strong DBs. Table 4 lists a batch of ceramic DBs reported in the open literature. As indicated in Table 4, the oxide species have excellent structural stability and extremely low diffusivity. However, the weak bonding for the metal/ceramic interface endangers the integrity of the coating system, which is highly possible for peeling off the entire coating system. Different from oxides, metal nitrides are not comparable in stability, where during thermal exposure, nitrides may decompose to other nitrides or even oxides, accompanied by chemical reactions. Due to this phase transformation, the bonding for nitride DB increases notably. Regardless of how excellent ceramic DBs succeed in inhibiting inter-diffusion, the weak adhesion confines the application of direct ceramic DBs, especially when the components are engaged in thermal fatigue service mode.

Table 4 Some ceramic DBs reported in the literature

Species	Category	Trait
Oxide	Al_2O_3 [237] and Cr_2O_3 [241,242]	High structural stability, low diffusion rate, and low bonding and strength
Nitride	TiN, CrN [238,243], and AlN [244,245]	Fair stability (transformable to other phases), low diffusion rate, and fair bonding

Unlike direct ceramic DB, active DB utilizes an oxide precursor to react with Al from the bond coat and substrate, forming an Al_2O_3/metal/Al_2O_3 sandwich structure. As this process implements an *in-situ* redox reaction from the oxide precursor to more stable alumina, the sandwich active DB connects well to both the bond coat and substrate. According to the Ellingham diagram, any metal oxide with the higher free energy of formation can be deoxidized by Al because Al_2O_3 holds the lowest partial oxygen pressure of formation. Figure 45 illustrates the active DB transformation from the oxide precursor to Al_2O_3/metal/Al_2O_3 sandwich.

In practice, the prevailing TBC ceramic layer of YSZ may serve well as the active DB precursor. The thermodynamics indicate that the energy required for Reaction (10) is negative, which ensures Reaction (10) goes forward:

$$3ZrO_2 + 4Al = 2Al_2O_3 + 3Zr \qquad (10)$$
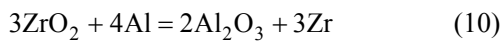
As a result, the Al_2O_3/Zr/Al_2O_3 sandwich is produced. Figure 46 demonstrates the sandwich structure formation after oxidation at 1000 ℃ for 1000 h in a NiCrAlY/YSZ/N5 coating system. As indicated, both Al_2O_3 layers in the sandwich are continuous and homogeneous.

The metal oxide of NiCrO can be another option for serving as the active DB precursor [240]. The bonding strengths of NiAl/NiCrO diffusion barrier on N5 SX superalloy for the three samples after vacuum annealing are listed in Table 5. By tailing-control of oxygen concentration and layer thickness, the bonding strength of *in-situ* formed Al_2O_3/NiCr/Al_2O_3 can be high enough (average 34 MPa shown in Table 5) for industrial application, which is comparable to YSZ coating deposited by APS. This feature of good adhesion comes from two aspects: (1) *In-situ* reaction ensures chemical bonding at the interfaces; (2) the thickness of NiCrO precursor is optimally adaptable. In fact, the design of the active DB precursor thickness should be carefully considered. The too-thin layer of precursor cannot afford sufficient O locally to form a consecutive Al_2O_3 dual-layer structure, while the too thick layer deteriorates the bonding because it is necessary to control the continuous Al_2O_3 bi-layers to be as thin as possible. The reported study of active DB confirms its excellent ability to inhibit interdiffusion while holding good
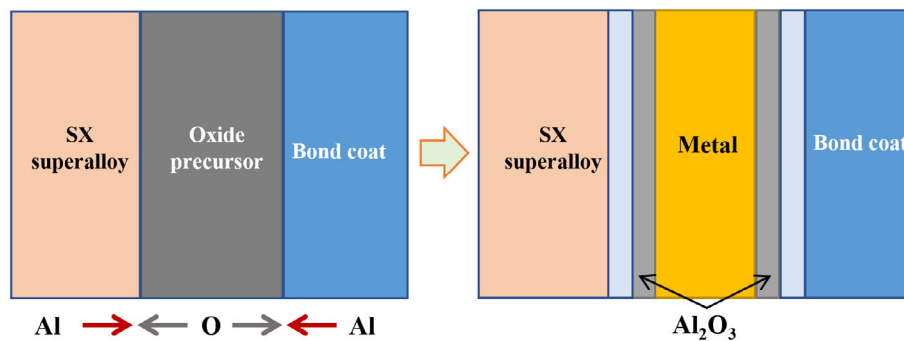

Fig. 45 Schematic showing the formation of active DB with sandwich structure.
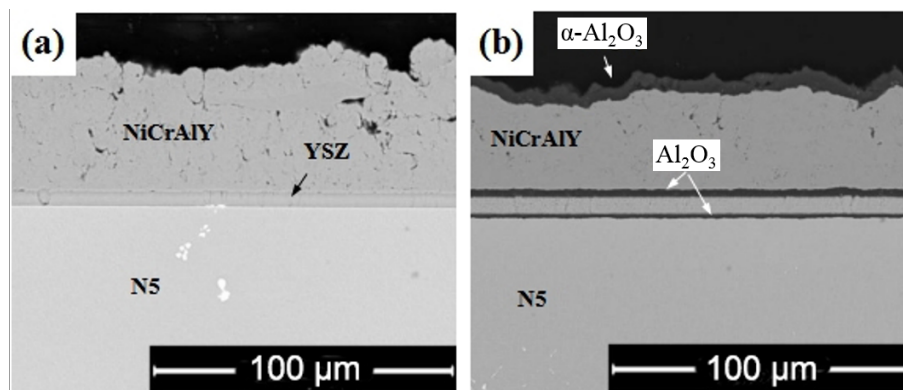

Fig. 46 Microstructure change in the NiCrAlY/YSZ coating system on N5 SX before and after 1000 h oxidation test at 1000 ℃ (YSZ is deposited by EB-PVD): (a) before oxidation and (b) after oxidation. Reproduced with permission from Ref [239], © Elsevier Ltd. 2015.

Table 5 Bonding strength of NiAl/NiCrO coating on N5 superalloy (the samples experienced post vacuum annealing)

Sample No.	σ_b (MPa)
1#	36
2#	41
3#	25

bonding strength. Compared with a direct ceramic DB, an active DB is highly promising for designing an overlay bond coat on single crystal superalloy components.

As good bonding requires a certain extent of element diffusion, it fundamentally conflicts with the barrier effect of inhibiting element inter-diffusion. That is, it is not possible to achieve an ideal DB with excellent bonding strength and inhibition capability at the same time. Further increasing the bonding strength of DB has to sacrifice its inhibition property, which is properly realizable by incorporating refractory metal as the DB. In this field, much research attention has been given to rhenium (Re) which has a melting point as high as 3186 ℃. It could combine other refractory metals, including Cr, Mo, W, and so on, to form the σ-Re phase, which is thermally stable at the currently applicable service temperature. As shown in Fig. 47, the Re-based DB is not fully continuous, and the remaining channels for elements pass through, which resembles a dam with a water channel preserved. By sacrificing partial

inhibiting property through those channels, the bonding strength could be maximized to a metallurgic bonding. In this case, the element inter-diffusion between the bond coat and SX substrate is effectively alleviated instead of completely inhibited. Figure 47 shows that the Re-based DB layer maintains excellent stability during long-term thermal exposure. In addition, the thickness of SRZ formation and density of acicular TCP precipitates have been effectively reduced by ~50% of normal coating [246].

Practically, designing a DB for SX components such as blades should consider key properties in the following sequence: bonding strength > structural stability > inhibiting capability > economical efficiency. That is why there is no report for direct ceramic DB in the service of industrial application, while bonding of active DB is still a worrisome concern for engineers. Subtle projection of the active DB (e.g., refining the optimal processing parameters) and increasing the operation window could pave the way for future application. By sacrificing partial inhibition capability and acquiring enhanced bonding strength, metal DBs are more prominent for practical utilization.

In short, DB can protect TBCs from early spalling or substrate degradation. If DB is well prepared between the bond coat and substrate, the lifetime of TBCs cannot be reduced by the unexpected reaction at the interface between the bond coat and substrate.
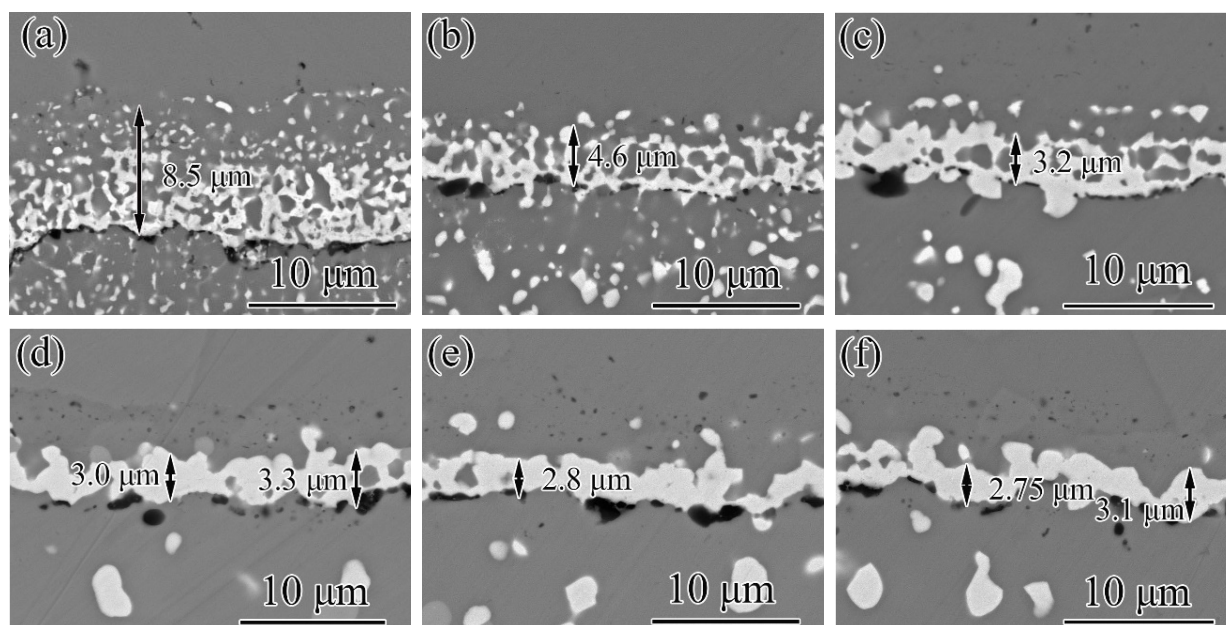

Fig. 47 Microstructure evolution of the Re-based DB during the isothermal oxidation test at 1100 ℃ for (a) 0 h, (b) 20 h, (c) 100 h, (d) 200 h, (e) 500 h, and (f) 1000 h. Reproduced with permission from Ref. [246], © Elsevier Ltd. 2020.

3. 3 Ceramic degradation by corrosion

3.3.1 *Corrosion of lamellar top coat*

The ceramic top coat in TBCs can be severely degraded by corrosion if molten deposits are introduced with the inlet air, although ceramic materials are usually resistant to corrosion. Such molten-deposit-induced corrosion has already been an important issue [19,247,248]. Degradation by molten salt deposits (especially alkaline sulfate-vanadate mixtures) was of early interest. They can infiltrate into TBCs and cause phase transformation of the coatings. In addition, the solidification of molten salts during cooling can result in the loss of the strain tolerance of coatings. For TBCs that will be used in advanced gas turbine engines, however, it is anticipated that corrosion by molten salts will eventually disappear because the TBC surface temperatures will surpass 1500 ℃, which is higher than the dew point of alkaline sulfate–vanadate [247]. In contrast, the degradation of TBCs caused by molten silicate deposits will still occur even at higher temperatures [247]. Since these silicate deposits are mainly composed of CaO, MgO, Al_2O_3, and SiO_2, they are usually referred to as CMASs.

Most CMAS debris originates from the inlet air [249], and a small concentration of debris in the air may introduce much debris into engines. For example, a turbo fan that forces 300 m^3 air per second into the engine can suck ~110 kg·s^{-1} dry air at an 11 km altitude cruising level [249]. The 2010 European Commission's "safe to fly" ash limit is 4 mg·m^{-3} [249]; at this concentration, 4.3 kg of debris will be ingested into an engine in only 10 min. This is only a simplified estimation. In fact, not all debris entering engines have a chance to be in contact with TBCs, because the state-of-the-art particle filters equipped in gas turbine engines can remove most of the large particles (larger than 80 μm) from the inlet air [250]. However, since large air flow is required by engines, debris cannot economically be entirely eliminated even with the best filtration system [251]. Therefore, small particles can still pass through the particle filters and come into contact with TBCs. After passing through particle filters, CMAS debris will go into combustion chambers, where the flame temperature may be as high as 1650 ℃ [252], which may cause the debris to melt and deposit on the TBC surfaces. Finally, the TBCs will be degraded by CMAS.

CMAS-induced degradation involves a series of processes, from the ingestion of CMAS debris into gas turbine engines to the spallation of TBCs. With the increasing research interest in this field in recent years, many processes have been understood more clearly. Some important aspects of the lamellar top coat will be reviewed briefly below.

First, a few points about the source of CMAS debris are worth noting here. CMAS may come from mineral sources such as sand and volcanic ash. Sometimes CMAS originates from industrial sources such as fly ash, cement, and runway dust. In addition, engine components may be worn off, and the component debris may deposit on TBC surfaces. Therefore, it is important to bear in mind that CMAS compositions and properties vary over a wide range, which may cause the different degradation behavior of TBCs.

Figure 48 is an optical image showing the appearance of CMAS deposits on an ex-service blade. CMAS deposits do not form a continuous layer covering the TBC. In such a situation, the spreading behavior of the CMAS deposits will influence the extent of CMAS degradation (lateral range and depth of CMAS attack). Yang *et al.* [253] studied the effect of TBC structure on CMAS spreading and infiltration behavior by using small CMAS beads instead of evenly covering CMAS on TBCs. They found that at each test temperature, the spreading process can be divided into three stages. In Stage I, the spreading areas on APS and EB-PVD TBCs are similar because the driving force for spreading and CMAS viscosity is relatively high during this stage. In Stage II, spreading on APS TBCs is fast relative to that on EB-PVD TBCs. Three reasons were proposed to account for this spreading difference. First, the infiltration speed in EB-PVD TBCs is higher, which lowers the spreading speed. Second, the surface roughness of APS TBCs is higher, so the wettability of CMAS on APS TBCs is better. Third, the trapped air between CMAS and APS TBCs (due to the rough
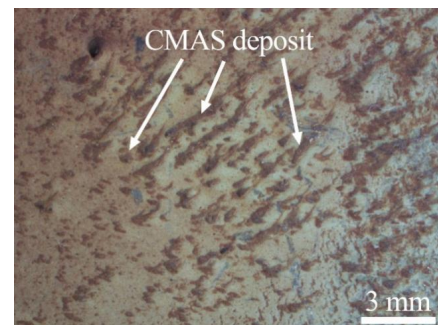

Fig. 48 Optical image showing the appearance of CMAS deposits on an ex-service blade.

surfaces) may also increase the spreading speed. In stage III, the spreading speed for APS TBCs is lower than that for EB-PVD TBCs. However, the spreading area on both TBCs becomes similar again. On the one hand, the high porosity of APS TBCs is beneficial for CMAS infiltration, so the spreading speed on APS TBCs is lowered. On the other hand, the higher connectivity of micro-pores in EB-PVD TBCs increases the subsurface lateral flow of CMAS, which can accelerate the surface spreading speed.

Molten CMAS can readily infiltrate into the open pores of an APS TBC. During the cooling process, CMAS solidifies, which increases the in-plane modulus of coating. The increase in CMAS infiltration depth increases the elastic energy release rate for the CMAS-infiltrated coating, making the coating more susceptible to delamination. Therefore, infiltration depth is a critical factor that influences the CMAS-induced failure of APS TBCs. Kang *et al.* [254] studied the effect of microstructural defects of APS TBCs on CMAS infiltration. They fabricated APS TBCs with different amounts of defects (samples A1, S1, S2, and S3) by tuning the velocity and temperature of the in-flight particles, as shown in Fig. 49. The spraying parameters for these four samples can be found in Ref. [254]. The subsequent CMAS attack test showed that CMAS infiltration depth could be effectively reduced in defect-depleted APS TBCs. Liu *et al.* [255] also studied the effect of microstructure on CMAS infiltration. The results indicated that increasing splat bonding in APS TBCs can lower the CMAS infiltration speed.

In APS TBCs, open pores offer fast paths for CMAS infiltration. Therefore, it is significant to understand how the pore characteristics influence the CMAS infiltration behavior. To fulfill this goal, Shan *et al.* [256] modified the pore characteristics of regular APS TBCs via the alumina sol impregnation technique. After one sol impregnation, ~18 vol% of the equiaxed pores are occupied by alumina, and ~36 vol% of the crack network pores are occupied. Cross-sectional observation of the pore-tailored APS TBC revealed that the pore-modifier Al_2O_3 could reduce the pore width, increase pore tortuosity, or even directly block them by forming horizontal connecting arrays, as shown in Fig. 50. CMAS attack test showed that the pore-modifier alumina could lower the CMAS infiltration speed. In addition, it was also found that although CMAS corrosion can cause alumina to disappear, crystalline anorthite will be formed in the pores and mitigate further infiltration.

Porosity decrease caused by CMAS degrades the strain tolerance of APS TBCs. One main factor causing porosity decrease is the pore filling by CMAS. There is evidence showing that after CMAS infiltration, not all
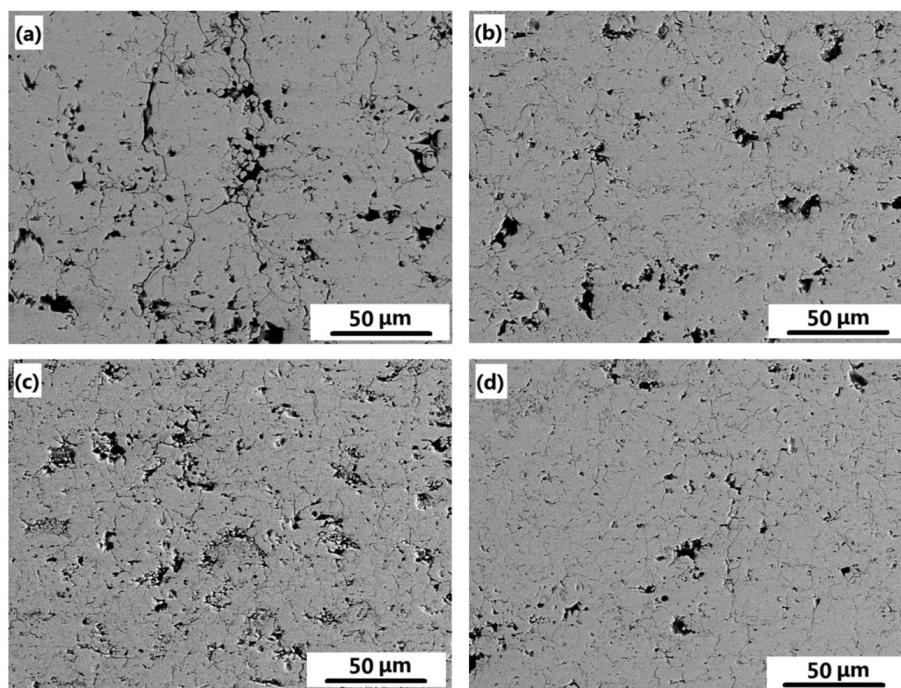

Fig. 49 Cross-sectional SEM images of plasma-sprayed TBCs with different amounts of defects for as-sprayed coatings: (a) A1, (b) S1, (c) S2, and (d) S3. Reproduced with permission from Ref. [254], © Elsevier B.V. 2016.
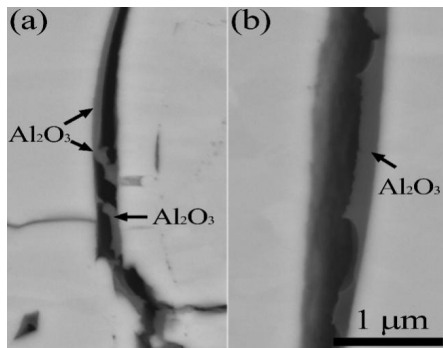
Fig. 50 Cross-sectional SEM images showing alumina distribution in a regular APS TBC whose pore characteristics are tailored via alumina sol impregnation technique: (a) Alumina reduces pore width and forms horizontal connecting arrays and (b) alumina increases pore tortuosity.

the pores are filled by CMAS [257]. Therefore, it is of practical importance to understand what kind of pores in APS TBCs can resist CMAS filling. Shan *et al.* [257] fabricated YSZ pellets with different sizes of globular pores using poly methyl methacrylate as pore-forming agents to understand the size of globular pores on CMAS filling behavior. CMAS attack test revealed that only small pores were easily filled by CMAS, whereas large pores could hardly be filled. Additionally, it was also confirmed that even open pores could resist CMAS filling. The proposed explanation is as follows. If a pore is large enough, its surface can hardly be wetted completely. In such a situation, molten CMAS cannot form a continuous meniscus, so the pore cannot be filled. This research implies that fabricating relatively large pores in APS TBCs may lower the extent of pore filling by CMAS.

Following this study wherein YSZ pellets instead of real TBCs were used, Shan *et al.* [258] studied the pore evolution and CMAS filling behavior in real APS TBCs. They found that although CMAS caused the total porosity of the APS TBC to decrease, the porosity of the top region increased, presumably because of the significant microstructure change in this region. In the region where microstructure was changed slightly by CMAS, almost all crack network pores disappeared, but 48 vol% of equiaxed pores existed. Further analysis indicated that larger equiaxed pores were more likely to remain. This study indicates that introducing large equiaxed pores into APS TBCs may be a potential way to lower the extent of porosity decrease.

CMAS also degrades lamellar top coat chemically. YSZ can be dissolved by CMAS, which causes

repreciptation of Y-lean t-ZrO_2 [259]. Upon cooling, such t-ZrO_2 will transform to m-ZrO_2, accompanied by a volume expansion (4–5 vol%) [260]. Witz *et al.* [261] investigated the corrosion behavior of plasma-sprayed YSZ TBCs by CMAS in natural environments. In their research, CMAS-attacked TBCs from an ex-service combustor were analyzed. It was demonstrated that Ca^{2+} cations from molten CMAS can diffuse into YSZ, causing (1) the stability of the c-YSZ phase to increase, (2) the volume of YSZ to expand, and (3) the residual stress distribution in the top coat to change. Many researchers have observed that CMAS prefers to attack YSZ grain boundaries [262,263]. Although it seems that the basic CMAS corrosion mechanisms in YSZ coatings are always similar, some factors influence the corrosion behavior. Recently, Morelli *et al.* [262] studied the effect of chemical purity and microstructure of plasma-sprayed YSZ top coat on CMAS corrosion behavior. An isothermal CMAS attack test was conducted on four kinds of lamellar YSZ top coats: APS coatings deposited with standard- and high-purity feedstock powders, a DVC coating, and a suspension plasma sprayed (SPS) one. Comparison between APS TBCs with similar structures but with different chemical purity levels revealed that degradation in the TBCs with higher purity was less pronounced. It was found that high purity can limit the extent of grain boundary dissolution. In addition, the results revealed that higher porosity and smaller grains tend to cause more severe degradation. For example, there are usually three kinds of grains in a regular APS TBC: (1) coarse equiaxed (originating from unmolten spray powders), (2) fine equiaxed (originating from molten spray particles that solidify before deposition), and (3) fine columnar (typical APS TBC structure). It was observed that CMAS attacks in fine-grained regions are more severe.

It is well known that the TBC sintering during service reduces the porosity, which results in the degradation of the thermal insulation performance of the coating. CMAS can aggravate sintering and hence the thermal insulation degradation. Boissonnet *et al.* [264] studied the influence of infiltration of a small amount of CMAS (0.25–3 mg·cm^{-2}) on the sintering behavior and the thermal insulation property of APS TBCs. It was found that the depth of the sintering increases with the CMAS amount, as illustrated by Fig. 51. The thin lamellar pores seem to be sintered to a depth of ~250 μm (full thickness) for 1 h heat treatment at 1250 ℃ when the CMAS load is 3 mg·cm^{-2}. In
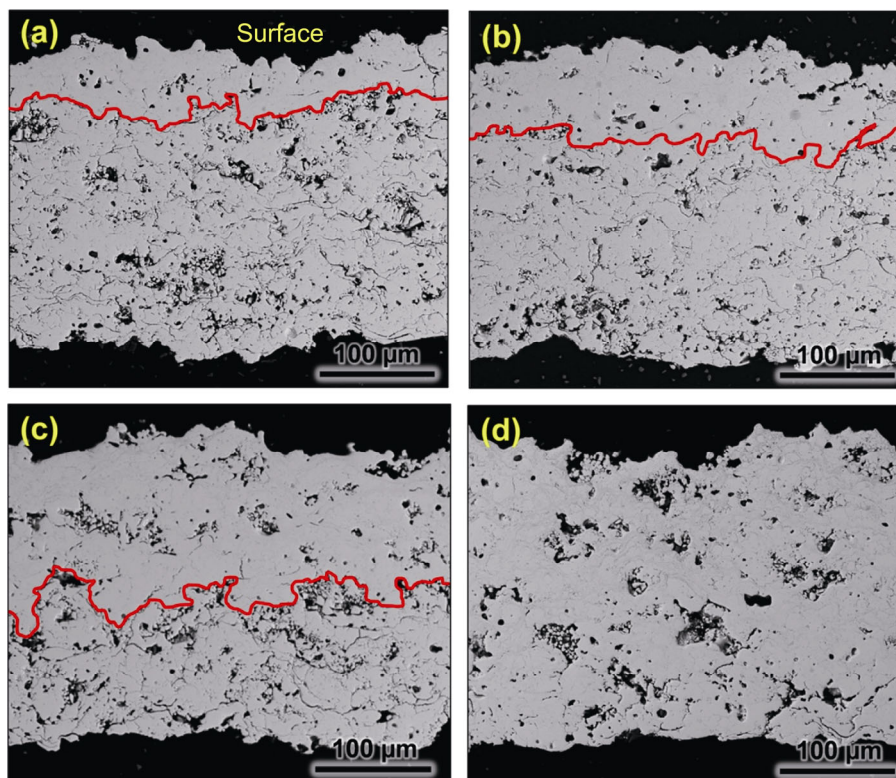
Fig. 51 Cross-sectional SEM images showing the microstructures of YSZ APS TBCs heat-treated at 1250 ℃ for 1 h with CMAS of (a) 0.25, (b) 0.50, (c) 1.0, and (d) 3.0 mg·cm^{-2}. Reproduced with permission from Ref. [264], © Elsevier Ltd. 2019.

addition, the CMAS-induced sintering was accompanied by local phase transformations. These two are the main factors responsible for the increase in the thermal diffusivity of the coatings. For the fully infiltrated coating, the increase in the thermal diffusivity can reach a maximum of ~110%.

Perhaps the primary role of CMAS is that it can stiffen the ceramic top coat and cause delamination and spallation, as shown in Fig. 52. Mercer *et al*. [265] proposed a CMAS-induced delamination mechanism. When rapid engine shutdown occurs (cold shock conditions), the TBC surface experiences a high cooling rate. This results in the tensile stresses in the TBC surface, which induce vertical separations (Mode I) in the coating. Under slow cooling conditions, molten CMAS in an APS TBC will gradually solidify, causing
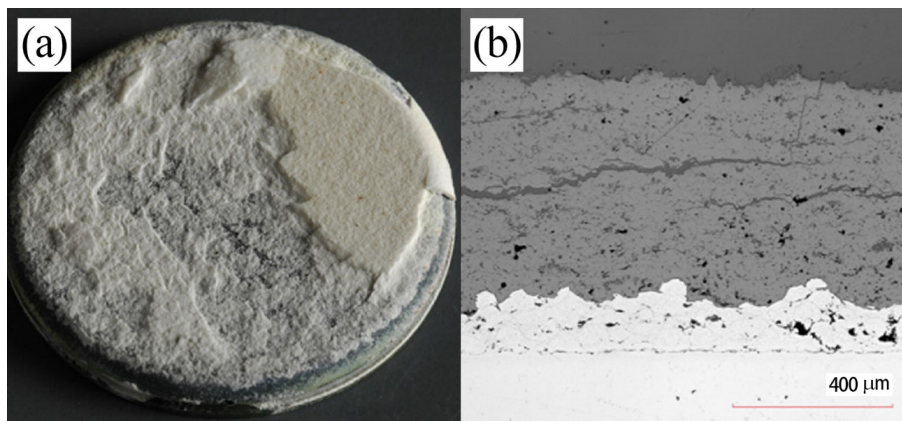
Fig. 52 (a) Macroscopic optical image and (b) cross-sectional SEM image of an APS TBC cycled to failure in thermal gradient conditions (~1250 ℃ at the TBC surface and ~1080 ℃ at the bond coat) on a burner rig with simultaneous CMAS injection. Reproduced with permission from Ref. [266], © Elsevier B.V. 2017.

the in-plane modulus to increase. Due to the CTE mismatch between the CMAS-attacked top coat and the metallic substrate, the strain energy accumulates in the top coat, which offers a driving force for delamination. Usually, such delamination emanates from vertical separations, which may be formed during processing, sintering during service, or cold shock. For APS TBCs, it is also possible that delamination emanates from the inherent defects in the coatings and deflects randomly toward the coating surfaces [266].

One point worth mentioning here is that laboratory experiments confirmed that CMAS could cause high-temperature volume expansion of APS TBCs. When the bonding between the top coat and bond coat is destroyed by CMAS, high-temperature delamination along the TC/BC interface can occur [267].

To mitigate CMAS damage, lamellar top coats composed of novel TBC materials have been proposed. For example, Drexler *et al.* [268] prepared APS TBCs using a rare-earth zirconate material ($Gd_2Zr_2O_7$) and investigated their CMAS resistance performance. It was found that such TBCs can mitigate CMAS infiltration effectively at high temperatures, due to the formation of a dense layer composed of a crystalline apatite phase. In addition, it was reported that plasma-sprayed $La_2Ce_2O_7$ (LCO) TBCs also exhibit excellent CMAS resistance [269]. However, LCO can react with TGO, which results in poor thermal cycling performance [270]. Therefore, Yin *et al.* [271] prepared double-layer APS LCO/YSZ TBCs. CMAS attack test on the double-layer TBCs showed that CMAS infiltration can be mitigated. Because of the reaction between CMAS and LCO, a dense layer composed of anorthite, spinel, and $La_2Si_2O_7$ can be formed, which can restrain CMAS infiltration.

In short, CMAS corrosion on a lamellar top coat depends on the infiltration of CMAS into the network pores within the top coat. By preparing a dense cover layer or *in-situ* producing a resultant layer, the infiltration of CMAS can be depressed. Further strategies to restrain the CMAS corrosion on the lamellar top coat are ongoing.

3.3.2 Corrosion of columnar top coat

The columnar top coat also suffers from corrosion due to the easy infiltration of reactants into the inside top coat via columnar pores, although columnar top coat has high thermal stress tolerance and potentially long thermal cyclic lifetime [272,273]. However, they are easily attacked by corrosion agents due to their gap-type structure. A premature failure event of gas turbine engines caused by hot corrosion in the marine environment was observed for the first time in the 1960s on the U.S. Navy shipboard [274,275]. Hot corrosion damage in the hot-section of the turbine hardware due to the intrusion of salts (sulfates and chloride salts) from the marine air and/or from sulfur in the gas turbine combustion fuels was found to be the major reason behind the failure [276]. Recently, hot corrosion has been reported to be observed on TBCs in marine and in non-marine environments. With a further understanding of the failure mechanism of TBCs, the types of hot corrosion can be roughly divided into marine hot corrosion and CMAS hot corrosion according to the engine application service environment.

The typical characteristics of the marine environment are high humidity and high salt fog. When the gas turbine works, the compressor continuously sucks in air from the outside, and after being compressed, it is mixed with the fuel for combustion. The generated high-temperature gas flow continuously pushes the turbine to do work. Under high-temperature conditions, Cl^-, Na^+, and K^+ in air can easily react with S, V, Pb, and other elements in the fuel. The resulting molten salt mixture is deposited on the surface of turbine blades and other components in the form of eutectic, eroding the TBC on the substrate surface and causing failure.

In the open literature, sulfur is considered to be the main marine corrosive element. In the process of marine hot corrosion, complex sulfidation and oxidation are mainly involved [276]. The research and elaboration of hot corrosion mechanisms have gone through two stages: the vulcanization model and salt melting mechanism model. Early research on the sulfidation model mainly focused on the reaction between metal elements (Ni, Cr, Al, etc.) and their oxides and Na_2SO_4, and the internal diffusion of S element. It was considered that the hot corrosion was caused by the high-temperature oxidation of S element and alkali metal ions in the fuel [277,278]. This discussion once occupied a dominant position in this research field for a long time. O'Dowd and de Leeuw [279] and Pettit [280] proposed the salt fluxing model: hot corrosion is a process in which the protective metal oxide film dissolves acidic or alkaline at the film/molten salt eutectic interface and then redeposits at the molten salt/vapor interface. This theory is improved on the

basis of the sulfurization model. The description of the hot corrosion phenomenon is more comprehensive and systematic and is still widely accepted.

However, with a further understanding of the corrosion mechanism, it is found that the model cannot explain all the experimental phenomena. In fact, according to the environmental temperature, hot corrosion is usually divided into two types: high-temperature and low-temperature hot corrosion [281]. As shown in Fig. 53, high-temperature hot corrosion (Type I corrosion in Fig. 53) generally occurs between 850 and 950 ℃, which is just between the melting point of the molten salt deposit and its dew point (the temperature at which the deposit begins to gasify); low-te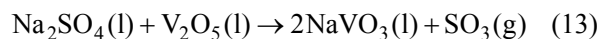mperature hot corrosion (Type II corrosion in Fig. 53) is relative to high-temperature hot corrosion, which usually occurs between 650 and 750 ℃. Many comprehensive factors (such as environmental temperature, corrosion products, matrix material type, thermodynamic conditions, and gas velocity) determine the type of hot corrosion [281,282].

In fact, the YSZ as a typical top ceramic material has strong corrosion resistance, which is less affected by NaCl and Na_2SO_4 in sea salt. However, in the observation of hot corrosion events, it is found that the introduction of fuel impurity V will have a strong corrosion effect on the YSZ ceramic layer [283]. The hot corrosion behavior and mechanism of columnar YSZ thermal barrier in V_2O_5 + Na_2SO_4 mixed salt at 800–900 ℃ are systematically studied [284]. The

results show that the molten V_2O_5 infiltrates into the coating along the columnar crystal gap and reacts with Y_2O_3, and the intermediate reactions follow:

$$Na_2SO_4 = Na_2O + SO_3 \tag{11}$$

$$Na_2O\,(l) + V_2O_5\,(l) \rightarrow 2NaVO_3\,(l) \tag{12}$$
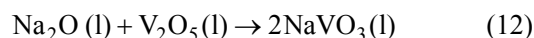
Comprehensive reaction:

$$Na_2SO_4\,(l) + V_2O_5\,(l) \rightarrow 2NaVO_3\,(l) + SO_3\,(g) \tag{13}$$

Finally, the hot corrosion reaction of the ceramic coating is

$$\begin{aligned} Y_2O_3\,(s) + t - ZrO_2\,(s) + 2NaVO_3 \rightarrow \\ 2YVO_4\,(s) + m - ZrO_2\,(s) + Na_2O\,(l) \end{aligned} \tag{14}$$
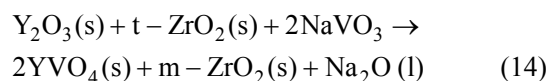
The process of the reaction is that the stabilizer Y_2O_3 is gradually reduced, and the t-ZrO_2 formed during the reaction will undergo phase transformation (t-$ZrO_2 \rightarrow$ m-ZrO_2) during the subsequent cooling process. The volume change caused by the transformation will lead to local stress concentration in the coating, which will lead to the failure of the coating [274]. At the same time, in a V_2O_5 + Na_2SO_4 molten salt environment, XRD patterns show that the corrosion products on the coating surface are "round rod" YVO_4 and "granular" m-ZrO_2 [275]. This is the source of two kinds of hot corrosion products. The accumulation of corrosion products on the surface of the YSZ coating, together with the gradual consumption of the stabilizer Y_2O_3, constitutes an important source of the collapse of the internal stress concentration area of the coating and the

Fig. 53 Profile of shipboard engine corrosion rates of Type I and Type II hot corrosion vs. temperature in a marine environment compared to the Arrhenius oxidation rate vs. temperature. Reproduced with permission from Ref. [281], © Elsevier B.V. 2012; Ref. [282], © China Academic Journal Electronic Publishing House 2015.

diffusion of molten salt corrosion along the grain boundary, which eventually destroys the columnar crystal structure of the coating [285].

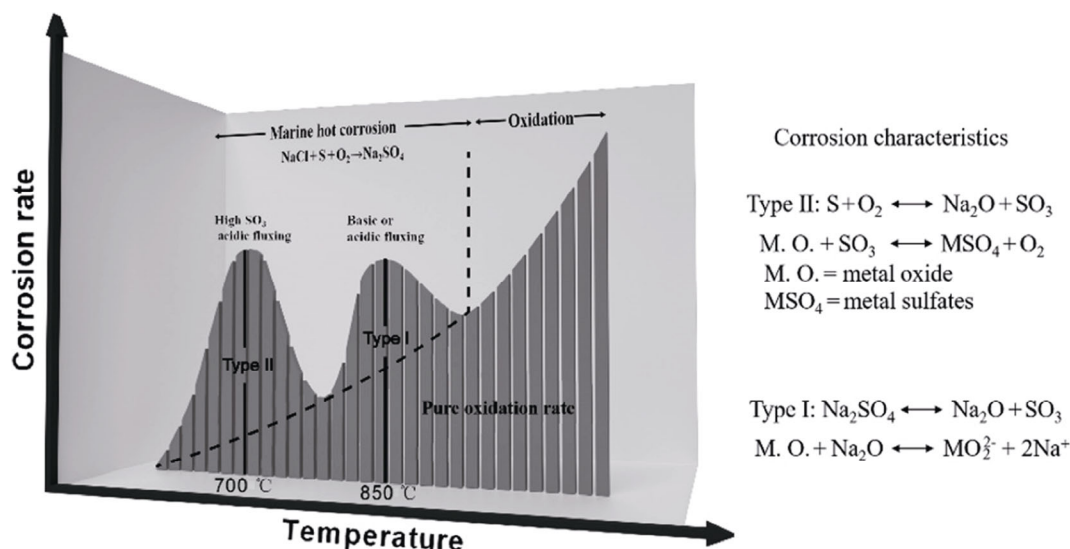In the relevant marine hot corrosion literature, the YSZ columnar coating was attacked by S, Cl, and other corrosive elements, the metal layer in the coating system will be damaged before the ceramic layer, and coating delamination often occurs due to the formation of a thick TGO layer between the ceramic layer and the metal layer [278]. During the corrosion process, the ceramic layer with a feather columnar structure only shows sintering acceleration, and no corrosion phenomenon is observed. However, the top coat of the gap-type structure has a large number of open pores, which promotes the erosion of the metal layer by the corrosive agent.

CMAS adheres to the surface of the ceramic coat and has a thermochemical reaction, thus leading to early failure of the TBC [286]. In recent years, CMAS hot corrosion research reports have confirmed that CMAS is harmful to YSZ columnar top coats [265]. On the one hand, CMAS molten salt not only dissolves the YSZ coat but also penetrates into the YSZ layer. After cooling, CMAS molten salt can compact the coating and produce large internal stress, resulting in the delamination and spalling of TBCs [287]. On the other hand, the CMAS molten will deplete the stabilizer of Y_2O_3, resulting in t'-ZrO_2 transformation to m-ZrO_2. This phase transformation of zirconia will lead to a significant change in volume, further leading to damage to the mechanical properties and stress accumulation of the coating [288]. The cross-section morphology of PS-PVD YSZ after CMAS hot corrosion is shown in Fig. 54 [289]. The YSZ coating prepared by PS-PVD

has a feather-like columnar structure with open pores. When the coating is corroded by CMAS, it is easily infiltrated with more molten salt. After cooling, it has a greater impact on the coating structure. Therefore, CMAS hot corrosion has a greater impact on PS-PVD TBC than another coating, and the microstructure of PS-PVD coating changes significantly after cooling.

In addition, it is considered that the penetration of CMAS and the corrosion of the YSZ layer are related to the initial position of the transverse crack and the spalling position [290]. PS-PVD 7YSZ failure is not caused by a single reason. In general, the damage of CMAS to TBCs mainly includes thermochemical and thermomechanical action, CMAS erosion and corrosion, and CMAS densification to the YSZ ceramic layer, which leads to the change in CTE and thermal conductivity of the coating and finally to delamination, cracking, and spalling of the coating [291].

The corrosion resistance of columnar top coat is considered to be improved. To enhance the hot corrosion resistance of columnar structure coating, new corrosion-resistant materials have been developed [292]. In recent years, the research on corrosion-resistant top coating materials has mainly focused on the rare-earth ion doping of YSZ materials and the development of new structural materials [293,294]. At present, currently commonly used doping systems for TBCs mainly include the following: (1) Single rare-earth ions such as Gd^{3+}, Yb^{3+}, Ce^{4+}, and Hf^{4+} are used to improve the phase stability of TBCs; (2) co-doping modification of TBCs with multiple ions, such as Sc^{3+} + Y^{3+} or Nb^{5+} + Ta^{5+} + Y^{3+} co-doped TBCs. The thermal physical properties of top coat materials are obviously improved by doping rare-earth oxides or transition metal oxides
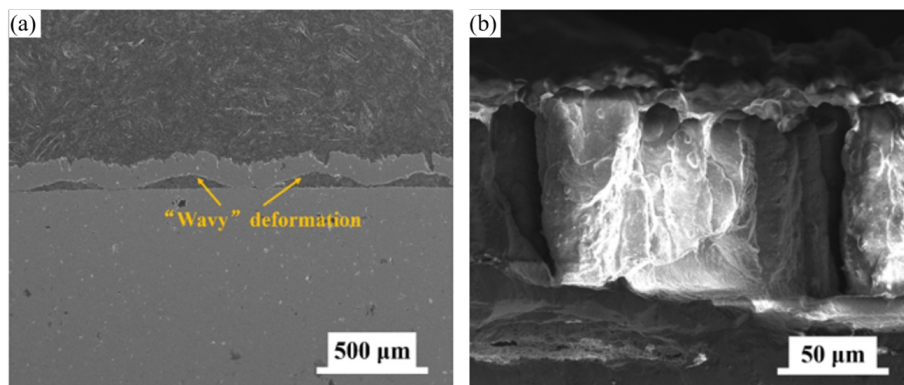

Fig. 54 Cross-section morphologies of PS-PVD YSZ after CMAS hot corrosion: (a) separation between coating and substrate and (b) filling of the gap between columns by CMAS. Reproduced with permission from Ref. [289], © China Academic Journal Electronic Publishing House 2019.

with good chemical stability and a high melting point [295]. New structural coating materials, such as rare-earth zirconates with pyrochlore structures ($La_2Zr_2O_7$, $Gd_2Zr_2O_2$, etc.) and zirconates with a perovskite structure ($SrZrO_3$, $CaZrO_3$, etc.) also show good prospects in the study of improving the adaptability of molten salt corrosion environments by virtue of their excellent characteristics such as low thermal conductivity and high-temperature phase stability [296,297]. Compared with the conventional YSZ material, the new TBC ceramic coat materials have certain advantages in one or several aspects, but the comprehensive performance of thermal cycle life and thermal protection need to be improved, and the process for preparing columnar structures of new corrosion-resistant materials also needs to be researched.

In conclusion, anti-corrosion is an important challenge for TBCs in aero-engines. In recent years, the feather-like columnar coating has presented better thermal insulation performance and higher thermal cycle life, but it is weaker under hot corrosion attacks. The optimization of the preparation materials and the structure and surface treatment of the coating will be a research hotspot in the future.

3.3.3 Multi-component coupling corrosion

TBCs work in a harsh environment, facing many types of high-temperature corrosion such as environmental deposit corrosion, namely, CMAS attack, and molten salt corrosion. These multi-component reactants cause coupling corrosion for the ceramic top coat.

Recently, it has been found that in the marine environment, there is coupling corrosion of CMAS and molten salt, which imposes much severer damage to TBCs. High-temperature corrosion has become one of the key factors which cause premature failure of TBCs. Hence, many researches have been carried out to investigate the corrosion behavior of TBCs, aiming to clarify the corrosion mechanisms and explore corrosion protection methods. Figure 55 shows a schematic diagram of corrosion mechanisms resulting from CMAS, molten salt, and CMAS + molten salt attack on APS TBCs.

Stott *et al.* [298] first examined the CMAS corrosion behavior of YSZ TBCs and the related mechanisms.
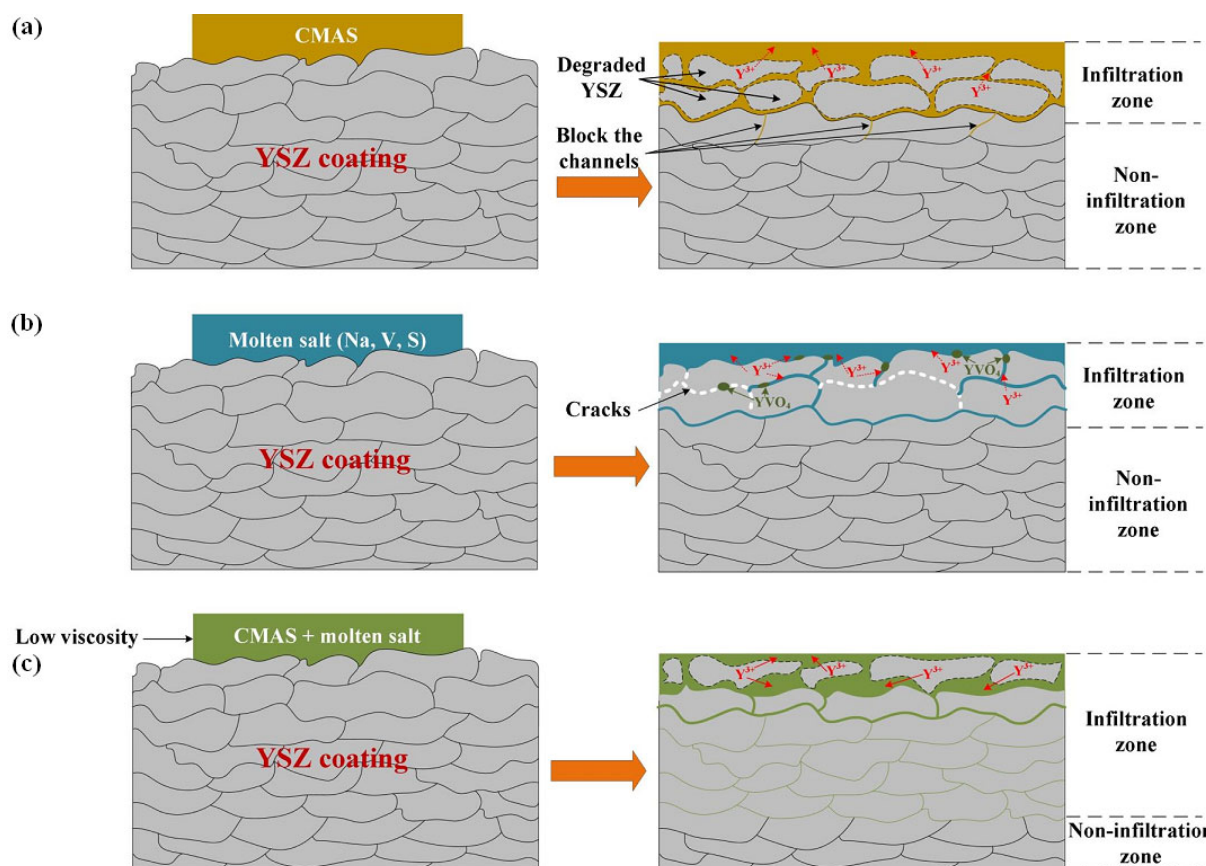

Fig. 55 Schematic diagram of different corrosion mechanisms for APS TBCs: (a) CMAS, (b) molten salt, and (c) CMAS + molten salt.

They deposited natural CMAS from the Middle East on APS TBCs, and heat-treated them at 1300–1600 ℃ for 120 h. It was found that at high temperatures, the stabilizer Y_2O_3 prefers to dissolve into the melt, causing the coating to deplete Y_2O_3. As a result, the coatings suffer from a phase transformation to the m phase accompanied by excessive volume expansion. Krämer *et al.* [259] conducted a systematic investigation on the corrosion mechanisms of TBCs by CMAS attack. They found that CMAS rapidly infiltrates the coating as soon as melting occurs, whereupon YSZ dissolves in the melt and reprecipitates ZrO_2 crystals with different morphologies and compositions depending on the local melt chemistry. This dissolution–reprecipitation model has been accepted by many researchers as the main mechanism for TBCs attacked by CMAS in terms of thermo-chemical interactions.

Additionally, CMAS corrosion causes TBC failure in another aspect, i.e., thermal-mechanical interaction. The penetrated molten CMAS fills the pores and microcracks in TBCs, which solidifies upon cooling. As a result, the coatings would be densified, losing much strain tolerance and producing large stress. Evans and Hutchinson [299] and Jackson *et al.* [300] proposed theoretical models to estimate the stress field of CMAS corroded TBCs based on the small deformation assumption. Cai *et al.* [301] built a numerical model considering the CMAS penetration in TBCs to investigate the effects of CMAS penetration depth and microstructure shape on the stress distribution and stress level in the coating. During the thermal cycling process, increasing stress accumulated, eventually causing premature TBC spallation. Mercer *et al.* [265] carried out thermal shock analysis and determined the critical infiltration thickness, above which the infiltrated layer is susceptible to delamination and spallation. Krämer *et al.* [302] characterized the delamination susceptibility of TBCs by CMAS penetration and found that CMAS penetrates to a depth of approximately 0.5 mm and infiltrates all open areas in coating zones, where cracks, delamination, and spallation exist. Yang *et al.* [303] determined the strain field of TBCs attacked by CMAS using digital image correlation techniques and obtained the critical strain values for the failure of TBCs.

When low-grade fuels are used, TBCs inevitably suffer from molten salt corrosion. The salts containing vanadium, sulfur, and phosphorous are extremely corrosive to TBCs, especially at a temperature of 600–1050 ℃. For YSZ TBCs and other rare-earth containing novel TBC candidates, molten salt easily leaches out the rare-earth elements in TBCs, which causes several adverse effects [304–307]. First, loss of rare-earth causes phase destabilization of TBCs such as in the case of YSZ TBCs. It undergoes phase transformation in the presence of molten salt. Second, for some TBCs containing high rare-earth contents, phase transformation resulting from rare-earth loss is not an important concern, but changes of thermo-physical and mechanical properties of the coating in the presence of molten salt could not be ignored, which significantly affect the coating lifetimes. Third, molten salt penetration in the coating and reaction with it destroys the coating microstructure, which largely degrades coating performance, such as thermal insulation and thermal shock.

Recently, Shifler from the Office of Naval Research (USA) and Choi from Naval Air Systems Command (USA) [308] inspected shipboard gas-turbine components and found that in the marine environment, CMAS corrosion could occur at temperatures much lower than its melting temperature. This phenomenon is peculiar, and some important questions arise, such as: What caused CMAS attack to components at a lower temperature? Was this triggered by the salt in the marine environment? How did salt reduce the melting temperature of CMAS? In summary, compared with CMAS corrosion or molten salt corrosion alone, the coupling corrosion of CMAS and molten salt is more complex and much more severe. Compared with CMAS, it is considered that the coupling of CMAS and molten salt causes accelerated corrosion of TBCs, which could be understood by the following aspects. First, coupling corrosion occurs at lower temperatures than CMAS corrosion. According to Shifler and Choi [308], the mixture of CMAS and molten salt has a lower melting point than CMAS. Guo *et al.* [309] found that $NaVO_3$ + CMAS mixture (CN) has a lower melting temperature (by ~50 ℃) than CMAS. As we know, only when the corrosion medium melt, it would cause obvious corrosion of TBC. Therefore, at a temperature at which CMAS + salt melts but CMAS does not, it is undoubtedly that the coupling of CMAS and molten salt has accelerated corrosion to TBC compared with CMAS. Second, at a temperature when both CMAS and CMAS + salt melt, the latter has a lower viscosity. Guo *et al.* [309] pointed out that the addition of salt such as $NaVO_3$ into CMAS could

significantly reduce the melt viscosity. A low viscosity means a higher penetration ability, which causes the melt to penetrate the coating more easily. As a result, the coupling of CMAS and molten salt induces severer corrosion to TBCs than to CMAS, which has been confirmed by Guo *et al*. [309], but the coupling corrosion mechanisms to TBCs still need further investigation.

For the corrosion protection of TBCs against CMAS and molten salt attack, much attention and investigation have been reported. To mitigate CMAS attacks on TBCs, a direct method is to induce CMAS crystallization, dragging the melt infiltration to TBCs. The reaction between coating constituents and the melt could produce crystallization products. However, the products generated on the surface of YSZ TBCs by reacting with CMAS cannot form a crystalline sealing layer; as a result, although some CMAS is crystallized, most of the melt has penetrated the coating. Therefore, some attempts have been made to promote reaction crystallization by forming a sealing layer on the coating surface. Drexler *et al*. [310] pointed out that doping Al_2O_3 and TiO_2 into YSZ coatings can promote molten CMAS crystallization, suppressing CMAS penetration. To better understand the interaction behavior between CMAS and TBCs, it is necessary to identify whether the crystalline products are formed as a result of CMAS self-crystallization or reactive crystallization between CMAS and TBCs. Wiesner and Bansal [311]

studied the crystallization kinetics of CMAS powder and bulks and the microstructure and chemical compositions of crystalline phases after heat treatments, but their dwelling temperature was not above 960 ℃ [311]. Guo *et al*. [312] systematically investigated the effects of cooling/heating rates and the heat treatment peak temperature on phases, morphologies, and microstructure of CMAS self-crystallization products, and pointed out that the products of diopside, wollastonite, and anorthite have different abilities to form. They also indicated that although self-crystallization can slow molten CMAS penetration, its function in protecting TBCs from damage is limited.

Other strategies for alleviating CMAS corrosion to TBCs have been developed. Wang *et al*. [313] reported that electroplating a dense and defect-free Pt film on YSZ TBCs effectively protected the coating from CMAS attack. Guo *et al*. [314,315] first reported a CMAS resistant material of Ti_2AlC MAX phase. They indicated that Ti_2AlC has a great ability to resist molten CMAS penetration, and the pre-oxidized one has obvious advantages over its non-oxidized counterpart. MAX phase of Ti_2AlC is thus strongly suggested to be used as a protective layer material on TBCs against CMAS attack. Yan *et al*. [316] adopted laser glazing to produce a modified layer on the YSZ TBC surface, which has a columnar microstructure with some open channels, as shown in Figs. 56(a) and 56(b). Exposed to CMAS attack, the glazed layer retains phase stability,
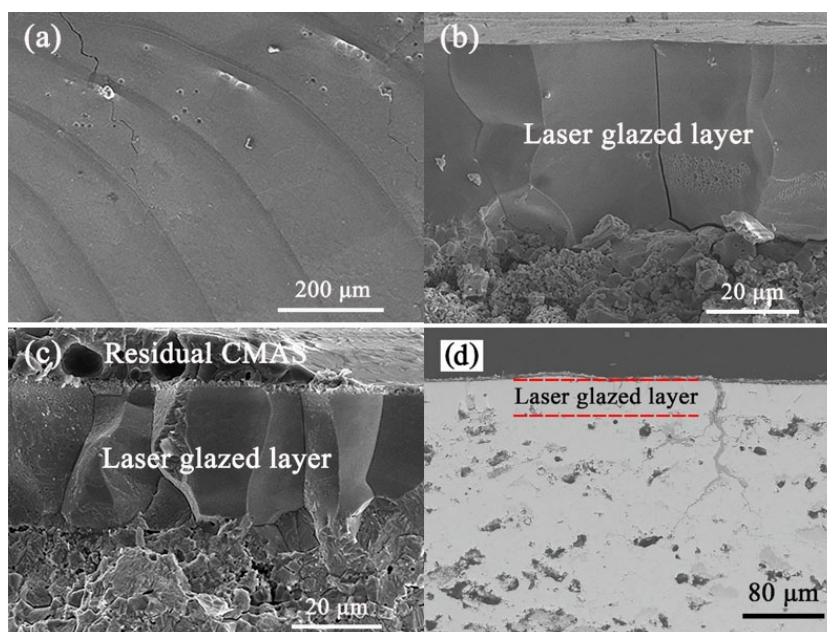

Fig. 56 (a) Surface morphology. (b–d) Cross-sectional microstructures of laser-glazed YSZ TBCs. (c) and (d) are images of the TBCs after corrosion by CMAS and V_2O_5, respectively. Reproduced with permission from Ref. [323], © The Author(s) 2020.

maintains structural integrity, and has good adhesion to the underlying coating (Fig. 56(c)), suggesting that laser glazing is an effective method to alleviate CMAS attack on TBCs.

In the aspect of protecting TBCs against molten salt corrosion, the emphasis is mostly focused on seeking an alternative stabilizer to Y_2O_3 in ZrO_2 based TBC materials, aiming at enhancing the phase stability in the presence of molten salt. It has been found that ZrO_2 doped with Sc_2O_3, In_2O_3, CeO_2, Ta_2O_5, and Gd_2O_3–Yb_2O_3 reveals higher phase stability than that of YSZ when exposed to molten salt suggesting better corrosion resistance [317–320]. Some newly-developed TBC materials were reported to have enhanced molten salt corrosion resistance, such as rare-earth phosphate and Sc_2O_3-doped $Gd_2Zr_2O_7$ [321,322]. In particular, $LaPO_4$ and $NdPO_4$ reveal excellent corrosion resistance. The penetrated molten salt elements such as V react with them to form $RE(P,V)O_4$ (RE = Nd and La) solid solution, which causes little damage to the original microstructure. Guo *et al*. [323] found that laser glazing also improves the corrosion resistance of YSZ TBCs in the presence of molten salt, as shown in Fig. 56(d). The glazed coating exhibits enhanced phase stability and is resistant to molten salt penetration.

For the case of coupling corrosion of CMAS and molten salt to TBCs, there has been no report on corrosion protection. According to previous studies by Guo *et al*. [316,323], laser glazing on TBC surfaces is beneficial to improving both CMAS and molten salt corrosion resistance. Hence, TBC surface modification by laser glazing might be a promising method to alleviate the coupling corrosion to TBCs. However, for

the application of this method, a large amount of work is needed, such as microstructure design of the modified coating, precise control of the glazed layer, and interface matching investigation. For the exploration of novel TBC materials that are resistant to the coupling corrosion, it is found that rare-earth phosphates have excellent resistance to both CMAS corrosion and molten salt corrosion, and thus they are considered to be a promising TBC candidate material in the coupling corrosion condition [321,324]. However, how rare-earth phosphate TBCs behave in the presence of a mixture of CMAS and molten salt is still not clear.

In short, to mitigate the coupling corrosion of top coat, in addition to typical YSZ, some novel ceramic materials have been developed, such as LCO, $LaMgAl_{11}O_{19}$, $Gd_2Zr_2O_7$, and $GdPO_4$ [325–327]. However, these newly developed TBC materials usually have poor mechanical properties, such as low toughness. Double ceramic layer (DCL) TBCs have been proposed to employ both YSZ and new ceramics [270,328]. Except for these approaches, a deeper understanding of the coupling corrosion mechanism at relatively low temperatures requires further effort.

3. 4   Ceramic degradation by erosion

Erosion failure of TBCs usually refers to the phenomenon that in the actual service process, the hard particles in airflow repeatedly impact the surface of TBCs, and the ceramic layer in the action area becomes dense, resulting in thickness thinning and crack initiation and propagation, and finally leading to coating spalling (Fig. 57). Generally, there are two main sources of hard
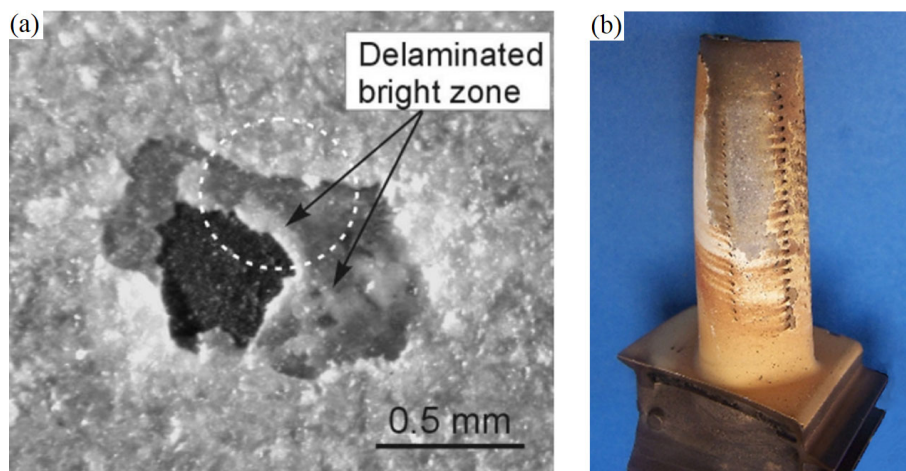
Fig. 57   Damage and spalling of TBCs under erosion conditions: (a) optical image showing the impact damage and (b) Macro photos after erosion failure. Reproduced with permission from Ref. [332] for (a), © Elsevier Science B.V. 2002; Ref. [334] for (b), © Elsevier Ltd. 2012.

particles (internal and external): One is carbon particles generated inside the engine or formed during combustion or particles formed due to erosion of engine combustion chamber wall and turbine blade. The other is from the external objects sucked into the gas turbine, such as sand, dust, aluminum, and other metal particles. Although the failure caused by the action of the second type of particles is caused by the impact damage of external objects, these two types of damage are generally unified as erosion, and only the differences in the failure modes of coating damage caused by particles of different properties are regarded as those caused by different failure mechanisms [288,329–331]. Generally, the erosion rate (w_e) of TBCs is defined as the ratio of the mass reduction in the ceramic layer to the mass of particles participating in erosion. It is determined by the properties of impact particles and ceramic layers. The main influencing factors have two groups of parameters. One group is particle mass (size and density), velocity, and angle. The other group is the physical and mechanical properties, such as density, elastic modulus, strength, hardness, and fracture toughness of both ceramic layer and erosive particles [332,333].

The coatings prepared by APS have typical layered structural characteristics and multiple irregular defects, while the coatings prepared by EB-PVD have a typical columnar crystal structure. Therefore, the macro behavior and micro mechanism of erosion resistance of the two coatings are very different. EB-PVD coatings have greater strain tolerance and better anti-erosion performance than APS coatings because of their columnar crystal structure. However, the preparation cost of APS is lower than that of EB-PVD, and it also has obvious advantages over the coating prepared by EB-PVD in terms of thermal insulation performance. Therefore, the APS TBCs will still play an irreplaceable role in some aspects of the application of some key components, such as power and aviation industries. To improve the anti-erosion performance of the coating prepared by APS, the preparation process of APS coating can be further optimized and improved. For example, some APS coatings with vertical microcracks on the surface can be artificially prefabricated during preparation, which is usually called segmented APS coating [335]. Generally, thick TBCs have this typical microstructure characteristic. In addition, the anti-erosion performance of the coating can be further improved by PS-PVD.

Cernuschi *et al*. [336] and Wellman and Nicholls [337] systematically compared the effects of the preparation process, state of erosion particles (velocity and angle), and erosion temperature on the anti-erosion performance of these coatings. It was concluded that under the conditions of the same erosion angle, velocity, and temperature, the anti-erosion performance of TBCs was ranked according to the preparation process, followed by EB-PVD, and segmented APS, PS-PVD, and APS. It was also found that w_e of APS coating was ten times or even more than that of EB-PVD coating. For all kinds of TBCs, w_e increases with increasing erosion angle (the angle between particle motion direction and ceramic surface) and particle velocity (v_p), and w_e is related to the particle erosion angle (φ) and v_p by the following relationship [336]:

$$w_e = (v_p \sin \varphi)^n \qquad (15)$$

where n is a constant and taken as 3.0 for bulk zirconia ceramics, 2.3 for APS YSZ coatings, and 1.4 for EB-PVD YSZ coatings [336]. The results show that temperature is not a sensitive factor affecting w_e of TBCs, which indicates that the erosion temperature may not change the erosion failure mechanism. However, some studies have found that w_e of TBCs decreases slightly with increasing temperature, which may be related to the increase in the plastic deformation capacity of the ceramic top coat at high temperatures [338].

Generally, there are many mechanical property parameters that affect the anti-erosion performance of TBCs. Among them, hardness often reflects the comprehensive mechanical properties of materials and is also one of the most important mechanical properties. Therefore, studying the relationship between anti-erosion performance and the hardness of TBCs can explain the influence of material mechanical properties on anti-erosion performance to a certain extent. Janos *et al*. [339] found that the relationship between w_e of APS coating and the micro-Vickers hardness (H_V) of the ceramic layer can be fitted as Eq. (16):

$$w_e = aH_V^{\,b} \qquad (16)$$

where a and b are constants related to experimental conditions. Generally, turbine blades coated with TBCs have very complex geometry and microstructure. In fact, different curved surface structures and different microstructures, such as the size of EB-PVD columnar grains and the spacing between adjacent columnar grains, will affect the erosion performance of TBCs. The porosity of the APS ceramic layer also has a great influence on the erosion performance of TBCs. Research

by Wellman *et al*. [340] has shown that the erosion rate of ceramic layer with convex geometry is much higher than that of a ceramic layer with concave geometry.

The micro defects of the coating also have a very significant impact on the anti-erosion resistance of the coating. APS coating has a typical layered structure. The whole ceramic layer can be regarded as the superposition of strip units layer by layer. In the process of spraying and cooling, the pores with a large volume fraction in the ceramic layer are formed due to the insufficient overlap of adjacent molten drop layers, the lack of gas to be excluded from the molten drop layer during spraying, and the effect of residual stress, and many microcracks parallel to the interface are formed. The existence of these micro defects (pores and cracks) makes the elastic modulus of the APS ceramic layer smaller, so its loading capacity decreases. Compared with EB-PVD coating, APS coating has poor anti-erosion performance. The collision between the particles and ceramic layer is the interaction between particles and single or multiple layered units in this area. The erosion failure mode is that cracks are formed and propagated at the boundary of layered units, and the ceramic layer flakes along these boundaries, without an obvious dense layer such as EB-PVD coating. For APS coating, the anti-erosion performance is closely related to the distribution of pores and cracks in the ceramic layer. The increase in pores and parallel cracks in the ceramic layer provides more initial sources for the spalling of layered elements, so the coating is easier to spall. In contrast, when the ceramic layer is relatively dense, that is, when there are few pores and cracks, the coating shows better anti-erosion performance.

The erosion test for the experimental study of TBCs is mainly to spray one or more hard particles to the ceramic surface of TBCs at a certain angle and speed at a certain temperature through a special wind tunnel device, gas spray gun device, or industrial combustion device. The damage modes of the ceramic layer will be observed, and the factors affecting its anti-erosion performance will be analyzed. Nicholls' and Wellman's research groups [340,341] of Cranfield University in the UK have carried out in-depth experimental research on the erosion failure of TBCs. In addition, Zhu's research group [342], and Padture's research group [343,344] have also carried out relevant experimental research on the erosion mechanism of TBCs.

From the perspective of modeling and simulation,

the current research at home and abroad mainly focuses on the static indentation simulation of TBCs prepared by EB-PVD, and the velocity effect of impact indenter has not been fully considered in a strict sense. Yan *et al*. [345] studied the stress, load–displacement curve, and other information of TBCs under the action of micro indentation by using the finite element numerical simulation method. The research results show that the coating with a multilayer structure does not necessarily prefer crack and delamination failure at the weakest interface under the action of indentation. Chen *et al*. [346] studied the high-temperature indentation behavior of a coating prepared by EB-PVD with columnar crystal structure by using the finite element numerical simulation method. The research results show that under indentation, the columnar crystal deformation of the TBCs has obvious "shear band" characteristics, different shape characteristics will be produced under the action of indenters with different shapes, and the shape characteristics of the shear band have a certain functional relationship with the width of the columnar crystal, the friction between indenter and TBC, and the friction between adjacent columnar crystals. Ramanujam and Nakamura [347] studied the failure mechanism of thermal sprayed coating with multi-phase under erosion conditions by using the finite element simulation method. The results show that adding a small amount of metal ductile phase to brittle ceramic coating phase can greatly improve the erosion resistance of the coating. However, the oxidation of metal addition during thermal exposure limits the application of this approach for TBCs in high-temperature environments.

In conclusion, based on the abovementioned erosion study mainly at room temperature, erosion experiments at high temperatures need further investigation. The relationship between erosion and corrosion by dusts in air should also be explored in future studies.

4 Structure design for long lifetime TBCs

The spalling of ceramic top coat limits the further development of coatings. The improvement of coating lifetime can be achieved by improving the fracture toughness of ceramic materials. In addition, designing a novel ceramic structure to reduce the cracking driving force of the coating can also realize the long lifetime of the coating. Some new structural designs

for ceramic layer are summarized, which will provide guidance for the development of high-performance coatings in the future.

4.1 Lamellar structure design

4.1.1 Multilayer design

To overcome the shortcomings of the state-of-the-art pure YSZ TBCs [143,146], multilayers TBCs with two or more ceramic top coat were developed [14,348–352]. In particular, to develop the higher-temperature application TBCs, pyrochlore-structured oxides such as $La_2Zr_2O_7$ (LZO) [353–355], $Gd_2Zr_2O_7$ (GZO) [356,357], and $La_2Ce_2O_7$ (LCO) [358] have been intensively reported. The double-ceramic-layered TBCs based on pyrochlore/YSZ are proposed. On the one hand, the LZO layer can protect the bottom 8YSZ from premature sintering. On the other hand, the 8YSZ layer alleviates the thermal mismatch between the LZO and substrate. LZO, as representative candidate material, is phase-stable up to melting points (2300 ℃). Moreover, LZO shows superior low thermal conductivity and the low diffusivity of oxygen ions [359], which may reduce the total thickness of the ceramic layer under the premise of ensuring the thermal insulation function and decelerate the growth of TGO [360], and eventually achieve a long life span of TBCs. However, $La_2Zr_2O_7$ exhibits a low CTE and fracture toughness, which may cause premature failure of TBCs during service [361]. Given this, LZO/YSZ coatings have been extensively investigated [362–364] to prolong the life span of the pyrochlore-structured TBCs.

During actual service, lifetime and thermal insulation performance are both important indicators for the application of TBCs. The thermal insulation performance of TBCs is generally considered to be the temperature difference between the surface of coating and substrate during service, which actually refers to the thermal insulation function of the coating, and it is applicable under certain circumstances. However, for a given TBC system, if the TBC environment is not specified, the thermal insulation function is not clear. For example, if the temperature difference between the surface of coating and substrate is zero, it does not mean that TBCs themselves have no thermal insulation capacity. Therefore, the description of heat insulation performance needs to be redefined to describe its heat insulation capacity, which is free from the service environment and truly guides production. At present,

the design of the TBC system is often based on the premise of the same thickness of the ceramic layer. Namely, when designing a new TBC system, the total thickness of the ceramic layer is fixed, and then changes the thickness ratio of different ceramic layers. This will result in completely different thermal insulation performance for each group, and the actual thermal insulation of 'short-lived' TBCs is often higher than that of 'long-lived' ones. Overall, for the lifespan assessment of TBCs under the premise of unequal thermal insulation functions, the results may not reflect the real TBC service behavior. Until now, there are few reports on distinguishing the thermal insulation performance.

In this section, a multilayer TBC design based on equivalent thermal insulation performance is proposed, and for convenience, the unit thermal resistance (R_{UT}) as an intrinsic parameter to describe the thermal insulation performance of TBCs can be expressed as [355]:

$$R_{UT} = \frac{\delta_{tc}}{\lambda} \tag{17}$$

where δ_{tc} is the thickness of the ceramic top coat.

For multilayered TBCs, the ceramic layers are in a series system, and the R_{UT} of the multilayers is the sum of each layer. Hence the R_{UT} of the DCL LZO/YSZ coating can be expressed as [355]:

$$R_{UT} = \frac{\delta_{LZO}}{\lambda_{LZO}} + \frac{\delta_{YSZ}}{\lambda_{YSZ}} \tag{18}$$

According to the analysis above, there are at least three advantages if TBCs are designed based on the equivalent thermal insulation performance: (1) The stress of TBC system can be reduced at the initial preparation process under the premise of ensuring heat insulation function; (2) the service behavior and failure mechanism may be clarified under the same conditions of service environment (same bond coat temperature), which is beneficial for developing strategies to extend the TBC life span; (3) the waste of materials and cost in the preparation process can be reduced.

Two strategies are proposed for designing high-temperature and long life span TBCs, overall modulus reduction, and sublayer structure design for LZO layer on a 200 μm YSZ layer basis, and the thermal insulation performance of 500 μm YSZ (5Y) is set as a benchmark, as shown in Fig. 58. Liu *et al.* [159] obtained that the measurement results for the thermal conductivities of LZO coatings with high-modulus (70 GPa), middle-modulus (60 GPa), and low-modulus (50 GPa)

exhibit 0.74, 0.62, and 0.53 W·m⁻¹·K⁻¹, respectively. The thermal conductivity of YSZ coatings is 1.1 W·m⁻¹·K⁻¹. The above parameters are employed for designing the long life span TBCs, and high modulus (70 GPa), middle modulus (60 GPa), and low modulus (50 GPa) can be obtained by the precise control of the preparation process, such as spraying distance. Therefore, if the thermal insulation effect of 100 μm thick YSZ coating is defined as 1 unit, 67 μm high-modulus LZO, 57 μm high-modulus LZO, and 48 μm LZO low-modulus coating are exactly the same thermal insulation effect. According to the analysis above, one group of TBCs had similar thermal insulation performance based on overall modulus reduction design, namely, 5Y, 200 μm YSZ + 201 μm high-modulus LZO (3 high *E*, 3H), 200 μm YSZ + 171 μm middle-modulus LZO (3 middle *E*, 3M), and 200 μm YSZ + 144 μm low-modulus LZO (3 low *E*, 3L). Another group of TBCs with similar thermal insulation performance based on sublayer structure design, namely, different combinations of high- and low-modulus LZO, are

deposited on 200 μm YSZ surface. Specifically, they are named as three units (201 μm) high-modulus LZO (3H), 2 units high-modulus LZO (134 μm) + 1 unit (48 μm) low *E* LZO (2H/1L), and 1 unit (67 μm) high-modulus LZO + 2 unit (96 μm) low *E* LZO (1H/2L).

The fracture mechanics approach is often adopted to simulate crack propagation, in which the crack driving force characterized by SERR is computed to evaluate the cracking tendency. For a given finite element model, the total SERR (G_t) converges to a certain value, which can be obtained by using the virtual crack closure technique (VCCT):

$$G_t = G_I + G_{II} \tag{19}$$

where G_I and G_{II} are the SERR components.

Figure 59 shows the G_t ($G_I + G_{II}$) of the overall modulus reduction design, and the sublayer structure design when 0.3% strain was applied to the TBC. The SERR of 3H is as high as 28.2 N·m⁻¹. When the elastic modulus of the whole LZO layer decreased to 50 GPa, the SERR decreased to only 18.8 N·m⁻¹. For the

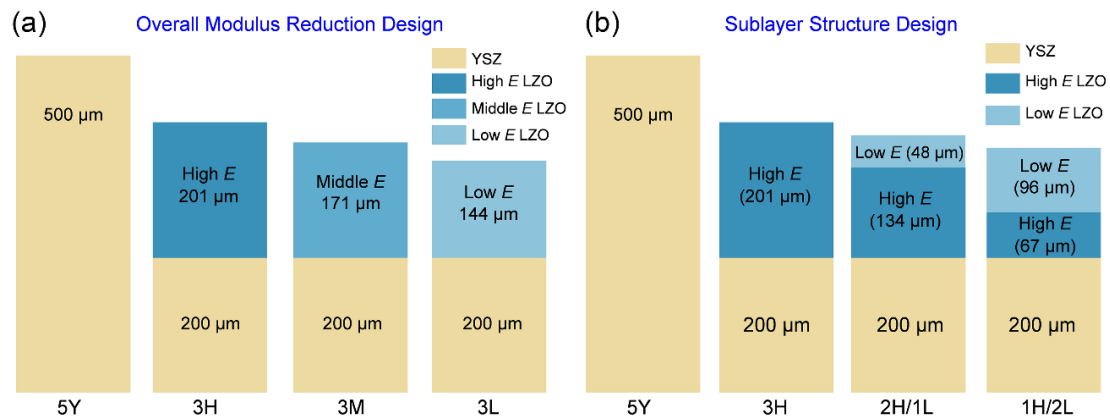**Fig. 58** Multilayer design for long life span TBCs: (a) overall modulus reduction design and (b) sublayer structure design. Reproduced with permission from Ref. [353], © Elsevier B.V. 2019; Ref. [354], © Elsevier Ltd. 2018.
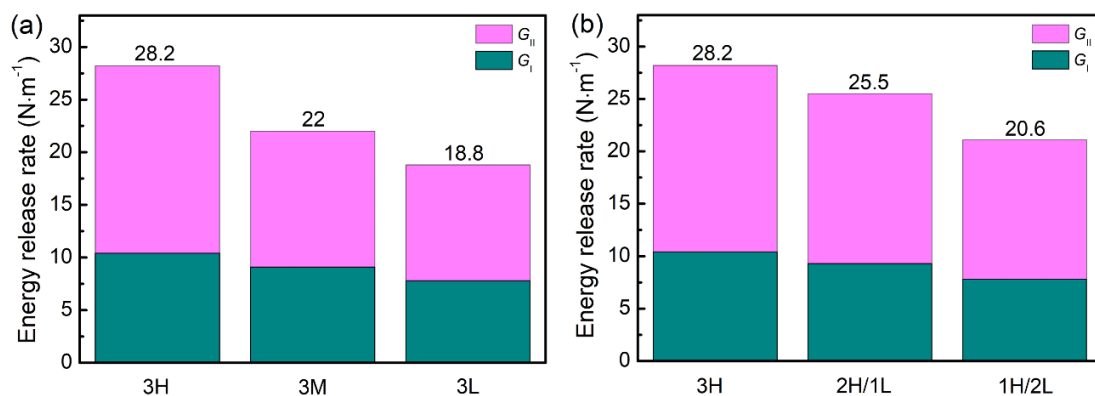

Fig. 59 Energy release rates under different designs: (a) overall modulus reduction design and (b) sublayer structure design. Reproduced with permission from Ref. [354], © Published by Elsevier Ltd. 2018.

sublayer structure design, the SERR G of 1H/2L TBCs is only 20.6 N·m^{-1}, which is far less than 28.2 N·m^{-1} of 3H TBCs. According to the accumulation of TBC failure mechanism, the 3L TBCs should have the longest thermal cycle life.

The above two groups of TBCs are successfully prepared by precisely controlling the spray distance from 70 to 145 mm, as shown in Fig. 60. The cross-sectional SEM images of long life span TBCs, Figs. 60(a)–60(d) are the overall modulus reduction design, and Figs. 60(e)–60(h) are the sublayer structure design.

To simulate the actual service condition, a gradient thermal cyclic test was performed with a gas burner. The surface of the TBCs was sustained at 1300±30 ℃, and at the same time, the backside temperature was kept at 940±30 ℃. The lifetime of TBCs was defined as the thermal cycle number when 10% area delamination of the ceramic top coat was observed. One thermal cycle is approximately 5 min. Figure 61 shows the lifetime of different groups of TBCs under thermal gradient cyclic test. The lifetime of single YSZ ceramic layer TBCs (5Y) is approximately 90 cycles, which is relatively low due to the thicker topcoat thickness of 500 μm combined with a higher surface temperature of 1300 ℃. When 300 μm YSZ was substituted with 201 μm high modulus LZO (3H), the lifetime was slightly beyond that of the single-layered YSZ coatings (5Y). With a further decrease in the substituted LZO elastic modulus, the lifetimes of 3M and 3L have increased to 111 and 206 cycles, respectively. For the sublayer structure design strategy, the lifetimes of 3H and 2H/1L are slightly higher than that of 5Y, which is approximately 100 cycles. The lifetime of 1H/2L is 50% higher than that of the single YSZ coatings. It is concluded from the above results that the lifetime of newly-designed TBCs in order from highest to lowest is: 5Y < 3H < 2H/1L < 3M < 1H/2L < 3L, which is the opposite of the energy release rate shown in Fig. 59.

Given the above fact, by maintaining the same
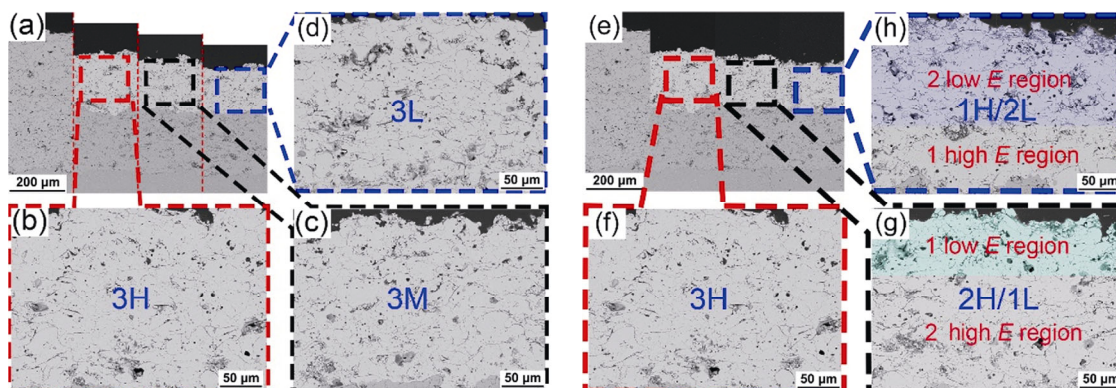
Fig. 60 Cross-sectional SEM images of long life span TBCs: (a–d) overall modulus reduction design and (e–h) sublayer structure design. Reproduced with permission from Ref. [353], © Elsevier B.V. 2019; Ref. [354], © Published by Elsevier Ltd. 2018.
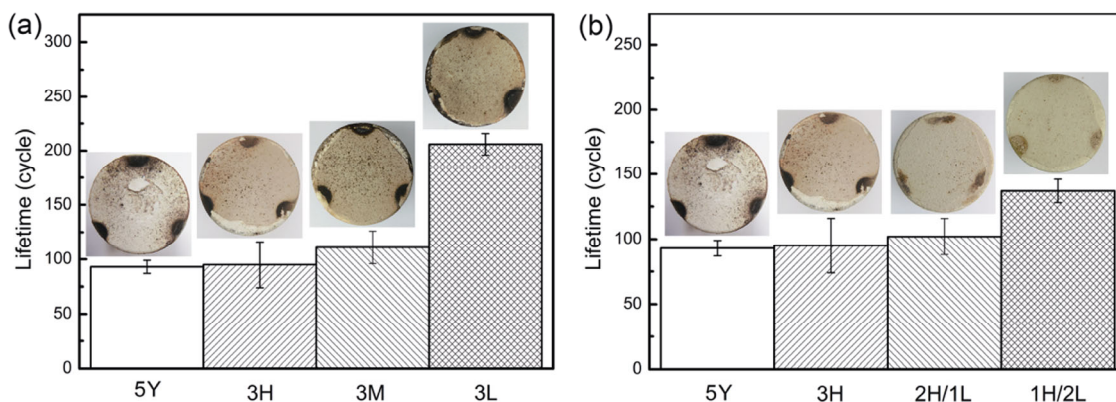

Fig. 61 Lifetime of newly designed TBCs under gradient thermal cyclic tests: (a) overall modulus reduction design and (b) sublayer structure design. Reproduced with permission from Ref. [353], © Elsevier B.V. 2019; Ref. [354], © Published by Elsevier Ltd. 2018.

thermal insulation function, further reducing total top coat thickness is an important future research direction.

4.1.2 Micro-lamellae/nano-zone bimodal design

Except for the lamellar structure of the plasma-sprayed ceramic top coat, the inclusion of specially designed nano-zone is a recently-reported strategy to improve the performance of TBCs. For typical plasma-sprayed top coat, spherical and disk-shaped pores (intra-splat cracks and inter-splat pores) have different types of effects on the thermal insulation of coatings. Disk-shaped pores with radial axes parallel to the substrate lead to a reduction in thermal conductivity, whereas the effect is the smallest when pores are perpendicular to the substrate [365]. As expected, the relative effect of spherical and randomly-oriented disk-shaped pores lies between the relative effect of intra-splat cracks and inter-splat pores.

Furthermore, pore aspect ratios play a significant role in the thermal insulation performance of TBCs [366,367]. Dutton *et al*. [368] found that if the volume fraction of pores was constant, but their aspect ratios changed from 500 to 20, there would be a fourfold increase in the thermal conductivity. Arai *et al*. [369] investigated the influence of pore aspect ratios on thermal conductivity with the help of the SEM-based finite element model. The results demonstrate that the thermal conductivity increases by 30% as the pore aspect ratios decrease from 5 to 2. Zhang *et al*. [365] developed a new model including inter-splat pores and intra-splat crack to investigate the effect of pore aspect ratios on thermal insulation performance. It was found that the coatings with a large-pore aspect ratio exhibited stronger thermal insulation. In detail, the pores in TBCs can interrupt thermal flux because the thermal resistance of pores is much larger than that of YSZ. The thermal conductivity of the air in the pores ($\sim$0.025 W·m^{-1}·K^{-1}) is merely 1% that of the YSZ bulk ($\sim$2.5 W·m^{-1}·K^{-1}). Consequently, the thermal flux

vector at the center of the pores passes through the pores directly, while it deviates somewhat from the original path and passes through the contact matrix areas near the edge of the pores. This means that the edges of the pores cannot block thermal transfer. Based on the thermal flux vector distributions, the pores can be divided into effective and invalid parts [365]. The effective normalized area is defined as the ratio of the effective area to the total area of the pore. As the aspect ratio increases, the normalized effective area increases, and the normalized thermal conductivity decreases (Fig. 62). This can be attributed to the larger effective areas of the pores.

Even more noteworthy is that a higher aspect ratio means better thermal insulation performance. It is important to insert pores with larger aspect ratios into coatings to effectively lower the thermal conductivity of the coatings [365]. Nanoparticles have a larger specific surface area and longer interfaces than other particles. For example, almost 50 vol% of the atoms are located at the interface when the crystal grain diameter is 10–20 nm [370]. Eventually, compared to micron particles, the nano-powder had a lower sintering activation energy and a faster sintering rate. Therefore, if the large aspect ratio nano-zones are used, numerous new pores with a large aspect ratio will appear at elevated temperatures in the form of interfacial openings between the micro-lamella zones and nano-zones [13].

The insertion of nano-zones into conventional coatings is challenging. For instance, the injection of fine particles into the core of high-enthalpy flow is quite difficult [371]. Generally, vapor deposition techniques, solution reduction techniques, and particle deposition techniques are mainly utilized to realize nano-structure features [372]. Racek *et al*. [373] used the APS method to prepare layers of nanostructured YSZ. Zhou *et al*. [374] prepared nanostructured TBCs using APS and found that they exhibited excellent
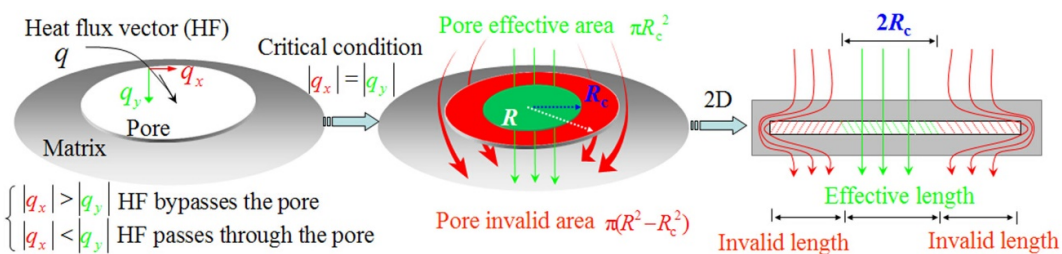

Fig. 62 Schematics describing the effective and invalid parts of the pore. Reproduced with permission from Ref. [365], © ASM International 2017.

thermal cycling resistance and low thermal diffusivity. Jordan *et al*. [375] used the solution precursor plasma spray (SPPS) process to create bimodal YSZ coatings. The APS–SPS method can spray powders and generate a suspension simultaneously. It can control the distribution of nano-zones by adjusting the input of particles and suspensions. The APS–SPS method was originally proposed by Skoog *et al*. [376]. Cipri *et al*. [377] used the APS–SPS method to prepare nanostructured material along with temperature-sensitive/ low melting point materials, such as solid lubricants, semiconducting oxides, or polymers. Joshi and Sivakumar [378] systematically studied the spraying mechanism of APS–SPS and deposited dual-mode YSZ, Mo alloy (Mo–NiCrBSiFe–NiAlMo)–YSZ, NiCoCrAlY–YSZ, and YSZ–Gd$_2$Zr$_2$O$_7$ coatings.

Figure 63(a) shows a schematic illustration of the co-spraying setup with a suspension and solid powders [13]. The co-spraying setup is formed by adding a suspension nozzle to a conventional APS spraying device. micro-lamella/nano-zone bimodal coatings comprising both dense and loose regions can be realized by the alternate control of the powder and suspension (Fig. 63(b)). As the bimodal coatings are built up by the stacking of layers from the multiple single-scans, the two distinguished structures may be formed by single-solution or single-particle steps. The loose zones represent the porous nano-particle heaps embedded in the coating microstructure during thermal spraying by a single-solution step. The dense zones composed of columnar grain structures represent the previously molten lamellar YSZ particles that form the matrix of the coating microstructure by a single-particle step. It is worth noting that the dense and loose regions of APS bimodal coatings are formed by porous nanostructure agglomerated powders that are fully molten or semi-molten in the spray jet (Fig. 63(c)) [379]. SPS comes from melting and solidification or not melting nanostructure suspension agglomerates (Fig. 63(d)) [380].

The bimodal coatings consist of alternating dense and loose zones, which correspond to melted layered splats and nano-zones, respectively. The sintering rate varies greatly between the micron- and nano-zones. As a result, two kinds of shrinkages are exhibited at both the global and local scales under thermal exposure. The continuously distributed micron splats shrink over the entire coating scale, while the nano-zones scattered therein undergo local shrinkage. Therefore, at elevated temperatures, numerous new pores will appear in the form of interfacial openings between the nano-zones and matrix (Fig. 64) [381].

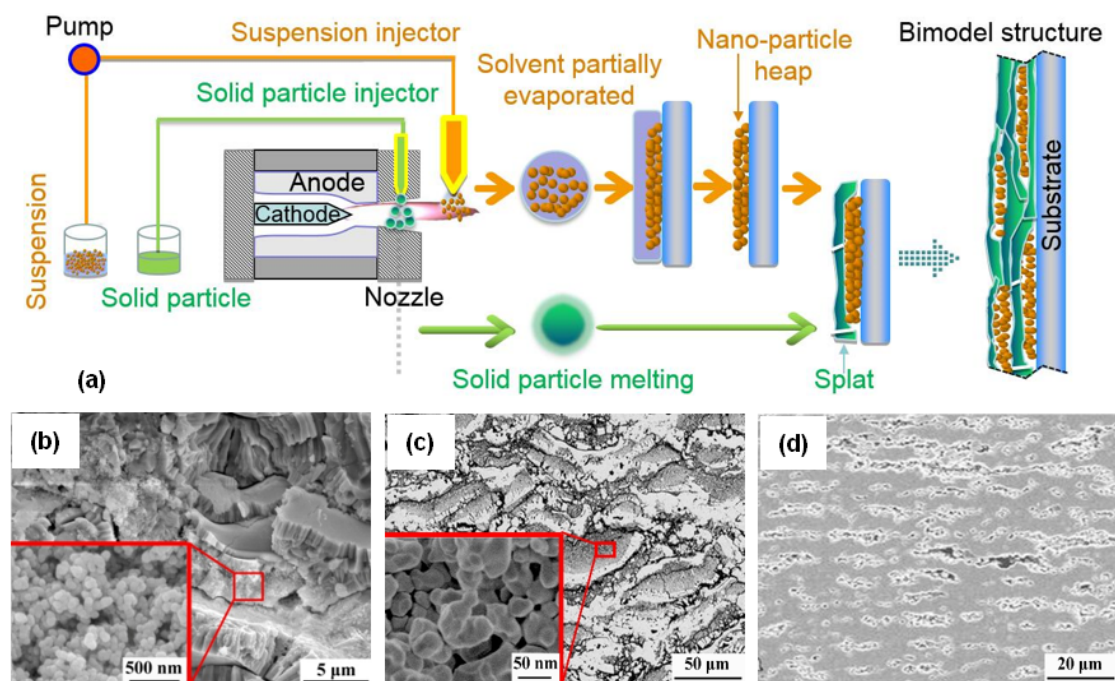**Fig. 63** Preparation process and microstructures of the bimodal coatings: (a) schematic demonstration of the plasma co-spraying with suspension and solid powder. (b–d) Morphologies of micro-lamellae/nano-zone bimodal coatings. Reproduced with permission from Ref. [13] for (a, b), © ASM International 2018; Ref. [379] for (c), © ASM International 2008; and Ref. [375] for (d), © ASM International 2014.
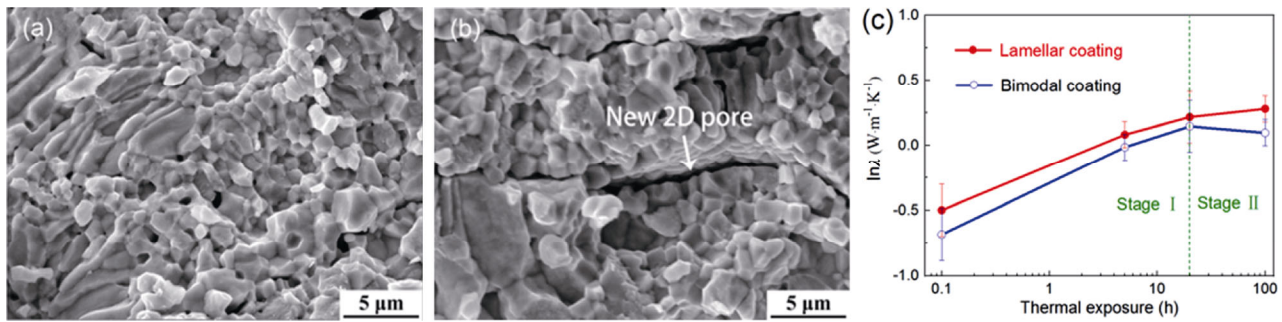
Fig. 64 Microstructure morphologies and thermal conductivities of the coatings: (a) morphologies of lamellae, (b) micro-lamella/nano-zone bimodal coatings that had been heat-treated at 1400 ℃ for 100 h, and (c) lnλ as a function of thermal exposure time. Reproduced with permission from Ref. [13], © ASM International 2018.

Figure 65 shows a schematic diagram of the different sintering mechanisms for the two kinds of coatings. (1) For the lamella coating, the increase in the thermal property at the initial thermal exposure duration (Stage I) was much faster with respect to that in the following longer duration (Stage II). At Stage I, the *in-situ* pore healing behavior revealed that the significantly faster sintering kinetics were attributed to the rapid healing induced by multipoint connection at the inter-splat pore tips, as well as a small quantity of narrow intra-splat cracks. In the following Stage II, the residual wide inter-splat pore parts and the wide intra-splat cracks decreased the possibility of multi-connection at their counter-surfaces, resulting in much lower sintering kinetics [160]. (2) For bimodal coating, an ultrafast increase in thermal conductivity occurs during an initial short thermal exposure (Stage I), and then the thermal conductivity begins to decline after long

thermal exposure (Stage II). In Stage I, a large number of pores are healed, and nanoparticle heaps are sintered together. In the following Stage II, the much lower activation energy of the nano-heaps causes a higher sintering-induced densification rate compared to the lamellar zones. The effect of the disappearance of the micro-pores is counteracted by the creation of openings between the lamellar zones and the nano-zones. Consequently, when the duration of thermal exposure is lengthened, a decline in thermal conductivity is observed [382].

For TBC applications, the micro-lamella/nano-zone bimodal coatings will reduce the increase in thermal conductivity significantly when exposed at high temperatures by counteracting densification effects via differential sintering. However, whether the newly-formed pores degrade the cracking resistance of the top coat needs further investigation.
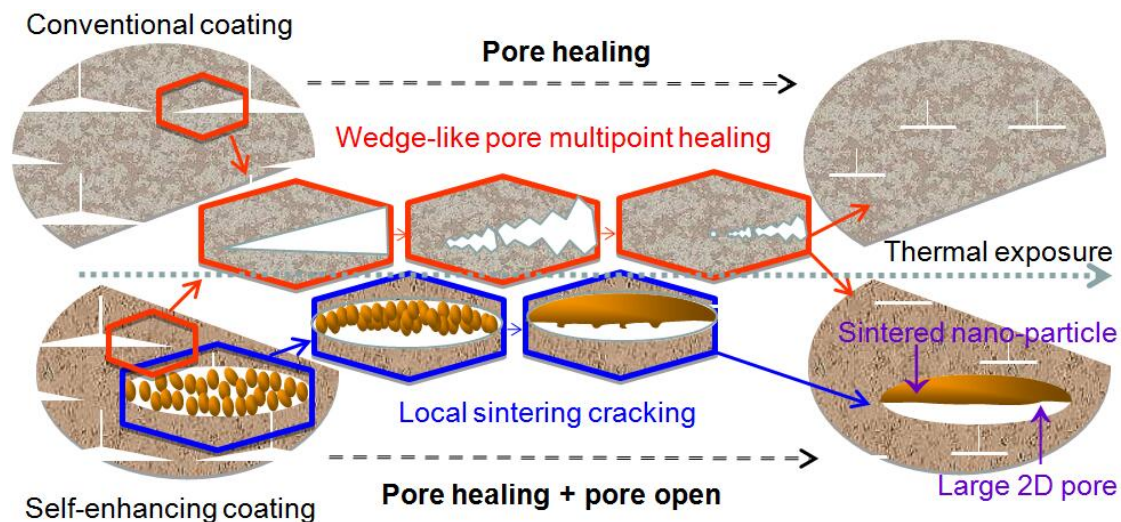

Fig. 65 Schematic diagram of sintering mechanisms of the conventional and self-enhancing coatings undergoing thermal exposure. Reproduced with permission from Ref. [383], © The Nonferrous Metals Society of China and Springer-Verlag GmbH Germany, part of Springer Nature 2020.

4. 2 Columnar structure design

4.2.1 SPS/SPPS

Columnar-structured TBCs have drawn significant attention due to their high strain tolerance and elevated thermal cycling life. Columnar-structured TBCs are commonly fabricated by the EB-PVD and PS-PVD processes, whereas the two processes face many limitations such as high equipment cost and restricted deposition space. SPS and SPPS are two processes using suspension and solution as feedstocks, respectively, and they are capable of rapidly depositing finely-structured coatings on large areas [384]. The use of liquid feedstocks allows the control of coating structures at sub-micron and nanometer-sized scales, thereby enabling the deposition of columnar-structured coatings. By tailoring the process parameters, columnar-structured TBCs with high porosity can be deposited via the SPS and SPPS processes, showing excellent thermal insulation capability and thermal cycling performance.

The deposition of columnar-structured TBCs via the SPS and SPPS processes has been extensively reported, especially for the SPS process. Suspension is used as the feedstock in the SPS process and is prepared by dispersing the submicron-/nanometer-sized particles into the solvent, which is generally water, ethanol, or a mixture of both. Dispersants are usually needed as additives to alleviate the agglomeration of fine particles and to alter the rheological properties of the suspension.

The SPS process is shown schematically in Fig. 66. The suspension is delivered by the pneumatic pump system or peristaltic pump system and injected into the plasma by mechanical injection or atomization injection.

The suspension has complex interactions with the plasma jet, as shown schematically in Fig. 66. When the suspension stream is injected into the plasma jet, it experiences a drastic aerodynamic breakup process due to the huge velocity difference between the suspension and plasma, resulting in numerous fine droplets. Fine particles inside the suspension agglomerate with solvent evaporation, which are further sintered and melted. Then the melted particles impact the substrate, accumulate, and gradually form coatings [384]. Different kinds of deposits can be formed depending on the behaviors of in-flight suspension droplets, which result in various microstructures upon impingement.

As the in-flight particles formed in the SPS process are extremely small, their motion is more readily affected by the plasma gas flow. When the plasma encounters the substrate or previously deposited coating, the gas flow is diverted to become parallel to the surface, forming a boundary layer. The in-flight particles can be deviated by the plasma flow in the vicinity of the substrate, as shown in Fig. 67(a). The large particles have enough inertia to penetrate the boundary layer and impinge on the surface orthogonally, whereas the small particles with low inertia tend to follow the diverted gas flow and impinge obliquely on
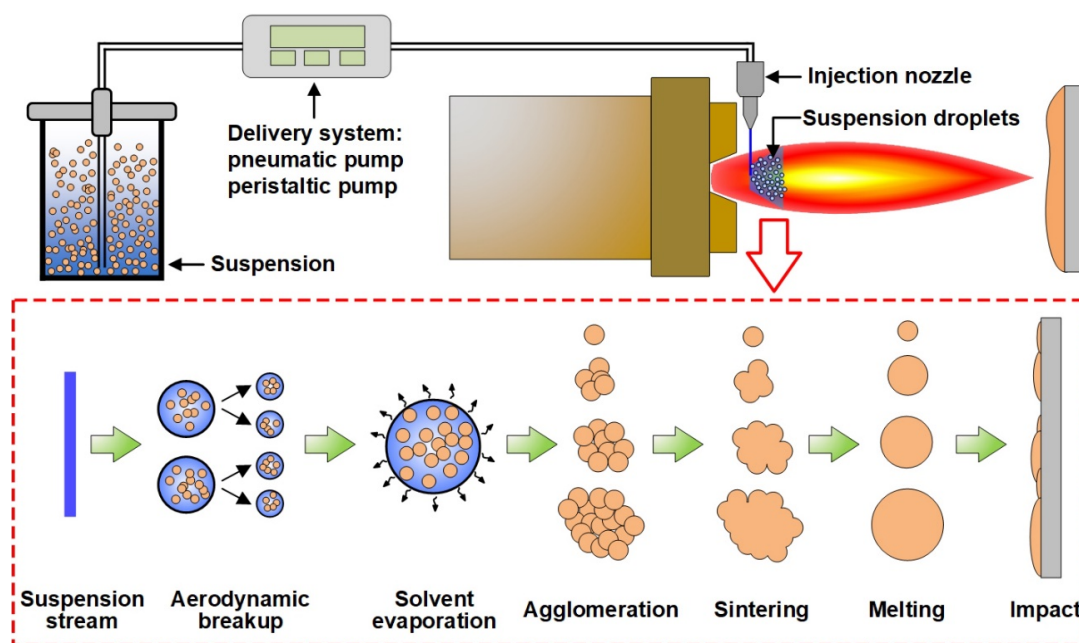

Fig. 66 Schematics of the SPS process and the interactions between suspension and plasma.
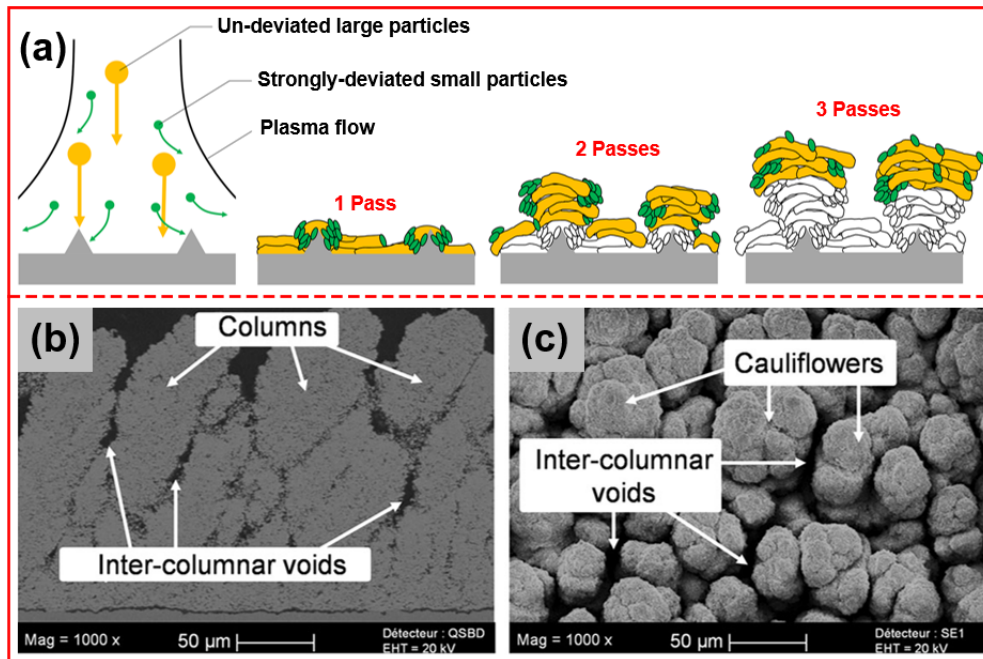
Fig. 67 Preparation process and microstructures of the SPS coating: (a) schematic of the formation of columnar structures in the SPS process and (b, c) representative columnar-structured YSZ coatings. Reproduced with permission from Ref. [385], © ASM International 2017.

the protrusions of the surface. In this way, columnar structures are formed gradually and shade the subsequent in-flight particles from impinging on the areas below the columns, which is referred to as the shadowing effect [385]. The typical microstructures of columnar-structured TBCs are shown in Figs. 67(b) and 67(c). The cross-section shows micron-sized columns with inter-columnar voids, and the top surface shows cauliflower structures.

The suspension properties, deposition parameters, and surface roughness are the main factors governing the formation of different columnar structures in the SPS process. Curry *et al*. [386] systematically investigated the effects of suspension properties, including solvent type, solid loading, and particle size, on the formation of coating microstructures. The results showed that using water solvent and large solid loading produced large droplets, which were less affected by the diverted plasma flow and formed vertically-cracked coatings upon impingement. In contrast, using ethanol solvent and small solid loading contributed to the formation of smaller droplets, which resulted in columnar structures.

The deposition parameters have significant effects on the aerodynamic breakup process of suspension and the heating/acceleration history of the droplets, which thereby results in different microstructures. Ganvir *et al*. [387] showed that different coating microstructures

could be obtained by tailoring the deposition parameters. When a low torch power, small plasma gas flow rate, and large suspension feed rate were used, the aerodynamic breakup was weakened, and the droplets were insufficiently heated, resulting in porous coatings without apparent columnar structures. In contrast, when high power, a large plasma gas flow rate, and a low suspension feed rate were applied, the suspension was atomized sufficiently, which were subsequently well heated. These small-melted particles formed feathery-like columnar structures upon impingement.

The protrusions on the surface where the ceramic top coat is deposited serve as effective sites for the formation of columns, indicating that the surface roughness is a critical factor affecting the formation of columnar structures in the SPS process. Sokolowski *et al*. [388] showed that high surface roughness facilitated the formation of columnar structures by comparing the deposition of YSZ coatings on substrates prepared by grit blasting, laser treatment, turning, and grinding. Zhou *et al*. [389] reported that the YSZ coatings deposited via the SPS process transitioned from vertically cracked microstructures to mixed crack/column microstructures and to columnar microstructures with increasing the bond coat roughness.

The thermal conductivity of columnar-structured SPS TBCs is not only dependent on the porosity but

also on the columnar morphologies, as the inter-column gaps can act as pathways for the hot gas ingress. The YSZ coatings with well-separated columns generally show higher thermal conductivity than the coatings with densely packed columns with comparable porosity. The thermal conductivities of some representative columnar-structured SPS YSZ coatings are summarized in Table 6.

The thermal cycling performance of columnar-structured SPS TBCs is dependent on many factors, including the column morphologies, top coat materials and microstructures, bond coat, etc. The thermal cycling life of columnar-structured coatings is significantly elevated, although the reported lifespan varies dramatically among different researchers. The thermo-cyclic fatigue life and thermal shock life reached approximately 2150 and 10,000 cycles, as reported by Bernard *et al.* [385] and Curry *et al.* [390], respectively. The columnar-structured TBCs show dramatic microstructural changes during long-term high-temperature exposure. The inter-column spacing of coatings is enlarged due to the severe sintering process, resulting in the formation of vertical cracks and the merging of narrow columns [391]. The pores within the columns show different changes depending on their size. The number of coarse pores usually increases due to the enlargement of inter-column spacing and pore coalescence, whereas the fine pores tend to disappear due to densification during thermal exposure. The microstructural change can thereby facilitate the ingress of hot gas, accelerate the oxidation of the bond coat, and reduce the thermal cycling life.

In brief, with good strain tolerance, more attention should be given to the relatively low cohesion within the SPS/SPPS ceramic top coat. Improving the coating cohesion will help to further prolong the coating lifetime.

4.2.2 Electron beam-physical vapor deposition

In the 1930s, the combination of electron beam technology and physical vapor deposition technology

was used to prepare various optical and microelectronic films, which marked the beginning of EB-PVD technology from research to industrial application [392]. In the early 1980s, EB-PVD technology was adopted in the laboratory to obtain high-quality TBCs with good repeatability. In the 1990s, some companies began to use the EB-PVD process to prepare TBCs on rotor blades of aero-turbine engines.

EB-PVD was developed from vacuum evaporation technology and is widely used in coating materials. The principle of this process is that the cathode heats up and emits a large number of electrons, which are accelerated in a high-voltage electrostatic field, and then focused by a focusing system to form an electron beam with extremely high energy density. The electron beam deflects by the action of the electromagnetic field, bombards the surface of the target material to heat the material to be evaporated to a molten and evaporated state, and condenses on the surface of the substrate to form a coating [11].

At present, the most widely-used methods for preparing TBCs are plasma spraying and EB-PVD. Due to the difference in deposition principle, EB-PVD coating and plasma spray coating have completely different microstructures. EB-PVD first forms a layer of fine equiaxed crystals on the substrate, and then forms texture and columnar crystals on it, as shown in Fig. 68 [6].

The deposited film consists of columnar crystals growing perpendicular to the substrate and separated from each other, which can deflect the crack propagation parallel to the substrate. SEM observation shows that the columnar crystallites in TBCs prepared by EB-PVD method contain a large number of nano-scale structural defects, and the surface of columnar crystals is not smooth and presents a feather-like structure [393,394]. Columnar crystallites contain tiny but numerous pores,

Table 6 Thermal conductivities of SPS TBCs with different column morphologies at 1200 ℃ [387]

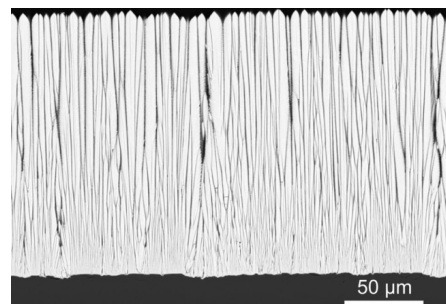| Coatings with different column morphologies	Thermal conductivity (W·m⁻¹·K⁻¹)
Dense compact columns	1.99
Dense feathery-like columns	1.45
Porous feathery-like columns	1.04

Fig. 68 Cross-sectional microstructure of EB-PVD coatings. Reproduced with permission from Ref. [6], © The Author(s) 2021.

which agglomerate when heated. The columnar crystal structure can significantly improve the strain tolerance of the coating and the thermal shock resistance of the coating. However, compared with the films deposited by APS, the films prepared by EB-PVD have higher overall thermal conductivities and poorer thermal shielding performance. The columnar microstructure of EB-PVD TBC was modified with controlled microporosity and diffuse sub-interfaces (Fig. 69), which can lead to lower (20%–30% depending up on microporosity volume fraction) thermal conductivity, higher (15%–20%) thermal reflectance, and more strain tolerance compared with standard TBC [395].

It is generally acknowledged that the thermal shock life of EB-PVD coating is much longer than that of APS coating due to high strain tolerance. The failures of both TBCs usually occur at or near the TBC/TGO or TGO/bond coat interfaces due to the strong influence of oxidation of the bond coats on TBC failure. The APS TBCs are more susceptible to failure out in the TBC away from the TBC/TGO interface due to the presence of splat boundaries in the TBCs [396]. It is reported that the double ceramic coating by EB-PVD exhibits a higher thermal cycling lifetime. Shen *et al.* [397] prepared the LaZrCeO/YSZ double ceramic layers (LZC/YSZ DCL) TBCs by EB-PVD technology. The thermal lifetimes of the three coatings (LZC, YSZ, and LZC/YSZ) were investigated under the same conditions. The thermal shock and the thermal cycling fatigue life of the LZC/YSZ DCL TBCs at 1100 ℃ are 13,508 and 1132 cycles, respectively. The LZC/YSZ DCL coatings have the longest lifetime compared with the single layer coating.

As a result, due to the dense structure and high thermal conductivity, EB-PVD top coat is suitable for rotating blades which need extremely high strain tolerance. The possibility of reducing the thermal conductivity of EB-PVD top coat needs further investigation.

4.2.3 PS-PVD

PS-PVD is a unique technology based on the combination of PS and PVD [398–400]. The feedstock powders will be melted [401] and even be gasified [9,398,402] because the input power of PS-PVD can be as high as ~120 kW, and a low operating pressure (50–200 Pa) is used. Therefore, PS-PVD bridges the gap between conventional thermal spray and vapor deposition and provides a variety of coating microstructures composed of vapor, liquid, and solid deposition units, such as layered coatings, columnar coatings, and layer/pillar hybrid structure coatings [403], which has attracted wide attention from experts from all over the world.

PS-PVD technology is rapidly developed based on low-pressure plasma spraying technology (LPPS) [404,405]. Figure 70 shows the plasma jet images of the three coating preparation technologies of APS, LPPS, and PS-PVD [8]. It is obvious that PS-PVD jet is obviously elongated and thickened due to the extremely low operating pressure.

At present, the regulation of the preparation process and coating structure is the main work of PS-PVD. The relationships among the coating structure and operating parameters, the coating properties, and the coating structure have been studied. With the efforts of many researchers, PS-PVD mechanism has gradually become clearer.

In the following, the material's footprint in PS-PVD is traced, and the mechanism of PS-PVD for preparing high thermal insulation and long-life columnar structure
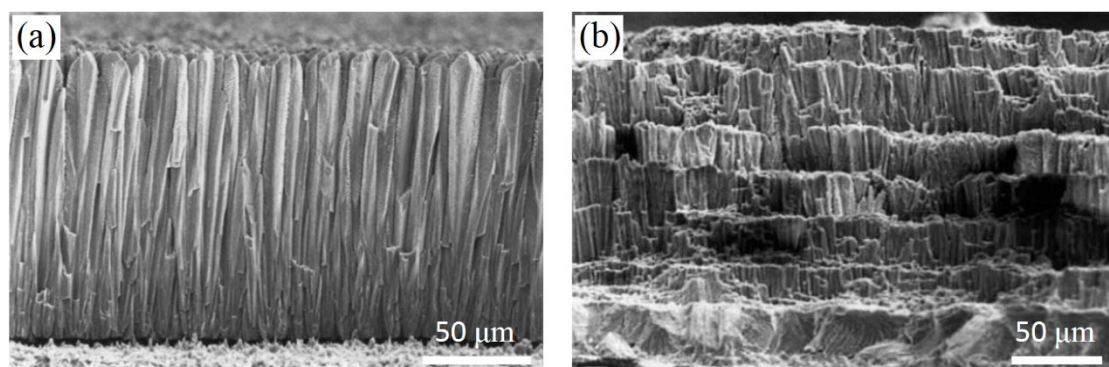

Fig. 69   SEM micrographs showing fracture surfaces of 8YSZ produced by EB-PVD using two different approaches: (a) "shutter" method and (b) "in & out" method. Reproduced with permission from Ref. [395], © Kluwer Academic Publishers 2004.
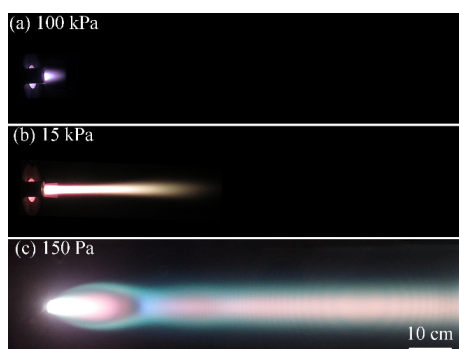
Fig. 70 Images of PS-PVD plasma jets expanding at different pressures: (a) 100 kPa (APS), (b) 15 kPa (LPPS), and (c) 150 Pa (PS-PVD). Reproduced with permission from Ref. [8], © The Nonferrous Metals Society of China and Springer-Verlag GmbH Germany, part of Springer Nature 2020.

Fig. 71 YSZ powder for PS-PVD. Reproduced with permission from Ref. [407], © Elsevier B.V. 2015.

coatings is introduced. In view of the transport and transformation behavior of the deposition units and the deposition mechanism, PS-PVD process can be divided into three steps [406]: (1) heating behavior of the material in the nozzle, (2) material transport and state change in plasma jet, and (3) the coating formation.

A typical powder for PS-PVD with a powder particle size of 5–22 μm is shown in Fig. 71 [406,407]. The results by Mauer [408] pointed out that the heat flux in the O3CP torch is as high as 10^8 W·m^{-2}. When applying Ar/He mixed gases, the enthalpy transferred from the plasma to the material powders is sufficient to evaporate particles of up to 0.92 μm in diameter, as shown in Fig. 72(a). Furthermore, the heat transfer between the plasma and powder particles at different input powers was theoretically studied [409], as shown in Fig. 72(b). The results indicated that at a power level

of 60 kW and above, particles smaller than ~1.5 μm can be fully evaporated.

After heat exchange in the nozzle, the materials exit the nozzle together with the high temperature and high-pressure plasma gas. The plasma jet can be enlarged to 1000–2000 mm in length and 20–40 mm in diameter due to the reduced pressure compared to the atmospheric conditions. Under this special plasma jet condition, whether the molten particles or the vapor materials, their state changes must be different from those of the conventional plasma spray. The state variation of liquid and gas phases in PS-PVD jet based on the plasma jet characteristics detected by optical emission spectroscopy (OES) was investigated [410–412]. The results show that molten ZrO_2 with a diameter of < 0.28 μm can be completely evaporated within a spray distance of 450 mm, as shown in Fig. 73. In addition, the maximum vapor material content that can be thermodynamically allowed to exist anywhere in the plasma jet was obtained, as shown in Fig. 74. The
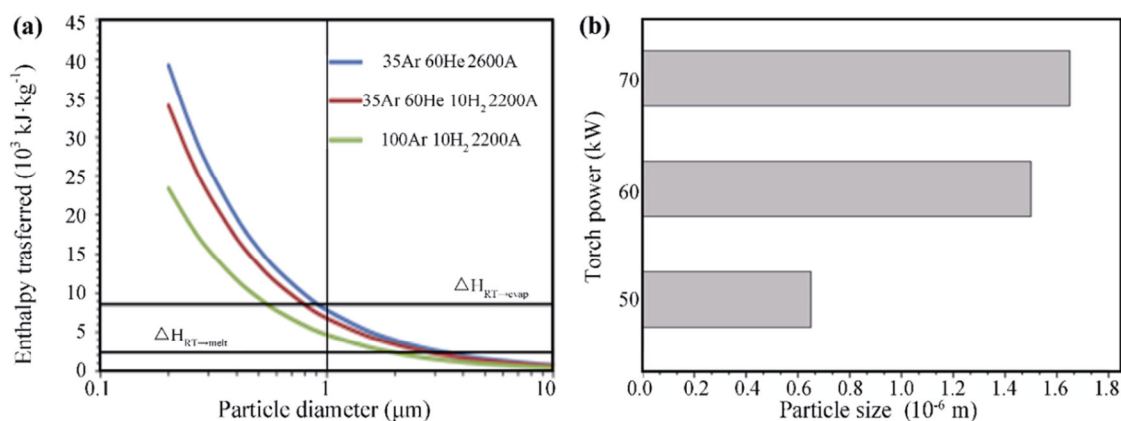
Fig. 72 Results of heat transfer calculations in torch nozzle: (a) enthalpy transferred to spherical particles as a function of particle diameter (all results for three investigated plasma parameters: 35Ar 60He 2600A, 35Ar 60He 10H$_2$ 2200A, and 100Ar 10H$_2$ 2200A) and (b) effect of power on evaporated particle size. Reproduced with permission from Ref. [408] for (a), © Springer Science+Business Media New York 2014; Ref. [409] for (b), © ASM International 2017.
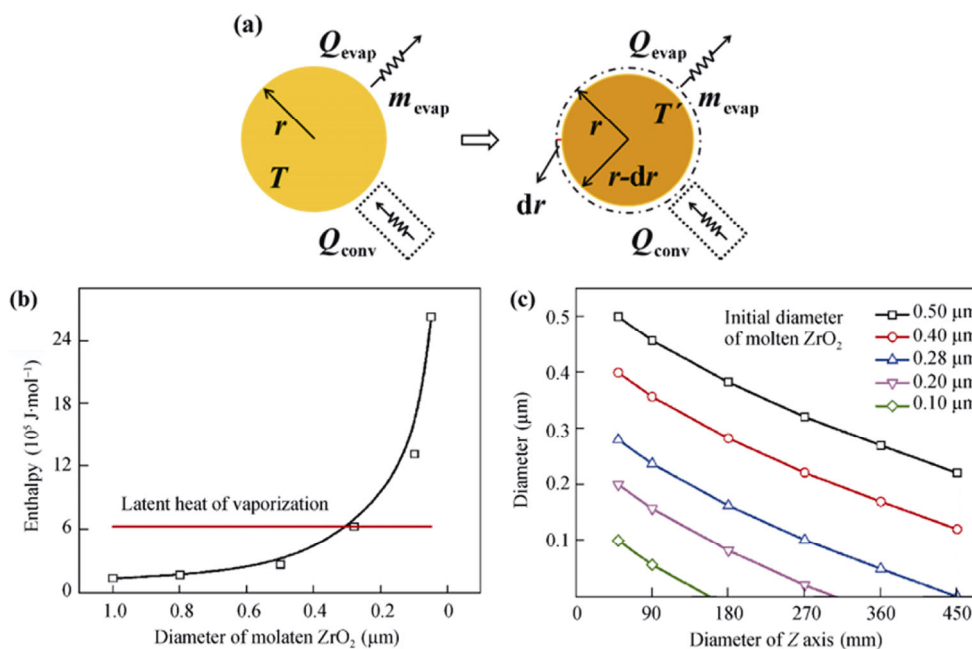
Fig. 73 Evaporation of molten ZrO_2 in plasma jet: (a) evaporation model of molten ZrO_2 in plasma jet. Here, Q_{evap} is the heat taken away by evaporation; r is the initial size of the molten ZrO_2; T is the initial temperature of molten ZrO_2; m_{conv} is the vaporized mass of molten ZrO_2; Q_{conv} is the heat transfer by the plasma jet; and T' is the temperature of residual molten ZrO_2. Enthalpy transferred from plasma jet to molten ZrO_2 as a function of (b) diameter and (c) change in molten ZrO_2 size along spray distance. Reproduced with permission from Ref. [410], © ASM International 2017.
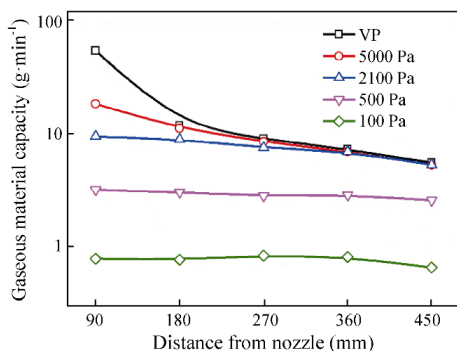
Fig. 74 Thermodynamic carrying capacities of the plasma jet. VP represents the vapor pressure of ZrO_2. Reproduced with permission from Ref. [411], © Elsevier B.V. 2017.

results indicate that both plasma temperature and operating pressure restrict the state of the vapor material in the plasma jet. More importantly, the boundary layer near the substrate is an important position for the state variation of gas phases, as shown in Fig. 75, and the gas phase is more likely to form into clusters when it is closer to the substrate and the edge of the plasma jet [413].

PS-PVD has received extensive attention due to its strong vapor deposition ability. Although the deposition mechanism of PS-PVD has been studied by coating morphology and classical nucleation theory, the vapor deposition mechanism of PS-PVD is still not available.
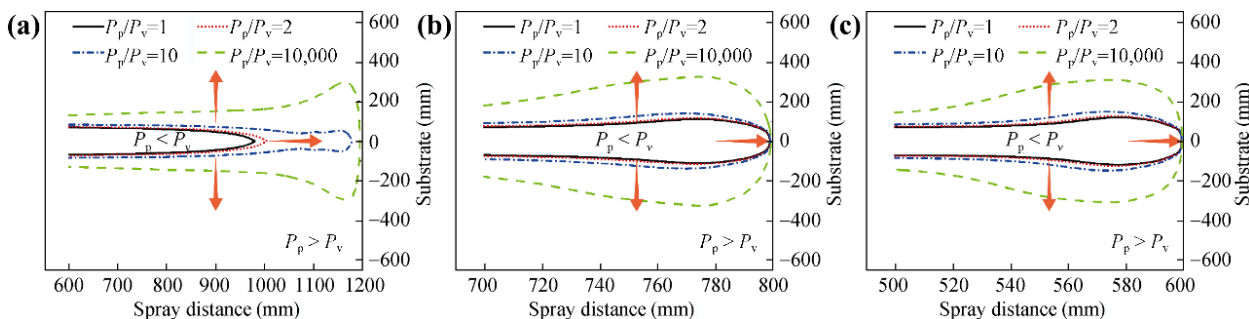
Fig. 75 Effects of spraying distances on boundary layer with spraying distance (SD): (a) 1200 mm, (b) 800 mm, and (c) 600 mm (the red arrows represent the increasing trend of supersaturation with a powder feed rate of 20 g·min^{-1}). Reproduced with permission from Ref. [413], © Elsevier B.V. 2018.

A microscopic line-of-sight deposition model of PS-PVD vapor deposition is proposed, as shown in Fig. 76 [414].

Based on this model, the Monte Carlo method is used to simulate the microscopic line-of-sight deposition behavior of vapor materials. The deposition process
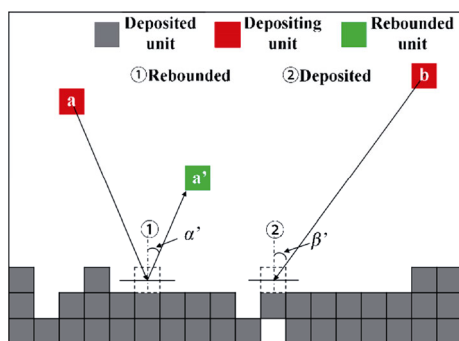
Fig. 76 Vapor ballistic deposition (VBD) model. Reproduced with permission from Ref. [414], © Published by Elsevier B.V. 2019.

and simulation results are compared with the actual coating, and the results are shown in Fig. 77 [414]. By comparing the simulation with the actual coating structure, it can be seen that the coating has a columnar structure. Because the simulation process does not consider the diffusion on the coating structure, the actual coating structure is denser than the simulation result. Figures 77(a)–77(d) are schematic diagrams of the vapor deposition process. It can be seen that in the initial stage of deposition, the substrate surface began to fluctuate, from smooth to rough, and further deposition, the columnar structure began to appear. As the deposition continued, the columnar structure continued to grow.

In short, PS-PVD top coat possesses the advantages of both APS lamellar top coat and EB-PVD columnar top coat. However, the erosion resistance of this coating limits long lifetime. Increasing the hardness and particle erosion resistance is a key point in future development.

Fig. 77 Structure development of coating: (a) rapid formation of rough fluctuations, (b) formation of initial columnar structures, (c) coating growth, (d) final coating with feather-like columnar structures, (e) polished section of coating, and (f) cross-section morphology of fractured coating. Reproduced with permission from Ref. [414], © Published by Elsevier B.V. 2019.

4. 3   TBCs with nanostructure inclusion

If unmelted parts of nanostructured power particles are included in the top coat during coating deposition, a TBC with nanostructure inclusions will be produced.

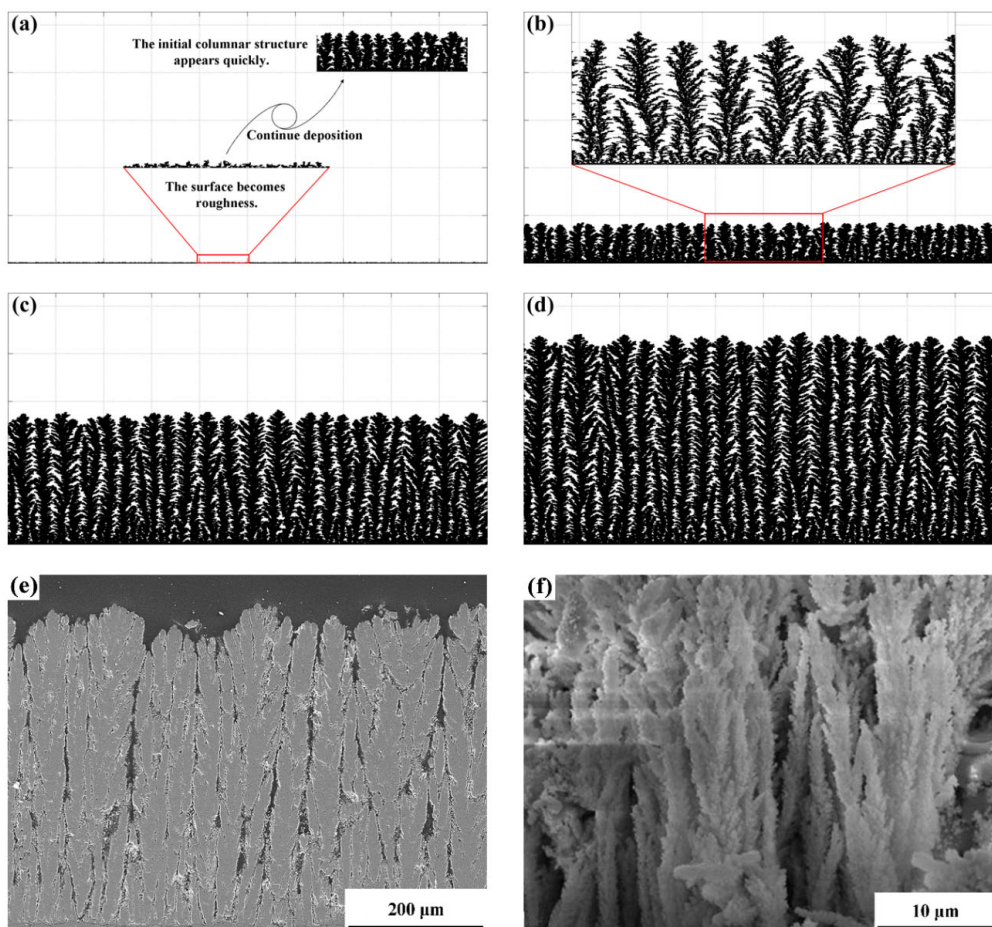It is known that the mechanical performance of materials (hardness, strength, ductility, and toughness) can be significantly improved when the grain size can be reduced from microscale to nanoscale (i.e., < 100 nm) [415–417]. Therefore, nanostructured TBCs have emerged as a potential choice to resist sintering-induced degradation during thermal service [418–421]. Nanostructured TBCs appear to have a bimodal structure, which means that the nanozones are often embedded in the lamellar zones, as shown in Fig. 78 [421].

A major challenge is how to retain the nanostructured feature in TBCs. In conventional plasma spraying, power particles are mainly fully melted and impacted on a substrate followed by lateral flattening, rapid solidification, and cooling [112,422]. However, the fully molten nanostructured powders will undergo solidification, nucleation, and growth, which is similar to the conventional behavior [423]. As a result, the coating will exhibit a typical lamellar structure [112,151]. This suggests that the fully molten particles are often
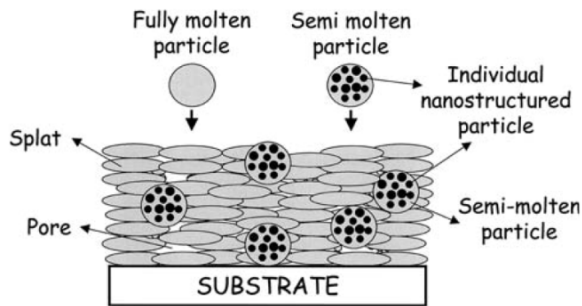
Fig. 78   Typical schematic of nanostructured TBCs with a bimodal structure. Reproduced with permission from Ref. [421], © ASM International 2007.

deleterious to the original nanoscale powders. Thus, it is necessary to retain the unmolten zones to inherit the desired properties. Therefore, nanostructured TBCs should be sprayed in a special state in which partially molten and fully molten particles co-exist. Figure 79 shows the structure of nanostructured TBCs [379]. The fully molten particles form a lamellar structure, which acts as the matrix of the coating to provide sufficient particle adhesion and cohesion. In contrast, the nanozones can be retained due to the partially molten particles. The nanozones are embedded into the lamellar zones, which can be regarded as binders.

It is clear that the spray parameters will determine the melting degree, and thus affect the properties of the nanostructured TBCs. It is suggested that the particle temperature in plasma flame should be slightly higher than its melting point [421,424]. In addition, the powder size distribution also affects the generated bimodal structure [425].

Figure 80 shows the microstructure evolution of conventional and nanostructured TBCs during thermal exposure [379]. For conventional TBCs, the initial lamellar structure disappeared, and the coating became much denser. In contrast, for nanostructured TBCs, some large-scale pores can be found at the interface of lamellar zone and nanozone, even though the lamellar zones become denser. This is highly related to the bimodal structure of nanostructured TBCs. At lamellar zones, the stacking of the splats results in a lamellar structure with connected 2D pores. During thermal exposure, the pore surface becomes roughened, which causes multiple contacts at counter-surfaces. As a result, the 2D pores are healed, and the lamellar zones become denser. The nanozones exhibit a loose structure with a large quantity of nano-voids. During thermal exposure, the isotropic nanozones will be contracted to be denser. The differential changes during sintering of
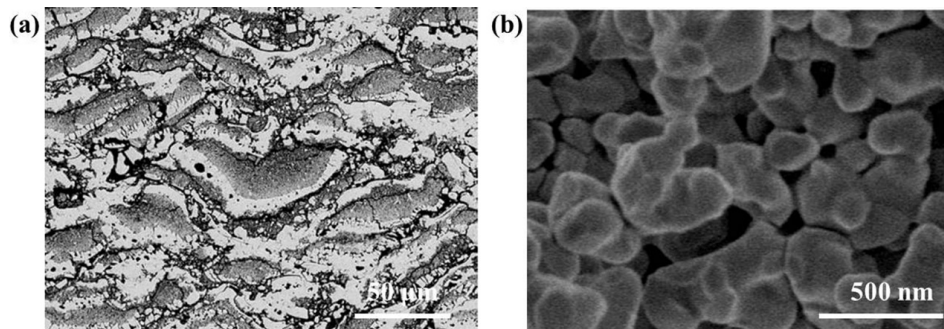
Fig. 79   Nanostructured TBCs: (a) bimodal structure of lamellar zones and nanozones and (b) nanozones at high magnification. Reproduced with permission from Ref. [379], © ASM International 2008.

the lamellar zones and nanozones will cause interfacial opening, which refers to the large-scale pores shown in Fig. 80.

Figure 81 shows the changes in thermal conductivity and elastic modulus as a function of thermal exposure [379]. A common phenomenon is that the increases in mechanical and thermal properties are non-linear. A very large increase at initial short durations changed into a slight increase at long durations. However, nanostructured TBCs appear to resist degradation. In the as-deposited state, the elastic modulus and thermal conductivity are lower with respect to the corresponding conventional TBCs. Moreover, during thermal exposure,

the increase of coating properties is not as significant as that of conventional TBCs. This suggests that the nanostructured TBCs can retain high thermal insulation and strain tolerance during thermal exposure. The main cause is the newly-formed large scale pores at the interface of lamellar zones and nanozones [138].

Owing to the bimodal structure that resists degradation in strain tolerance, nanostructured TBCs often have superior reliability compared to conventional TBCs. It has been reported that nanostructured TBCs have the potential to achieve longer lifetimes during thermal shock tests [426], as shown in Fig. 82.

In brief, TBCs with nanostructure inclusions also
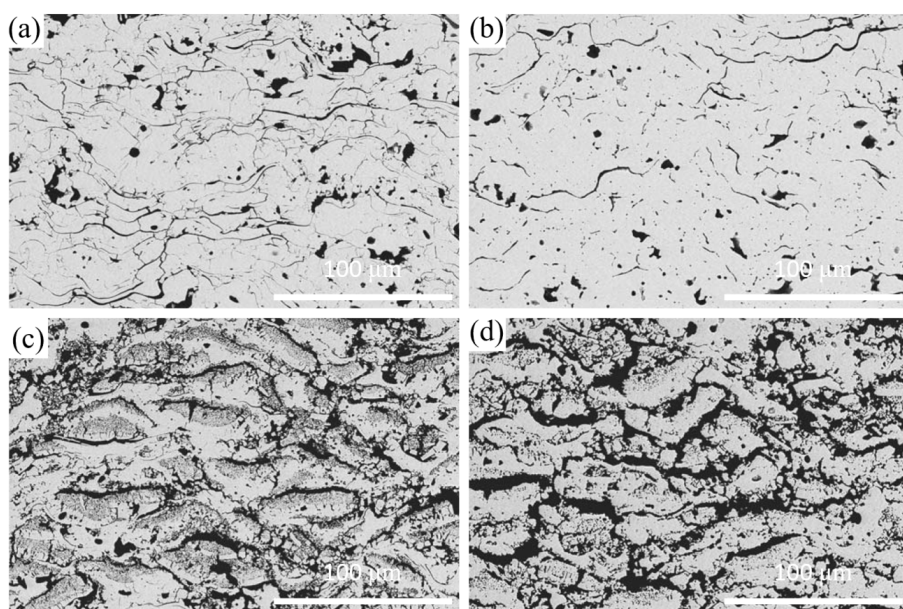
Fig. 80 Microstructural evolution of conventional and nanostructured TBCs during thermal exposure at 1400 ℃: (a) conventional TBCs at 0 h, (b) conventional TBCs at 20 h, (c) nanostructured TBCs at 0 h, and (d) nanostructured TBCs at 20 h. Reproduced with permission from Ref. [379], © ASM International 2008.
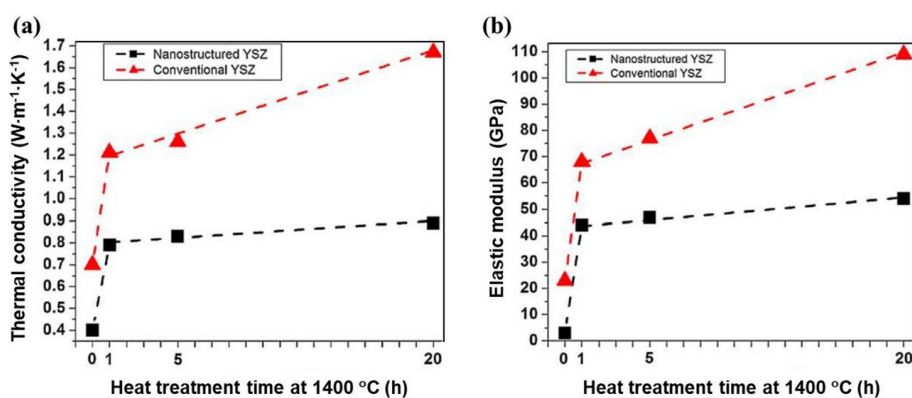
Fig. 81 Changes in (a) thermal conductivity and (b) elastic modulus during thermal exposure. Reproduced with permission from Ref. [379], © ASM International 2008.
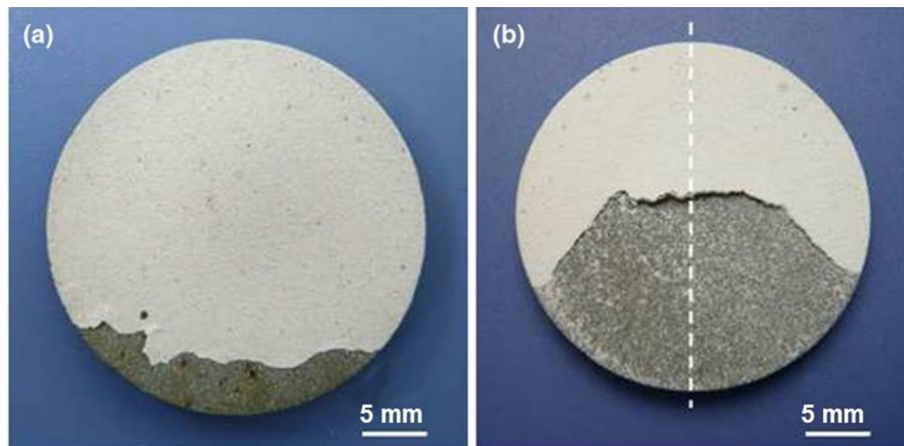
Fig. 82 Comparison of lifetime during the thermal shock test: (a) conventional TBCs with 200 cycles and (b) nanostructured TBCs with 530 cycles. Reproduced with permission from Ref. [426], © ASM International 2010.

suffer from the degradation of cracking resistance of the top coat, which is similar to micro-lamellar-zone/ nano-zone bimodal design. Further efforts should be made to enhance the top coat cohesion and thereby improve the cracking and delamination resistance.

5 Conclusions and future outlook

To meet the requirements for the continuous pursuit of higher operating temperatures for gas turbine of higher power generation efficiency, the TBCs with larger thermal barrier, better environmental tolerance, and longer lifetime are required. Thus, both new ceramic materials and novel designs of ceramic coating structures for TBCs are reviewed in this paper based on a comprehensive understanding of stress induced cracking and delamination behavior during thermal exposure and thermal cycling.

For ceramic top coat, zirconia-based ceramics are still widely used because they have high toughness and good thermal matching with the substrate. Except for purification and multi-components alloying of zirconia-based materials, some newly-developed rare-earth oxides, such as rare-earth niobates (RE_3NbO_7 and $RENbO_4$), rare-earth tantalates ($RETaO_4$), and rare-earth zirconates, show better high-temperature stability without unexpected phase transformation and lower thermal conductivity, while the fracture toughness and CTE should be further improved, aiming at better thermal matching with the substrate and better strain tolerance and thereby a longer lifetime.

To comprehensively understand the durability of TBCs, the generation of various stresses, stress

induced cracking-delamination, and the final spallation of ceramic top coat are summarized together with the oxidation scale growth. In addition, the corrosion and erosion of the top coat also contribute to the coating failure. Aiming at a longer lifetime, reducing multi-source stresses, increasing top coat cohesion and adhesion, enhancing corrosion resistance, and improving erosion resistance need to be extensively investigated, as well as improving the oxidation resistance of metallic bond coat in high-temperature oxidation environments.

To further improve the functions and lifetime of TBCs, novel structure design is also an important issue. For lamellar structures with higher thermal barrier performance, multilayer design and micro-lamella/ nano-zone bimodal design can lead to longer lifetime. For columnar structures with better strain tolerance, SPS/SPPS and PS-PVD are probed to decrease the thermal conductivity and thereby increase the thermal barrier performance. How to combine these two typical structures into one novel structure remains an open question aiming at simultaneously improving both the functions and durability of TBCs.

Author contributions

This article is a result of group effort. Zhi-Yuan WEI and Guan-Jun YANG wrote Section 1; Zhi-Yuan WEI and Hong-Neng CAI wrote Sections 3.1.2, 3.2.2, and 4.2.2; Guo-Hui MENG and Guan-Jun YANG wrote Section 3.2.1; Lin CHEN and Guan-Jun YANG wrote Section 3.1.1; Guang-Rong LI wrote Section 3.1.3; Mei-Jun LIU wrote Section 4.2.3; Wei-Xu ZHANG wrote Section 3.1.4; Li-Na ZHAO, Hong CUI, Xiao-Dong ZHANG, and You Wang wrote Section 2.1; Guang-Rong LI, Qiang ZHANG,

and Zhi-Xue QU wrote Section 4.3; Chun-Lei WAN and Wei PAN wrote Section 2.2; Lin CHEN and Jing FENG wrote Section 2.3; Ling LIU and Zhuang MA wrote Section 2.4; Hui DONG wrote Section 3.2.3; Ze-Bin BAO wrote Section 3.2.4; Xiao-Feng ZHAO wrote Section 3.3.1; Xiao-Feng ZHANG, Min LIU, and Ke-Song ZHOU wrote Section 3.3.2; Lei GUO and Fu-Xing YE wrote Section 3.3.3; Liang WANG wrote Section 3.4; Bo CHENG wrote Section 4.1.1; Wei-Wei ZHANG wrote Section 4.1.2; Peng-Yun XU wrote Section 4.2.1; Guan-Jun YANG and Chang-Jiu LI designed the whole structure of the paper, wrote the Abstract and Section 5, and also rewrote and reorganized the whole paper and made the final check.

Declaration of competing interest

The authors have no competing interests to declare that are relevant to the content of this article.

References

[1] Thakare JG, Pandey C, Mahapatra MM, *et al*. Thermal barrier coatings—A state of the art review. *Met Mater Int* 2021, **27**: 1947–1968.

[2] Chen HF, Zhang C, Liu YC, *et al*. Recent progress in thermal/environmental barrier coatings and their corrosion resistance. *Rare Met* 2020, **39**: 498–512.

[3] Lakiza SM, Grechanyuk MI, Ruban OK, *et al*. Thermal barrier coatings: Current status, search, and analysis. *Powder Metall Met Ceram* 2018, **57**: 82–113.

[4] Li CJ, Li Y, Yang GJ, *et al*. A novel plasma-sprayed durable thermal barrier coating with a well-bonded YSZ interlayer between porous YSZ and bond coat. *J Therm Spray Technol* 2012, **21**: 383–390.

[5] Sun JY, Pei YL, Li SS, *et al*. Improved mechanical properties of Ni-rich Ni$_3$Al coatings produced by EB-PVD for repairing single crystal blades. *Rare Met* 2017, **36**: 556–561.

[6] Chevallier J, Isern L, Almandoz Forcen K, *et al*. Modelling evaporation in electron-beam physical vapour deposition of thermal barrier coatings. *Emergent Mater* 2021, **4**: 1499–1513.

[7] Li GR, Lv BW, Yang GJ, *et al*. Relationship between lamellar structure and elastic modulus of thermally sprayed thermal barrier coatings with intra-splat cracks. *J Therm Spray Technol* 2015, **24**: 1355–1367.

[8] Liu MJ, Zhang G, Lu YH, *et al*. Plasma spray–physical vapor deposition toward advanced thermal barrier coatings: A review. *Rare Met* 2020, **39**: 479–497.

[9] Von Niessen K, Gindrat M, Refke A. Vapor phase deposition using plasma spray-PVD^{TM}. *J Therm Spray Technol* 2010, **19**: 502–509.

[10] Yu ZY, Wei LL, Guo XY, *et al*. Microstructural evolution, mechanical properties and degradation mechanism of PS-PVD quasi-columnar thermal barrier coatings exposed to glassy CMAS deposits. *Rare Met* 2018, https://doi.org/10.1007/s12598-018-1128-5.

[11] Singh J, Wolfe DE. Review nano and macro-structured component fabrication by electron beam-physical vapor deposition (EB-PVD). *J Mater Eng Perform* 2005, **40**: 1–26.

[12] Bakan E, Vaßen R. Ceramic top coats of plasma-sprayed thermal barrier coatings: Materials, processes, and properties. *J Therm Spray Technol* 2017, **26**: 992–1010.

[13] Zhang WW, Li GR, Zhang Q, *et al*. Self-enhancing thermal insulation performance of bimodal-structured thermal barrier coating. *J Therm Spray Technol* 2018, **27**: 1064–1075.

[14] Zhao ZF, Chen H, Xiang HM, *et al*. High entropy defective fluorite structured rare-earth niobates and tantalates for thermal barrier applications. *J Adv Ceram* 2020, **9**: 303–311.

[15] Li F, Zhou L, Liu JX, *et al*. High-entropy pyrochlores with low thermal conductivity for thermal barrier coating materials. *J Adv Ceram* 2019, **8**: 576–582.

[16] Qu ZX, Wan CL, Pan W, *et al*. Thermal expansion and defect chemistry of MgO-doped Sm$_2$Zr$_2$O$_7$. *Chem Mater* 2007, **19**: 4913.

[17] Guo L, Li BW, Cheng YX, *et al*. Composition optimization, high-temperature stability, and thermal cycling performance of Sc-doped Gd$_2$Zr$_2$O$_7$ thermal barrier coatings: theoretical and experimental studies. *J Adv Ceram* 2022, **11**: 454–469.

[18] Xue Y, Zhao XQ, An YL, *et al*. High-entropy (La$_{0.2}$Nd$_{0.2}$Sm$_{0.2}$Eu$_{0.2}$Gd$_{0.2}$)$_2$Ce$_2$O$_7$: a potential thermal barrier material with improved thermo-physical properties. *J Adv Ceram* 2022, **11**: 615–628.

[19] Sun YN, Xiang HM, Dai FZ, *et al*. Preparation and properties of CMAS resistant bixbyite structured high-entropy oxides RE$_2$O$_3$ (RE = Sm, Eu, Er, Lu, Y, and Yb): Promising environmental barrier coating materials for Al$_2$O$_{3f}$/Al$_2$O$_3$ composites. *J Adv Ceram* 2021, **10**: 596–613.

[20] Li CJ, Li Y, Yang GJ, *et al*. Evolution of lamellar interface cracks during isothermal cyclic test of plasma-sprayed 8YSZ coating with a columnar-structured YSZ interlayer. *J Therm Spray Technol* 2013, **22**: 1374–1382.

[21] Dong H, Yang GJ, Cai HN, *et al*. Propagation feature of cracks in plasma-sprayed YSZ coatings under gradient thermal cycling. *Ceram Int* 2015, **41**: 3481–3489.

[22] Patel NV, Jordan EH, Sridharan S, *et al*. Cyclic furnace testing and life predictions of thermal barrier coating spallation subject to a step change in temperature or in cycle duration. *Surf Coat Technol* 2015, **275**: 384–391.

[23] Kishore MB, Lee HG, Abera AG, *et al*. Quantitative evaluation of partial delamination in thermal barrier

coatings using ultrasonic C-scan imaging. *Int J Precis Eng Manuf* 2020, **21**: 157–165.

[24] Dai MQ, Song XM, Lin CC, *et al*. Investigation of microstructure changes in Al$_2$O$_3$–YSZ coatings and YSZ coatings and their effect on thermal cycle life. *J Adv Ceram* 2022, **11**: 345–353.

[25] Lee MJ, Lee BC, Lim JG, *et al*. Residual stress analysis of the thermal barrier coating system by considering the plasma spraying process. *J Mech Sci Technol* 2014, **28**: 2161–2168.

[26] Zhu JG, Chen W, Xie HM. Simulation of residual stresses and their effects on thermal barrier coating systems using finite element method. *Sci China Phys Mech Astron* 2015, **58**: 1–10.

[27] Fry AT, Patel M, Gorman D, *et al*. The effect of cracking of thermally grown oxide layers in thermal barrier coatings examined using FIB tomography and inverse modelling. *Oxid Met* 2021, **96**: 157–168.

[28] Huang H, Liu C, Ni LY, *et al*. Evaluation of TGO growth in thermal barrier coatings using impedance spectroscopy. *Rare Met* 2011, **30**: 643–646.

[29] Tsipas SA, Golosnoy IO, Damani R, *et al*. The effect of a high thermal gradient on sintering and stiffening in the top coat of a thermal barrier coating system. *J Therm Spray Technol* 2004, **13**: 370–376.

[30] Ahrens M, Lampenscherf S, Vaßen R, *et al*. Sintering and creep processes in plasma-sprayed thermal barrier coatings. *J Therm Spray Technol* 2004, **13**: 432–442.

[31] Zhang PP, Zhang XF, Li FH, *et al*. Hot corrosion behavior of YSZ thermal barrier coatings modified by laser remelting and Al deposition. *J Therm Spray Technol* 2019, **28**: 1225–1238.

[32] Arai M. Mechanistic study on the degradation of thermal barrier coatings induced by volcanic ash deposition. *J Therm Spray Technol* 2017, **26**: 1207–1221.

[33] Gomez Chavez JJ, Naraparaju R, Mechnich P, *et al*. Effects of yttria content on the CMAS infiltration resistance of yttria stabilized thermal barrier coatings system. *J Mater Sci Technol* 2020, **43**: 74–83.

[34] Guo L, Li G, Gan ZL. Effects of surface roughness on CMAS corrosion behavior for thermal barrier coating applications. *J Adv Ceram* 2021, **10**: 472–481.

[35] Li DX, Jiang P, Gao RH, *et al*. Experimental and numerical investigation on the thermal and mechanical behaviours of thermal barrier coatings exposed to CMAS corrosion. *J Adv Ceram* 2021, **10**: 551–564.

[36] Essa SK, Chen KY, Liu R, *et al*. Failure mechanisms of APS–YSZ–CoNiCrAlY thermal barrier coating under isothermal oxidation and solid particle erosion. *J Therm Spray Technol* 2021, **30**: 424–441.

[37] Doleker KM, Ahlatci H, Karaoglanli AC. Investigation of isothermal oxidation behavior of thermal barrier coatings (TBCs) consisting of YSZ and multilayered YSZ/Gd$_2$Zr$_2$O$_7$ ceramic layers. *Oxid Met* 2017, **88**: 109–119.

[38] Ahmadian H, Kiahoseyni SR. Investigation of thermal shock resistant in three kinds thermal barrier cerium oxide coating (CeO$_2$) with MCrAlY intermediate layer. *SN Appl Sci* 2019, **1**: 1619.

[39] Chen DY, Rocchio-Heller R, Dambra C. Segmented thermal barrier coatings for ID and OD components using the SinplexPro plasma torch. *J Therm Spray Technol* 2019, **28**: 1664–1673.

[40] Zhu W, Li ZY, Yang L, *et al*. Real-time detection of CMAS corrosion failure in APS thermal barrier coatings under thermal shock. *Exp Mech* 2020, **60**: 775–785.

[41] Li CJ, Dong H, Ding H, *et al*. The correlation of the TBC lifetimes in burner cycling test with thermal gradient and furnace isothermal cycling test by TGO effects. *J Therm Spray Technol* 2017, **26**: 378–387.

[42] Malvi B, Roy M. Elevated temperature erosion of plasma sprayed thermal barrier coating. *J Therm Spray Technol* 2021, **30**: 1028–1037.

[43] Clarke DR, Levi CG. Materials design for the next generation thermal barrier coatings. *Annu Rev Mater Res* 2003, **33**: 383–417.

[44] Clarke DR, Phillpot SR. Thermal barrier coating materials. *Mater Today* 2005, **8**: 22–29.

[45] Fergus JW. Zirconia and pyrochlore oxides for thermal barrier coatings in gas turbine engines. *Metall Mater Trans E* 2014, **1**: 118–131.

[46] Perepezko JH. The hotter the engine, the better. *Science* 2009, **326**: 1068–1069.

[47] Padture NP, Gell M, Jordan EH. Thermal barrier coatings for gas-turbine engine applications. *Science* 2002, **296**: 280–284.

[48] Li F, Li YY, Song ZX, *et al*. Grain growth characteristics of hydrothermally prepared yttria stabilized zirconia nanocrystals during calcination. *Rare Metal Mat Eng* 2017, **46**: 0899–0905.

[49] Kumar A, Gu S, Tabbara H, *et al*. Study of impingement of hollow ZrO$_2$ droplets onto a substrate. *Surf Coat Technol* 2013, **220**: 164–169.

[50] Zhao LN, Zhang Z, Duan YG, *et al*. Preparation of yttria-stabilized zirconia hollow sphere with reduced shell thickness by controlling ambient temperature during plasma process. *Coatings* 2018, **8**: 245.

[51] Zhang Z, Zhao LN, Ma YP. Preparing hollow spherical hydroxyapatite powder with a thin shell structure by the plasma process with a heat preservation zone. *Ceram Int* 2019, **45**: 19562–19566.

[52] Solonenko OP, Gulyaev IP, Smirnov AV. Plasma processing and deposition of powdered metal oxides consisting of hollow spherical particles. *Tech Phys Lett* 2008, **34**: 1050–1052.

[53] Gulyaev IP. Production and modification of hollow powders in plasma under controlled pressure. *J Phys Conf Ser* 2013, **441**: 012033.

[54] Kulkarni A, Wang Z, Nakamura T, *et al*. Comprehensive microstructural characterization and predictive property modeling of plasma-sprayed zirconia coatings. *Acta Mater* 2003, **51**: 2457–2475.

[55] Chi W, Sampath S, Wang H. Ambient and high-

temperature thermal conductivity of thermal sprayed coatings. *J Therm Spray Technol* 2006, **15**: 773–778.

[56] Tan Y, Srinivasan V, Nakamura T, *et al*. Optimizing compliance and thermal conductivity of plasma sprayed thermal barrier coatings via controlled powders and processing strategies. *J Therm Spray Technol* 2012, **21**: 950–962.

[57] Vaßen R, Czech N, Malléner W, *et al*. Influence of impurity content and porosity of plasma-sprayed yttria-stabilized zirconia layers on the sintering behaviour. *Surf Coat Technol* 2001, **141**: 135–140.

[58] Paul S, Cipitria A, Golosnoy IO, *et al*. Effects of impurity content on the sintering characteristics of plasma-sprayed zirconia. *J Therm Spray Technol* 2007, **16**: 798–803.

[59] Xie L, Dorfman MR, Cipitria A, *et al*. Properties and performance of high-purity thermal barrier coatings. *J Therm Spray Technol* 2007, **16**: 804–808.

[60] Vassen R, Cao XQ, Tietz F, *et al*. Zirconates as new materials for thermal barrier coatings. *J Am Ceram Soc* 2000, **83**: 2023–2028.

[61] Zhu DM, Nesbitt JA, Barrett CA, *et al*. Furnace cyclic oxidation behavior of multicomponent low conductivity thermal barrier coatings. *J Therm Spray Technol* 2004, **13**: 84–92.

[62] Ji XJ, Gong SK, Xu HB, *et al*. Influence of rare earth elements additions in YSZ ceramic coatings of thermal barrier coatings on lattice distortion. *Acta Aeronautica Et Astronautica Sinica* 2007, **28**: 196–200. (in Chinese)

[63] Bansal NP, Zhu DM. Effects of doping on thermal conductivity of pyrochlore oxides for advanced thermal barrier coatings. *Mater Sci Eng A* 2007, **459**: 192–195.

[64] Wu J, Padture NP, Klemens PG, *et al*. Thermal conductivity of ceramics in the ZrO_2–$GdO_{1.5}$ system. *J Mater Res* 2002, **17**: 3193–3200.

[65] Wakeshima M, Nishimine H, Hinatsu Y. Crystal structures and magnetic properties of rare earth tantalates RE_3TaO_7 (RE = rare earths). *J Phys Condens Matter* 2004, **16**: 4103–4120.

[66] Chesnaud A, Braida M-D, Estradé S, *et al*. High-temperature anion and proton conduction in RE_3NbO_7 (RE = La, Gd, Y, Yb, Lu) compounds. *J Eur Ceram Soc* 2015, **35**: 3051–3061.

[67] Cai L, Nino JC. Structure and dielectric properties of Ln_3NbO_7 (Ln = Nd, Gd, Dy, Er, Yb and Y). *J Eur Ceram Soc* 2007, **27**: 3971–3976.

[68] Abe R, Higashi M, Sayama K, *et al*. Photocatalytic activity of R_3MO_7 and $R_2Ti_2O_7$ (R = Y, Gd, La; M = Nb, Ta) for water splitting into H_2 and O_2. *J Phys Chem B* 2006, **110**: 2219–2226.

[69] Xiang HM, Xing Y, Dai FZ, *et al*. High-entropy ceramics: Present status, challenges, and a look forward. *J Adv Ceram* 2021, **10**: 385–441.

[70] Huang MZ, Li LY, Feng YJ, *et al*. Y_3NbO_7 transparent ceramic series for high refractive index optical lenses. *J Am Ceram Soc* 2021, **104**: 5776–5783.

[71] Masuno A, Inoue H, Yoshimoto K, *et al*. Thermal and optical properties of La_2O_3–Nb_2O_5 high refractive index glasses. *Opt Mater Express* 2014, **4**: 710–718.

[72] Yang J, Qian X, Pan W, *et al*. Diffused lattice vibration and ultralow thermal conductivity in the binary Ln–Nb–O oxide system. *Adv Mater* 2019, **31**: 1808222.

[73] Chen L, Wu P, Song P, *et al*. Potential thermal barrier coating materials: RE_3NbO_7 (RE = La, Nd, Sm, Eu, Gd, Dy) ceramics. *J Am Ceram Soc* 2018, **101**: 4503–4508.

[74] Huang MZ, Liu XY, Zhang P, *et al*. Thermal conductivity modeling on highly disordered crystalline $Y_{1-x}Nb_xO_{1.5+x}$: Beyond the phonon scenario. *Appl Phys Lett* 2021, **118**: 073901.

[75] Yang J, Pan W, Han Y, *et al*. Mechanical properties, oxygen barrier property, and chemical stability of RE_3NbO_7 for thermal barrier coating. *J Am Ceram Soc* 2020, **103**: 2302–2308.

[76] Chen L, Guo J, Zhu YK, *et al*. Features of crystal structures and thermo-mechanical properties of weberites RE_3NbO_7 (RE = La, Nd, Sm, Eu, Gd) ceramics. *J Am Ceram Soc* 2021, **104**: 404–412.

[77] Zhang P, Feng YJ, Li Y, *et al*. Thermal and mechanical properties of ferroelastic $RENbO_4$ (RE = Nd, Sm, Gd, Dy, Er, Yb) for thermal barrier coatings. *Scripta Mater* 2020, **180**: 51–56.

[78] Wu FS, Wu P, Zhou YX, *et al*. The thermo-mechanical properties and ferroelastic phase transition of $RENbO_4$ (RE = Y, La, Nd, Sm, Gd, Dy, Yb) ceramics. *J Am Ceram Soc* 2020, **103**: 2727–2740.

[79] Zhu JT, Xu J, Zhang P, *et al*. Enhanced mechanical and thermal properties of ferroelastic high-entropy rare-earth-niobates. *Scripta Mater* 2021, **200**: 113912.

[80] Sarin P, Hughes RW, Lowry DR, *et al*. High-temperature properties and ferroelastic phase transitions in rare-earth niobates ($LnNbO_4$). *J Am Ceram Soc* 2014, **97**: 3307–3319.

[81] Wang J, Zhou Y, Chong XY, *et al*. Microstructure and thermal properties of a promising thermal barrier coating: $YTaO_4$. *Ceram Int* 2016, **42**: 13876–13881.

[82] Zhang QL, Zhou WL, Liu WP, *et al*. Crystal growth by Czochralski method and spectral properties of Yb^{3+}:$GdTaO_4$. *Acta Optica Sinica* 2010, **30**: 849–853. (in Chinese)

[83] Feng J, Shian S, Xiao B, *et al*. First-principles calculations of the high-temperature phase transformation in yttrium tantalate. *Phys Rev B* 2014, **90**: 094102.

[84] Wang J, Chong XY, Zhou R, *et al*. Microstructure and thermal properties of $RETaO_4$ (RE = Nd, Eu, Gd, Dy, Er, Yb, Lu) as promising thermal barrier coating materials. *Scripta Mater* 2017, **126**: 24–28.

[85] Ubaldini A, Carnasciali MM. Raman characterisation of powder of cubic RE_2O_3 (RE = Nd, Gd, Dy, Tm, and Lu), Sc_2O_3 and Y_2O_3. *J Alloys Compd* 2008, **454**: 374–378.

[86] Swalin RA, Rice SA. Thermodynamics of solids. *Phys*

Today 1963, **16**: 72–74.

[87] Zhang YL, Guo L, Yang YP, *et al*. Influence of Gd$_2$O$_3$ and Yb$_2$O$_3$ co-doping on phase stability, thermo-physical properties and sintering of 8YSZ. *Chin J Aeronaut* 2012, **25**: 948–953.

[88] Chen L, Hu MY, Wu P, *et al*. Thermal expansion performance and intrinsic lattice thermal conductivity of ferroelastic RETaO$_4$ ceramics. *J Am Ceram Soc* 2019, **102**: 4809–4821.

[89] Du AB, Wan CL, Qu ZX, *et al*. Thermal conductivity of monazite-type REPO$_4$ (RE = La, Ce, Nd, Sm, Eu, Gd). *J Am Ceram Soc* 2009, **92**: 2687–2692.

[90] Chen L, Feng J. Influence of HfO$_2$ alloying effect on microstructure and thermal conductivity of HoTaO$_4$ ceramics. *J Adv Ceram* 2019, **8**: 537–544.

[91] Wu P, Hu MY, Chen L, *et al*. Investigation on microstructures and thermo-physical properties of ferroelastic (Y$_{1-x}$Dy$_x$)TaO$_4$ ceramics. *Materialia* 2018, **4**: 478–486.

[92] Wu J, Wei XZ, Padture NP, *et al*. Low-thermal-conductivity rare-earth zirconates for potential thermal-barrier-coating applications. *J Am Ceram Soc* 2002, **85**: 3031–3035.

[93] Maloney MJ. Thermal barrier coating systems and materials. U.S. patent 6 924 040, Aug. 2005.

[94] Feng J, Xiao B, Zhou R, *et al*. Thermal conductivity of rare earth zirconate pyrochlore from first principles. *Scripta Mater* 2013, **68**: 727–730.

[95] Wang JD, Pan W, Xu Q, *et al*. Thermal conductivity of the new candidate materials for thermal barrier coatings. *Key Eng Mater* 2005, **280–283**: 1503–1506.

[96] Xu Q, Pan W, Wang JD, *et al*. Preparation and thermophysical properties of Dy$_2$Zr$_2$O$_7$ ceramic for thermal barrier coatings. *Mater Lett* 2005, **59**: 2804–2807.

[97] Aruna ST, Sanjeeviraja C, Balaji N, *et al*. Properties of plasma sprayed La$_2$Zr$_2$O$_7$ coating fabricated from powder synthesized by a single-step solution combustion method. *Surf Coat Technol* 2013, **219**: 131–138.

[98] Yu JH, Zhao HY, Tao SY, *et al*. Thermal conductivity of plasma sprayed Sm$_2$Zr$_2$O$_7$ coatings. *J Eur Ceram Soc* 2010, **30**: 799–804.

[99] Wan CL, Qu ZX, Du AB, *et al*. Order–disorder transition and unconventional thermal conductivities of the (Sm$_{1-x}$Yb$_x$)$_2$Zr$_2$O$_7$ series. *J Am Ceram Soc* 2011, **94**: 592–596.

[100] Li T, Ma Z, Liu L, *et al*. Thermal properties of Sm$_2$Zr$_2$O$_7$–NiCr$_2$O$_4$ composites. *Ceram Int* 2014, **40**: 11423–11426.

[101] Ma Z, Zhang Q, Liu L, *et al*. Preparation and heat insulating capacity of Sm$_2$Zr$_2$O$_7$–SiC composites based on photon thermal transport. *J Adv Ceram* 2020, **9**: 454–461.

[102] Fan QB, Zhang F, Wang FC, *et al*. Molecular dynamics calculation of thermal expansion coefficient of a series of rare-earth zirconates. *Comput Mater Sci* 2009, **46**: 716–719.

[103] Shimamura K, Arima T, Idemitsu K, *et al*. Thermophysical properties of rare-earth-stabilized zirconia and zirconate pyrochlores as surrogates for actinide-doped zirconia. *Int J Thermophys* 2007, **28**: 1074–1084.

[104] Zhou HM, Yi DQ. Effect of rare earth doping on thermo-physical properties of lanthanum zirconate ceramic for thermal barrier coatings. *J Rare Earths* 2008, **26**: 770–774.

[105] Liu L, Wang FC, Ma Z, *et al*. Thermophysical properties of (Mg$_x$La$_{0.5-x}$Sm$_{0.5}$)$_2$(Zr$_{0.7}$Ce$_{0.3}$)$_2$O$_{7-x}$ (x = 0, 0.1, 0.2, 0.3) ceramic for thermal barrier coatings. *J Am Ceram Soc* 2011, **94**: 675–678.

[106] Liu L, Xu Q, Wang FC, *et al*. Thermophysical properties of complex rare-earth zirconate ceramic for thermal barrier coatings. *J Am Ceram Soc* 2008, **91**: 2398–2401.

[107] Xue ZL, Wu SQ, Qian LH, *et al*. Influence of Y$_2$O$_3$ and Ta$_2$O$_5$ co-doping on microstructure and thermal conductivity of Gd$_2$Zr$_2$O$_7$ ceramics. *J Mater Eng Perform* 2020, **29**: 1206–1213.

[108] Tian WZ, Liu L, Ma Z, *et al*. The preparation and properties of Sm$_2$Zr$_2$O$_7$ coatings by plasma spraying. *Mater Res Innov* 2015, **19**: S24–S28.

[109] Guo W, Ma Z, Liu L, *et al*. Influence of feedstock on the microstructure of Sm$_2$Zr$_2$O$_7$ thermal barrier coatings deposited by plasma spraying. *J Therm Spray Technol* 2018, **27**: 1524–1531.

[110] Doleker KM, Ozgurluk Y, Karaoglanli AC. TGO growth and kinetic study of single and double layered TBC systems. *Surf Coat Technol* 2021, **415**: 127135.

[111] Jasik A, Moskal G, Mikuśkiewicz M, *et al*. Oxidation behavior of the monolayered La$_2$Zr$_2$O$_7$, composite La$_2$Zr$_2$O$_7$ + 8YSZ, and double-cceramic layered La$_2$Zr$_2$O$_7$/ La$_2$Zr$_2$O$_7$ + 8YSZ/8YSZ thermal barrier coatings. *Materials* 2020, **13**: 3242.

[112] Kuroda S, Clyne TW. The quenching stress in thermally sprayed coatings. *Thin Solid Films* 1991, **200**: 49–66.

[113] Li CJ, Ohmori A. Relationships between the microstructure and properties of thermally sprayed deposits. *J Therm Spray Technol* 2002, **11**: 365–374.

[114] Bohn S, Douady S, Couder Y. Four sided domains in hierarchical space dividing patterns. *Phys Rev Lett* 2005, **94**: 054503.

[115] Bohn S. Hierarchical crack patterns: A comparison with two-dimensional soap foams. *Colloids Surf A Physicochem Eng Aspects* 2005, **263**: 46–51.

[116] Chen L, Yang GJ, Li CX, *et al*. Hierarchical formation of intrasplat cracks in thermal spray ceramic coatings. *J Therm Spray Technol* 2016, **25**: 959–970.

[117] Chen L, Yang GJ, Li CX, *et al*. Edge effect on crack patterns in thermally sprayed ceramic splats. *J Therm Spray Technol* 2017, **26**: 302–314.

[118] Li CJ, Li JL. Transient contact pressure during flattening of thermal spray droplet and its effect on splat formation. *J Therm Spray Technol* 2004, **13**: 229–238.

[119] Jiang XY, Wan YP, Herman H, *et al*. Role of condensates and adsorbates on substrate surface on fragmentation of impinging molten droplets during thermal spray. *Thin*

Solid Films 2001, **385**: 132–141.

[120] Xue MX, Chandra S, Mostaghimi J. Investigation of splat curling up in thermal spray coatings. *J Therm Spray Technol* 2006, **15**: 531–536.

[121] Chen L, Yang GJ. Epitaxial growth and cracking of highly tough 7YSZ splats by thermal spray technology. *J Adv Ceram* 2018, **7**: 17–29.

[122] Chen L, Yang GJ. Hetero-orientation epitaxial growth of TiO₂ splats on polycrystalline TiO₂ substrate. *J Therm Spray Technol* 2018, **27**: 880–897.

[123] Chen L, Gao LL, Yang GJ. Imaging slit pores under delaminated splats by white light interference. *J Therm Spray Technol* 2018, **27**: 319–335.

[124] Chen L, Yang GJ. Epitaxial growth and cracking mechanisms of thermally sprayed ceramic splats. *J Therm Spray Technol* 2018, **27**: 255–268.

[125] Chen L, Yang GJ, Li CX. Formation of lamellar pores for splats via interfacial or sub-interfacial delamination at chemically bonded region. *J Therm Spray Technol* 2017, **26**: 315–326.

[126] Chen L, Yang GJ. Anomalous epitaxial growth in thermally sprayed YSZ and LZ splats. *J Therm Spray Technol* 2017, **26**: 1168–1182.

[127] Ranjbar-Far M, Absi J, Mariaux G, et al. Effect of residual stresses and prediction of possible failure mechanisms on thermal barrier coating system by finite element method. *J Therm Spray Technol* 2010, **19**: 1054–1061.

[128] Tahir A, Li GR, Liu MJ, et al. Improving WC–Co coating adhesive strength on rough substrate: Finite element modeling and experiment. *J Mater Sci Technol* 2020, **37**: 1–8.

[129] Bobzin K, Bagcivan N, Parkot D, et al. Modeling and simulation of microstructure formation for porosity prediction in thermal barrier coatings under air plasma spraying condition. *J Therm Spray Technol* 2009, **18**: 975–980.

[130] Samadi H, Coyle TW. Modeling the build-up of internal stresses in multilayer thick thermal barrier coatings. *J Therm Spray Technol* 2009, **18**: 996–1003.

[131] Wu LF, Zhu JG, Xie HM. Numerical and experimental investigation of residual stress in thermal barrier coatings during APS process. *J Therm Spray Technol* 2014, **23**: 653–665.

[132] Li SL, Qi HY, Song JN, et al. Effect of bond-coat surface roughness on failure mechanism and lifetime of air plasma spraying thermal barrier coatings. *Sci China Technol Sci* 2019, **62**: 989–995.

[133] Wei ZY, Cai HN, Feng RX, et al. The combined effect of creep and TGO growth on the cracking driving force in a plasma-sprayed thermal barrier system. *J Therm Spray Technol* 2019, **28**: 1000–1016.

[134] Bäker M, Seiler P. A guide to finite element simulations of thermal barrier coatings. *J Therm Spray Technol* 2017, **26**: 1146–1160.

[135] Krishnasamy J, Ponnusami SA, Turteltaub S, et al.

Numerical investigation into the effect of splats and pores on the thermal fracture of air plasma-sprayed thermal barrier coatings. *J Therm Spray Technol* 2019, **28**: 1881–1892.

[136] Ranjbar-Far M, Absi J, Mariaux G. Finite element modeling of the different failure mechanisms of a plasma sprayed thermal barrier coatings system. *J Therm Spray Technol* 2012, **21**: 1234–1244.

[137] Vaßen R, Bakan E, Mack D, et al. Performance of YSZ and Gd₂Zr₂O₇/YSZ double layer thermal barrier coatings in burner rig tests. *J Eur Ceram Soc* 2020, **40**: 480–490.

[138] Li GR, Yang GJ. Understanding of degradation-resistant behavior of nanostructured thermal barrier coatings with bimodal structure. *J Mater Sci Technol* 2019, **35**: 231–238.

[139] Paul S, Cipitria A, Tsipas SA, et al. Sintering characteristics of plasma sprayed zirconia coatings containing different stabilisers. *Surf Coat Technol* 2009, **203**: 1069–1074.

[140] Cernuschi F, Bison PG, Marinetti S, et al. Thermophysical, mechanical and microstructural characterization of aged free-standing plasma-sprayed zirconia coatings. *Acta Mater* 2008, **56**: 4477–4488.

[141] Shinozaki M, Clyne TW. A methodology, based on sintering-induced stiffening, for prediction of the spallation lifetime of plasma-sprayed coatings. *Acta Mater* 2013, **61**: 579–588.

[142] Cocks A, Fleck N, Lampenscherf S. A brick model for asperity sintering and creep of APS TBCs. *J Mech Phys Solids* 2014, **63**: 412–431.

[143] Li GR, Cheng B, Yang GJ, et al. Strain-induced stiffness-dependent structural changes and the associated failure mechanism in TBCs. *J Eur Ceram Soc* 2017, **37**: 3609–3621.

[144] Cipitria A, Golosnoy IO, Clyne TW. A sintering model for plasma-sprayed zirconia thermal barrier coatings. Part II: Coatings bonded to a rigid substrate. *Acta Mater* 2009, **57**: 993–1003.

[145] Lv BW, Fan XL, Xie H, et al. Effect of neck formation on the sintering of air-plasma-sprayed thermal barrier coating system. *J Eur Ceram Soc* 2017, **37**: 811–821.

[146] Cheng B, Yang N, Zhang Q, et al. Sintering induced the failure behavior of dense vertically crack and lamellar structured TBCs with equivalent thermal insulation performance. *Ceram Int* 2017, **43**: 15459–15465.

[147] Yang L, Liu QX, Zhou YC, et al. Finite element simulation on thermal fatigue of a turbine blade with thermal barrier coatings. *J Mater Sci Technol* 2014, **30**: 371–380.

[148] Xie H, Xie YC, Yang GJ, et al. Modeling thermal conductivity of thermally sprayed coatings with intrasplat cracks. *J Therm Spray Technol* 2013, **22**: 1328–1336.

[149] Fauchais P, Fukumoto M, Vardelle A, et al. Knowledge concerning splat formation: An invited review. *J Therm Spray Technol* 2004, **13**: 337–360.

[150] Zhong X, Zhu T, Niu YR, et al. Effect of microstructure evolution and crystal structure on thermal properties for

plasma-sprayed RE₂SiO₅ (RE = Gd, Y, Er) environmental barrier coatings. *J Mater Sci Technol* 2021, **85**: 141–151.

[151] Cipitria A, Golosnoy IO, Clyne TW. A sintering model for plasma-sprayed zirconia TBCs. Part I: Free-standing coatings. *Acta Mater* 2009, **57**: 980–992.

[152] Chi WG, Sampath S, Wang H. Microstructure-thermal conductivity relationships for plasma-sprayed yttria-stabilized zirconia coatings. *J Am Ceram Soc* 2008, **91**: 2636–2645.

[153] Marple BR, Lima RS, Moreau C, *et al*. Yttria-stabilized zirconia thermal barriers sprayed using N₂–H₂ and Ar–H₂ plasmas: Influence of processing and heat treatment on coating properties. *J Therm Spray Technol* 2007, **16**: 791–797.

[154] Tan Y, Longtin JP, Sampath S, *et al*. Effect of the starting microstructure on the thermal properties of as-sprayed and thermally exposed plasma-sprayed YSZ coatings. *J Am Ceram Soc* 2009, **92**: 710–716.

[155] Thompson JA, Clyne TW. The effect of heat treatment on the stiffness of zirconia top coats in plasma-sprayed TBCs. *Acta Mater* 2001, **49**: 1565–1575.

[156] Lima RS, Kruger SE, Lamouche G, *et al*. Elastic modulus measurements via laser-ultrasonic and Knoop indentation techniques in thermally sprayed coatings. *J Therm Spray Technol* 2005, **14**: 52–60.

[157] Guo SQ, Kagawa Y. Young's moduli of zirconia top-coat and thermally grown oxide in a plasma-sprayed thermal barrier coating system. *Scripta Mater* 2004, **50**: 1401–1406.

[158] Tan Y, Shyam A, Choi WB, *et al*. Anisotropic elastic properties of thermal spray coatings determined via resonant ultrasound spectroscopy. *Acta Mater* 2010, **58**: 5305–5315.

[159] Liu T, Chen X, Yang GJ, *et al*. Properties evolution of plasma-sprayed La₂Zr₂O₇ coating induced by pore structure evolution during thermal exposure. *Ceram Int* 2016, **42**: 15485–15492.

[160] Li GR, Xie H, Yang GJ, *et al*. A comprehensive sintering mechanism for TBCs—Part I: An overall evolution with two-stage kinetics. *J Am Ceram Soc* 2017, **100**: 2176–2189.

[161] Wang LS, Tang CH, Dong H, *et al*. Dominant effects of 2D pores on mechanical behaviors of plasma sprayed ceramic coatings during thermal exposure. *Ceram Int* 2020, **46**: 6774–6781.

[162] Yang GJ, Li CJ, Li CX, *et al*. Improvement of adhesion and cohesion in plasma-sprayed ceramic coatings by heterogeneous modification of nonbonded lamellar interface using high strength adhesive infiltration. *J Therm Spray Technol* 2013, **22**: 36–47.

[163] Li GR, Wang LS, Yang GJ, *et al*. Combined effect of internal and external factors on sintering kinetics of plasma-sprayed thermal barrier coatings. *J Eur Ceram Soc* 2019, **39**: 1860–1868.

[164] Liu T, Luo XT, Chen X, *et al*. Morphology and size evolution of interlamellar two-dimensional pores in plasma-sprayed La₂Zr₂O₇ coatings during thermal exposure at 1300 ℃. *J Therm Spray Technol* 2015, **24**: 739–748.

[165] Li GR, Xie H, Yang GJ, *et al*. A comprehensive sintering mechanism for TBCs—Part II: Multiscale multipoint interconnection-enhanced initial kinetics. *J Am Ceram Soc* 2017, **100**: 4240–4251.

[166] Li CJ, Ohmori A, McPherson R. The relationship between microstructure and Young's modulus of thermally sprayed ceramic coatings. *J Mater Sci* 1997, **32**: 997–1004.

[167] Wang LS, Wei ZY, Cheng B, *et al*. Gradient stiffening induced interfacial cracking and strain tolerant design in thermal barrier coatings. *Ceram Int* 2020, **46**: 2355–2364.

[168] Li GR, Tang CH, Yang GJ. Dynamic-stiffening-induced aggravated cracking behavior driven by metal-substrate-constraint in a coating/substrate system. *J Mater Sci Technol* 2021, **65**: 154–163.

[169] Liu MJ, Zhang G, Lu YH, *et al*. Plasma spray-physical vapor deposition toward advanced thermal barrier coatings: A review. *Rare Metals* 2020, **39**: 479–497.

[170] Chen C, Guo HB, Gong SK, *et al*. Sintering of electron beam physical vapor deposited thermal barrier coatings under flame shock. *Ceram Int* 2013, **39**: 5093–5102.

[171] Guo HB, Kuroda S, Murakami H. Microstructures and properties of plasma-sprayed segmented thermal barrier coatings. *J Am Ceram Soc* 2006, **89**: 1432–1439.

[172] Chevalier J, Gremillard L, Virkar AV, *et al*. The tetragonal–monoclinic transformation in zirconia: Lessons learned and future trends. *J Am Ceram Soc* 2009, **92**: 1901–1920.

[173] Fadda G, Zanzotto G, Colombo L. First-principles study of the effect of pressure on the five zirconia polymorphs. I. Structural, vibrational, and thermoelastic properties. *Phys Rev B* 2010, **82**: 064105.

[174] Béchade J-L, Brenner R, Goudeau P, *et al*. Determination of residual stresses in a zirconia layer by X-ray diffraction and by a micromechanical approach: Thermoelastic anisotropy effect. *Rev Met Paris* 2003, **100**: 1151–1156.

[175] Sibil A, Douillard T, Cayron C, *et al*. Microcracking of high zirconia refractories after t→m phase transition during cooling: An EBSD study. *J Eur Ceram Soc* 2011, **31**: 1525–1531.

[176] Hallmann L, Ulmer P, Reusser E, *et al*. Effect of blasting pressure, abrasive particle size and grade on phase transformation and morphological change in dental zirconia surface. *Surf Coat Technol* 2012, **206**: 4293–4302.

[177] Saemi H, Rastegari S, Sarpoolaky H, *et al*. Oxidation resistance of double-ceramic-layered thermal barrier coating system with an intermediate Al₂O₃–YAG layer. *J Therm Spray Technol* 2021, **30**: 1049–1058.

[178] Cao YP, Ning XJ, Wang QS. Thermal shock behavior of Ba(Mg₁/₃Ta₂/₃)O₃–YSZ double-ceramic-layer thermal barrier coatings prepared by atmospheric plasma spraying.

Surf Coat Technol 2021, **409**: 126842.

[179] Schulz U. Phase transformation in EB-PVD yttria partially stabilized zirconia thermal barrier coatings during annealing. *J Am Ceram Soc* 2000, **83**: 904–910.

[180] Mamivand M, Asle Zaeem M, El Kadiri H, *et al*. Phase field modeling of the tetragonal-to-monoclinic phase transformation in zirconia. *Acta Mater* 2013, **61**: 5223–5235.

[181] Chevalier J, Liens A, Reveron H, *et al*. Forty years after the promise of «ceramic steel?»: Zirconia-based composites with a metal-like mechanical behavior. *J Am Ceram Soc* 2020, **103**: 1482–1513.

[182] Chai YJ, Lin C, Wang X, *et al*. Study on stress development in the phase transition layer of thermal barrier coatings. *Materials* 2016, **9**: 773.

[183] Sun YL, Li JG, Zhang WX, *et al*. Local stress evolution in thermal barrier coating system during isothermal growth of irregular oxide layer. *Surf Coat Technol* 2013, **216**: 237–250.

[184] Fan XL, Zhang WX, Wang TJ, *et al*. The effect of thermally grown oxide on multiple surface cracking in air plasma sprayed thermal barrier coating system. *Surf Coat Technol* 2012, **208**: 7–13.

[185] Zhang WX, Fan XL, Wang TJ. The surface cracking behavior in air plasma sprayed thermal barrier coating system incorporating interface roughness effect. *Appl Surf Sci* 2011, **258**: 811–817.

[186] Xie F, Sun YL, Li DJ, *et al*. Modelling of catastrophic stress development due to mixed oxide growth in thermal barrier coatings. *Ceram Int* 2019, **45**: 11353–11361.

[187] Lv BW, Xie H, Xu R, *et al*. Effects of sintering and mixed oxide growth on the interface cracking of air-plasma-sprayed thermal barrier coating system at high temperature. *Appl Surf Sci* 2016, **360**: 461–469.

[188] Sait F, Gurses E, Aslan O. Modeling and simulation of coupled phase transformation and stress evolution in thermal barrier coatings. *Int J Plast* 2020, **134**: 102790.

[189] Liu PF, Jiang P, Sun YL, *et al*. Numerical analysis of stress evolution in thermal barrier coating system during two-stage growth of heterogeneous oxide. *Ceram Int* 2021, **47**: 14311–14319.

[190] Xie F, Li DJ, Zhang WX. Long-term failure mechanisms of thermal barrier coatings in heavy-duty gas turbines. *Coatings* 2020, **10**: 1022.

[191] Wang X, Atkinson A, Chirivì L, *et al*. Evolution of stress and morphology in thermal barrier coatings. *Surf Coat Technol* 2010, **204**: 3851–3857.

[192] El Kadiri H, Utegulov ZN, Khafizov M, *et al*. Transformations and cracks in zirconia films leading to breakaway oxidation of Zircaloy. *Acta Mater* 2013, **61**: 3923–3935.

[193] Wu LT, Wu RT, Xiao P, *et al*. A prominent driving force for the spallation of thermal barrier coatings: Chemistry dependent phase transformation of the bond coat. *Acta Mater* 2017, **137**: 22–35.

[194] Zhang BY, Yang GJ, Li CX, *et al*. Non-parabolic isothermal oxidation kinetics of low pressure plasma sprayed MCrAlY bond coat. *Appl Surf Sci* 2017, **406**: 99–109.

[195] Meng GH, Liu H, Xu PY, *et al*. Superior oxidation resistant MCrAlY bond oats prepared by controlled atmosphere heat treatment. *Corros Sci* 2020, **170**: 108653.

[196] Meng GH, Liu H, Liu MJ, *et al*. Large-grain α-Al$_2$O$_3$ enabling ultra-high oxidation-resistant MCrAlY bond coats by surface pre-agglomeration treatment. *Corros Sci* 2020, **163**: 108275.

[197] Meng GH, Liu H, Liu MJ, *et al*. Highly oxidation resistant MCrAlY bond coats prepared by heat treatment under low oxygen content. *Surf Coat Technol* 2019, **368**: 192–201.

[198] Meng GH, Zhang BY, Liu H, *et al*. Highly oxidation resistant and cost effective MCrAlY bond coats prepared by controlled atmosphere heat treatment. *Surf Coat Technol* 2018, **347**: 54–65.

[199] Sun YL, Zhang WX, Li JG, *et al*. Local stress around cap-like portions of anisotropically and nonuniformly grown oxide layer in thermal barrier coating system. *J Mater Sci* 2013, **48**: 5962–5982.

[200] Ding J, Li FX, Kang KJ. Numerical simulation of displacement instabilities of surface grooves on an alumina forming alloy during thermal cycling oxidation. *J Mech Sci Technol* 2009, **23**: 2308–2319.

[201] Osorio JD, Giraldo J, Hernández JC, *et al*. Diffusion–reaction of aluminum and oxygen in thermally grown Al$_2$O$_3$ oxide layers. *Heat Mass Transf* 2014, **50**: 483–492.

[202] Chen WR, Archer R, Huang X, *et al*. TGO growth and crack propagation in a thermal barrier coating. *J Therm Spray Technol* 2008, **17**: 858–864.

[203] Ali MS, Song SH, Xiao P. Degradation of thermal barrier coatings due to thermal cycling up to 1150 ℃. *J Mater Sci* 2002, **37**: 2097–2102.

[204] Chen WR, Irissou E, Wu X, *et al*. The oxidation behavior of TBC with cold spray CoNiCrAlY bond coat. *J Therm Spray Technol* 2011, **20**: 132–138.

[205] Eriksson R, Gupta M, Broitman E, *et al*. Stresses and cracking during chromia–spinel–NiO cluster formation in TBC systems. *J Therm Spray Technol* 2015, **24**: 1002–1014.

[206] Naumenko D, Shemet V, Singheiser L, *et al*. Failure mechanisms of thermal barrier coatings on MCrAlY-type bondcoats associated with the formation of the thermally grown oxide. *J Mater Sci* 2009, **44**: 1687–1703.

[207] Gupta M, Skogsberg K, Nylén P. Influence of topcoat-bondcoat interface roughness on stresses and lifetime in thermal barrier coatings. *J Therm Spray Technol* 2014, **23**: 170–181.

[208] Chen WR, Wu X, Dudzinski D. Influence of thermal cycle frequency on the TGO growth and cracking behaviors of an APS–TBC. *J Therm Spray Technol* 2012, **21**: 1294–1299.

[209] Xiao BJ, Robertson T, Huang X, *et al.* Fracture performance and crack growth prediction of SPS TBCs in isothermal experiments by crack numbering density. *Ceram Int* 2020, **46**: 2682–2692.

[210] Li Y, Li CJ, Yang GJ, *et al.* Thermal fatigue behavior of thermal barrier coatings with the MCrAlY bond coats by cold spraying and low-pressure plasma spraying. *Surf Coat Technol* 2010, **205**: 2225–2233.

[211] Liu JH, Liu YB, Liu L, *et al.* Submodeling method to study the residual stress of TBCs near the interfacial asperity on a vane. *Eng Fail Anal* 2021, **122**: 105220.

[212] Jiang P, Yang LY, Sun YL, *et al.* Local residual stress evolution of highly irregular thermally grown oxide layer in thermal barrier coatings. *Ceram Int* 2021, **47**: 10990–10995.

[213] Hu ZC, Wang L, Zhuang MX, *et al.* Influence of internal oxidation of the bond-coat on the residual stress around the TGO and failure modes of the APS–TBCs: A finite element simulation study. *Ceram Int* 2021, **47**: 5364–5373.

[214] Rabiei A, Evans AG. Failure mechanisms associated with the thermally grown oxide in plasma-sprayed thermal barrier coatings. *Acta Mater* 2000, **48**: 3963–3976.

[215] Dong H, Yang GJ, Li CX, *et al.* Effect of TGO thickness on thermal cyclic lifetime and failure mode of plasma-sprayed TBCs. *J Am Ceram Soc* 2014, **97**: 1226–1232.

[216] Weng WX, Zheng ZH, Li Q. Cracking evolution of atmospheric plasma-sprayed YSZ thermal barrier coatings subjected to isothermal heat treatment. *Surf Coat Technol* 2020, **402**: 125924.

[217] Huang YP, Wei ZY, Cai HN, *et al.* The effects of TGO growth stress and creep rate on TC/TGO interface cracking in APS thermal barrier coatings. *Ceram Int* 2021, **47**: 24760–24769.

[218] Shen Q, Yang L, Zhou YC, *et al.* Models for predicting TGO growth to rough interface in TBCs. *Surf Coat Technol* 2017, **325**: 219–228.

[219] Xu HB, Gong SK, Zhang Y, *et al.* Experimental and computational study on hot fatigue process of thermal barrier coatings by EB-PVD. *Intermetallics* 2005, **13**: 315–322.

[220] Ebach-Stahl A, Schulz U, Swadźba R, *et al.* Lifetime improvement of EB-PVD 7YSZ TBCs by doping of Hf or Zr in NiCoCrAlY bond coats. *Corros Sci* 2021, **181**: 109205.

[221] Shi JQ, Zhang TB, Sun B, *et al.* Isothermal oxidation and TGO growth behavior of NiCoCrAlY–YSZ thermal barrier coatings on a Ni-based superalloy. *J Alloys Compd* 2020, **844**: 156093.

[222] Chen WR, Wu X, Marple BR, *et al.* TGO growth behaviour in TBCs with APS and HVOF bond coats. *Surf Coat Technol* 2008, **202**: 2677–2683.

[223] Dong H, Yang G-J, Luo X-T, *et al.* Effect of mixed oxides on thermal cyclic lifetime of plasma-sprayed thermal barrier coatings. *China Surf Eng* 2015, **28**: 21–28. (in Chinese)

[224] Dong H, Yao JT, Li X, *et al.* The sintering behavior of plasma-sprayed YSZ coating over the delamination crack in low temperature environment. *Ceram Int* 2018, **44**: 3326–3332.

[225] Wang JL, Chen MH, Yang LL, *et al.* Nanocrystalline coatings on superalloys against high temperature oxidation: A review. *Corros Commun* 2021, **1**: 58–69.

[226] Yang YF, Jiang CY, Bao ZB, *et al.* Effect of aluminisation characteristics on the microstructure of single phase β-(Ni,Pt)Al coating and the isothermal oxidation behaviour. *Corros Sci* 2016, **106**: 43–54.

[227] Yang YF, Jiang CY, Yao HR, *et al.* Preparation and enhanced oxidation performance of a Hf-doped single-phase Pt-modified aluminide coating. *Corros Sci* 2016, **113**: 17–25.

[228] Bao ZB, Wang QM, Li WZ, *et al.* Corrosion behaviour of AIP NiCoCrAlYSiB coating in salt spray tests. *Corros Sci* 2008, **50**: 847–855.

[229] Bao ZB, Wang QM, Li WZ, *et al.* Preparation and hot corrosion behaviour of an Al-gradient NiCoCrAlYSiB coating on a Ni-base superalloy. *Corros Sci* 2009, **51**: 860–867.

[230] Narita T. Diffusion barrier coating system concept for high temperature applications. *Can Metall Quart* 2011, **50**: 278–290.

[231] Liang JJ, Matsumoto K, Kawagishi K, *et al.* Morphological evolution of thermal barrier coatings with equilibrium (EQ) and NiCoCrAlY bond coats during thermal cycling. *Surf Coat Technol* 2012, **207**: 413–420.

[232] Mercer C, Kawagishi K, Tomimatsu T, *et al.* A comparative investigation of oxide formation on EQ (equilibrium) and NiCoCrAlY bond coats under stepped thermal cycling. *Surf Coat Technol* 2011, **205**: 3066–3072.

[233] Wang JL, Chen MH, Yang LL, *et al.* Comparative study of oxidation and interdiffusion behavior of AIP NiCrAlY and sputtered nanocrystalline coatings on a nickel-based single-crystal superalloy. *Corros Sci* 2015, **98**: 530–540.

[234] Yang LL, Chen MH, Wang JL, *et al.* Diffusion of Ta and its influence on oxidation behavior of nanocrystalline coatings with different Ta, Y and Al contents. *Corros Sci* 2017, **126**: 344–355.

[235] Ghasemi R, Valefi Z. The effect of the Re–Ni diffusion barrier on the adhesion strength and thermal shock resistance of the NiCoCrAlY coating. *Surf Coat Technol* 2018, **344**: 359–372.

[236] Narita T, Thosin KZ, Fengqun L, *et al.* Development of Re-based diffusion barrier coatings on nickel based superalloys. *Mater Corros* 2005, **56**: 923–929.

[237] Li HQ, Wang QM, Jiang SM, *et al.* Ion-plated Al–Al_2O_3 films as diffusion barriers between NiCrAlY coating and orthorhombic-Ti_2AlNb alloy. *Corros Sci* 2010, **52**: 1668–1674.

[238] Li WZ, Wang QM, Gong J, *et al.* Interdiffusion reaction in the CrN interlayer in the NiCrAlY/CrN/DSM11 system

during thermal treatment. *Appl Surf Sci* 2009, **255**: 8190–8193.

[239] Guo CA, Wang W, Cheng YX, *et al*. Yttria partially stabilised zirconia as diffusion barrier between NiCrAlY and Ni-base single crystal René N5 superalloy. *Corros Sci* 2015, **94**: 122–128.

[240] Yao HR, Bao ZB, Shen ML, *et al*. A magnetron sputtered microcrystalline β-NiAl coating for SC superalloys. Part II. Effects of a NiCrO diffusion barrier on oxidation behavior at 1100 ℃. *Appl Surf Sci* 2017, **407**: 485–494.

[241] Cheng YX, Wang W, Zhu SL, *et al*. Arc ion plated-Cr₂O₃ intermediate film as a diffusion barrier between NiCrAlY and γ-TiAl. *Intermetallics* 2010, **18**: 736–739.

[242] Sim JK, Lee SK, Kim JS, *et al*. Efficiency enhancement of CIGS compound solar cell fabricated using homomorphic thin Cr₂O₃ diffusion barrier formed on stainless steel substrate. *Appl Surf Sci* 2016, **389**: 645–650.

[243] Wang CX, Chen W, Chen MH, *et al*. Corrosion behavior and elements interdiffusion between a Ni coating and GH3535 alloy with and without a CrN barrier in molten fluoride salts. *J Nucl Mater* 2019, **514**: 348–357.

[244] Ren P, Zhu SL, Wang FH. TEM study of the evolution of sputtered Ni + CrAlYSiHfN nanocomposite coating with an AlN diffusion barrier at high temperature. *Surf Coat Technol* 2016, **286**: 262–267.

[245] Zhu LJ, Zhu SL, Wang FH. Preparation and oxidation behaviour of nanocrystalline Ni + CrAlYSiN composite coating with AlN diffusion barrier on Ni-based superalloy K417. *Corros Sci* 2012, **60**: 265–274.

[246] Liu H, Li S, Jiang CY, *et al*. Preparation and oxidation performance of a low-diffusion Pt-modified aluminide coating with Re-base diffusion barrier. *Corros Sci* 2020, **168**: 108582.

[247] Levi CG, Hutchinson JW, Vidal-Sétif MH, *et al*. Environmental degradation of thermal-barrier coatings by molten deposits. *MRS Bull* 2012, **37**: 932–941.

[248] Wang YH, Ma Z, Liu L, *et al*. Reaction products of Sm₂Zr₂O₇ with calcium–magnesium–aluminum–silicate (CMAS) and their evolution. *J Adv Ceram* 2021, **10**: 1389–1397.

[249] Giehl C, Brooker RA, Marxer H, *et al*. An experimental simulation of volcanic ash deposition in gas turbines and implications for jet engine safety. *Chem Geol* 2017, **461**: 160–170.

[250] Ghoshal A, Murugan M, Walock MJ, *et al*. Molten particulate impact on tailored thermal barrier coatings for gas turbine engine. *J Eng Gas Turbines Power* 2017, **140**: 022601.

[251] Crosby JM, Lewis S, Bons JP, *et al*. Effects of particle size, gas temperature and metal temperature on high pressure turbine deposition in land based gas turbines from various synfuels. In: Proceedings of the Turbo Expo: Power for Land, Sea and Air, Montreal, Canada, 2007: 1365–1376.

[252] Shinozaki M, Roberts KA, van de Goor B, *et al*. Deposition of ingested volcanic ash on surfaces in the turbine of a small jet engine. *Adv Eng Mater* 2013, **15**: 986–994.

[253] Yang SJ, Song WJ, Lavallee Y, *et al*. Dynamic spreading of re-melted volcanic ash bead on thermal barrier coatings. *Corros Sci* 2020, **170**: 108659.

[254] Kang YX, Bai Y, Bao CG, *et al*. Defects/CMAS corrosion resistance relationship in plasma sprayed YPSZ coating. *J Alloys Compd* 2017, **694**: 1320–1330.

[255] Liu T, Yao SW, Wang LS, *et al*. Plasma-sprayed thermal barrier coatings with enhanced splat bonding for CMAS and corrosion protection. *J Therm Spray Technol* 2016, **25**: 213–221.

[256] Shan X, Cai HY, Luo LR, *et al*. Influence of pore characteristics of air plasma sprayed thermal barrier coatings on calcia–magnesia–alumino–silicate (CMAS) attack behavior. *Corros Sci* 2021, **190**: 109636.

[257] Shan X, Luo LR, Chen WF, *et al*. Pore filling behavior of YSZ under CMAS attack: Implications for designing corrosion-resistant thermal barrier coatings. *J Am Ceram Soc* 2018, **101**: 5756–5770.

[258] Shan X, Chen WF, Yang LX, *et al*. Pore filling behavior of air plasma spray thermal barrier coatings under CMAS attack. *Corros Sci* 2020, **167**: 108478.

[259] Krämer S, Yang J, Levi CG, *et al*. Thermochemical interaction of thermal barrier coatings with molten CaO–MgO–Al₂O₃–SiO₂ (CMAS) deposits. *J Am Ceram Soc* 2006, **89**: 3167–3175.

[260] Garces HF, Senturk BS, Padture NP. *In situ* Raman spectroscopy studies of high-temperature degradation of thermal barrier coatings by molten silicate deposits. *Scripta Mater* 2014, **76**: 29–32.

[261] Witz G, Shklover V, Steurer W, *et al*. High-temperature interaction of yttria stabilized zirconia coatings with CaO–MgO–Al₂O₃–SiO₂ (CMAS) deposits. *Surf Coat Technol* 2015, **265**: 244–249.

[262] Morelli S, Testa V, Bolelli G, *et al*. CMAS corrosion of YSZ thermal barrier coatings obtained by different thermal spray processes. *J Eur Ceram Soc* 2020, **40**: 4084–4100.

[263] Holgate CS, Seward GGE, Ericks AR, *et al*. Dissolution and diffusion kinetics of yttria-stabilized zirconia into molten silicates. *J Eur Ceram Soc* 2021, **41**: 1984–1994.

[264] Boissonnet G, Chalk C, Nicholls J, *et al*. Thermal insulation of CMAS (calcium–magnesium–alumino–silicates)-attacked plasma-sprayed thermal barrier coatings. *J Eur Ceram Soc* 2020, **40**: 2042–2049.

[265] Mercer C, Faulhaber S, Evans AG, *et al*. A delamination mechanism for thermal barrier coatings subject to calcium–magnesium–alumino–silicate (CMAS) infiltration. *Acta Mater* 2005, **53**: 1029–1039.

[266] Mack DE, Wobst T, Jarligo MOD, *et al*. Lifetime and failure modes of plasma sprayed thermal barrier coatings in thermal gradient rig tests with simultaneous CMAS injection. *Surf Coat Technol* 2017, **324**: 36–47.

[267] Shan X, Zou ZH, Gu LJ, *et al*. Buckling failure in

air-plasma sprayed thermal barrier coatings induced by molten silicate attack. *Scripta Mater* 2016, **113**: 71–74.

[268] Drexler JM, Chen CH, Gledhill AD, *et al*. Plasma sprayed gadolinium zirconate thermal barrier coatings that are resistant to damage by molten Ca–Mg–Al–silicate glass. *Surf Coat Technol* 2012, **206**: 3911–3916.

[269] Gao LH, Guo HB, Gong SK, *et al*. Plasma-sprayed $La_2Ce_2O_7$ thermal barrier coatings against calcium–magnesium–alumina–silicate penetration. *J Eur Ceram Soc* 2014, **34**: 2553–2561.

[270] Ma W, Gong SK, Li HF, *et al*. Novel thermal barrier coatings based on $La_2Ce_2O_7$/8YSZ double-ceramic-layer systems deposited by electron beam physical vapor deposition. *Surf Coat Technol* 2008, **202**: 2704–2708.

[271] Yin BB, Xia J, Liu WW, *et al*. Experimental study on CMAS corrosion resistance performance of $La_2Ce_2O_7$/YSZ thermal barrier coatings. *J Xiangtan University Nat Sci* 2020, **42**: 62–72. (in Chinese)

[272] Dolmaire A, Goutier S, Joulia A, *et al*. Experimental study of the impact of substrate shape and tilting on particle velocity in suspension plasma spraying. *J Therm Spray Technol* 2020, **29**: 358–367.

[273] Yin JN, Zhang X, Feng JL, *et al*. Effect of powder composition upon plasma spray-physical vapor deposition of 8YSZ columnar coating. *Ceram Int* 2020, **46**: 15867–15875.

[274] Danek JR GJ. State-of-the-art survey on hot corrosion in marine gas turbine engines. *Nav Eng J* 1965, **77**: 859–869.

[275] Shifler DA. Hot corrosion: A modification of reactants causing degradation. *Mater High Temp* 2018, **35**: 225–235.

[276] Kosieniak E, Biesiada K, Kaczorowski J, *et al*. Corrosion failures in gas turbine hot components. *J Fail Anal Prev* 2012, **12**: 330–337.

[277] Gurrappa I. Identification of hot corrosion resistant MCrAlY based bond coatings for gas turbine engine applications. *Surf Coat Technol* 2001, **139**: 272–283.

[278] Sreedhar G, Raja VS. Hot corrosion of YSZ/Al_2O_3 dispersed NiCrAlY plasma-sprayed coatings in Na_2SO_4–10 wt.% NaCl melt. *Corros Sci* 2010, **52**: 2592–2602.

[279] O'Dowd CD, de Leeuw G. Marine aerosol production: A review of the current knowledge. *Phil Trans R Soc A* 2007, **365**: 1753–1774.

[280] Pettit F. Hot corrosion of metals and alloys. *Oxid Met* 2011, **76**: 1–21.

[281] Mauer G, Hospach A, Vaßen R. Process development and coating characteristics of plasma spray-PVD. *Surf Coat Technol* 2013, **220**: 219–224.

[282] Zhang X-F, Zhou K-S, Song J-B, *et al*. Deposition and CMAS corrosion mechanism of 7YSZ thermal barrier coatings prepared by plasma spray-physical vapor deposition. *J Inorg Mater* 2015, **30**: 287–293. (in Chinese)

[283] Ozgurluk Y, Doleker KM, Karaoglanli AC. Hot corrosion behavior of YSZ, $Gd_2Zr_2O_7$ and $YSZ/Gd_2Zr_2O_7$ thermal barrier coatings exposed to molten sulfate and vanadate salt. *Appl Surf Sci* 2018, **438**: 96–113.

[284] Jonnalagadda KP, Mahade S, Curry N, *et al*. Hot corrosion mechanism in multilayer suspension plasma sprayed $Gd_2Zr_2O_7$/YSZ thermal barrier coatings in the presence of V_2O_5 + Na_2SO_4. *J Therm Spray Technol* 2017, **26**: 140–149.

[285] Zhu C, Wang YG, An LN, *et al*. Microstructure and oxidation behavior of conventional and pseudo graded NiCrAlY/YSZ thermal barrier coatings produced by supersonic air plasma spraying process. *Surf Coat Technol* 2015, **272**: 121–128.

[286] Kakuda TR, Levi CG, Bennett TD. The thermal behavior of CMAS-infiltrated thermal barrier coatings. *Surf Coat Technol* 2015, **272**: 350–356.

[287] Poerschke DL, Levi CG. Effects of cation substitution and temperature on the interaction between thermal barrier oxides and molten CMAS. *J Eur Ceram Soc* 2015, **35**: 681–691.

[288] Evans AG, Fleck NA, Faulhaber S, *et al*. Scaling laws governing the erosion and impact resistance of thermal barrier coatings. *Wear* 2006, **260**: 886–894.

[289] Fan J-F, Zhang X-F, Zhou K-S, *et al*. Influence of Al-modification on CMAS corrosion resistance of PS-PVD 7YSZ thermal barrier coatings. *J Inorg Mater* 2019, **34**: 938–946. (in Chinese)

[290] Zhang XF, Zhou KS, Liu M, *et al*. CMAS corrosion and thermal cycle of Al-modified PS-PVD environmental barrier coating. *Ceram Int* 2018, **44**: 15959–15964.

[291] Zhang XF, Liu M, Li H, *et al*. Structural evolution of Al-modified PS-PVD 7YSZ TBCs in thermal cycling. *Ceram Int* 2019, **45**: 7560–7567.

[292] Hua YF, Pan W, Li ZX, *et al*. Research progress of hot corrosion-resistance for thermal barrier coatings, *Rare Metal Mat Eng* 2013, **42**: 1976–1980. (in Chinese)

[293] Costa GCC, Zhu DM, Kulis MJ, *et al*. Reactivity between rare-earth oxides based thermal barrier coatings and a silicate melt. *J Am Ceram Soc* 2018, **101**: 3674–3693.

[294] Teja Pasupuleti K, Manikanta Dunna U, Ghosh S, *et al*. Synthesis and studies on partially stabilized zirconia and rare-earth zirconate pyrochlore structured multilayered coatings. *Mater Today Proc* 2020, **22**: 1244–1252.

[295] Jana P, Jayan PS, Mandal S, *et al*. Hot corrosion behaviour of rare-earth magnesium hexaaluminate based thermal barrier coatings under molten sulphate–vanadate salts. *Surf Coat Technol* 2017, **322**: 108–119.

[296] Shen ZY, Liu Z, Huang ZY, *et al*. Thermal shock life and failure behaviors of $La_2Zr_2O_7$/YSZ, $La_2Ce_2O_7$/YSZ and $Gd_2Zr_2O_7$/YSZ DCL TBCs by EB-PVD. *Mater Charact* 2021, **173**: 110923.

[297] Liu Y, Bai Y, Li EB, *et al*. Preparation and characterization of $SrZrO_3$–$La_2Ce_2O_7$ composite ceramics as a thermal barrier coating material. *Mater Chem Phys* 2020, **247**: 122904.

[298] Stott FH, de Wet DJ, Taylor R. Degradation of thermal-barrier coatings at very high temperatures. *MRS*

Bull 1994, **19**: 46–49.

[299] Evans AG, Hutchinson JW. The mechanics of coating delamination in thermal gradients. *Surf Coat Technol* 2007, **201**: 7905–7916.

[300] Jackson RW, Zaleski EM, Poerschke DL, *et al*. Interaction of molten silicates with thermal barrier coatings under temperature gradients. *Acta Mater* 2015, **89**: 396–407.

[301] Cai ZW, Jiang JS, Wang WZ, *et al*. CMAS penetration-induced cracking behavior in the ceramic top coat of APS TBCs. *Ceram Int* 2019, **45**: 14366–14375.

[302] Krämer S, Faulhaber S, Chambers M, *et al*. Mechanisms of cracking and delamination within thick thermal barrier systems in aeroengines subject to calcium–magnesium–alumino–silicate (CMAS) penetration. *Mater Sci Eng A* 2008, **490**: 26–35.

[303] Yang L, Yang J, Xia J, *et al*. Characterization of the strain in the thermal barrier coatings caused by molten CaO–MgO–Al$_2$O$_3$–SiO$_2$ using a digital image correlation technique. *Surf Coat Technol* 2017, **322**: 1–9.

[304] Jamali H, Mozafarinia R, Shoja-Razavi R, *et al*. Comparison of hot corrosion behaviors of plasma-sprayed nanostructured and conventional YSZ thermal barrier coatings exposure to molten vanadium pentoxide and sodium sulfate. *J Eur Ceram Soc* 2014, **34**: 485–492.

[305] Xu ZH, He LM, Mu RD, *et al*. Hot corrosion behavior of rare earth zirconates and yttria partially stabilized zirconia thermal barrier coatings. *Surf Coat Technol* 2010, **204**: 3652–3661.

[306] Guo L, Li MZ, Ye FX. Comparison of hot corrosion resistance of Sm$_2$Zr$_2$O$_7$ and (Sm$_{0.5}$Sc$_{0.5}$)$_2$Zr$_2$O$_7$ ceramics in Na$_2$SO$_4$ + V$_2$O$_5$ molten salt. *Ceram Int* 2016, **42**: 13849–13854.

[307] Shifler DA. The increasing complexity of corrosion in gas turbines. In: Proceedings of the Turbo Expo: Power for Land, Sea and Air, Pheonix, USA, 2019: GT2019-90111.

[308] Shifler DA, Choi SR. CMAS effects on ship gas-turbine components/materials. In: Proceedings of the Turbo Expo: Power for Land, Sea and Air, Oslo, Norway, 2018: GT2018-75865.

[309] Guo L, Xin H, Hu CW. Comparison of NaVO$_3$ + CMAS mixture and CMAS corrosion to thermal barrier coatings. *Corros Sci* 2020, **177**: 108968.

[310] Drexler JM, Shinoda K, Ortiz AL, *et al*. Air-plasma-sprayed thermal barrier coatings that are resistant to high-temperature attack by glassy deposits. *Acta Mater* 2010, **58**: 6835–6844.

[311] Wiesner VL, Bansal NP. Crystallization kinetics of calcium–magnesium aluminosilicate (CMAS) glass. *Surf Coat Technol* 2014, **259**: 608–615.

[312] Guo L, Xin H, Li YY, *et al*. Self-crystallization characteristics of calcium–magnesium–alumina–silicate (CMAS) glass under simulated conditions for thermal barrier coating applications. *J Eur Ceram Soc* 2020, **40**: 5683–5691.

[313] Wang L, Guo L, Li ZM, *et al*. Protectiveness of Pt and Gd$_2$Zr$_2$O$_7$ layers on EB-PVD YSZ thermal barrier coatings against calcium–magnesium–alumina–silicate (CMAS) attack. *Ceram Int* 2015, **41**: 11662–11669.

[314] Guo L, Yan Z, Wang XH, *et al*. Ti$_2$AlC MAX phase for resistance against CMAS attack to thermal barrier coatings. *Ceram Int* 2019, **45**: 7627–7634.

[315] Yan Z, Guo L, Zhang Z, *et al*. Versatility of potential protective layer material Ti$_2$AlC on resisting CMAS corrosion to thermal barrier coatings. *Corros Sci* 2020, **167**: 108532.

[316] Yan Z, Guo L, Li ZH, *et al*. Effects of laser glazing on CMAS corrosion behavior of Y$_2$O$_3$ stabilized ZrO$_2$ thermal barrier coatings. *Corros Sci* 2019, **157**: 450–461.

[317] Habibi MH, Wang L, Liang JD, *et al*. An investigation on hot corrosion behavior of YSZ–Ta$_2$O$_5$ in Na$_2$SO$_4$ + V$_2$O$_5$ salt at 1100 ℃. *Corros Sci* 2013, **75**: 409–414.

[318] Nejati M, Rahimipour MR, Mobasherpour I. Evaluation of hot corrosion behavior of CSZ, CSZ/micro Al$_2$O$_3$ and CSZ/nano Al$_2$O$_3$ plasma sprayed thermal barrier coatings. *Ceram Int* 2014, **40**: 4579–4590.

[319] Loghman-Estarki MR, Razavi RS, Edris H, *et al*. Comparison of hot corrosion behavior of nanostructured ScYSZ and YSZ thermal barrier coatings. *Ceram Int* 2016, **42**: 7432–7439.

[320] Guo L, Zhang CL, Li MZ, *et al*. Hot corrosion evaluation of Gd$_2$O$_3$–Yb$_2$O$_3$ co-doped Y$_2$O$_3$ stabilized ZrO$_2$ thermal barrier oxides exposed to Na$_2$SO$_4$ + V$_2$O$_5$ molten salt. *Ceram Int* 2017, **43**: 2780–2785.

[321] Guo L, Zhang CL, He Q, *et al*. Corrosion products evolution and hot corrosion mechanisms of REPO$_4$ (RE = Gd, Nd, La) in the presence of V$_2$O$_5$ + Na$_2$SO$_4$ molten salt. *J Eur Ceram Soc* 2019, **39**: 1496–1506.

[322] Guo L, Xin H, Zhang Z, *et al*. Preparation of (Gd$_{0.9}$Sc$_{0.1}$)$_2$Zr$_2$O$_7$/YSZ thermal barrier coatings and their corrosion resistance to V$_2$O$_5$ molten salt. *Surf Coat Technol* 2020, **389**: 125677.

[323] Guo L, Xin H, Zhang Z, *et al*. Microstructure modification of Y$_2$O$_3$ stabilized ZrO$_2$ thermal barrier coatings by laser glazing and the effects on the hot corrosion resistance. *J Adv Ceram* 2020, **9**: 232–242.

[324] Guo L, Yan Z, Yu Y, *et al*. CMAS resistance characteristics of LaPO$_4$/YSZ thermal barrier coatings at 1250 ℃–1350 ℃. *Corros Sci* 2019, **154**: 111–122.

[325] Chen XL, Zhao Y, Fan XZ, *et al*. Thermal cycling failure of new LaMgAl$_{11}$O$_{19}$/YSZ double ceramic top coat thermal barrier coating systems. *Surf Coat Technol* 2011, **205**: 3293–3300.

[326] Guo L, Yan Z, Li ZH, *et al*. GdPO$_4$ as a novel candidate for thermal barrier coating applications at elevated temperatures. *Surf Coat Technol* 2018, **349**: 400–406.

[327] Guo L, Gao Y, Ye FX, *et al*. CMAS corrosion behavior and protection method of thermal barrier coatings for aeroengine. *Acta Metall Sin* 2021, **57**: 1184–1198. (in Chinese)

[328] Doleker KM, Ozgurluk Y, Ahlatci H, *et al*. Evaluation of oxidation and thermal cyclic behavior of YSZ, Gd$_2$Zr$_2$O$_7$ and YSZ/Gd$_2$Zr$_2$O$_7$ TBCs. *Surf Coat Technol* 2019, **371**: 262–275.

[329] Chen X, He MY, Spitsberg I, *et al*. Mechanisms governing the high temperature erosion of thermal barrier coatings. *Wear* 2004, **256**: 735–746.

[330] Fleck NA, Zisis T. The erosion of EB-PVD thermal barrier coatings: The competition between mechanisms. *Wear* 2010, **268**: 1214–1224.

[331] Zisis T, Fleck NA. The elastic–plastic indentation response of a columnar thermal barrier coating. *Wear* 2010, **268**: 443–454.

[332] Chen X, Wang R, Yao N, *et al*. Foreign object damage in a thermal barrier system: Mechanisms and simulations. *Mater Sci Eng A* 2003, **352**: 221–231.

[333] Wellman RG, Nicholls JR. Erosion, corrosion and erosion–corrosion of EB PVD thermal barrier coatings. *Tribol Int* 2008, **41**: 657–662.

[334] Crowell MW, Schaedler TA, Hazel BH, *et al*. Experiments and numerical simulations of single particle foreign object damage-like impacts of thermal barrier coatings. *Int J Impact Eng* 2012, **48**: 116–124.

[335] Karger M, Vaßen R, Stöver D. Atmospheric plasma sprayed thermal barrier coatings with high segmentation crack densities: Spraying process, microstructure and thermal cycling behavior. *Surf Coat Technol* 2011, **206**: 16–23.

[336] Cernuschi F, Lorenzoni L, Capelli S, *et al*. Solid particle erosion of thermal spray and physical vapour deposition thermal barrier coatings. *Wear* 2011, **271**: 2909–2918.

[337] Wellman RG, Nicholls JR. A review of the erosion of thermal barrier coatings. *J Phys D Appl Phys* 2007, **40**: R293–R305.

[338] Wellman RG, Nicholls JR, Murphy K. Effect of microstructure and temperature on the erosion rates and mechanisms of modified EB PVD TBCs. *Wear* 2009, **267**: 1927–1934.

[339] Janos BZ, Lugscheider E, Remer P. Effect of thermal aging on the erosion resistance of air plasma sprayed zirconia thermal barrier coating. *Surf Coat Technol* 1999, **113**: 278–285.

[340] Wellman RG, Deakin MJ, Nicholls JR. The effect of TBC morphology on the erosion rate of EB PVD TBCs. *Wear* 2005, **258**: 349–356.

[341] Wellman RG, Nicholls JR. On the effect of ageing on the erosion of EB-PVD TBCs. *Surf Coat Technol* 2004, **177–178**: 80–88.

[342] Zhu DM, Miller RA, Kuczmarski M. Development and life prediction of erosion resistant turbine low conductivity thermal barrier coatings. In: Proceedings of the 65th Annual Forum and Technology Display, Grapevine, USA, 2010: 20100011004.

[343] Drexler JM, Aygun A, Li DS, *et al*. Thermal-gradient testing of thermal barrier coatings under simultaneous attack by molten glassy deposits and its mitigation. *Surf Coat Technol* 2010, **204**: 2683–2688.

[344] Drexler JM, Gledhill AD, Shinoda K, *et al*. Jet engine coatings for resisting volcanic ash damage. *Adv Mater* 2011, **23**: 2419–2424.

[345] Yan J, Karlsson AM, Bartsch M, *et al*. On stresses induced in a thermal barrier coating due to indentation testing. *Comput Mater Sci* 2009, **44**: 1178–1191.

[346] Chen X, Hutchinson JW, Evans AG. Simulation of the high temperature impression of thermal barrier coatings with columnar microstructure. *Acta Mater* 2004, **52**: 565–571.

[347] Ramanujam N, Nakamura T. Erosion mechanisms of thermally sprayed coatings with multiple phases. *Surf Coat Technol* 2009, **204**: 42–53.

[348] Chen L, Hu MY, Guo J, *et al*. Mechanical and thermal properties of RETaO$_4$ (RE = Yb, Lu, Sc) ceramics with monoclinic-prime phase. *J Mater Sci Technol* 2020, **52**: 20–28.

[349] Zhao ZF, Chen H, Xiang HM, *et al*. High-entropy (Y$_{0.2}$Nd$_{0.2}$Sm$_{0.2}$Eu$_{0.2}$Er$_{0.2}$)AlO$_3$: A promising thermal/environmental barrier material for oxide/oxide composites. *J Mater Sci Technol* 2020, **47**: 45–51.

[350] Cong LK, zhang SY, Gu SY, *et al*. Thermophysical properties of a novel high entropy hafnate ceramic. *J Mater Sci Technol* 2021, **85**: 152–157.

[351] Chen H, Zhao ZF, Xiang HM, *et al*. High entropy (Y$_{0.2}$Yb$_{0.2}$Lu$_{0.2}$Eu$_{0.2}$Er$_{0.2}$)$_3$Al$_5$O$_{12}$: A novel high temperature stable thermal barrier material. *J Mater Sci Technol* 2020, **48**: 57–62.

[352] Zhao ZF, Chen H, Xiang HM, *et al*. (Y$_{0.25}$Yb$_{0.25}$Er$_{0.25}$Lu$_{0.25}$)$_2$(Zr$_{0.5}$Hf$_{0.5}$)$_2$O$_7$: A defective fluorite structured high entropy ceramic with low thermal conductivity and close thermal expansion coefficient to Al$_2$O$_3$. *J Mater Sci Technol* 2020, **39**: 167–172.

[353] Wei ZY, Cheng B, Wang J, *et al*. Extend the thermal cyclic lifetime of La$_2$Zr$_2$O$_7$/YSZ DCL TBCs by reducing modulus design on a toughening ceramic surface. *Surf Coat Technol* 2019, **374**: 134–143.

[354] Cheng B, Wei ZY, Chen L, *et al*. Prolong the durability of La$_2$Zr$_2$O$_7$/YSZ TBCs by decreasing the cracking driving force in ceramic coatings. *J Eur Ceram Soc* 2018, **38**: 5482–5488.

[355] Cheng B, Yang GJ, Zhang Q, *et al*. Gradient thermal cyclic behaviour of La$_2$Zr$_2$O$_7$/YSZ DCL-TBCs with equivalent thermal insulation performance. *J Eur Ceram Soc* 2018, **38**: 1888–1896.

[356] Bakan E, Mack DE, Mauer G, *et al*. Porosity–property relationships of plasma-sprayed Gd$_2$Zr$_2$O$_7$/YSZ thermal barrier coatings. *J Am Ceram Soc* 2015, **98**: 2647–2654.

[357] Ma W, Mack D, Malzbender J, *et al*. Yb$_2$O$_3$ and Gd$_2$O$_3$ doped strontium zirconate for thermal barrier coatings. *J Eur Ceram Soc* 2008, **28**: 3071–3081.

[358] Guo HB, Wang Y, Wang L, *et al*. Thermo-physical properties and thermal shock resistance of segmented La$_2$Ce$_2$O$_7$/YSZ thermal barrier coatings. *J Therm Spray*

Technol 2009, **18**: 665–671.

[359] Chen HF, Gao YF, Tao SY, *et al*. Thermophysical properties of lanthanum zirconate coating prepared by plasma spraying and the influence of post-annealing. *J Alloys Compd* 2009, **486**: 391–399.

[360] Rai AK, Schmitt MP, Bhattacharya RS, *et al*. Thermal conductivity and stability of multilayered thermal barrier coatings under high temperature annealing conditions. *J Eur Ceram Soc* 2015, **35**: 1605–1612.

[361] Cao XQ, Vassen R, Jungen W, *et al*. Thermal stability of lanthanum zirconate plasma-sprayed coating. *J Am Ceram Soc* 2001, **84**: 2086–2090.

[362] Wang L, Wang Y, Sun XG, *et al*. Thermal shock behavior of 8YSZ and double-ceramic-layer La$_2$Zr$_2$O$_7$/8YSZ thermal barrier coatings fabricated by atmospheric plasma spraying. *Ceram Int* 2012, **38**: 3595–3606.

[363] Kokini K, DeJonge J, Rangaraj S, *et al*. Thermal shock of functionally graded thermal barrier coatings with similar thermal resistance. *Surf Coat Technol* 2002, **154**: 223–231.

[364] Chen HF, Liu Y, Gao YF, *et al*. Design, preparation, and characterization of graded YSZ/La$_2$Zr$_2$O$_7$ thermal barrier coatings. *J Am Ceram Soc* 2010, **93**: 1732–1740.

[365] Zhang WW, Li GR, Zhang Q, *et al*. Multiscale pores in TBCs for lower thermal conductivity. *J Therm Spray Technol* 2017, **26**: 1183–1197.

[366] Cernuschi F, Ahmaniemi S, Vuoristo P, *et al*. Modelling of thermal conductivity of porous materials: Application to thick thermal barrier coatings. *J Eur Ceram Soc* 2004, **24**: 2657–2667.

[367] Wang L, Wang Y, Sun XG, *et al*. Influence of pores on the thermal insulation behavior of thermal barrier coatings prepared by atmospheric plasma spray. *Mater Des* 2011, **32**: 36–47.

[368] Dutton R, Wheeler R, Ravichandran KS, *et al*. Effect of heat treatment on the thermal conductivity of plasma-sprayed thermal barrier coatings. *J Therm Spray Technol* 2000, **9**: 204–209.

[369] Arai M, Ochiai H, Suidzu T. A novel low-thermal-conductivity plasma-sprayed thermal barrier coating controlled by large pores. *Surf Coat Technol* 2016, **285**: 120–127.

[370] Tjong SC, Chen H. Nanocrystalline materials and coatings. *Mater Sci Eng R Rep* 2004, **45**: 1–88.

[371] Fauchais P, Etchart-Salas R, Rat V, *et al*. Parameters controlling liquid plasma spraying: Solutions, sols, or suspensions. *J Therm Spray Technol* 2008, **17**: 31–59.

[372] Fauchais P, Montavon G, Lima RS, *et al*. Engineering a new class of thermal spray nano-based microstructures from agglomerated nanostructured particles, suspensions and solutions: An invited review. *J Phys D Appl Phys* 2011, **44**: 093001.

[373] Racek O, Berndt CC, Guru DN, *et al*. Nanostructured and conventional YSZ coatings deposited using APS and TTPR techniques. *Surf Coat Technol* 2006, **201**: 338–346.

[374] Zhou CG, Wang N, Wang ZB, *et al*. Thermal cycling life and thermal diffusivity of a plasma-sprayed nanostructured thermal barrier coating. *Scripta Mater* 2004, **51**: 945–948.

[375] Jordan EH, Jiang C, Roth J, *et al*. Low thermal conductivity yttria-stabilized zirconia thermal barrier coatings using the solution precursor plasma spray process. *J Therm Spray Technol* 2014, **23**: 849–859.

[376] Skoog A, Murphy J, Tomlinson T. Method for applying a plasma sprayed coating using liquid injection. U.S. patent 11 099 264, Oct. 2006.

[377] Cipri F, Marra F, Pulci G, *et al*. Plasma sprayed composite coatings obtained by liquid injection of secondary phases. *Surf Coat Technol* 2009, **203**: 2116–2124.

[378] Joshi SV, Sivakumar G. Hybrid processing with powders and solutions: A novel approach to deposit composite coatings. *J Therm Spray Technol* 2015, **24**: 1166–1186.

[379] Lima RS, Marple BR. Toward highly sintering-resistant nanostructured ZrO$_2$–7 wt.% Y$_2$O$_3$ coatings for TBC applications by employing differential sintering. *J Therm Spray Technol* 2008, **17**: 846–852.

[380] Ozturk A, Cetegen BM. Modeling of plasma assisted formation of precipitates in zirconium containing liquid precursor droplets. *Mater Sci Eng A* 2004, **384**: 331–351.

[381] Li GR, Yang GJ, Li CX, *et al*. Stage-sensitive microstructural evolution of nanostructured TBCs during thermal exposure. *J Eur Ceram Soc* 2018, **38**: 3325–3332.

[382] Zhang WW, Li GR, Zhang Q, *et al*. Bimodal TBCs with low thermal conductivity deposited by a powder-suspension co-spray process. *J Mater Sci Technol* 2018, **34**: 1293–1304.

[383] Zhang WW, Wei ZY, Zhang LY, *et al*. Low-thermal-conductivity thermal barrier coatings with a multi-scale pore design and sintering resistance following thermal exposure. *Rare Met* 2020, **39**: 352–367.

[384] Fauchais P, Rat V, Coudert JF, *et al*. Operating parameters for suspension and solution plasma-spray coatings. *Surf Coat Technol* 2008, **202**: 4309–4317.

[385] Bernard B, Quet A, Bianchi L, *et al*. Effect of suspension plasma-sprayed YSZ columnar microstructure and bond coat surface preparation on thermal barrier coating properties. *J Therm Spray Technol* 2017, **26**: 1025–1037.

[386] Curry N, VanEvery K, Snyder T, *et al*. Performance testing of suspension plasma sprayed thermal barrier coatings produced with varied suspension parameters. *Coatings* 2015, **5**: 338–356.

[387] Ganvir A, Curry N, Björklund S, *et al*. Characterization of microstructure and thermal properties of YSZ coatings obtained by axial suspension plasma spraying (ASPS). *J Therm Spray Technol* 2015, **24**: 1195–1204.

[388] Sokołowski P, Kozerski S, Pawłowski L, *et al*. The key process parameters influencing formation of columnar microstructure in suspension plasma sprayed zirconia coatings. *Surf Coat Technol* 2014, **260**: 97–106.

[389] Zhou DP, Guillon O, Vaßen R. Development of YSZ

thermal barrier coatings using axial suspension plasma spraying. *Coatings* 2017, **7**: 120.

[390] Curry N, Tang ZL, Markocsan N, *et al*. Influence of bond coat surface roughness on the structure of axial suspension plasma spray thermal barrier coatings—Thermal and lifetime performance. *Surf Coat Technol* 2015, **268**: 15–23.

[391] Ekberg J, Ganvir A, Klement U, *et al*. The influence of heat treatments on the porosity of suspension plasma-sprayed yttria-stabilized zirconia coatings. *J Therm Spray Technol* 2018, **27**: 391–401.

[392] Movchan BA. Inorganic materials and coatings produced by EBPVD. *Surf Eng* 2006, **22**: 35–46.

[393] Yoshiya M, Wada K, Jang BK, *et al*. Computer simulation of nano-pore formation in EB-PVD thermal barrier coatings. *Surf Coat Technol* 2004, **187**: 399–407.

[394] Matsumoto M, Kato T, Yamaguchi N, *et al*. Thermal conductivity and thermal cycle life of La_2O_3 and HfO_2 doped ZrO_2–Y_2O_3 coatings produced by EB-PVD. *Surf Coat Technol* 2009, **203**: 2835–2840.

[395] Singh J, Wolfe DE, Miller RA, *et al*. Tailored microstructure of zirconia and hafnia-based thermal barrier coatings with low thermal conductivity and high hemispherical reflectance by EB-PVD. *J Mater Sci* 2004, **39**: 1975–1985.

[396] Yanar NM, Helminiak M, Meier GH, *et al*. Comparison of the failures during cyclic oxidation of yttria-stabilized (7 to 8 weight percent) zirconia thermal barrier coatings fabricated via electron beam physical vapor deposition and air plasma spray. *Metall Mater Trans A* 2011, **42**: 905–921.

[397] Shen ZY, He LM, Xu ZH, *et al*. LZC/YSZ double layer coatings: EB-PVD, microstructure and thermal cycling life. *Surf Coat Technol* 2019, **367**: 86–90.

[398] Von Niessen K, Gindrat M. Plasma spray-PVD: A new thermal spray process to deposit out of the vapor phase. *J Therm Spray Technol* 2011, **20**: 736–743.

[399] Liu MJ, Yang GJ. Condensation behavior of gaseous phase during transported in the near-substrate boundary layer of plasma spray-physical vapor deposition. *J Mater Sci Technol* 2021, **67**: 127–134.

[400] Dong L, Liu MJ, Zhang XF, *et al*. Pressure infiltration of molten aluminum for densification of environmental barrier coatings. *J Adv Ceram* 2022, **11**: 145–157.

[401] Gao LH, Wei LL, Guo HB, *et al*. Deposition mechanisms of yttria-stabilized zirconia coatings during plasma spray physical vapor deposition. *Ceram Int* 2016, **42**: 5530–5536.

[402] Goral M, Kotowski S, Sieniawski J. The technology of plasma spray physical vapour deposition. *High Temp Mater Process* 2013, **32**: 33–39.

[403] Hospach A, Mauer G, Vaßen R, *et al*. Columnar-structured thermal barrier coatings (TBCs) by thin film low-pressure plasma spraying (LPPS-TF). *J Therm Spray Technol* 2011, **20**: 116–120.

[404] Von Niessen K, Eschendorff G, Gindrat M, *et al*. Advanced TBC systems by vapor deposition using LPPS thin film. In: Proceedings of the ASME Turbo Expo: Power for Land, Sea, and Air. Berlin, Germany, 2008: 263–268.

[405] Góral M, Kotowski S, Drajewicz M, *et al*. The PS-PVD method—Formation of columnar TBCs on CMSX-4 superalloy. *J Achiev Mater Manu Eng* 2012, **55**: 907–911.

[406] Mauer G, Hospach A, Zotov N, *et al*. Process conditions and microstructures of ceramic coatings by gas phase deposition based on plasma spraying. *J Therm Spray Technol* 2013, **22**: 83–89.

[407] Zhang XF, Zhou KS, Liu M, *et al*. Toughness and elasticity behaviors in nano-structured 7 wt.% Y_2O_3-stabilized ZrO_2 coating. *Surf Coat Technol* 2015, **276**: 316–319.

[408] Mauer G. Plasma characteristics and plasma-feedstock interaction under PS-PVD process conditions. *Plasma Chem Plasma Process* 2014, **34**: 1171–1186.

[409] Anwaar A, Wei LL, Guo HB, *et al*. Plasma–powder feedstock interaction during plasma spray–physical vapor deposition. *J Therm Spray Technol* 2017, **26**: 292–301.

[410] Liu MJ, Zhang M, Zhang Q, *et al*. Evaporation of droplets in plasma spray–physical vapor deposition based on energy compensation between self-cooling and plasma heat transfer. *J Therm Spray Technol* 2017, **26**: 1641–1650.

[411] Liu MJ, Zhang M, Zhang Q, *et al*. Gaseous material capacity of open plasma jet in plasma spray-physical vapor deposition process. *Appl Surf Sci* 2018, **428**: 877–884.

[412] Chen Q-Y, Peng X-Z, Yang G-J, *et al*. Characterization of plasma jet in plasma spray-physical vapor deposition of YSZ using a < 80 kW shrouded torch based on optical emission spectroscopy. *J Therm Spray Technol* 2015, **24**: 1038–1045.

[413] Liu MJ, Zhang KJ, Zhang Q, *et al*. Thermodynamic conditions for cluster formation in supersaturated boundary layer during plasma spray-physical vapor deposition. *Appl Surf Sci* 2019, **471**: 950–959.

[414] Liu MJ, Zhang M, Zhang XF, *et al*. Transport and deposition behaviors of vapor coating materials in plasma spray-physical vapor deposition. *Appl Surf Sci* 2019, **486**: 80–92.

[415] Gell M. Application opportunities for nanostructured materials and coatings. *Mater Sci Eng A* 1995, **204**: 246–251.

[416] Siegel RW. Nanostructured materials—Mind over matter. *Nanostruct Mater* 1993, **3**: 1–18.

[417] Lu YL, Liaw PK. The mechanical properties of nanostructured materials. *J Min Met Mater Soc* 2001, **53**: 31–35.

[418] Chen H, Ding CX. Nanostructured zirconia coating prepared by atmospheric plasma spraying. *Surf Coat Technol* 2002, **150**: 31–36.

[419] Zeng Y, Lee SW, Gao L, *et al*. Atmospheric plasma sprayed coatings of nanostructured zirconia. *J Eur Ceram Soc* 2002, **22**: 347–351.

[420] Wang N, Zhou CG, Gong SK, *et al*. Heat treatment of

nanostructured thermal barrier coating. *Ceram Int* 2007, **33**: 1075–1081.

[421] Lima RS, Marple BR. Thermal spray coatings engineered from nanostructured ceramic agglomerated powders for structural, thermal barrier and biomedical applications: A review. *J Therm Spray Technol* 2007, **16**: 40–63.

[422] Yang GJ, Li CX, Hao S, *et al*. Critical bonding temperature for the splat bonding formation during plasma spraying of ceramic materials. *Surf Coat Technol* 2013, **235**: 841–847.

[423] McPherson R. A review of microstructure and properties of plasma sprayed ceramic coatings. *Surf Coat Technol* 1989, **39–40**: 173–181.

[424] Lima RS, Kucuk A, Berndt CC. Bimodal distribution of mechanical properties on plasma sprayed nanostructured partially stabilized zirconia. *Mater Sci Eng A* 2002, **327**: 224–232.

[425] Lima RS, Kucuk A, Berndt CC. Integrity of nanostructured partially stabilized zirconia after plasma spray processing. *Mater Sci Eng A* 2001, **313**: 75–82.

[426] Wu J, Guo HB, Zhou L, *et al*. Microstructure and thermal properties of plasma sprayed thermal barrier coatings from nanostructured YSZ. *J Therm Spray Technol* 2010, **19**: 1186–1194.